

University of Potsdam  
Applied Condensed-Matter Physics

---

**Preparation and Investigation of  
Polymer-Foam Films and Polymer-Layer Systems  
for Ferroelectrets**

Dissertation

in partial fulfillment of the  
requirements of the degree of  
**Doctor rerum naturalium**  
in Applied Materials Physics

submitted to

Faculty of Science  
University of Potsdam

presented by

Peng Fang

Potsdam, May 2010

This work is licensed under a Creative Commons License:  
Attribution - Noncommercial - Share Alike 3.0 Unported  
To view a copy of this license visit  
<http://creativecommons.org/licenses/by-nc-sa/3.0/>

Published online at the  
Institutional Repository of the University of Potsdam:  
URL <http://opus.kobv.de/ubp/volltexte/2010/4841/>  
URN <urn:nbn:de:kobv:517-opus-48412>  
<http://nbn-resolving.org/urn:nbn:de:kobv:517-opus-48412>

Peng Fang,  
Student Matriculation Number 734259 (University of Potsdam)

I, Peng Fang, formally submit my thesis  
“Preparation and Investigation of Polymer-Foam Films and Polymer-Layer Systems for  
Ferroelectrets”  
in fulfillment of the requirements set forth by the Regulations for awarding the title “doctor rerum  
naturalium” (Dr. rer. nat.) in the Faculty of Science of the University of Potsdam.

I declare that the work presented in this thesis has not been submitted as an exercise for a degree  
to any other university. The work described herein is entirely my own, except for the assistance  
mentioned in the acknowledgments and collaborative work mentioned in the list of publications.  
The present thesis work was completed within the “Applied Condensed-Matter Physics” (ACMP)  
group at the Institute of Physics and Astronomy of the University of Potsdam.

May 2010





# Summary

Piezoelectric materials are very useful for applications in sensors and actuators. In addition to traditional ferroelectric ceramics and ferroelectric polymers, ferroelectrets have recently become a new group of piezoelectrics. Ferroelectrets are functional polymer systems for electromechanical transduction, with elastically heterogeneous cellular structures and internal quasi-permanent dipole moments. The piezoelectricity of ferroelectrets stems from linear changes of the dipole moments in response to external mechanical or electrical stress. Over the past two decades, polypropylene (PP) foams have been investigated with the aim of ferroelectret applications, and some products are already on the market. PP-foam ferroelectrets may exhibit piezoelectric  $d_{33}$  coefficients of 600 pC/N and more. Their operating temperature can, however, not be much higher than 60 °C. Recently developed polyethylene-terephthalate (PET) and cyclo-olefin copolymer (COC) foam ferroelectrets show slightly better  $d_{33}$  thermal stabilities, but usually at the price of smaller  $d_{33}$  values. Therefore, the main aim of this work is the development of new thermally stable ferroelectrets with appreciable piezoelectricity. Physical foaming is a promising technique for generating polymer foams from solid films without any pollution or impurity. Supercritical carbon dioxide (CO<sub>2</sub>) or nitrogen (N<sub>2</sub>) are usually employed as foaming agents due to their good solubility in several polymers. Polyethylene propylene (PEN) is a polyester with slightly better properties than PET. A “voiding + inflation + stretching” process has been specifically developed to prepare PEN foams. Solid PEN films are saturated with supercritical CO<sub>2</sub> at high pressure and then thermally voided at high temperatures. Controlled inflation (Gas-Diffusion Expansion or GDE) is applied in order to adjust the void dimensions. Additional biaxial stretching decreases the void heights, since it is known lens-shaped voids lead to lower elastic moduli and therefore also to stronger piezoelectricity. Both, contact and corona charging are suitable for the electric charging of PEN foams. The light emission from the dielectric-barrier discharges (DBDs) can be clearly observed. Corona charging in a gas of high dielectric strength such as sulfur hexafluoride (SF<sub>6</sub>) results in higher gas-breakdown strength in the voids and therefore increases the piezoelectricity. PEN foams can exhibit piezoelectric  $d_{33}$  coefficients as high as 500 pC/N. Dielectric-resonance spectra show elastic moduli  $c_{33}$  of 1 – 12 MPa, anti-resonance frequencies of 0.2 – 0.8 MHz, and electromechanical coupling factors of 0.016 – 0.069. As expected, it is found that PEN foams show better thermal stability than PP and PET. Samples charged at room temperature can be utilized up to 80 – 100 °C. Annealing after charging or charging at elevated temperatures may improve thermal stabilities. Samples charged at suitable elevated temperatures show working temperatures as high as 110 – 120 °C. Acoustic measurements at frequencies of 2 Hz – 20 kHz show that PEN foams can be well applied in this frequency range. Fluorinated ethylene-propylene (FEP) copolymers are fluoropolymers with very good physical, chemical and electrical properties. The charge-storage ability of solid FEP films can be significantly improved by adding boron nitride (BN) filler particles. FEP foams are prepared by means of a one-step procedure consisting of CO<sub>2</sub> saturation and subsequent *in-situ* high-temperature voiding. Piezoelectric  $d_{33}$  coefficients up to 40 pC/N are measured on such FEP foams. Mechanical fatigue tests show that the as-prepared PEN and FEP foams are mechanically stable for long periods of time. Although polymer-foam ferroelectrets have a high application potential, their piezoelectric properties strongly depend on the cellular morphology, i.e. on size, shape, and distribution of the voids. On

the other hand, controlled preparation of optimized cellular structures is still a technical challenge. Consequently, new ferroelectrets based on polymer-layer system (sandwiches) have been prepared from FEP. By sandwiching an FEP mesh between two solid FEP films and fusing the polymer system with a laser beam, a well-designed uniform macroscopic cellular structure can be formed. Dielectric resonance spectroscopy reveals piezoelectric  $d_{33}$  coefficients as high as 350 pC/N, elastic moduli of about 0.3 MPa, anti-resonance frequencies of about 30 kHz, and electromechanical coupling factors of about 0.05. Samples charged at elevated temperatures show better thermal stabilities than those charged at room temperature, and the higher the charging temperature, the better is the stability. After proper charging at 140 °C, the working temperatures can be as high as 110 – 120 °C. Acoustic measurements at frequencies of 200 Hz – 20 kHz indicate that the FEP layer systems are suitable for applications at least in this range.

## **Keywords**

Electroactive material, cellular structure, polymer foam, polymer film, polyethylene naphthalate (PEN), polyethylene terephthalate (PET), fluorinated ethylene-propylene (FEP), ferroelectret, piezoelectricity, thermal stability, frequency response.

# Zusammenfassung

## Präparation und Untersuchung von Polymerschaumfolien und Polymerschichtsystemen für Ferroelektrete

Piezoelektrische Materialien haben große technische und wirtschaftliche Bedeutung für Anwendungen in Sensoren und Aktuatoren. Neben den traditionellen ferroelektrischen Keramiken und Polymeren bilden Ferroelektrete eine neue Gruppe der Piezoelektrika. Ferroelektrete sind reversible funktionelle Polymersysteme zur Umwandlung von elektrischer in mechanische Energie und umgekehrt. Sie zeichnen sich aus durch eine elastische zelluläre Struktur mit internen quasi-permanenten Dipolen. Der Mechanismus der Piezoelektrizität in Ferroelektreten wird dominiert von der Änderung der einzelnen Dipolmomente bei Einwirkung einer äußeren mechanischen Kraft. Insbesondere zelluläres Polypropylen (PP) war in den vergangenen zwei Jahrzehnten Gegenstand intensiver Forschung und Entwicklung im Hinblick auf die grundlegenden Eigenschaften und Anwendungen von Ferroelektreten. Einige bereits erhältliche kommerzielle Produkte nutzen die in geladenem zellulären PP erreichbaren hohen piezoelektrischen  $d_{33}$ -Koeffizienten von 600 pC/N und mehr, sind aber durch eine relativ geringe maximale Betriebstemperatur von ungefähr 60 °C eingeschränkt. Die kürzlich entwickelten Ferroelektrete aus zellulärem Polyethylenterephthalat (PET) und zellulären Cyclo-Olefin-Copolymeren (COC) zeigen eine bessere Temperaturbeständigkeit (vor allem COC), allerdings gewöhnlich auf Kosten von geringeren  $d_{33}$ -Koeffizienten. Das Ziel der vorliegenden Arbeit ist es, temperaturbeständige Ferroelektrete mit für den Markt geeigneten piezoelektrischen Eigenschaften zu entwickeln. Physikalisches Schäumen ist eine beliebte Methode, um besonders reine Polymerschäume herzustellen. Häufig werden, wegen ihrer guten Löslichkeit in vielen Polymeren, Kohlenstoffdioxid (CO<sub>2</sub>) und Stickstoff (N<sub>2</sub>) im superkritischen Zustand als Treibmittel eingesetzt. Der Polyester Polyethylnaphtalat (PEN) hat ähnliche Eigenschaften wie PET, ist jedoch temperaturbeständiger. Ein Dreistufenprozess (Schäumen, Aufblähen und Strecken) wurde entwickelt, um PEN-Schäume für hochwertige Ferroelektrete herzustellen. Ungeschäumte PEN-Folien werden mit superkritischem CO<sub>2</sub> unter hohem Druck gesättigt und anschließend unter geringem Druck bei Temperaturen nahe der Glasatemperatur geschäumt. Um die Hohlräume zu vergrößern, wird der Schaum anschließend mittels Gasdiffusionsexpansion (GDE) aufgebläht. Nach zusätzlichem biaxialen Verstrecken erhält man die optimalen linsenförmigen Zellen, welche zu einer minimalen mechanischen Steifigkeit und einem maximalen piezoelektrischen  $d_{33}$ -Koeffizienten des Ferroelektrets führen. Sowohl Korona- als auch Kontaktaufladung werden an zellulärem PEN erfolgreich eingesetzt. Die Lichtemission der dielektrisch behinderten Entladungen (DBDs) kann klar beobachtet werden. Korona-Aufladung in Gasen mit hohen dielektrischen Durchbruchfestigkeiten, wie z.B. Schwefelhexafluorid (SF<sub>6</sub>), ermöglicht es, das Paschen-Durchbruchfeld in den Hohlräumen und damit die erzielbare interne Ladungsdichte zu erhöhen. Dadurch können für zelluläres PEN piezoelektrische  $d_{33}$ -Koeffizienten bis zu 500 pC/N erzielt werden. Piezoelektrischen Resonanzmessungen der Ferroelektrete liefern Steifigkeiten  $c_{33}$  im Bereich von 1 – 12 MPa, Antiresonanzfrequenzen von 0.2 – 0.8 MHz und elektromechanische Kopplungsfaktoren zwischen 0.016 und 0.069. PEN-Ferroelektrete zeigen eine bessere

Temperaturstabilität als solche aus PP und PET. Der Anwendungsbereich von unbehandeltem PEN reicht bis etwa 80 – 100°C, jener von getemperten oder bei 120°C geladenen Proben bis etwa 110 – 120 °C. Akustische Messungen im Frequenzbereich von 2 Hz – 20 kHz zeigen die Eignung von PEN-Ferroelektretwandlern für Luftschallanwendungen. Fluoriertes Ethylen-Propylen (FEP) ist ein Fluorpolymer mit sehr guten physikalischen, chemischen und elektrischen Eigenschaften. Die Ladungsspeichereigenschaften von ungeschäumtem FEP können durch die Beimengung von Bornitrid deutlich verbessert werden. In dieser Arbeit wird zelluläres FEP mittels eines einstufigen Prozesses, dem schon erwähnten Schäumen mit überkritischem CO<sub>2</sub>, hergestellt. Die geladenen FEP-Proben weisen  $d_{33}$ -Koeffizienten von bis zu 40 pC/N auf. Ermüdungstests zeigen eine sehr gute mechanische Stabilität von PEN- und FEP-Ferroelektreten. Zelluläre Polymerferroelektrete haben großes Potenzial für Anwendungen, und die Suche nach geeigneten zellulären Morphologien ist eng verknüpft mit dem technischen Aufwand ihrer Herstellung. Alternativ wurden Ferroelektrete mit Sandwich-Strukturen aus FEP-Folien entwickelt. Durch Laserverschmelzen eines FEP-Foliengitters mit zwei umgebenden FEP-Folien wird eine definierte, einheitliche zelluläre Struktur gebildet. Aus dielektrischen Resonanzspektren können effektive piezoelektrische  $d_{33}$ -Koeffizienten bis zu 350 pC/N, effektive mechanische Steifigkeiten um 0.3 MPa, Antiresonanzfrequenzen um 30 kHz und elektromechanische Kopplungsfaktoren von etwa 0.05 abgeleitet werden. Proben, welche bei erhöhter Temperatur geladen werden, zeigen höhere Ladungsstabilitäten. Nach geeigneter Aufladung bei 140 °C kann die Arbeitstemperatur bis auf 110 – 120 °C gesteigert werden. Akustische Messungen im Frequenzbereich von 2 Hz – 20 kHz zeigen die Eignung von FEP-Sandwich-Strukturen für Luftschallanwendungen.

# Acknowledgment

This thesis would not be possible without the support of the “Applied Condensed-Matter Physics” group at the Institute of Physics and Astronomy, Faculty of Science, University of Potsdam.

I would like to express my sincere gratitude to my advisor, Prof. Dr. Reimund Gerhard, for giving me the opportunity to work in his group and for his support, comments and advises during the course of research.

I would like to thank all (past and present) “Applied Condensed-Matter Physics” group members with whom I worked during the past few years. Especially, I would like to thank Dipl.-Ing. Werner Wirges for the valuable advises which provided a pathway to solve the problems, and for all the technical supports during the whole research work. I would like to thank Sandra Zeretzke for the constant assistance with the arrangement of my administrative tasks.

I have profited a lot from the collaboration when working in the joint research projects. Special thanks to Prof. Dr. Helmut Münstedt and Dipl.-Ing. Larissa Zirkel (University of Erlangen-Nürnberg) for supplying part of the samples and inspiring discussions. Many thanks to Prof. Dr. Ruy Alberto Correa Altafim and Prof. Dr. Heitor Cury Basso (University of São Paulo) for their support during my stay in São Carlos. Many thanks to Prof. Dr. Zhongfu Xia (Tongji University) for stimulating discussions during his visit in Potsdam.

I am indebted to my family for the affection, support and encouragement throughout my graduate studies. Finally, I would also like to thank all my friends.

This research was partly supported by the funding from DFG project (Germany) (GE 945/8-3), and from CAPES (Brazil) and DAAD (Germany) (PROBRAL No. D/08/11608).



# Content

<b>1 Introduction</b> .....	1
<b>1.1 Background</b> .....	1
<b>1.2 Aim of this work</b> .....	3
<b>2 Piezoelectricity</b> .....	5
<b>2.1 A short history</b> .....	5
<b>2.2 Piezoelectric coefficient</b> .....	6
<b>2.3 Typical piezoelectric materials</b> .....	8
<b>2.3.1 Crystal – Rochelle salt</b> .....	8
<b>2.3.2 Ceramic – Lead zirconate titanate (PZT)</b> .....	8
<b>2.3.3 Ferroelectric polymer – <math>\beta</math>-phase polyvinylidene fluoride (<math>\beta</math>-PVDF)</b> .....	8
<b>3 Ferroelectrets</b> .....	11
<b>3.1 Physical description</b> .....	11
<b>3.2 Piezoelectric properties</b> .....	12
<b>3.3 Stability</b> .....	12
<b>3.4 Model</b> .....	14
<b>3.5 Typical ferroelectrets</b> .....	15
<b>3.5.1 Polypropylene (PP)</b> .....	15
<b>3.5.2 Polyethylene terephthalate (PET)</b> .....	15
<b>3.5.3 Cyclo-olefin copolymer (COC)</b> .....	16
<b>3.6 Applications</b> .....	17
<b>4 Cellular structure development</b> .....	19
<b>4.1 Polypropylene (PP) foam</b> .....	19
<b>4.2 Polyethylene-terephthalate (PET) foam</b> .....	20
<b>4.3 Fluorinated ethylene-propylene (FEP) foam</b> .....	22
<b>4.4 Heterogeneous multilayer structure</b> .....	24
<b>5 Electrical charging</b> .....	25
<b>5.1 Dielectric-barrier discharge (DBD)</b> .....	25
<b>5.2 Description of charging process</b> .....	28
<b>5.3 Threshold behavior and saturation phenomenon</b> .....	30
<b>5.4 Charging techniques</b> .....	32
<b>5.4.1 Contact (direct) charging</b> .....	32
<b>5.4.2 Tip-to-plane corona charging</b> .....	32
<b>5.4.3 Comparison between contact charging and corona charging</b> .....	33
<b>5.5 Optimized charging conditions</b> .....	34
<b>5.5.1 Charging in sulfur hexafluoride (<math>\text{SF}_6</math>)</b> .....	34
<b>5.5.2 Charging at elevated temperatures</b> .....	34

<b>6 Experimental techniques</b> .....	35
<b>6.1 Investigation of structure</b> .....	35
6.1.1 Microscopy.....	35
6.1.2 Porosity.....	36
6.1.3 Elastic modulus.....	38
<b>6.2 Investigation of charging behavior</b> .....	40
6.2.1 Contact charging and corona charging.....	40
6.2.2 Observation of light emission from dielectric-barrier discharge.....	41
<b>6.3 Investigation of surface potential</b> .....	42
<b>6.4 Dynamic measurement</b> .....	43
<b>6.5 Dielectric-resonance spectroscopy (DRS)</b> .....	45
<b>6.6 Acoustic measurement</b> .....	47
<b>6.7 Fourier transform infrared (FTIR) spectroscopy</b> .....	51
<b>6.8 Differential scanning calorimetry (DSC)</b> .....	51
<b>7 Polyethylene-naphthalate (PEN) foam ferroelectrets</b> .....	53
<b>7.1 Properties of PEN</b> .....	53
<b>7.2 Formation and optimization of PEN foam</b> .....	56
7.2.1 Description of technique.....	56
7.2.2 Investigation of foaming behavior.....	58
<b>7.3 Investigation of cellular structure</b> .....	61
<b>7.4 Investigation of electric charging behavior</b> .....	64
<b>7.5 Investigation of piezoelectric properties</b> .....	67
7.5.1 Dynamic measurement.....	67
7.5.2 Dielectric-resonance spectroscopy (DRS).....	70
7.5.3 Acoustic measurement.....	75
7.5.4 Density dependent piezoelectricity.....	78
7.5.5 Temporal stability of piezoelectricity.....	78
7.5.6 Thermal stability of piezoelectricity and its improvement.....	79
<b>8 Fluorinated ethylene-propylene (FEP) foam ferroelectrets</b> .....	87
<b>8.1 Properties of FEP</b> .....	87
<b>8.2 Investigation of solid FEP film</b> .....	89
8.2.1 Preparation.....	89
8.2.2 Charge stability.....	91
<b>8.3 Preparation and investigation of FEP foam</b> .....	94
8.3.1 Description of technique.....	94
8.3.2 Investigation of cellular structure.....	95
8.3.3 Investigation of electric charging behavior.....	97
<b>8.4 Investigation of piezoelectric properties</b> .....	101
<b>9 Fluorinated ethylene-propylene (FEP) layer ferroelectrets</b> .....	105
<b>9.1 Preparation of FEP layer system</b> .....	106



<b>9.2 Investigation of cellular structure</b> .....	109
<b>9.3 Investigation of piezoelectric properties</b> .....	110
<b>9.3.1 Limitation of dynamic measurement</b> .....	110
<b>9.3.2 Dielectric-resonance spectroscopy (DRS)</b> .....	111
<b>9.3.3 Acoustic measurement</b> .....	112
<b>9.3.4 Thermal stability of piezoelectricity and its improvement</b> .....	114
<b>9.4 Extension of structure</b> .....	119
<b>10 Conclusion and outlook</b> .....	121
<b>10.1 Conclusion</b> .....	121
<b>10.2 Outlook</b> .....	125
<b>References</b> .....	127
<b>Contributions</b> .....	139



# Chapter 1

## Introduction

### 1.1 Background

Since the discovery of piezoelectricity in the late 19th century, a great deal of interest has been shown in this novel electromechanical property. A lot of materials including crystals and ceramics are under investigation and some of them were developed into piezoelectric devices for actual applications. Piezoelectricity was intimately connected with ferroelectricity, which is the property to store a permanent electric field. All ferroelectrics are piezoelectric, but they additionally possess a reversible, nonvolatile spontaneous electric dipole moment in the absence of an external electric field. At the end of 1960s, a strong piezoelectric effect was discovered in  $\beta$ -phase polyvinylidene fluoride (PVDF) when it is electrically poled [[Kawai 1969](#)]. This was a great improvement for the applications of piezoelectricity since polymer-based devices can be completely flexible, light-weight, inexpensive, and easily fabricated on large scale [[Wang 1988](#)].

A few decades ago, the concept of ferroelectret was introduced based on non-polar polymer foams and has gained more and more attention. Polymer foams are frequently used both in industry and in daily life. Compared with the non-cellular (solid) polymer films, they have significant advantages such as low density, low thermal conductivity, etc, which make them especially good for food packaging, thermal and electrical insulation [[Behrendt 2006](#)], and acoustical absorption. All of these applications utilize some of the appreciable properties of polymer foams. If their electric and mechanical properties are combined, however, a novel application as an electromechanical transducer can be realized. Electrically charged polymer foams can act as sensors and actuators by converting between electrical and mechanical signals, and they are called ferroelectrets [[Bauer 2004](#), [Wegener 2005\(1\)](#), [Bauer 2006](#)].

In an ideal ferroelectret, a cellular structure consists of gas-filled voids, surrounded by a polymer matrix. Positive and negative charges are stored separately on the internal gas/polymer interfaces facing each other, and form a permanent dipole moment. The piezoelectric activity arises from the combination of the internal dipole moment and the anisotropic cellular polymer matrix [[Paajanen 2001\(1\)](#), [Bauer 2004](#), [Wegener 2005\(1\)](#)]. For application as ferroelectrets, the electrically charged polymer foams should be metallized with electrodes on both outer surfaces. The internal stored charges generate compensating charges in the electrodes, in order to compensate the electric field in the voids. If the polymer foam is compressed by a mechanical stress, the height of the cellular voids is decreased due to the lower elastic modulus of gas compared to the polymer bulk. The distance between the positive and negative charges, i.e. the dipole moment, and therefore the amount of compensating charges, is then decreased. If the electrodes are short-circuited, a current is generated. The important feature of the ferroelectrets is their anisotropic heterogeneous structure with low elastic stiffness. Ferroelectrets exhibit

permanent orientation of the inner dipoles and a hysteresis in response to an outer electric field, by which the direction of the dipoles can be reversed.

Since the introduction of ferroelectrets, their application-relevant properties have been intensively investigated [[Lekkala 1996](#), [Paajanen 2000\(1\)](#)]. Ferroelectrets can be implemented as functional materials in electromechanical sensors and actuators, and as electrically charged layers in electrostatic transducers. Their applications also include microphones and loudspeakers that operate either in the electromechanical mode [[Backman 1990](#), [Kressmann 2001](#), [Hillenbrand 2004](#), [Wegener 2004\(1\)](#), [Wegener 2005\(2\)](#)] or in the electret mode of a classical electrostatic transducer (flat sensors or actuators) [[Paajanen 2000\(2\)](#)]. The electromechanical operation of ferroelectrets is based on the change in the film thickness, while the electret operation relies on the movement of the film with respect to an air gap. Polymer foams are light-weight and flexible, which provide the opportunity to easily form complicated shapes. Therefore they can be combined with flexible electronic components to form a thin and flexible product, such as ferroelectret field-effect transistor [[Graz 2006](#)].

For a long time after the introduction of the ferroelectret concept, polypropylene (PP) was almost the only polymer that was investigated for ferroelectret applications. Therefore, PP became the standard material for the production of ferroelectret films [[Räisänen 1995](#), [Sessler 1999\(1\)](#), [Hillenbrand 2000](#), [Paajanen 2001\(2\)](#)]. The basic preparation and further optimization of PP foams, as well as the resulting electromechanical properties of PP-based ferroelectret transducers were explored in detail [[Bauer 2004](#), [Wegener 2005\(1\)](#)]. After optimized structure preparation and proper electrical charging, PP ferroelectrets show high piezoelectric  $d_{33}$  coefficients up to some hundred pC/N. PP ferroelectrets have already been developed into industrial products with the applications such as pick-ups for musical instruments, motion sensors for health-care applications or sensors for touch panels [[Wegener 2005\(1\) and references therein](#)].

For most piezoelectric devices, including ferroelectrics and ferroelectrets, the working temperature is a critical parameter which determines their application area. For ferroelectrics, the application of  $\beta$ -phase PVDF is limited to below 90 °C, because a de-poling occurs at higher temperatures and the piezoelectric activity is lost [[Sessler 1981](#)]. For ferroelectrets, although PP shows a strong piezoelectric response, its maximum service temperature is in the range between 60 and 80 °C, depending on the preparation. This is due to the low thermal stability of the charges stored inside the voids, especially at temperatures above 50 °C [[Taylor 2005](#), [Mellinger 2006](#)]. The thermally stimulated discharge (TSD) under short-circuit conditions and the decay of piezoelectricity at elevated temperatures show that PP ferroelectrets should not be used or stored at temperatures higher than 70 °C [[Yang 1993](#), [Sessler 1999\(2\)](#), [Guarrotxena 2000](#), [Paajanen 2001\(2\)](#)]. Therefore, both the  $\beta$ -phase PVDF and cellular PP are not appropriate for applications at higher surrounding temperatures such as for automobile interiors.

Recently, ferroelectrets based on polyethylene terephthalate (PET), cyclo-olefin polymer (COP) and cyclo-olefin copolymer (COC) have been prepared and investigated [[Lekkala 1999](#), [Sessler 1999\(3\)](#), [Saarimäki 2006](#), [Wirges 2007](#), [Voronina 2008](#)]. Due to the enhanced thermal and temporal charge stability, PET ferroelectrets show enhanced working temperature up to

80 – 100 °C [[Lekkala 1999](#), [Sessler 1999\(3\)](#), [Wirges 2007](#), [Voronina 2008](#)]. Further more, COP as well as COC ferroelectrets show an even higher working temperature up to 110 °C, but at the price of much lower piezoelectric activity [[Saarimäki 2006](#), [Voronina 2008](#)].

Piezoelectric properties of ferroelectrets strongly depend on the morphology of the cellular structure, i.e. the size and the distribution of the voids. However, present foaming techniques generate cellular voids with dimension of a few to dozens of micrometers, where the void shapes are not uniform, and the void sizes are sometimes distributed over a large range. This disadvantage usually influences the resulting piezoelectric properties and also limits the reproducibility in industry, where relatively uniform products with well controlled property deviation are required.

Mainly due to the difficulty of preparing an ideal cellular structure in polymer foams, some other approaches were proposed. By sandwiching a layer of highly expanded polytetrafluoroethylene (PTFE) between two layers of solid fluorinated ethylene-propylene (FEP) films, strong piezoelectricity and improved thermal stability were achieved in this sandwich system [[Hu 2006](#)]. Recently, a new technique towards macroscopic cellular polymer systems was introduced [[Altafim 2003](#), [Altafim 2006](#), [Zhang 2006\(1\)](#)]. Polymer films with thermo-formed cupolas are sandwiched and thermally fused between continuous polymer films, therefore relatively large but uniform cells are formed. Due to the rather large dipole moment in the macroscopic voids, strong piezoelectric activity can be achieved. This new scheme has been demonstrated on fluoropolymer films with good thermal and long-term stabilities [[Altafim 2003](#), [Altafim 2006](#), [Zhang 2006\(1\)](#)]. More recently, another new concept of template-based fluorinated ethylene-propylene ferroelectrets with tubular channels has also been presented, which can serve as a material platform for several types of piezoelectric or even multifunctional ferroelectret films [[Altafim 2009](#)]. In these template-based piezoelectrets, a structure with well-defined uniform tubular channels is formed by means of a lamination process at 300 °C. Due to the excellent thermal charge stability of FEP, a working temperature up to 130 °C can be achieved when samples are properly charged at elevated temperatures of 140 °C.

## 1.2 Aim of this work

Based on this introduced background, the main aim of this work is to develop and characterize new ferroelectrets with enhanced properties.

In this work, polyethylene naphthalate (PEN) and fluorinated ethylene-propylene (FEP) were utilized as the candidates for preparing piezoelectric active polymer foams. A special structure foaming and optimization process was realized on PEN films. Proper electrical and thermal treatments were performed on PEN foams in order to achieve and further more, to enhance the resulting piezoelectric properties. Collaborating with a project partner (Institute of Polymer Material, University of Erlangen-Nürnberg, Germany), solid FEP films and FEP foams were investigated and primarily developed into ferroelectrets. As well as polymer foams, piezoelectric active multilayer polymer systems with macroscopic cellular structures were also developed based on FEP. The related piezoelectric properties and possible extension will be discussed.

In this work, the structure investigation and charging behavior are discussed in detail with respect to the resulting properties. Temporal and thermal stability were studied and possible improvement was attempted. Different investigation techniques such as dielectric-resonance spectra and acoustic measurements were widely utilized.

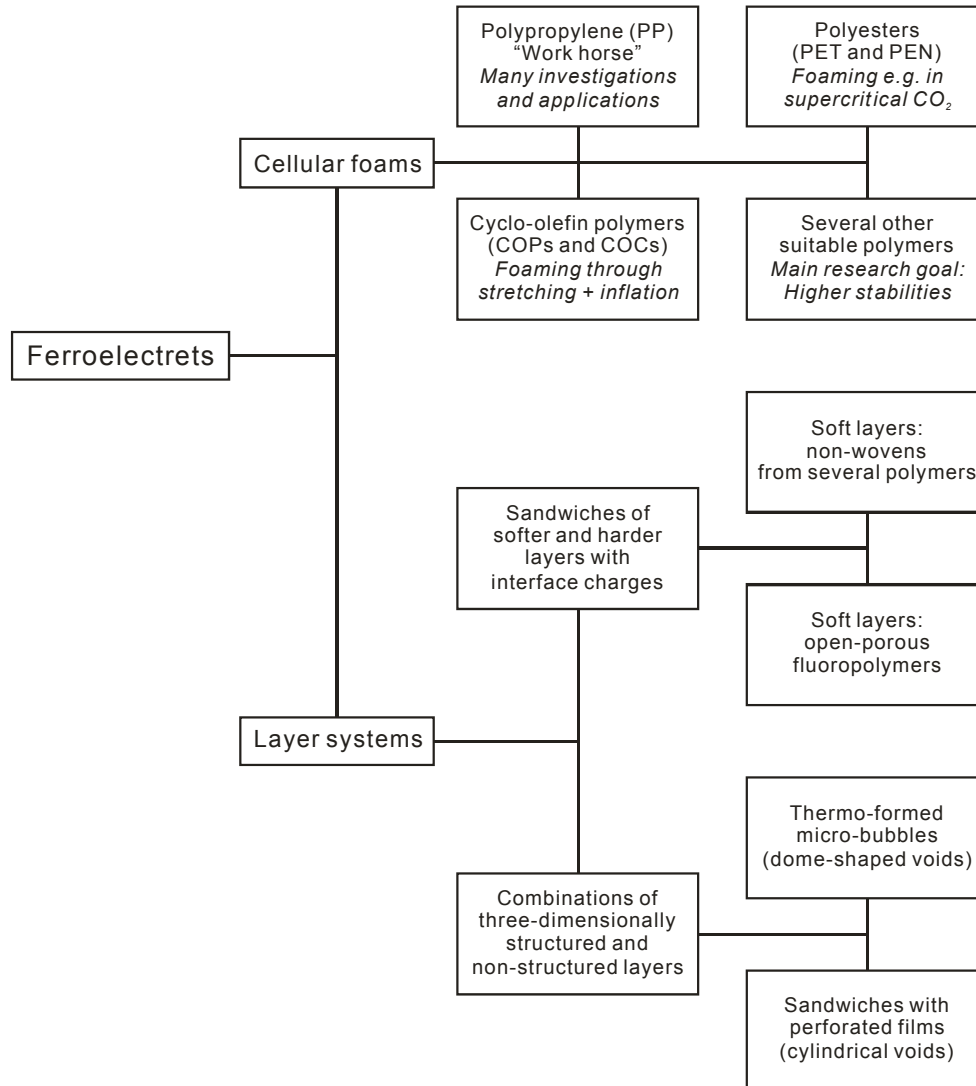


Figure 1.1: Family tree of ferroelectrets: Demonstrated and investigated variants of ferroelectrets (as of mid-2007).

# Chapter 2

## Piezoelectricity

### 2.1 A short history

In 1880, Pierre Curie and Jacques Curie discovered a special phenomenon that some crystals including tourmaline, quartz, and Rochelle salt could generate electrical polarization when they were subjected to mechanical stress and this effect was quickly named as piezoelectricity. Formally, piezoelectricity is defined as the ability to generate a voltage in response to applied mechanical stress. In 1881, Lippmann mathematically deduced the reverse piezoelectricity (stress in response to electric field) from thermodynamics. The Curies immediately confirmed this reverse effect, and obtained quantitative proof of the complete reversibility of electro-elasto-mechanical deformations in piezoelectric crystals. In the early 20th century the first generation of piezoelectric devices based on natural crystals were conceived. These special properties make piezoelectric crystals extremely versatile as electromechanical transducers including microphones, ultrasonic transducers, bender element actuators, phonograph pick-ups, etc. However, the materials available at that time often limited the performance and certainly the commercial applications. During the Second World War, ceramic materials which exhibited dielectric constants up to 100 times higher than that of common crystals were prepared by sintering metallic oxide powders. The discovery of easily manufactured piezoelectric ceramics with outstanding performance characteristics naturally touched off a revival of intense research and development into piezoelectric devices.

Piezoelectricity was intimately connected with ferroelectricity, which was discovered by J. Valasek in 1921 [[Gonzalo 2005](#)]. Ferroelectricity is the property to store a permanent electric field. All ferroelectrics are piezoelectric, but they additionally possess a reversible, nonvolatile spontaneous electric dipole moment in the absence of an external electric field. Ferroelectricity was first discovered in Rochelle salt, and significant progress in applications became possible after the discovery of lead zirconate titanate ( $\text{Pb}(\text{Zr},\text{Ti})\text{O}_3$ , PZT) which has a strong piezoelectric response. Up to the 1960s all piezoelectric devices utilized either single-crystal structures such as quartz, or polycrystalline ceramics such as PZT. In 1969, Kawai [[Kawai 1969](#)] discovered that a strong piezoelectric effect could be induced in  $\beta$ -phase polyvinylidene fluoride ( $\beta$ -PVDF) by application of an electric field. This was a great contribution to the applications of piezoelectricity, due to the advantages of polymer-based devices: flexible, light-weight, inexpensive, and easily fabricated on large scale [[Wang 1988](#)].

About two decades ago, the concept of ferroelectret was introduced based on non-polar polymer foams [[Bauer 2004](#), [Wegener 2005\(1\)](#), [Bauer 2006](#)]. Separated positive and negative charges are stored on the internal gas/polymer surfaces of voids facing each other, forming macroscopic electric dipoles across the void height. The piezoelectric activity arises from the

combination of the internal dipole moment and the anisotropic cellular polymer matrix with relatively low elastic stiffness. Several polymers, such as polypropylene (PP) [Räsänen 1995, Sessler 1999(1), Hillenbrand 2000, Paajanen 2001(1), Bauer 2004, Wegener 2005(1)] have been investigated in detail and some of their applications have become available commercially [Wegener 2005(1) and references therein].

## 2.2 Piezoelectric coefficient

Piezoelectricity can be represented by the piezoelectric coefficient, which is defined from thermodynamics. In thermodynamics, the Gibbs free energy density is

$$G = U - \tau_i \sigma_i - D_m E_m - ST; i = 1 \dots 6, m = 1 \dots 3, \quad (2.1)$$

where  $U$  is the internal energy per unit volume,  $\tau$  and  $\sigma$  are the strain and stress tensors with components denotation  $i$ , respectively;  $D_m$  and  $E_m$  are the components of the electric displacement  $D$  and the electric field  $E$ ;  $S$  is the entropy per unit volume, and  $T$  is the temperature. In a full tensorial form, strain and stress can be expressed by the  $3 \times 3$  matrices  $\tau_{pq}$  and  $\sigma_{pq}$ . Figure 2.1 shows the components of the stress tensor  $\sigma_{pq}$ .

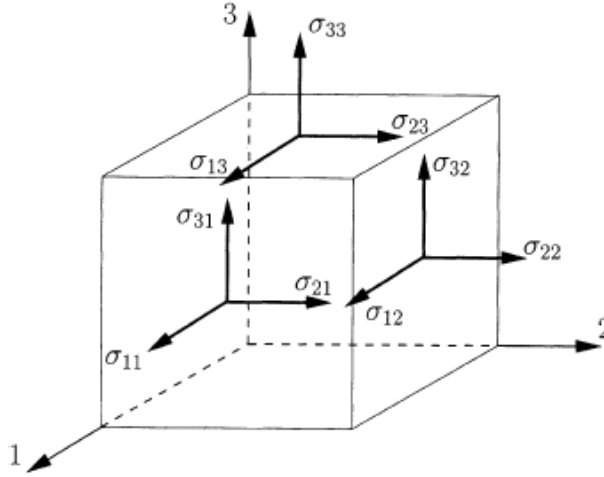


Figure 2.1: Components of the stress tensor shown on a cube.

$\sigma$  and  $\tau$  can be written as  $\sigma = (\sigma_{11}, \sigma_{22}, \sigma_{33}, 2\sigma_{13}, 2\sigma_{23}, 2\sigma_{12})$  and  $\tau = (\tau_{11}, \tau_{22}, \tau_{33}, 2\tau_{13}, 2\tau_{23}, 2\tau_{12})$ , because they are symmetric tensors with only 6 independent elements. In addition, the electric field  $E$  and electric displacement  $D$  are vectors specified by three independent components:  $E = (E_1, E_2, E_3)$  and  $D = (D_1, D_2, D_3)$ . From the differential

$$dG = -\tau_i d\sigma_i - D_m dE_m - SdT, \quad (2.2)$$

it is clear that the temperature is a free variable and  $G$  is suited for describing isothermal processes which means  $dT = 0$ .

In another case, fast oscillation processes are far from thermal equilibrium and therefore



should be treated as an adiabatic process (constant entropy,  $dS = 0$ ), and described by enthalpy

$$H = U - \tau_i \sigma_i - D_m E_m; i = 1 \dots 6, m = 1 \dots 3. \quad (2.3)$$

The adiabatic piezoelectric strain coefficient  $d_{mi}$  is defined as [\[Mellinger 2003\]](#)

$$d_{mi} = - \left( \frac{\partial^2 H}{\partial E_m \partial \sigma_i} \right)_S, \quad (2.4)$$

where the subscript  $S$  denotes that entropy is kept constant. Since the derivative of enthalpy

$$dH = -\tau_i d\sigma_i - D_m dE_m + TdS \quad (2.5)$$

is a perfect differential, the derivatives can be taken in arbitrary order, so that

$$d_{mi} = \left( \frac{\partial D_m}{\partial \sigma_i} \right)_{E,S} = \left( \frac{\partial \tau_i}{\partial E_m} \right)_{\sigma,S}. \quad (2.6)$$

Here  $(\partial D_m / \partial \sigma_i)_{E,S}$  describes the direct piezoelectricity which means an electric displacement caused by mechanical stress, and  $(\partial \tau_i / \partial E_m)_{\sigma,S}$  represents the reverse piezoelectricity which means a dimensional change caused by an electric field. The subscripts  $m$  and  $i$  denote the direction of displacement (field) and stress (strain). For example,  $d_{33}$  means induced polarization in direction 3 per unit stress applied in direction 3 or induced strain in direction 3 per unit electric field applied in direction 3.  $d_{31}$  means induced polarization in direction 3 per unit stress applied in direction 1 or induced strain in direction 1 per unit electric field applied in direction 3.  $d_{15}$  means induced polarization in direction 1 per unit shear stress applied about direction 2 or induced shear strain about direction 2 per unit electric field applied in direction 1.

Considering an infinite parallel plate capacitor placed in vacuum (or in any medium) with no free charges present except on the capacitor, the charge density on the plates is equal to the value of  $D$  between the plates. This follows directly from Gauss's law, by integrating over a small rectangular box

$$\oint_A D \cdot dA = Q. \quad (2.7)$$

The part of the box inside the capacitor plate has no field, so this part of the integral is zero. On the sides of the box,  $dA$  is perpendicular to  $D$ , so this part of the integral is also zero, leaving

$$|D| = \frac{Q}{A}, \quad (2.8)$$

which is the charge density on the plate. In addition, the stress  $\sigma$  is defined as

$$\sigma = \frac{F}{A}. \quad (2.9)$$

If considering  $A$  is constant, the piezoelectric  $d_{mi}$  coefficient can be written as

$$d_{mi} = \left( \frac{\partial D_m}{\partial \sigma_i} \right)_{E,S} = \left( \frac{\partial (Q/A)_m}{\partial (F/A)_i} \right)_{E,S} = \left( \frac{\partial Q_m}{\partial F_i} \right)_{E,S} = \left( \frac{\Delta Q_m}{\Delta F_i} \right)_{E,S}, \quad (2.10)$$

which describes the piezoelectric coefficient more directly: charges generated by application of force, with units of C/N, but pC/N is mostly used. According to equation 2.10, the piezoelectric coefficient can be easily determined by measuring the generated charge and the applied force.

## 2.3 Typical piezoelectric materials

### 2.3.1 Crystal – Rochelle salt

Piezoelectricity and ferroelectricity were first discovered in Rochelle salt (potassium sodium tartrate). It is a colorless to blue-white double salt in the orthorhombic system with the molecular formula  $\text{KNaC}_4\text{H}_4\text{O}_6 \cdot 4\text{H}_2\text{O}$  and is slightly soluble in alcohol but more soluble in water. It has a density of about  $1.77 \text{ g/cm}^3$  and a melting point of approximately  $75 \text{ }^\circ\text{C}$ . The piezoelectric coefficients of Rochelle salt determined by X-ray multiple diffraction are reported as  $d_{21} = 700 \text{ pC/N}$ ,  $d_{22} = 2200 \text{ pC/N}$ ,  $d_{23} = 2100 \text{ pC/N}$  and  $d_{25} = 37 \text{ pC/N}$  [Santos 2001].

### 2.3.2 Ceramic – Lead zirconate titanate (PZT)

There has been significant progress in the application of piezoelectricity since the discovery of lead zirconate titanate (PZT) due to its strong piezoelectric response. PZT ( $\text{Pb}(\text{Zr}_x\text{Ti}_{1-x})\text{O}_3$ ) is a ceramic perovskite material that has a spontaneous polarization, which can be reversed in the presence of an electric field. The material features an extremely large dielectric constant at the morphotropic phase boundary (MPB) near  $x = 0.52$ . For PZT with 54% zirconate and 46% titanate, piezoelectric coefficients in the range from 155 to 590 pC/N have been reported [IEEE Micro Electro Mechanical Systems Workshop 1991].

### 2.3.3 Ferroelectric polymer – $\beta$ -phase polyvinylidene fluoride ( $\beta$ -PVDF)

Polyvinylidene fluoride (PVDF, Poly-1,1-difluoroethene) is a very unreactive and pure thermoplastic fluoropolymer which is used for applications requiring the highest purity, strength, and resistance to solvents, acids, bases and heat. It is a transparent solid insoluble in water with an amorphous density of  $1.74 \text{ g/cm}^3$  and a crystalline density of  $2.00 \text{ g/cm}^3$  at  $25 \text{ }^\circ\text{C}$ . Its melting point ( $T_m$ ) is about  $160 \text{ }^\circ\text{C}$  and the glass-transition temperature ( $T_g$ ) is about  $-38 \text{ }^\circ\text{C}$ .

Dipoles in PVDF arise from the difference in the atom's electron affinity in the molecular chains, as illustrated in figure 2.2. Because fluorine is more electronegative than hydrogen, the fluorine atoms will pull electrons away from the hydrogen atoms to which they are attached. This means the  $-\text{CF}_2-$  groups will be very polar, with a partial negative charge on the fluorine atoms and a partial positive charge on the hydrogen atoms. The direction of the dipole is defined as from negative charge to positive charge, as here from fluorine atom to hydrogen atom for PVDF.

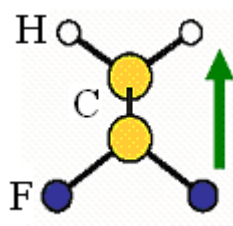


Figure 2.2: Model of a PVDF repeat unit ( $-\text{CF}_2-\text{CH}_2-$ ) with dipole moment.



where  $N$  is the number of dipoles within the volume  $V$  and  $\mu$  is the dipole moment which is the product of the charge  $q$  and the distance  $l$  between positive and negative charge.  $\langle \cos\theta \rangle$  is the average value of the cosine of the angle between the dipole direction and the net polarization direction. The piezoelectric activity derives from the change of volume induced by mechanical stress, which causes an imbalance of surface charges with respect to the volume polarization. For example, if the film is compressed, the volume  $V$  decreases; however, the distance  $l$  between the charges, which is in the magnitude of nanometers, can be considered constant, thus the dipole moment stays constant. The dipole density or the volume polarization  $P$  increases, resulting in more compensating charges. Therefore a flow of charge in the direction indicated in figure 2.4 (c) is generated.

# Chapter 3

## Ferroelectrets

### 3.1 Physical description

An electret is a dielectric material that can store quasi-permanent electrical charges. The word “quasi-permanent” means the time constant for the charge decay is much longer than the time over which any investigations are performed. The charge may be real charges, such as surface-charge layers or space charges, or charge carriers displaced within molecular or domain structures within the material.

A ferroelectret is a polymer based electret which shows piezoelectric properties. Morphologically, it is a polymer film with cellular structure, as depicted in figure 3.1 (left). The film thickness is usually in the range from a few dozen to a hundred micrometers. The voids are lens-shaped, a few to a dozen micrometers in the thickness direction, and a few dozen micrometers in the transverse direction. Its piezoelectricity comes from the separated positive and negative charges which are trapped on the upper and lower gas/polymer interfaces of the voids. The separated charges form macroscopic dipoles in the voids, with a dipole moment  $\mu = q \times l$ , where  $q$  is the charge and  $l$  is the distance between the separated charges, i.e. the void height. In addition, compensating charges are generated on the metal electrodes, with the polarity as shown in the figure. If the ferroelectret is compressed with mechanical stress, its volume decreases. However, unlike the change of volume in ferroelectric polymers such as  $\beta$ -PVDF, the majority of volume change takes place in the voids, since the gas inside voids is much more compressible than the polymer bulk. Therefore the distance between positive and negative charges decreases, meaning a decrease of dipole moment. Although the dipole density increases due to the decrease of the whole volume, the extent of the dipole density increase is much less than that of the dipole moment decrease. Thus the amount of compensating charges decreases and a flow of charge is generated, in the direction shown in figure 3.1 (right).

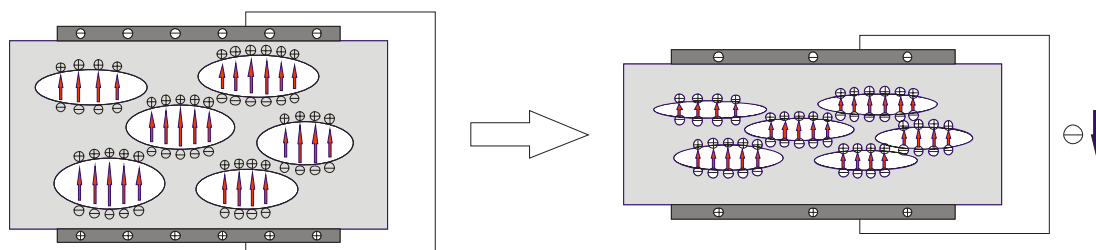


Figure 3.1: Schematic description of a ferroelectret with metal electrodes on both sides. Macroscopic dipoles are formed by the trapped charges on the gas/polymer interfaces, with direction from negative to positive charges. Change of dipole moment due to thickness compression results in a flow of charge.

## 3.2 Piezoelectric properties

Compared with traditional piezoelectric materials, foremost among the favorable properties of ferroelectrets are their large piezoelectric  $d_{33}$  coefficients, as listed in table 3.1. Optimized PP ferroelectrets can show  $d_{33}$  up to 600 pC/N. However,  $\beta$ -PVDF exhibits only around 20 pC/N and there has been almost no enhancement since the discovery of its piezoelectricity. Although PZT also has  $d_{33}$  of a few hundred pC/N, it does not have the polymer advantages such as softness and light-weight.

Piezoelectric material	$d_{33}$ (pC/N)
Crystal: Quartz (silicon dioxide)	2 ( $d_{11}$ )
Ceramic: Lead zirconate titanate (PZT)	170 – 600
Ferroelectrics: $\beta$ -phase polyvinylidene fluoride ( $\beta$ -PVDF)	20
Ferroelectret: optimized cellular polypropylene (PP)	600

Table 3.1: Comparison of piezoelectric coefficients of several piezoelectric materials [Bauer 2004].

Ferroelectrets can exhibit a large piezoelectric  $d_{33}$  coefficient and this is an advantage in applications relying on thickness change. However, they have a small value for  $d_{31}$ , which relates the voltage across a sample to the length change in the transverse direction. This disadvantage limits their applications requiring large deflections due to thermostat-like bending. Usually  $d_{33}$  is the only coefficient used to evaluate the piezoelectric properties of ferroelectrets.

Since the piezoelectric activity derives from the change of thickness by the external mechanical pressure, the sample's compressibility is critical for achieving strong piezoelectricity. Actually, piezoelectric activity strongly depends on the cellular structural, elastic stiffness and some other factors. Investigations [Wegener 2004(2), Wegener 2005(3)] showed that there is an inversely-U-shaped relation between the piezoelectric activity and the sample density, as shown in figure 3.2. Samples with small voids are relatively stiff and therefore have low piezoelectric activity. A controlled increase of the void height can decrease the elastic stiffness and enhance the piezoelectric activity. Too large a void height, i.e. more spherical voids, however, causes a large elastic stiffness, and lowers the piezoelectric activity.

## 3.3 Stability

For ferroelectrets, their piezoelectricity comes from two aspects: the charges which form dipoles, and the cellular structure, which can change the dipole moment in response to external stress. Therefore the stability of ferroelectrets is determined by two aspects: stability of the cellular structure and stability of the charge. Temperature is sometimes a critical factor which limits the applications of a polymer. Obviously, a cellular structure cannot be operated at temperatures higher than the polymer's melting temperature  $T_m$ . Actually the  $T_m$  is much higher than the temperature of charge de-trapping. Therefore the charge stability usually determines the application temperature range for ferroelectrets.

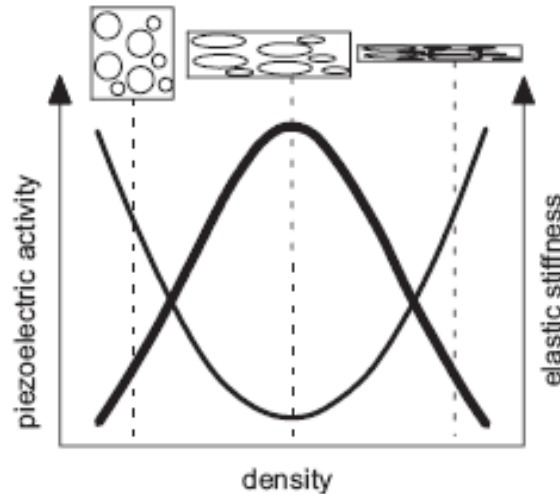


Figure 3.2: Dependence of piezoelectricity (thick line) and elastic stiffness (thin line) on the density and the corresponding void shape.

Charges on the gas/polymer interfaces are stored in trap levels located in the band gap between the conduction and valence bands. Electron and hole traps are present and the former are in equilibrium with the conduction band and the latter with the valence band. However, these charges are not stable and will decay. There are two types of decay in ferroelectrets, the internal phenomena such as ohmic conduction, or the external process of ion deposition. Ohmic conduction depends on positive or negative intrinsic carriers, which are available in the valence and conduction bands of the materials, especially at high temperature. The external process are due to the action of electrical fields extending outside the ferroelectret and attracting compensation charges in the form of ions from the surrounding medium [Sessler 1998(1)].

Many factors may influence the charge stability, such as time, humidity, temperature, radiation, etc. Charges decay with time, however, they are quasi-stable under normal conditions for many polymers. In a humid environment, charges decay faster due to the increase of charge carriers. High temperature and radiation can activate charges in trap levels and the charges de-trap if they achieve enough energy. For some polymer electrets, excellent charge stability is only found for the negative charges [Gerhard-Multhaupt 1999(1)]. This is because in these polymers, due to their electronegative character, the hole mobility greatly exceeds the electron mobility.

Charging conditions and some treatments can influence the charge stability. Processing at elevated temperatures, such as corona charging at elevated temperatures, controlled aging or annealing after charging, and quenching or pre-aging before charging, has a significant influence on the charge stability of polymer electrets. Several experiments [Perlman 1974, Turnhout 1975, Seggern 1984, Xia 1991] have shown that, for most electrets, charge stability can be enhanced by means of charging at suitable elevated temperatures. Charges are stored in trap levels with different energy wells, and the deeper the energy well, the more energy is needed to de-trap the charges. At elevated temperatures, charges are mostly captured in deep traps, which are more stable than those captured in shallow traps. When a charged sample is annealed at elevated temperature, charges that are trapped in relatively shallow traps are thermally de-trapped, leading

to a higher portion of charges in deep traps. As a result, the overall thermal stability of the remaining charges is improved. It should, however, be noted that the annealing process itself causes less charge to be stored in the electrets, which reduces the final piezoelectricity.

### 3.4 Model

Piezoelectricity of ferroelectrets has been theoretically analyzed with a simplified model based on charged parallel polymeric and gaseous layers [Paajanen 1999, Sessler 1999(2), Hillenbrand 2000, Paajanen 2001(2), Zhang 2004, Hillenbrand 2005, Zhang 2006(2)], including finite-element calculations [Tuncer 2005(1), Tuncer 2005(2)]. Figure 3.3 shows the simplified model, where  $V_{\text{charging}}$  is the voltage applied between the sample electrodes;  $\sigma_i$  is the charge density on the interface of the  $i^{\text{th}}$  layer;  $\epsilon_1$  and  $\epsilon_2$  are the permittivity of polymer bulk and gas;  $s_{1i}$ ,  $E_{1i}$  and  $s_{2i}$ ,  $E_{2i}$  is the thickness, electric field in the  $i^{\text{th}}$  polymer layer and gas layer, respectively.

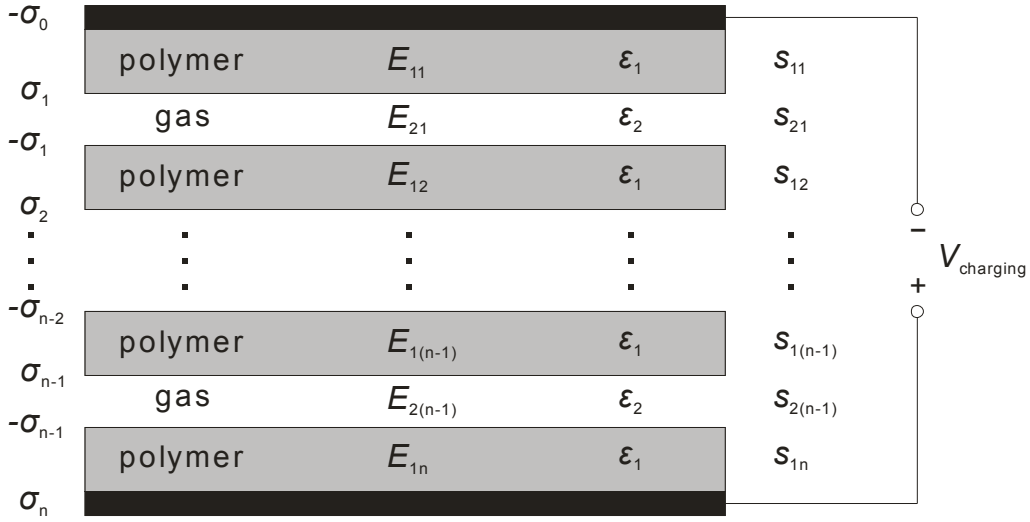


Figure 3.3: Simplified model based on charged parallel polymeric and gaseous layers.

Based on the simplified layer-mode, the piezoelectric  $d_{33}$  coefficient is derived as

$$d_{33} = \frac{\epsilon_2 \epsilon_1 s}{c_{33}} \frac{s_1 \sum_i s_{2i} \sigma_i}{s_2 (\epsilon_2 s_1 + \epsilon_1 s_2)^2}, \quad (3.1)$$

here  $s_1 = \sum s_{1i}$  and  $s_2 = \sum s_{2i}$  is the total thickness of polymer and gas layers,  $s = s_1 + s_2$  is the total film thickness. Assuming that the charge density on each interface is equal and  $\sigma_i = \sigma$ , there is

$$d_{33} = \frac{\epsilon_2 \epsilon_1 \sigma}{c_{33}} \frac{s s_1}{(\epsilon_2 s_1 + \epsilon_1 s_2)^2}, \quad (3.2)$$

The quantities  $s_1$  and  $s_2$  follow directly from the area density of the sample, and the charge density  $\sigma$  can be estimated from scanning electron microscopy (SEM) data. With equation 3.2 the piezoelectric  $d_{33}$  coefficient can be theoretically calculated.



## 3.5 Typical ferroelectrets

### 3.5.1 Polypropylene (PP)

Polypropylene (PP) is a thermoplastic polymer with a variety of applications, including food packaging, textiles, laboratory equipment, automotive components, etc. It is an addition polymer made from the monomer propylene, and is unusually resistant to many chemical solvents, bases and acids. PP has an amorphous density of  $0.85 \text{ g/cm}^3$  and crystalline density of  $0.95 \text{ g/cm}^3$ . Its melting point is  $173 \text{ }^\circ\text{C}$  and degradation point is  $286 \text{ }^\circ\text{C}$ .

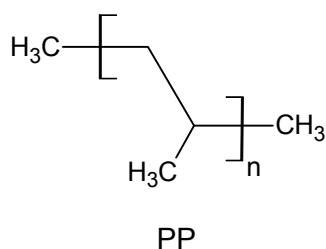


Figure 3.4: Chemical structure of polypropylene (PP).

Up to now, cellular PP is the most prominent ferroelectret. Cellular PP films are suitable transducer materials in audible and ultrasonic frequency range, because of their low density which can be adjusted over the range from  $0.15$  to  $0.7 \text{ g/cm}^3$  and their low acoustic impedance of about  $2.6 \times 10^4 \text{ kg/m}^2\text{s}$ . Microphones and vibration pickups made from cellular PP films are already available on the market.

Properties	Unit	P(VDF-TrFE) (Thickness $100 \mu\text{m}$ )	Cellular PP (Thickness $58 \mu\text{m}$ )
Density	$\text{g/cm}^3$	1.79	0.33
Piezoelectric coefficient $d_{33}$	$\text{pC/N}$	20	300
Thickness-extension resonance frequency	MHz	12.3	0.73
Coupling factor	1	0.23	0.06
Elastic stiffness $c_{33}$	$\text{N/m}^2$	$10.8 \times 10^9$	$1.3 \times 10^6$

Table 3.2: Comparison of some piezoelectric properties between P(VDF-TrFE) and cellular PP [Wegener 2004(1)].

### 3.5.2 Polyethylene terephthalate (PET)

Polyethylene terephthalate (PET) is a thermoplastic resin with density of  $1.37 \text{ g/cm}^3$ , glass transition temperature  $T_g$  of  $75 \text{ }^\circ\text{C}$  and melting temperature  $T_m$  of  $260 \text{ }^\circ\text{C}$ . It is used to make beverage and food containers, synthetic fibers, as well as for some other thermoforming applications. It can be synthesized by a transesterification reaction between ethylene glycol and dimethyl terephthalate.

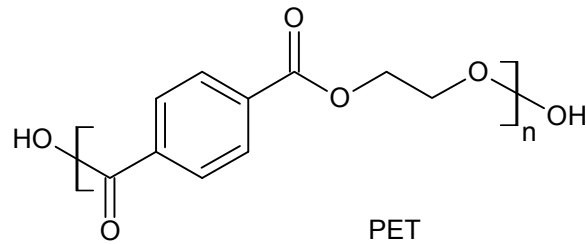


Figure 3.5: Chemical structure of polyethylene terephthalate (PET).

Investigations show that the voided and stretched PET films charged with a corona-tip voltage of  $-25$  kV show a significant  $d_{33}$  of about 20 pC/N if their density is in the range between 0.6 and 0.95 g/cm<sup>3</sup>. Films with a lower density show lower piezoelectric activity and films with densities higher than 1 g/cm<sup>3</sup> are not piezoelectric. Piezoelectric properties are also found in voided but non-stretched PET films if a higher charging field is applied [[Wegener 2005\(4\)](#)].

### 3.5.3 Cyclo-olefin copolymer (COC)

Cyclo-olefin copolymer (COC) consists of ethylene and cyclic olefin monomer 2-norbornene. By changing the ethylene pressure during polymerization, the fraction of these two constituents can be adjusted. The COCs are usually amorphous, with a glass-transition temperature  $T_g$  from 130 to 160 °C.

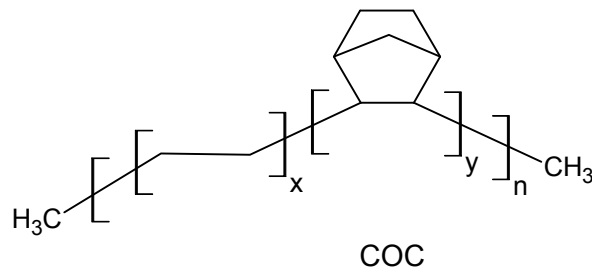


Figure 3.6: Chemical structure of cyclo-olefin copolymers (COC).

$d_{33}$  coefficients up to 43 pC/N are reported but typically they are in the range from 10 to 20 pC/N. COC ferroelectrets show better thermal stability than PP ferroelectrets: The  $d_{33}$  decreases from 15 to 11 pC/N after a short-term treatment at 110 °C for 1 hour, and a heat treatment at 100 °C for at least 200 hours reduces the initial  $d_{33}$  slightly from 11 to 9.4 pC/N in a long-term test [[Wegener 2005\(5\)](#)].

### 3.6 Applications

The application of ferroelectrets was developed much later than that of ferroelectric crystals and ferroelectric polymers, and it was inappreciable at the beginning. An example of the oldest applications was a ferroelectret transducer first described in 1928. These transducers, as well as the ferroelectret microphone discussed in the following years, proved unsatisfactory, because the wax electrets used had insufficient electrical stability under usual conditions [Sessler 1998(2)]. This situation did not change until the applications based on polymeric electrets were introduced in the second half of the 20th century, which gained widespread acceptance.

Compared with the traditional piezoelectric materials, ferroelectrets have desirable advantages for a variety of transducer applications. Some market available products are illustrated in figure 3.7 (a). Polymer films are thin and light-weight, and therefore they can be easily fabricated into any size or shape, as shown in figure 3.7 (b), the ferroelectret keypad can be installed on curved surfaces. Furthermore, they are relatively inexpensive and can be easily processed. Another significant advantage over most classical piezoelectrics is that the majority of cellular polymers consist of nontoxic constituents. A vital-signs-monitoring system based on ferroelectrets has been developed as shown in figure 3.7 (c). The self-biased sensor is installed below a mattress, it responds to micro pressure changes caused by patient's ballistocardiogram and respiration, and generates a reflective output voltage, by which the heart and respiration rates and movement activity can be calculated from the sensor signal. In addition, the rather small specific acoustic impedance of ferroelectrets is another advantage in transducer applications. Compared with ceramics, the impedance of polymers is much closer to that of water. As a consequence, polymers can emit a larger portion of acoustic energy generated in an underwater sound source [Bauer 2004]. Except for the traditional application as transducers, ferroelectret devices including ferroelectret gas filters, ferroelectret motors and generators, relay switches, optical display systems and ferroelectret radiation dosimeters have also been introduced.



Figure 3.7(a): Ferroelectret-based keyboard made by Screentec® [www.screentec.com].



Figure 3.7(b): Keypad elements can be installed also on curved surfaces [\[www.screenotec.com\]](http://www.screenotec.com).



Figure 3.7(c): Bed sensor produced by EMFIT<sup>®</sup> [\[www.emfit.com\]](http://www.emfit.com).

# Chapter 4

## Cellular structure development

Cellular polymer systems with internal electrically charged voids have become an attractive research topic, and lots of work has been contributed to this area. There are two main cellular structures: polymer foams where a number of voids are generated in a single film, and polymer multilayer system where the voids are formed by a well designed combination of polymer film layers and frames. During the last two decades, several manufacturing and processing techniques have been proposed and demonstrated, both for cellular single films (foams) and heterogeneous multilayer piezo- and ferro- electrets [[Bauer 2004](#), [Wilson 2007](#)]. In the following some typical structure preparation methods, as well as optimizations, are introduced.

### 4.1 Polypropylene (PP) foam

Up to now, polypropylene (PP) foams are the mostly studied ferroelectrets. Industrial sensor and actuator products based on PP foams are already available on the market. The preparation technique for cellular PP is also used as the basis for the development of other cellular polymers. PP can be melt-processed into cellular films at moderate temperatures. Since the obtained cellular structure strongly depends on the manufacturing process, the technique used to generate voids is of outstanding importance for the resulting ferroelectret properties.

There are two main routes to generate voids in PP films. One of these was developed in the late 1980s [[Savolainen 1989](#), [Hämäläinen 1996](#)]. Cellular PP films are produced in a modified blow-extrusion process, where spherical voids are generated by gas injection into the polymer melt. The polymer melt is first extruded into a tube and cooled, and then the tube is reheated and biaxially oriented by film blowing. Depending on the draw ratio the polymer structure of the foamed biaxially oriented PP films is highly crystalline and highly anisotropic. The resulting voids are lens-shaped with typical diameters above 10  $\mu\text{m}$  and typical thicknesses on the order of 1  $\mu\text{m}$ . In another technique which was developed later [[Raukola 1998](#), [Paajanen 2000\(2\)](#), [Raukola 2002](#)], suitable inorganic filler particles such as titanium dioxide, hydrated magnesium silicate (talcum) are incorporated into PP melt within an extruder. The filled melt is extruded into films, which are subsequently stretched. Voids are formed through de-lamination of a partially molten polymer matrix from mineral filler particles during stretching, due to the development of stress peaks during the stretching deformation in the machine direction (MD) and in the transverse direction (TD). After the stretching in the MD, needle-shaped voids appear, which become flat and lens like during the second stretching in the TD. Another possibility for creating voids of this shape is the simultaneous biaxial stretching in the MD and the TD at the same time. The resulting cellular structure is strongly influenced by material properties like the melt viscosity, as well as the compounded inorganic filler material (type, geometry, size, and dispersion). The size, shape, and dispersion of the voids can also be improved by variation of the stretching parameters, such as

temperature, stretching ratio and speed. Most cellular PP films have co-extruded outer layers of compact PP in order to get homogeneous film thickness, a higher surface smoothness, and an improved adhesion of the electrodes on the film surface [[Paajanen 2000\(2\)](#), [Gerhard-Multhaupt 2002](#)].

Besides the initial foaming, void size and shape can be varied and therefore the overall cellular structure can be optimized by means of an additional Gas-Diffusion Expansion (GDE) procedure [[Paajanen 2001\(3\)](#), [Paajanen 2002](#), [Wegener 2004\(2\)](#), [Wegener 2004\(3\)](#), [Zhang 2004](#)]. Cellular PP films are saturated with gas at high pressure (usually in N<sub>2</sub> at 20 bar). Then a fast reduction of the pressure to atmospheric pressure leads to the expansion of the voids due to the large pressure difference between the gas inside and outside the voids. Usually, for ferroelectret applications, a cellular structure should have a closed lens-like voids with dimensions of  $100 \times 100 \times 10 \mu\text{m}^3$ , porosity of more than 50%, and non-voided coating layers on both outer surfaces of the film.

## 4.2 Polyethylene-terephthalate (PET) foam

Due to the limited working temperature of PP ferroelectrets, several new ferroelectrets based on other polymers are under investigation. One of those successfully developed into ferroelectrets is polyethylene-terephthalate (PET) foams [[Wirges 2007](#), [Voronina 2008](#)]. PET has many attractive thermal and mechanical properties which make it a very attractive candidate for thermally stable ferroelectrets. As an industrial product, solid PET films are available on large scale with standard uniform parameters.

The ability of gas molecules to penetrate into polymer bulk under high pressure opens the possibility for physical foaming of polymer films. Supercritical carbon dioxide (CO<sub>2</sub>) is well known as a molecular fluid that can penetrate relatively easily into several polymers as there is preferred absorption by the polymers for CO<sub>2</sub> compared to that of air. It is known that CO<sub>2</sub> in the supercritical state can be absorbed (soaked) into several polymers and is able to swell and even plasticize them [[Arora 1999](#)]. The size of the resulting voids is also known to be dependent on the gas used. Supercritical CO<sub>2</sub> has been used as a physical foaming agent for generating low-density foams [[Liang 2000](#)] and for producing microcellular PVDF foams [[Cooper 2003](#)]. Voids ranging from micrometers down to nanometers in size can be obtained by a suitable treatment with supercritical CO<sub>2</sub>. In addition, CO<sub>2</sub> has also been used to create low-k (dielectric constant) polymers with nano-sized voids as dielectric materials for electronic devices [[Krause 2001](#)]. Supercritical CO<sub>2</sub> is also used to make low-density (0.1 g/cm<sup>3</sup>) PET foams in a combined process with gas and temperature treatments [[Japon 2000](#)]. Besides CO<sub>2</sub>, N<sub>2</sub> can also be used. Due to their smaller size, N<sub>2</sub> molecules exhibit a higher diffusion rate and therefore result in finer voids than CO<sub>2</sub>. Figure 4.1 shows a phase diagram of CO<sub>2</sub> [[Jacobs 2004](#)]. Above 31 °C and 72.9 bar, CO<sub>2</sub> behaves as a supercritical fluid and shows properties of both liquid and gas. As a liquid CO<sub>2</sub> has a high density which results in solvent properties, and as a gas it has a low viscosity and thus can easily penetrate into small pores.

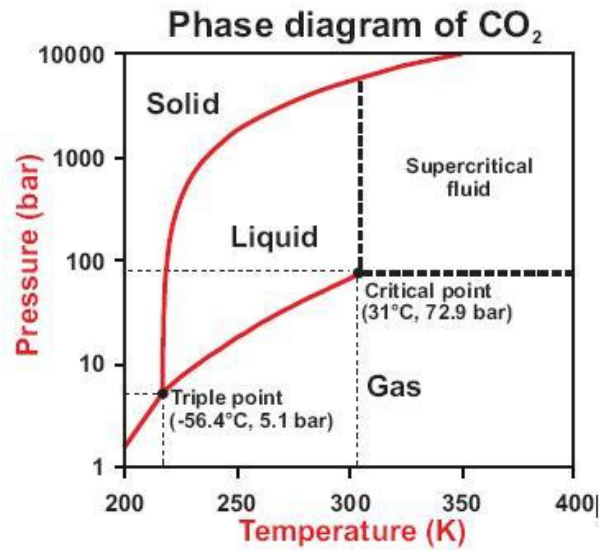


Figure 4.1: Phase diagram of CO<sub>2</sub> [Jacobs 2004].

Phase	Density (g/cm <sup>3</sup> )	Viscosity (μPa×s)
Gas	0.001	10
Liquid	1	1000
Supercritical fluid	0.2 – 0.9	10 – 50

Table 4.1: Density and viscosity of CO<sub>2</sub> in different phases [Jacobs 2004].

Based on the above knowledge, a physical foaming and optimization process for preparation of cellular PET which is suitable for ferroelectrets has been developed in laboratory [Wirges 2007, Voronina 2008]. It was found that, a two-step foaming process with supercritical CO<sub>2</sub> is required to prepare the necessary cellular structure. In the first step, PET films cut from commercial sample sheets undergo a high pressure treatment with CO<sub>2</sub> in a closed steel chamber where the inner gas pressure and temperature can be adjusted. Under high pressures up to 150 bar, PET samples are saturated with supercritical CO<sub>2</sub>. In the second step, a heat treatment is applied on the CO<sub>2</sub>-saturated polymer immediately after the release of the high pressure. Sudden heating of the sample at atmospheric pressure to a temperature higher than 31 °C leads to a transformation of supercritical CO<sub>2</sub> into gas state. Due to the large volume increase during the phase change, a large expansion of CO<sub>2</sub> inside the polymer occurs. The heat treatment should be applied homogeneously over the whole sample and two routes have been attempted. The first is heating in an oil bath (Jjoba oil, organic) where the sample can be heated homogeneously but the residual oil should be removed with surfactants, in order to avoid the influence of the oil on the charge-storage ability. The second is heating by placing the sample between two pre-heated glass plates where a homogeneous heating can also be realized but at the risk of making bubbles on the sample surface if the temperature is too high. The gas-saturation pressure, time, temperature, as well as the heat-treatment temperature may influence the final structure with varied sample density, void shape, etc.

The formed cellular structure should be optimized, in order to achieve better piezoelectric



properties. As reported, the elastic properties of the cellular materials strongly depend on the size, relative density and shape anisotropy of their voids [Gibson 1997]. Therefore, a biaxial stretching at elevated temperatures is performed with a laboratory-scale film stretcher. Stretching changes the void size and geometry, as well as the interconnection between the voids. Stretched films show even smoother surfaces than the non-stretched ones. After stretching, the void height is decreased and the void length is increased, therefore stretching increases the sample density and decreases the sample thickness. In addition, the micrographs of cross sections show that the stretching destroys some of the small polymer fibrils that are visible in the voids of the non-stretched films. Consequently, the elastic stiffness is significantly lowered. In addition, part of the cellular voids after stretching are not completely closed, leading to a structure with partially open voids.

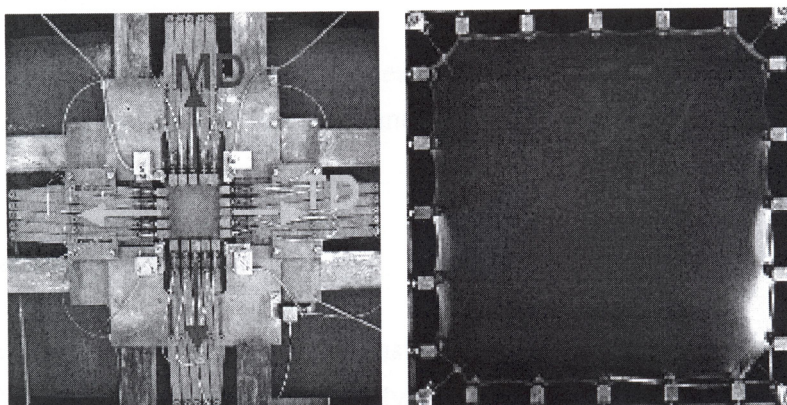


Figure 4.2: Photograph of the stretching unit of the biaxial stretching machine (KARO IV, Bruckner Maschinenbau, Germany) and a stretched sample with the same stretching ratio in both directions (MD: machine direction; TD: transverse direction).

If necessary, a further structure optimization can be fulfilled by a two-step inflation (Gas-Diffusion Expansion, GDE) process. Firstly, samples are placed in a pressure chamber and subjected to pressurized  $N_2$  for a period of time. Because these relatively smaller molecules can penetrate more easily through the polymer films [Wegener 2004(2)], a very high pressure is not necessary. Subsequently, the pressure is quickly released, and the voids are inflated due to the large pressure difference between the gas inside and outside the voids. Next, the sample is immediately heated between two pre-heated glass plates, in order to stabilize the structure change. The inflation can be controlled by varying the inflation parameters such as the heating temperature. This additional inflation can lower the sample density, but a sample which is inflated too much can be very stiff.

### 4.3 Fluorinated ethylene-propylene (FEP) foam

Fluorinated ethylene-propylene copolymers (FEP) possess excellent chemical resistance and high flame retardance combined with a very low smoke emission, high continuous use temperatures, outstanding ageing and weathering stability along with appropriate mechanical properties. Due to its good UV-stability ferroelectrets made of FEP would also be suitable for



applications which have to resist environmental impact. However, fluoropolymers are quite expensive and the processing is more complex compared to PP, not only because of the higher manufacturing temperatures but also due to the tendency to release hydrofluoric acid.

Because small amounts of hydrofluoric acid are present in the fluoropolymer melts at all times, there are chemical reactions between the acid and the common fillers during the melt-mixing process. The compounds result in a huge amount of bubbles which cause defects in the pressure molded films. These defects result in a failure of the samples when being stretched. Instead of the common fillers like calcium carbonate or talcum, boron nitride (plate-shaped), calcium fluoride (cubical structure) and barium sulphate (very fine particles) which are resistant to hydrofluoric acid were used. However, due to a very unusual mechanical deformation behavior of the FEP, which becomes noticeable in a significant decrease of elongation at break with increasing temperature, all the films fracture at low stretching ratios before void generation at the filler particles could be achieved. Similar to the technique used for generation of cellular PP films, extrusion foaming was also considered. Using CO<sub>2</sub> as a physical blowing agent, the FEP was dissolved by the supercritical fluid, resulting in the extrusion of polymer powders. The reduction of blowing agent content and the introduction of boron nitride as a nucleation agent do not lead to a successful foaming of FEP. Chemical foaming was also attempted. Magnesium hydroxide was selected as a chemical blowing agent which is adapted to the high required melting temperature of FEP. The characterization of the cellular FEP films indicates that they are not suitable for the application as ferroelectrets as the charge stability is very low. The reason was suspected to be the presence of residues of the chemical blowing agent in the foam.

Due to the unsuccessful preparation of cellular FEP for ferroelectret applications with the techniques discussed above, a new process should be proposed. Recently, cellular PET which shows appreciable piezoelectricity was successfully prepared by means of a two-step physical foaming process consisting of a supercritical CO<sub>2</sub> saturation and a thermal voiding. Therefore this method is also applied to FEP. However, it is found that in contrast to other polymers treated in this way, the density reduction achieved for filled and unfilled FEP films is poor due to a very fast diffusion of the dissolved CO<sub>2</sub> out of the film before the voiding step. The low porosity of the films obtained by this method makes the samples nearly non-piezoelectric. Therefore, this process has to be altered to a one-step method performing pressure release after the film saturation and foaming at the same time inside the autoclave [Zirkel 2009]. The autoclave together with the FEP sample is heated up to the final foaming temperature. CO<sub>2</sub> is fed into the heated cylinder at the selected pressure. After the saturation of the films the pressure is subsequently released by quickly opening a valve attached to the autoclave. At a temperature in the range of the melting point of FEP, the polymer is soft enough to be foamed by the evaporation of the CO<sub>2</sub> dissolved inside the material.

The as-prepared cellular FEP films were still quite stiff, probably due to the spherical shape of the voids. A structure optimization can be realized by changing the void geometry to lens-like shape. Therefore, the films were biaxially stretched at elevated temperatures by means of a laboratory stretching frame. However, it is found that only very low stretching ratios can be realized without breaking the films.

## 4.4 Heterogeneous multilayer structure

In the above discussed techniques, microscopic cellular voids with dimensions of a few to dozens of micrometers were generated. The void shape is not uniform, and the void size is sometimes distributed over a large range. However to achieve an ideal cellular structure is at present technically difficult. This disadvantage usually influences the final piezoelectric properties and as a result limits large-scale production in industry, where relatively uniform products with well controlled properties are required. Therefore, a macroscopic cellular structure with well-designed uniform voids is also a route to prepare piezoelectric active polymer systems. In addition, due to the enlarged dimension from microscopic to macroscopic, the structure can be easily controlled.

Recently, a technique towards macroscopic cellular polymer systems was introduced [[Altafim 2003](#), [Altafim 2006](#), [Zhang 2006\(1\)](#)], where polymer films with thermo-formed cupolas are sandwiched and thermally fused between continuous polymer films. Relatively large, but more or less uniform cells are therefore formed between the polymer films. After charging, these cells can have a rather large dipole moment so that the layer systems exhibit relatively high piezoelectric coefficients. The new scheme has been demonstrated on fluoropolymer films with good thermal and long-term stabilities [[Altafim 2003](#), [Altafim 2006](#), [Zhang 2006\(1\)](#)]. More recently, another new concept of template-based fluoroethylenepropylene piezoelectrets with tubular channels was also presented, which can serve as a material platform for several types of piezoelectric or even multifunctional ferroelectret films [[Altafim 2009](#)]. In this template-based polymer system, a structure with well-defined uniform tubular channels is formed by means of a lamination process. The laboratory template consists of a Teflon PTFE film with parallel rectangular openings cut into the PTFE films by means of laser ablation. Before lamination, the PTFE template is inserted between two Teflon FEP films. The three-layer fluoropolymer-film sandwich is fed into the lamination apparatus which has been preheated to 300 °C. The chosen lamination temperature is substantially higher than the melting temperature of FEP but still well below the melting point of PTFE. After cooling under ambient conditions in the laboratory, the two FEP layers are permanently fused to each other through the openings of the PTFE template. Because of the anti-adhesive properties of fluoropolymers, the PTFE template can be easily removed after cutting it open at one end. Therefore the resulting FEP-film system contains well-defined tubular channels. With this technique, it is possible to generate uniform channels with a large range of widths, heights, and lengths, as well as arbitrary channel patterns. Due to the excellent thermal charge stability of FEP, the working temperature of this piezoelectric system is quite enhanced, compared with the PP and PET foams.

# Chapter 5

## Electrical charging

### 5.1 Dielectric-barrier discharge (DBD)

Electric charging of ferroelectrets is achieved by a series of dielectric-barrier discharges (DBDs) [Savolainen 1989, Neugeschwandtner 2000, Kogelschatz 2001, Neugeschwandtner 2001, Paaianen 2001(3), Lindner 2002]. DBD comprises a specific class of high-voltage, gaseous discharges that typically occur in the near-atmospheric pressure range. Its defining feature is the presence of dielectric layers that make it impossible for charges generated in the gas to reach the conducting electrode surfaces. DBD was originally called silence discharge, and is also referred to as barrier discharge (BD). In ferroelectrets, the discharge gap is insulated from the electrodes by polymer layers.

Paschen breakdown is considered to be responsible for the DBD in cellular structural polymer systems with void heights from about 5 to 200  $\mu\text{m}$  [Anderson 2002]. As described by Paschen's law, the breakdown voltage  $V_{\text{breakdown}}$  and the breakdown electric field  $E_{\text{breakdown}}$  are determined by the product of the gas pressure  $p$  in the void and the gas-gap distance  $d$ , which is the void height here

$$V_{\text{breakdown}} = B \times \frac{(p \times d)}{C + \ln(p \times d)}, \quad (5.1)$$

$$E_{\text{breakdown}} = B \times \frac{p}{C + \ln(p \times d)}, \quad (5.2)$$

and

$$C = \ln \left( \frac{A}{\ln \left( 1 + \frac{1}{\gamma} \right)} \right), \quad (5.3)$$

where the constants  $A$  and  $B$  depend upon the composition of the gas, and  $\gamma$  is the secondary ionization coefficient which is poorly known. By differentiation  $V_{\text{breakdown}}$  and  $E_{\text{breakdown}}$  with respect to  $(p \times d)$  and setting the deviation to zero, the minimum voltage and electric field for Paschen breakdown can be calculated.

For air,  $B = 365 \text{ Vcm}^{-1}\text{Torr}^{-1}$ ,  $A = 15 \text{ cm}^{-1}\text{Torr}^{-1}$  (1 Torr = 133.3 Pa), and  $\gamma = 0.01$ ,  $C = 1.18$  [Bazelyan 1998], so the Paschen curve for air at 1 bar can be plotted as shown in figure 5.1. At a fixed air pressure, the breakdown voltage decreases with the decrease of the gas-gap distance until its minimum value of about 300 V at about 10  $\mu\text{m}$ , and then increases very fast when the gas-gap

distance is further decreased. Figure 5.2 shows the corresponding breakdown electric field as a function of the gas-gap distance. It is found that small gap distances require high electric field to generate gas-breakdown. In relatively small air gaps of a few micrometers, the required breakdown field is already as high as several hundred MV/m, which makes the gas-breakdown difficult. Actually, the curve for breakdown field is used more. For the simplified layer model of ferroelectrets (section 3.4), the relation between the electric field inside voids and the charging voltage applied between the sample electrodes is

$$E_{void} = \frac{V_{charging}}{\frac{\epsilon_2}{\epsilon_1} s_1 + s_2}, \quad (5.4)$$

where  $\epsilon_1$ ,  $s_1$  and  $\epsilon_2$ ,  $s_2$  are the permittivity, total thickness of the polymer and the gas layers, respectively. By obtaining the geometry of the cellular structure, the required charging voltage for a certain gas distance can be estimated.

Table 5.1 shows the relative breakdown strength for some gases. Sulfur hexafluoride ( $\text{SF}_6$ ) is a strong dielectric gas with a high electron-capturing ability and has a high breakdown strength. By replacement of air with  $\text{SF}_6$ , a higher breakdown voltage and electric field would be achieved.

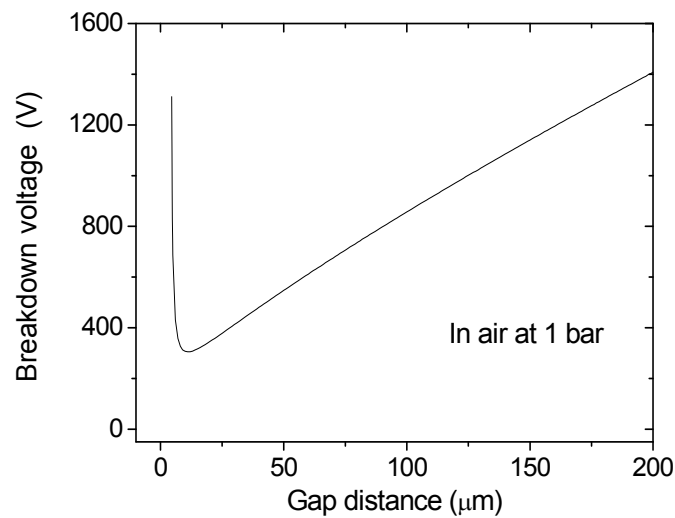


Figure 5.1: Breakdown voltage as a function of the gap distance in air at a pressure of 1 bar according to Paschen's law.

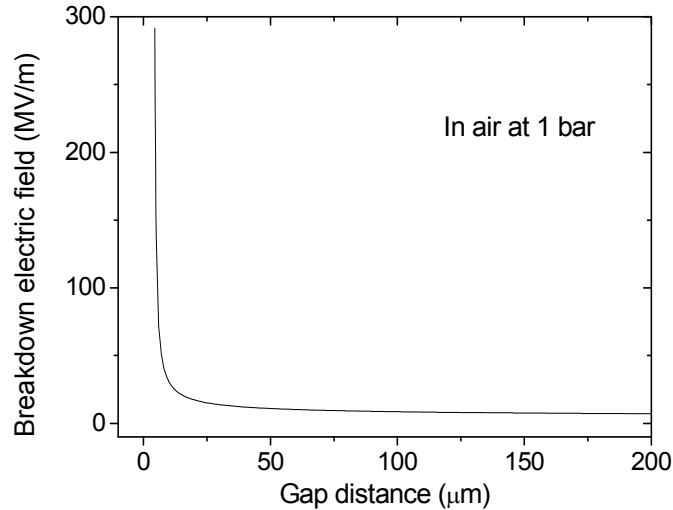


Figure 5.2: Breakdown electric field as a function of the gap distance in air at a pressure of 1 bar according to Paschen's law.

Gas	Relative breakdown strength in an uniform DC field
SF <sub>6</sub>	1.00
N <sub>2</sub> O	0.44
N <sub>2</sub>	0.36
Air	0.30
Ar	0.07

Table 5.1: Relative breakdown strength for some gases at atmospheric pressure [Paajanen 2001(3)].

It should be noted that if the charging voltage (or electric field) is too high, electric breakdown of the polymer may occur, which creates a hole through the sample thickness and therefore destroys the sample. The breakdown depends on the material's dielectric strength, and polymer with higher dielectric strength has a higher breakdown electric field. For polymers, the dielectric strength is of the order of a few MV/cm<sup>-1</sup>, e.g. 2.2 MV/cm<sup>-1</sup> for 12.5 μm polytetrafluoroethylene (PTFE) and 0.14 MV/cm<sup>-1</sup> for polyamide (PA). Usually the dielectric strength of a polymer is much higher than that of gas. Taking into account the dielectric strength both for polymer and gas, a proper voltage range that generates gas-breakdown but does not destroy the sample can be determined.

DBD is always accompanied by the emission of a short light pulse from the discharge gap, which can be recorded and analyzed [Wegener 2002, Qiu 2007(1), Zhukov 2007]. Figure 5.3 (left) shows a typical signal of light emission from DBD triggered by an AC voltage (back-discharge is not shown) and figure 5.3 (right) shows a photograph of the light emission from the gas-breakdown in a polymer foam. During the DBD a plasma treatment occurs which influence the resulting piezoelectricity of the polymer foams [Qiu 2008(2)]. DBD is widely used for ozone synthesis [Eliasson 1987], for plasma remediation of toxic gases [Xu 1998], for surface chemistry (e.g. etching and surface modification) [Sankaran 2001], as an incoherent ultraviolet source (excimer lamps) [Kogelschatz 1990], for plasma display panels [Oversluizen 2000], and has attracted extensive research [Kogelschatz 2003].

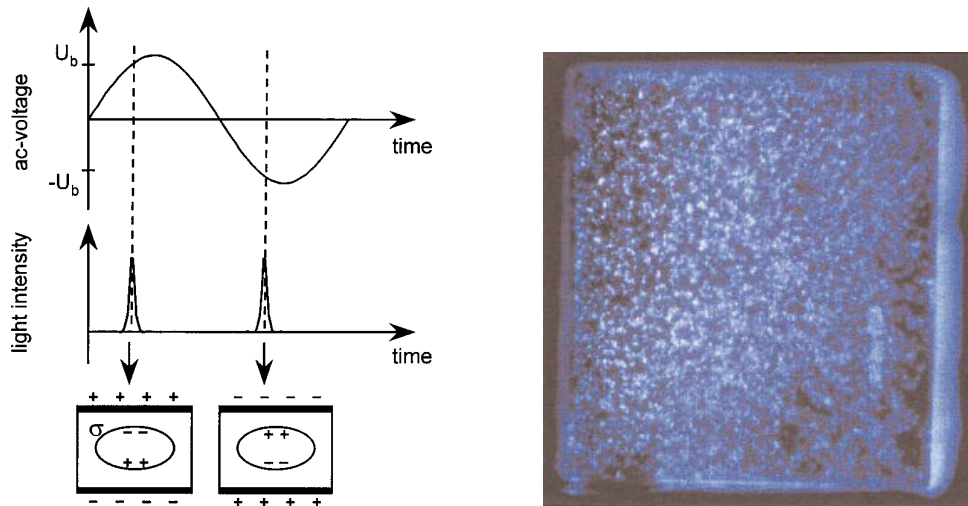
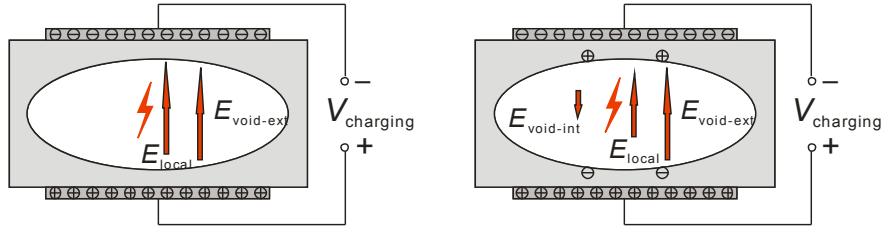


Figure 5.3 Left: Dielectric-barrier microdischarges within a polymer foam (back-discharge is not shown). A self-extinguishing microdischarge is ignited, accompanied by the emission of a short light pulse and by a transfer of a sheet charge across the gap. Right: Photograph of microdischarges within a polymer foam. Light emission from the voids within the polymer is observed during the breakdown [Lindner 2002].

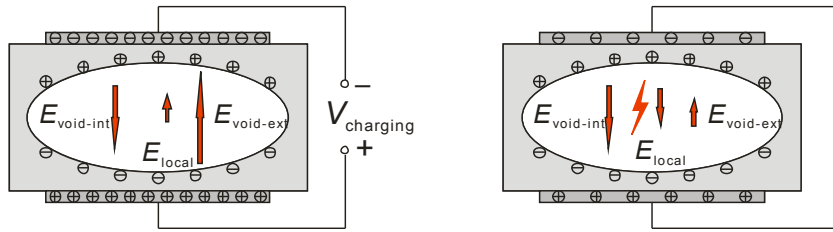
## 5.2 Description of charging process

Cellular polymers must be electrically charged in order to exhibit piezoelectric activity. The charging process is schematically illustrated in figure 5.4, and the cellular structure is simplified as the polymer bulk with one void.  $V_{\text{charging}}$  is the charging voltage applied between the sample electrodes;  $E_{\text{local}}$  is the actual electric field in the void, which is the superposition of  $E_{\text{void-ext}}$  from the external charges on the electrodes (charging-voltage-induced), and  $E_{\text{void-int}}$  from the internal deposited charges (deposited-charge-induced);  $E_{\text{breakdown}}$  is the breakdown threshold determined by Paschen's law as discussed above. When a charging voltage is applied, the actual electric field in the void comes from the external charges on the electrodes ( $E_{\text{void-ext}}$ ) due to the charging voltage. If this field is larger than the threshold, gas-breakdown occurs in the void (figure 5.4 (1)) and charges of both polarities are generated. Driven by the electric field, they flow in opposite directions until trapped on the gas/polymer interfaces [Sessler 1998(1)]. The deposited charges induce an additional electric field ( $E_{\text{void-int}}$ ) in the void, which is opposite to the field from the external charges on the electrodes, and therefore lowers the actual field in the void (figure 5.4 (2)). With more and more charges accumulated on the gas/polymer interfaces, the field from the deposited charges increases and further lowers the actual field in the void. Consequently, the gas-breakdown is extinguished once the actual field is no longer higher than the breakdown threshold (figure 5.4 (3)). When the charging voltage is decreased or switched off, the field from internal charges may over compensate the field from the external charges, and if the actual field is again larger than the breakdown threshold (in the opposite direction), gas-breakdown occurs, which is called back-discharge (figure 5.4 (4)) [Kogelschatz 2001, Qiu 2007(1), Qiu 2007(2)]. The back-discharge destroys some of the previously deposited charges, and simultaneously lowers the actual field. It is quenched as long as the actual field is not higher than the threshold. The remaining charges are the final charges that can be trapped on the gas/polymer interfaces (figure 5.4 (5)).



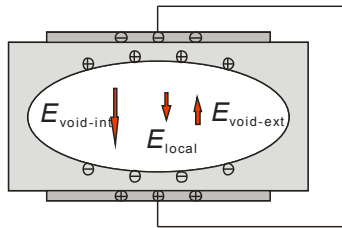
$$(1) E_{\text{local}} = E_{\text{void-ext}} > E_{\text{breakdown}}$$

$$(2) E_{\text{local}} = E_{\text{void-ext}} - E_{\text{void-int}} > E_{\text{breakdown}}$$



$$(3) E_{\text{local}} = E_{\text{void-ext}} - E_{\text{void-int}} < E_{\text{breakdown}}$$

$$(4) E_{\text{local}} = E_{\text{void-int}} - E_{\text{void-ext}} > E_{\text{breakdown}}$$



$$(5) E_{\text{local}} = E_{\text{void-int}} - E_{\text{void-ext}} < E_{\text{breakdown}}$$

Figure 5.4: Electric charging process in a void.  $V_{\text{charging}}$  is the charging voltage between the sample electrodes;  $E_{\text{local}}$  is the actual electric field in the void, which is the superposition of  $E_{\text{void-ext}}$  from the external charges on the electrodes (charging-voltage-induced), and  $E_{\text{void-int}}$  from the internal deposited charges (deposited-charge-induced);  $E_{\text{breakdown}}$  is the breakdown threshold determined by Paschen's law.

(1) Actual electric field in the void equals the field from the external charges on the electrodes. If it is larger than the threshold, gas-breakdown occurs.

(2) Deposited charges on the gas/polymer interfaces induce an additional electric field, which is opposite to the field from the external charges on the electrodes, and therefore lowers the actual field.

(3) With more and more charges deposited, the actual field in the void is further decreased. As long as it is not higher than the breakdown threshold, gas-breakdown is extinguished.

(4) When the charging voltage is decreased or switched off, the field from internal charges may over compensate the field from external charges, and if the actual field is larger than the breakdown threshold (in opposite direction), back-discharge occurs again, which destroys some previous deposited charges.

(5) As long as the actual electric field is not higher than the threshold, the back-discharge is extinguished.

### 5.3 Threshold behavior and saturation phenomenon

When the charging voltage applied between sample electrodes is increased to a threshold value  $V_{\text{threshold}}$ , the field from the external charges (charging-voltage-induced)  $E_{\text{void-ext}}$  reaches the breakdown threshold  $E_{\text{breakdown}}$ , and gas-breakdown occurs. Charges are generated, separated and then deposited, resulting in an additional opposite field  $E_{\text{void-int}}$  (deposited-charge-induced). As discussed above, when the charging voltage is decreased or switched off, the over compensation of the field from internal charges to the field from external charges may trigger a back-discharge, as long as the actual local field is higher than the breakdown threshold, which destroys some of the previously deposited charges. Therefore for a certain sample, the maximum amount of charges that can be retained is limited, and there exists a saturation charging voltage  $V_{\text{saturation}}$ , above which no more charges can be retained even if a higher charging voltage is applied.

Based on the layer-model (section 3.4), assume that the thickness of each gas layer is equal and the charges trapped at each gas/polymer interface are uniformly distributed,  $s_{21} = s_{22} = \dots = s_{2(n-1)}$ ,  $\sigma_1 = \sigma_2 = \dots = \sigma_n = \sigma_i$ , the electric field in the void is

$$E_{\text{local}} = \frac{\epsilon_0 \epsilon_1 V_{\text{charging}} - \sigma_i s_1}{\epsilon_0 \epsilon_2 s_1 + \epsilon_0 \epsilon_1 s_2}, \quad (5.5)$$

where  $V_{\text{charging}}$  is the voltage applied between the sample electrodes,  $\sigma_i$  is the charge density,  $\epsilon_0$ ,  $\epsilon_1$ , and  $\epsilon_2$  is the permittivity of vacuum, polymer, and gas,  $s_1$  and  $s_2$  is the total thickness of the polymer layers and gas layers, respectively. Electric breakdown occurs only when the breakdown threshold is reached ( $E_{\text{local}} = E_{\text{breakdown}}$ ), therefore the relation between the charging voltage and the charge density is

$$\sigma_i = \frac{\epsilon_0 \epsilon_1 V_{\text{charging}} - E_{\text{breakdown}} (\epsilon_0 \epsilon_2 s_1 + \epsilon_0 \epsilon_1 s_2)}{s_1}. \quad (5.6)$$

In addition, only when there are some charges deposited already on the gas/polymer interfaces ( $\sigma_i > 0$ ), cellular polymer is piezoelectric, therefore

$$\frac{\epsilon_0 \epsilon_1 V_{\text{charging}} - E_{\text{breakdown}} (\epsilon_0 \epsilon_2 s_1 + \epsilon_0 \epsilon_1 s_2)}{s_1} > 0, \quad (5.7)$$

so

$$V_{\text{charging}} > E_{\text{breakdown}} \left( \frac{\epsilon_2}{\epsilon_1} s_1 + s_2 \right) = V_{\text{threshold}}. \quad (5.8)$$

After charging, the charging voltage is switched off ( $V_{\text{charging}} = 0$ ). If the actual field from internal charges (in opposite direction) is higher than the breakdown threshold, a back-discharge is triggered:

$$\left| E'_{\text{local}} \right| = \left| \frac{-\sigma'_i s_1}{\epsilon_0 \epsilon_2 s_1 + \epsilon_0 \epsilon_1 s_2} \right| > E_{\text{breakdown}}, \quad (5.9)$$



so

$$\sigma'_i > E_{breakdown} \left( \epsilon_0 \epsilon_2 + \epsilon_0 \epsilon_1 \frac{s_2}{s_1} \right). \quad (5.10)$$

Combine equation 5.10 and 5.6, there is

$$V'_{charging} > 2E_{breakdown} \left( \frac{\epsilon_2}{\epsilon_1} s_1 + s_2 \right) = V_{saturation}. \quad (5.11)$$

Therefore

$$V_{saturation} = 2V_{threshold}. \quad (5.12)$$

The saturation voltage is twice as large as the threshold voltage, a further increase of charging voltage does not result in more charges retained.

If the charge density  $\sigma_i$  is substituted in equation 3.1 with equation 5.6 and combined with equation 5.8, the piezoelectric  $d_{33}$  coefficient can be expressed as

$$\begin{aligned} d_{33} &= \frac{\epsilon_2 \epsilon_1 s \left[ \epsilon_0 \epsilon_1 V_{charging} - E_{breakdown} (\epsilon_0 \epsilon_2 s_1 + \epsilon_0 \epsilon_1 s_2) \right]}{c_{33} (\epsilon_2 s_1 + \epsilon_1 s_2)^2} \\ &= \frac{\epsilon_0 \epsilon_2 \epsilon_1^2 s}{c_{33} (\epsilon_2 s_1 + \epsilon_1 s_2)^2} (V_{charging} - V_{threshold}) = k (V_{charging} - V_{threshold}), \end{aligned} \quad (5.13)$$

where  $k$  is a constant. Therefore,  $d_{33}$  is linear with charging voltage during a contact charging. When the charging voltage is higher than the saturation voltage, the charge density is always the same as the one at the saturation voltage, and therefore the maximum  $d_{33}$  is

$$d_{33}^* = \frac{\epsilon_0 \epsilon_2 \epsilon_1 s E_{breakdown}}{c_{33} (\epsilon_2 s_1 + \epsilon_1 s_2)}. \quad (5.14)$$

The relation between piezoelectric  $d_{33}$  coefficient and the charging voltage for a contact charging is summarized as

$$d_{33} = \begin{cases} 0 & V_{charging} < V_{threshold} \\ k(V - V_0) & V_{threshold} < V_{charging} < V_{saturation} = 2V_{threshold} \\ d_{33}^* & V_{charging} > V_{saturation} \end{cases} \quad (5.15)$$

The threshold behavior can be proved directly by the light emission of DBD [Lindner 2002]: Light emission is only observed when the charging voltage is higher than a certain value. Moreover, according to equation 5.15, by measuring  $d_{33}$  as a function of charging voltage, the threshold behavior and saturation phenomenon can also be observed and experimental values for threshold voltage and saturation voltage can be determined.

## 5.4 Charging techniques

### 5.4.1 Contact (direct) charging

Contact (direct) charging is one of the most used charging techniques in the lab, which can be easily operated with simple equipment. Metal electrodes, usually aluminum or gold, should be deposited in advance onto both surfaces of the sample. A DC voltage is applied directly across the electrodes, and the electric field between electrodes triggers the electric breakdown, as shown in figure 5.5. Contact charging can be performed at elevated temperatures as well. In this case, the sample holder is also used as the heating plate, with an internal heater monitored by the temperature control system.

Usually a charging voltage larger than the expected saturation value is applied since the void sizes are not uniform and relatively smaller voids require higher voltages to trigger sufficient gas-breakdown. The disadvantage of this technique is that the breakdown of the polymer may occur if any defect exists on the sample, which usually results in a hole through the sample thickness. In addition, a bypass-breakdown may take place when too high voltage is applied and therefore burns parts of the electrodes. In order to avoid the bypass-breakdown, the total sample area should be larger than the electrode area.

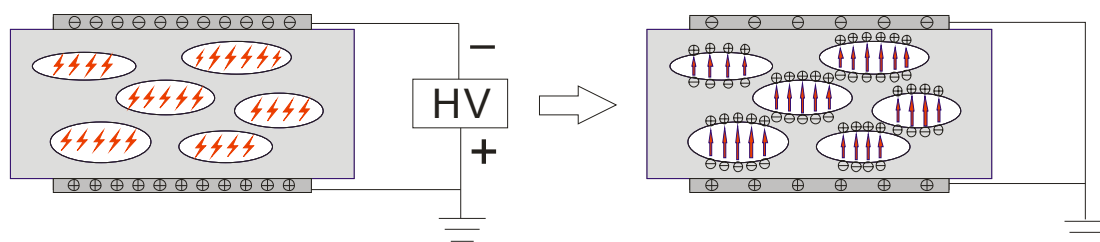


Figure 5.5: Illustration of the negative contact charging.

### 5.4.2 Tip-to-plane corona charging

Corona is a self-sustainable discharge occurring if a sufficiently high voltage is applied to asymmetric electrodes such as a point (needle tip) and a metal plate. The ionization section of the corona discharge is confined to a small region near the point, where ions and excited molecules are produced, and the accelerated movement of gas is due to numerous collisions between the charged particles and neutral molecules. The drift region extends from the corona tip to the plate, and is characterized by the presence of charge carriers of only one polarity with mobility of the order of a few  $\text{cm}^2 \cdot \text{V}^{-1} \cdot \text{s}^{-1}$  [Giacometti 1999]. Corona discharge is a cold plasma, and the energy to strip off the electrons comes from the very strong electric fields. In air, the corona is seen as a faint blue-violet glow region, although it emits much more ultraviolet light than visible light. Depending on the corona polarity, either positive or negative ions are produced. In air, negative coronas mainly generate  $\text{CO}_3^-$  ions, whereas for positive coronas  $(\text{H}_2\text{O})_n\text{H}^+$  ions predominate. Because the ions have an average thermal energy, they are deposited in the surface layer and do not penetrate into the material. They transfer their charges and leave the surface as neutral atoms

or molecules [Giacometti 1999, Sessler 1998(3)].

Corona charging is widely used both in the lab and in industry, with the setup schematically shown in figure 5.6. Electrodes are not needed, but an electrode on the bottom is preferred in order to ensure good contact to the ground. An outer electric field is formed by applying a high voltage between a needle-shaped upper electrode which is placed a few centimeters above the sample, and a planar grounded back electrode. The outer field deposits a large amount of charge on the sample surface, which is expressed by the surface potential. The surface charges generate an electric field across the sample thickness and trigger gas-breakdown in the voids. Corona charging can be carried out in different ambient atmospheres [Paajanen 2001(3)]. A gas with larger electrical breakdown strength (table 5.1) provides a chance to achieve a higher potential difference between the needle tip and the sample surfaces, where more charges can be deposited. Corona charging can also be applied at elevated temperatures.

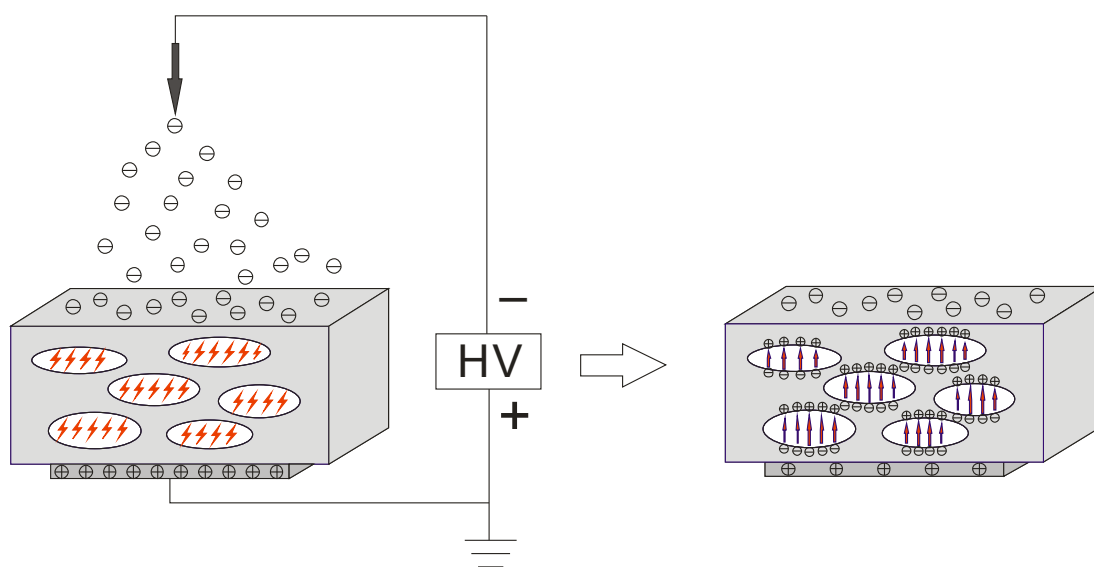


Figure 5.6: Illustration of the negative tip-to-plane corona charging.

### 5.4.3 Comparison between contact charging and corona charging

Both contact charging and corona charging can trigger gas-breakdown in the voids. The difference between them is the way the internal electric field forms in the voids, which is used to trigger gas-breakdown. For contact charging, the internal field is formed directly by the voltage between electrodes, and for corona charging, the field is formed by the deposited surface charges. Contact charging is very easy to operate but sometimes it is dangerous as it can destroy the sample if any structural defect exists. Since electrodes are not required, corona charging is more versatile and therefore can be applied on a large scale for use in industry.

## 5.5 Optimized charging conditions

### 5.5.1 Charging in sulfur hexafluoride (SF<sub>6</sub>)

As described above, a back-discharge occurs if the over-compensation of the electric field from the internal charges to the field from the external charges is larger than the breakdown threshold, which destroys some previously deposited charges. In order to avoid the back-discharge, a large breakdown threshold is needed, where more charges can be retained on the gas/polymer interfaces. The breakdown threshold is correlated to the breakdown strength of the gas (table 5.1), and a relatively larger breakdown threshold can be achieved by replacing air with a gas with a larger breakdown strength, for example sulfur hexafluoride (SF<sub>6</sub>).

The replacement of the gas in the voids is done in a closed chamber with a pumping system and a pressurized-gas supply. This process can be monitored by measuring the capacitance change of the sample with a LCR meter. The sample has electrodes deposited on both surfaces and is considered as a parallel plate capacitor. The chamber pressure is first decreased quickly to 10<sup>-2</sup> bar. The sample thickness initially increases due to the pressure difference across the void walls because the gas inside voids cannot escape immediately. Therefore a fast decay of sample capacitance is observed. Gradually, the internal gas flows out through the void walls and the sample thickness recovers to its initial value. Thus a slow increase of capacitance is observed. In the next step, SF<sub>6</sub> at a few bars is introduced into the chamber. The sample thickness decreases because the pressure outside the voids is much larger than inside, resulting in an increase of the capacitance. SF<sub>6</sub> diffuses into the voids until the pressures across the void walls are balanced. The sample thickness increases again, accompanied by a decrease of capacitance to its initial value. However, the replacement of the internal gas may not be possible in some polymer foams. It depends on the properties of polymer and the size of the gas molecules. Electrodes are not necessary for the gas-replacement when process monitoring is not necessary.

### 5.5.2 Charging at elevated temperatures

The applications of the present ferroelectrets are sometimes limited mainly because of the low thermal charge stability at elevated temperatures. Charging at elevated temperatures is a possible method to improve the thermal charge stability [[Perlman 1974](#), [Turnhout 1975](#), [Seggern 1984](#), [Xia 1991](#)]. Both contact and corona charging can be applied at elevated temperatures. What is important is that, the charging voltage is switched off only after the sample has cooled down to room temperature. Otherwise charges may be lost due to thermally stimulated discharge. Usually a higher charging temperature results in a better charge stability; however, it should be controlled in order to not destroy the cellular structure.

# Chapter 6

## Experimental techniques

### 6.1 Investigation of structure

#### 6.1.1 Microscopy

- Scanning electron microscopy (SEM)

Scanning electron microscope (SEM) is a type of electron microscope that images the sample surfaces by scanning it with a high-energy beam of electrons in a raster scan pattern. The electrons interact with the atoms that make up the sample, producing signals containing information about the sample's surface topography, composition and other properties such as electrical conductivity. Therefore by taking SEM images of the cross section, the cellular structure can be directly observed. As an example, figure 6.1 shows a SEM image of the cross-section for a typical PP foam sample. The dimensions of the voids can be measured directly from this image. Samples should be cut after being frozen in liquid nitrogen and the surfaces of the cross section should be metalized. In this work the SEM (LEO 435VP, Carl Zeiss NTS, Germany) was applied to investigate microscopic cellular structures.

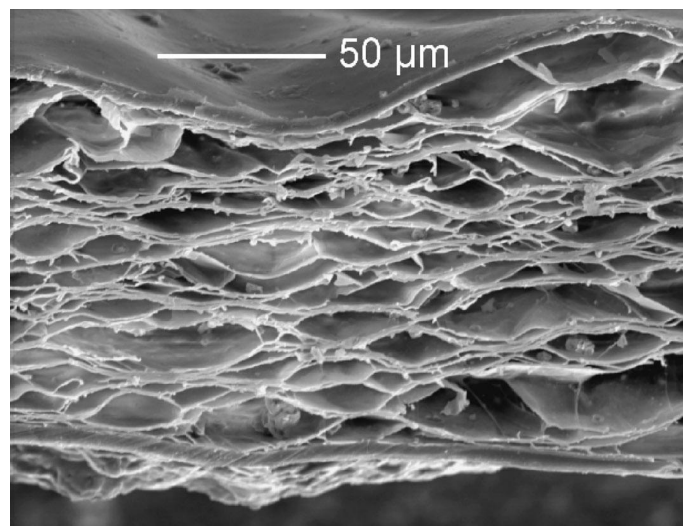


Figure 6.1: SEM image of a typical PP-foam cross section [Mellinger 2006].

By analyzing the SEM image of the cross section, the void-height distribution can be measured directly by means of a software package “ImageJ” [Rasband 1996]. Void boundaries for the sample shown in figure 6.1 are detected automatically and fitted as ellipses, as shown in figure 6.2. The minor axes of the ellipses are taken as the void heights and their distribution is thus calculated. The void-height distribution is plotted in figure 6.3, with void heights up to 20 μm but

most voids have heights below 12  $\mu\text{m}$ .

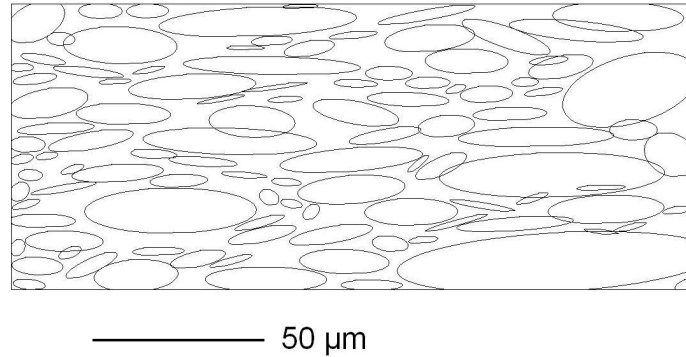


Figure 6.2: Ellipses-fitting of the voids for the sample shown in figure 6.1.

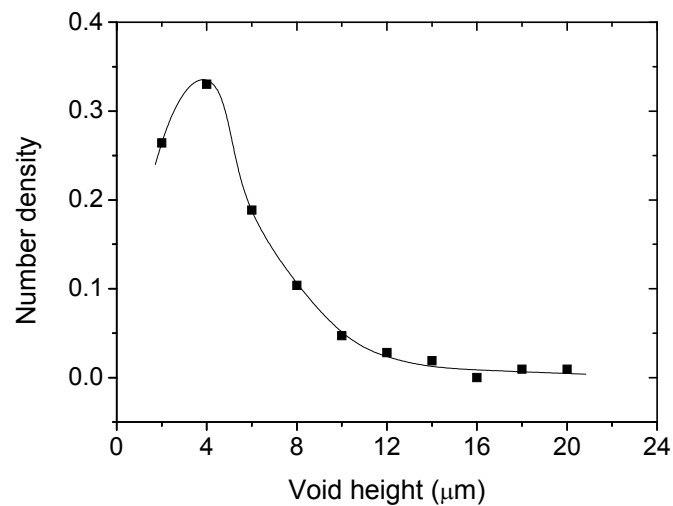


Figure 6.3: Void-height distribution of the sample shown in figure 6.1.

- Optical microscopy

In this work, an optical microscope (Keyence Digital Microscope System, VH-Z100R VHX-600) was also used to investigate the macroscopic cellular structures. The structures can be directly observed, and the related parameters can be measured easily.

### 6.1.2 Porosity

Assuming that  $\rho_{\text{solid}}$ ,  $m_{\text{solid}}$  and  $\rho_{\text{cellular}}$ ,  $m_{\text{cellular}}$  are the density and mass of the sample before and after foaming,  $V_{\text{gas}}$  and  $V_{\text{polymer}}$  are the volume of the voids and polymer bulk after foaming, respectively, therefore the total volume after foaming is

$$V_{total} = V_{gas} + V_{polymer} = \frac{m_{cellular}}{\rho_{cellular}}. \quad (6.1)$$

In addition, the volume of polymer bulk is not changed after foaming, so

$$V_{polymer} = \frac{m_{solid}}{\rho_{solid}}. \quad (6.2)$$

Thus the volume of voids is

$$V_{gas} = V_{total} - V_{polymer} = \frac{m_{cellular}}{\rho_{cellular}} - \frac{m_{solid}}{\rho_{solid}}. \quad (6.3)$$

The porosity  $P$  is defined as the void portion from the total volume, thus

$$P = \frac{V_{gas}}{V_{total}} = \frac{V_{total} - V_{polymer}}{V_{total}} = \frac{\frac{m_{cellular}}{\rho_{cellular}} - \frac{m_{solid}}{\rho_{solid}}}{\frac{m_{cellular}}{\rho_{cellular}}}. \quad (6.4)$$

Considering that the mass of gas inside the voids (CO<sub>2</sub> in this work) is very small compared to the polymer bulk and therefore can be neglected, so the mass of the sample is not changed after foaming and  $m_{cellular} = m_{solid}$ , equation 6.4 can be simplified as

$$P = \frac{\frac{1}{\rho_{cellular}} - \frac{1}{\rho_{solid}}}{\frac{1}{\rho_{cellular}}} = 1 - \frac{\rho_{cellular}}{\rho_{solid}}. \quad (6.5)$$

By measuring the mass, thickness and geometry of the sample before and after foaming, the porosity can be easily calculated.

Assuming that in the simplified layer-model with parallel polymeric and gaseous layers (section 3.4) as shown in figure 6.4,  $s_1$  and  $s_2$  are the total thickness of the polymer and the gas layer, respectively, and  $s = s_1 + s_2$  is the thickness of the whole sample, so the polymer and gas portion in the thickness direction is

$$\frac{s_1}{s} = \frac{V_{polymer}}{V_{total}} = 1 - P = \frac{\rho_{cellular}}{\rho_{solid}}, \quad (6.6)$$

and

$$\frac{s_2}{s} = \frac{V_{gas}}{V_{total}} = P = 1 - \frac{\rho_{cellular}}{\rho_{solid}}. \quad (6.7)$$

The height ratio between the gas layer and the polymer layer is

$$\frac{s_2}{s_1} = \frac{V_{gas}}{V_{polymer}} = \frac{P}{1 - P} = \frac{\rho_{solid}}{\rho_{cellular}} - 1. \quad (6.8)$$

### 6.1.3 Elastic modulus

The stiffness of a cellular sample is critical for its piezoelectric activity (figure 3.2) because the electromechanical property derives from the change of dipole moment on the application of mechanical stress, and the change of dipole moment depends on the strain of the cellular structure. A large strain by an applied stress results in a strong piezoelectric response. Actually, a direct measurement of the strain is not simple since the cellular films are usually only a few dozen micrometers in thickness. However, the capacitance is related to the sample thickness, and by measuring the change of capacitance according to stress, the strain and thus the elastic modulus  $c_{33}$  can be determined.

In order to calculate the strain of the sample from the load-dependent capacitance, the layer-model of the cellular polymer discussed in section 3.4 is further simplified, as shown in figure 6.4. The foam is represented by a serial connection of polymer layers with a total thickness  $s_1$  and by an air gap with total thickness  $s_2$  [Sessler 1999(2), Neugeschwandtner 2001].

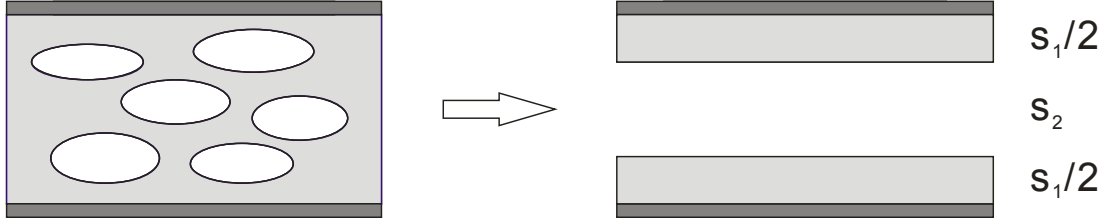


Figure 6.4: Simplified model for the cellular polymer as a parallel-plate capacitor. The foam is represented by a serial connection of polymer layers with a total thickness  $s_1$  and by an air gap with total thickness  $s_2$ .

The capacitance of the sample is given by

$$\frac{1}{C(T)} = \frac{s_1}{\epsilon_0 \epsilon_1 A} + \frac{s_2(T)}{\epsilon_0 A}, \quad (6.9)$$

where  $\epsilon_0$  and  $\epsilon_1$  are the permittivity of vacuum and the polymer, respectively,  $A$  is the electrode area. Here it is assumed that the applied compressive stress  $T$  solely results in a reduction of the void height  $s_2$ . This assumption is self-consistent as the foam is much softer than polymer bulk, and therefore the voids are more easily compressed than the surrounding polymers. Under this assumption, the strain of the polymer is calculated from the stress-dependent capacitance according to

$$\begin{aligned} S(T) &= \frac{\Delta s}{s} = \frac{s_2(T) - s_2(T=0)}{s} = \frac{\left[ \frac{1}{C(T)} - \frac{s_1}{\epsilon_0 \epsilon_1 A} \right] \epsilon_0 A - \left[ \frac{1}{C(T=0)} - \frac{s_1}{\epsilon_0 \epsilon_1 A} \right] \epsilon_0 A}{s} \\ &= \frac{\epsilon_0 A}{s} \left[ \frac{1}{C(T)} - \frac{1}{C(T=0)} \right], \end{aligned} \quad (6.10)$$

where  $s = s_1 + s_2(T=0)$  is the initial total thickness of the foam.



Figure 6.5 shows the experimental setup for the determination of elastic modulus. The metalized sample was sandwiched between two light-weight electrode plates, which were the same size as the sample electrode. The use of these two plates was to transfer the applied force homogeneously to the sample. Next, they were placed together onto a bottom electrode, with a small, light-weight top electrode on it. The force sensor (KM03, Type 8435-5200, Burster, measuring range: 0 – 200 N) was fixed under the bottom electrode. However, it can only measure the force correctly when the force is perpendicular to it, without any torsional moment or tilting. To this end, a smooth, frictionless ball bearing was set between the bottom electrode and the force sensor. A shaker (Type 4810, Brüel&Kjaer), with a PMMA isolated cylindrical loading stamp, was mounted on a vertical moveable platform. By changing the platform position, a controllable static force applied to the top electrode and thus to the sample, could be increased or decreased. The top and bottom electrodes were connected to a precision LCR meter (HP4284A), where the capacitance of the sample was simultaneously measured. In an actual measurement, the stress  $T$  was increased, and the capacitance as a function of stress,  $C(T)$ , was recorded. With equation 6.10, the strain-stress dependence  $S(T)$  was plotted and the elastic modulus  $c_{33}$  could be deduced from the slope of the strain-stress curve.

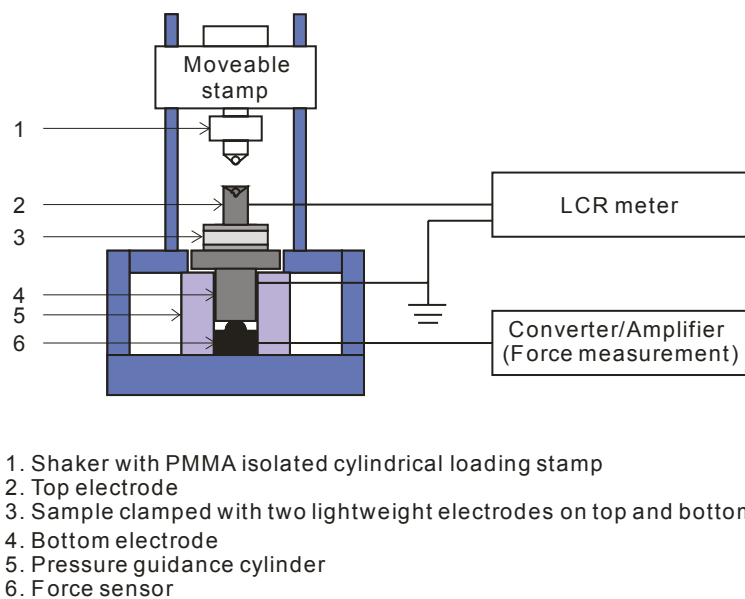


Figure 6.5: Experimental setup for the elastic modulus determination.

Alternatively, a dynamic technique for elastic modulus determination was also applied (by project partner in Soft-Matter Physics, Johannes Kepler University, Linz, Austria). As illustrated in figure 6.6, a polytetrafluoroethylene bar was loaded to the sample by means of pressurized air. The air pressure was adjusted by a computer-controlled valve and could be static (constant) or dynamic (with frequency), and measured with a pressure gauge. With this setup mechanical stresses up to 1 MPa could be achieved, suitable for the investigation of foams with an elastic modulus up to 100 MPa. For the determination of the sample strain and of the elastic modulus, the stress-dependent capacitance of the sample was measured with an HP 4285 LCR meter.

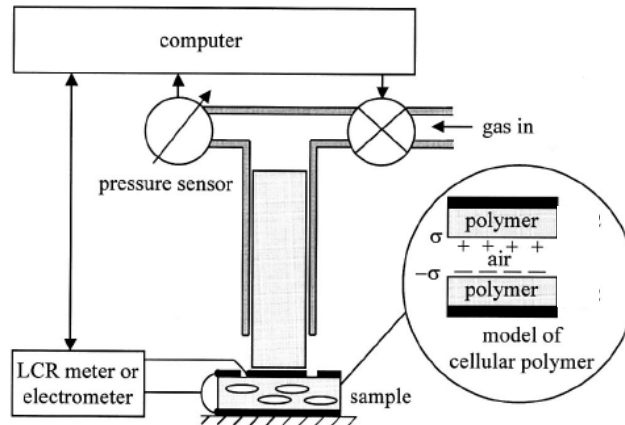


Figure 6.6: Experimental setup for the dynamic method of elastic modulus determination [Dansachmüller 2005].

## 6.2 Investigation of charging behavior

### 6.2.1 Contact charging and corona charging

Both contact charging and corona charging were used to charge samples in this work, depending on the actual requirements. Figure 6.7 schematically illustrates a lab-built contact charging system. A sample with electrodes (Al or Au) on both sides was placed between a top electrode and a metal holder that was grounded. High voltage (Eltex KNH64, Fug HCN 140-65000, or NSE model 3807) was applied directly to the sample through the electrodes. In addition, a temperature control system (lab-built) was also installed in combination with the metal holder, allowing an elevated charging temperature. Samples could be charged at temperatures from room temperature up to 200 °C. Since the charging process was finished in a very short time, a charging period of up to half a minute was quite sufficient. In the case of charging at elevated temperatures, the charging voltage was switched off only when the sample had cooled to room temperature. To this end, a ventilator (lab-built) was used to accelerate the cooling process.

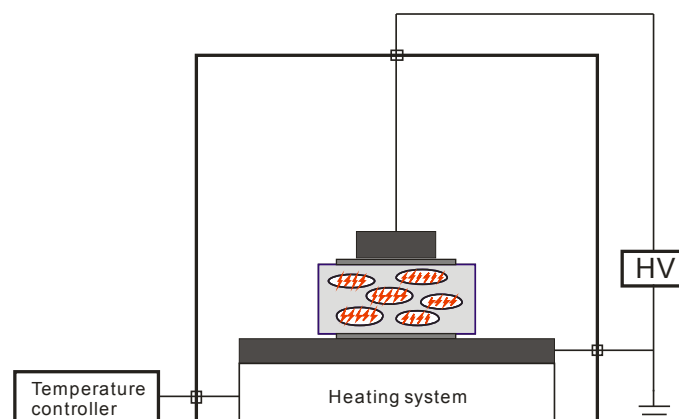


Figure 6.7: Schematic illustration of the contact charging system with temperature controller.

Figure 6.8 shows the lab-built corona charging system applied in this work. A sample without electrode or only with a bottom electrode was placed onto a grounded metal holder. A needle, with its tip about 3 – 4 cm above the sample surface, was connected to a high voltage supply (Eltex KNH64, Fug HCN 140-65000, or NSE model 3807). A metal grid, placed between the sample and the tip, at a distance about 0.5 – 1 cm above the sample surface and with the same area as the metal holder, was also connected to a voltage supply (Keithley model 248 High voltage supply). The grid was used only when the control of the surface potential was necessary. In addition, the chamber was equipped with an air pump (AEG type LN38066008) and a gas supply, when charging in an atmosphere with a higher dielectric strength (e.g. SF<sub>6</sub>) was required. In this case, the chamber was sealed and then pumped for 5 – 10 minutes to a relatively low pressure of approximately 1 Pa. Then the SF<sub>6</sub> was introduced into the chamber with a pressure of 3 bar. Usually the charging voltage was applied for a period from a half to a few minutes. During charging, a corona with blue color could be observed.

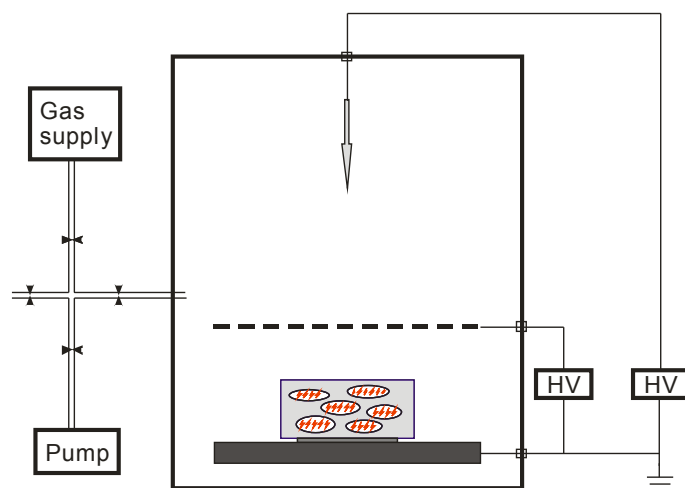


Figure 6.8: Schematic illustration of the tip-to-plane corona charging system with gas supply.

## 6.2.2 Observation of light emission from dielectric-barrier discharge

Dielectric-barrier discharge (DBD) is always accompanied with light emission that can be observed and recorded. Sample electrodes should be thin enough in order to transmit the internal light signal inside the voids. In this work gold (Au) electrodes with a thickness less than 20 nm were deposited. The experimental setup is shown in figure 6.9. The sample was mounted in a dark chamber, with both electrodes connected to a high-voltage supply (contact charging). The light emission was synchronously recorded with a photomultiplier (PMT, R7205-01, Hamamatsu) from one side of the sample where the PMT signal was recorded on a digital storage oscilloscope (Agilent 54833A), and with a computer-controlled electron-multiplying charge-coupled device camera (EM-CCD, iXon, Andor Technology) from the other side. In order to block any light originating from a discharge at the electrode edge, both sides of the samples were covered by a mask with a circular hole, where the hole area was significantly smaller than the electrode area. A typical charging voltage, the corresponding light signal and the observed light emission are shown in figure 5.3.

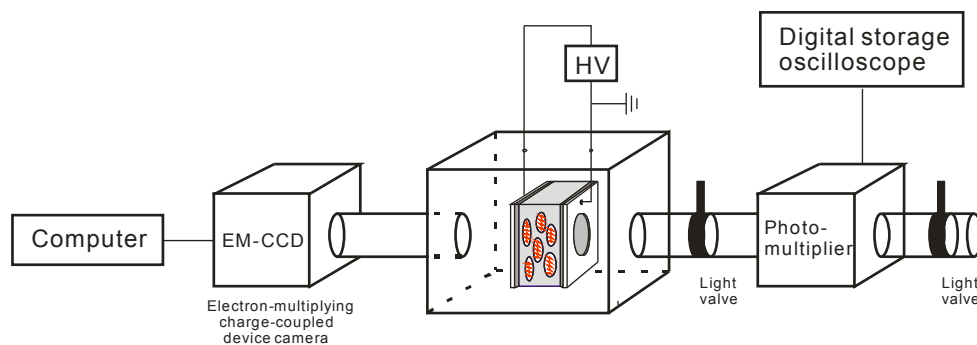


Figure 6.9: Experimental setup for observing and recording light emission from dielectric-barrier discharge. Sample with gold electrodes (20 nm thick) was covered with a mask with a circular hole. The camera was used to take photos or videos of the light emission, and the photomultiplier was to record the light signal which was then showed with the oscilloscope.

### 6.3 Investigation of surface potential

Charge-storage ability is a very important property for a polymer film. By investigating the surface potential, the temporal and the thermal stability of surface charge can be studied. Figure 6.10 illustrates a surface-potential investigation setup, which consists of an electrostatic voltmeter (TREK model 370 High speed electrostatic voltmeter) and a digital multimeter (Votcraft M4650CR) monitored by a computer. A charged sample (solid or cellular) with an electrode on the bottom surface is placed on the grounded sample holder. The detector should be close to the sample surface, but a gas-breakdown between the detector and the sample should be avoided. Taking into account the breakdown strength of air, a distance of around 1 mm per kV of surface potential is required. The sample holder is equipped with a heating system (Grundig PN300 Programmable power supply, and EA-PS 3060-05B power supply) underneath and monitored by a temperature controller (Votcraft MXD-4660A Digital multimeter). In this work, the temporal stability of the surface charge was measured as a function of time at room temperature. For the thermal stability, the samples were heated with a constant heating rate (3 °C/min) and the decay of surface potential was measured as a function of temperature. It should be noted that, the temperature was monitored at the bottom of the sample, and there was a decay of temperature through the sample thickness. Therefore the actual temperature for the surface charges was lower than the monitored one. For a thicker sample, a temperature calibration would be necessary.

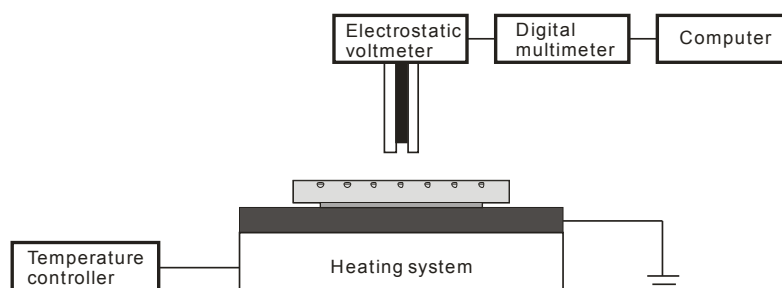
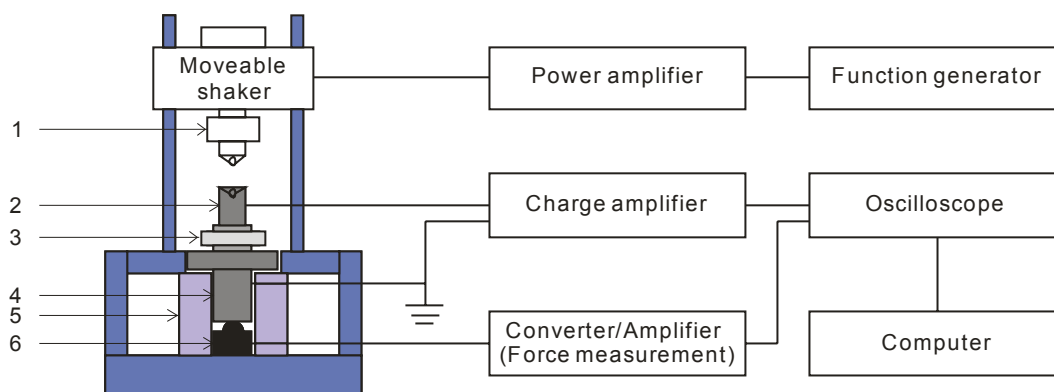


Figure 6.10 Schematic illustration of the surface potential measurement system.

## 6.4 Dynamic measurement

By measuring the amount of generated charges and the applied mechanical stress, the piezoelectric activity can be directly deduced, which is represented by the piezoelectric  $d_{33}$  coefficient (equation 2.10). A certain amount of charges can be generated when a fixed force is applied, however, some of those charges may come from other contributions such as triboelectric charges. To solve this problem, a dynamic method was applied in this work: A dynamic force, for example a sinusoidal force, was used. A sinusoidal charge signal only due to the piezoelectric effect, which is proportional to the periodic force, is generated, and it can be easily separated from the other contributions. In addition, a fixed static force (bias) was also applied, in order to ensure good mechanical contact between the sample electrodes and the external electrodes. Thus the sample was loaded with a static force and a dynamic force, but only the dynamic charge signal generated by the dynamic force was recorded. Samples were metalized with electrodes of about 50 nm on both sides, in order to collect all real compensating charges.

In general, there were three parts to the measuring system, the “force part” to generate and to monitor the applied force, the “charge part” to collect and to measure the generated charges, and the “calculation part” to calculate and show the  $d_{33}$  coefficient, as schematically illustrated in figure 6.11.



1. Shaker with PMMA isolated cylindrical loading stamp
2. Top electrode
3. Sample with electrodes on both sides
4. Bottom electrode
5. Pressure guidance cylinder
6. Force sensor

Figure 6.11: Illustration of the dynamic determination system for piezoelectric  $d_{33}$  coefficient.

The sample was placed on the bottom electrode, with a small, light-weight top electrode on it, which was used to collect the generated compensating charges. The force sensor (KM03, Type 8435-5200, Burster, measuring range: 0 – 200 N) was fixed under the bottom electrode. However, this force sensor could measure the force correctly only when the force was perpendicular to it, without any torsional moment or tilting. To this end, a smooth, frictionless ball bearing was set between the bottom electrode and the force sensor. A shaker (Type 4810, Brüel&Kjaer), with a

PMMA isolated cylindrical loading stamp, was mounted on a vertical moveable platform. By changing the platform position, a controllable static force applied to the top electrode and thus to the sample, could be increased or decreased. Usually a static force of 3 N was applied. In addition, a dynamic force, which was generated by a function generator (Model DS345, Stanford Research Systems), and enlarged by a power amplifier (Type 2718, Brüel&Kjaer), was transferred to the shaker and then applied to the sample. Normally a dynamic force with a peak-to-peak value of 1 N, and frequency 2 Hz was applied. The force sensor measured both the static and dynamic forces and its output was converted and amplified with a module amplifier (Type 9243, Burster) and then fed back to a storage oscilloscope (200 MHz Oscilloscope, 800 Ms/sec, Type 4094, GOULD). In order to measure the compensating charges, both sides of the sample were electrically connected to the charge amplifier (Type 2635, Brüel&Kjaer, precision 0.1 pC), and the bottom electrode was grounded together with the amplifier. Charges were collected by the top electrode which was electrically isolated from the shaker. The charge signal was amplified and also recorded by the oscilloscope.

In order to calculate the piezoelectric  $d_{33}$  coefficient from the charge and force signals, the measurement outputs were transferred from the oscilloscope to a computer and analyzed by software. The applied force consists of a dynamic force and a static force

$$F(t) = F_m \sin(2\pi ft + \varphi) + F_{static}, \quad (6.11)$$

where  $F_m$ ,  $f$ , and  $\varphi$  is the amplitude (peak value), frequency, and phase of the dynamic force, respectively. The charge signal is also sinusoid

$$Q(t) = Q_m \sin(2\pi ft + \varphi + \Delta\varphi), \quad (6.12)$$

where  $Q_m$  is the amplitude of the charge, i.e. the maximum generated charge when the largest thickness change occurs;  $f$  is the frequency of charge signal, the same as the force frequency, and  $\varphi + \Delta\varphi$  is the phase of charge signal, with a phase difference  $\Delta\varphi$  to force. The charge signal can be “in phase”, where  $\Delta\varphi = 0$  (figure 6.12 (left)), or “out of phase”, where  $\Delta\varphi = 180^\circ$  (figure 6.12 (right)), to the applied force signal, depending on the orientation of the sample. In this experimental setup, if the positively charged side is facing the charge amplifier, the charge signal is in phase with the force signal; if the positively charged side is facing the ground, with the negatively charged side facing the charge amplifier, the charge signal is out of phase with the force signal. The piezoelectric  $d_{33}$  coefficient can be calculated from the generated charge in the 3-direction (the thickness direction) and the applied force in the 3-direction

$$d_{33} = \frac{\Delta Q_3}{\Delta F_3}, \quad (6.13)$$

without knowing any of the geometric parameters of the sample. In a dynamic measurement, the static force is kept constant and has no contribution to  $\Delta F$ , therefore

$$\text{in phase: } d_{33} = \frac{\Delta Q_3}{\Delta F_3} = \frac{Q(t)}{F(t)} = \frac{Q_m \sin(2\pi ft + \varphi)}{F_m \sin(2\pi ft + \varphi)} = \frac{Q_m}{F_m}, \quad (6.14)$$

$$\text{out of phase: } d_{33} = \frac{\Delta Q_3}{\Delta F_3} = \left| \frac{Q(t)}{F(t)} \right| = \left| \frac{Q_m \sin(2\pi ft + \varphi + 180^\circ)}{F_m \sin(2\pi ft + \varphi)} \right| = \left| -\frac{Q_m}{F_m} \right| = \frac{Q_m}{F_m}. \quad (6.15)$$

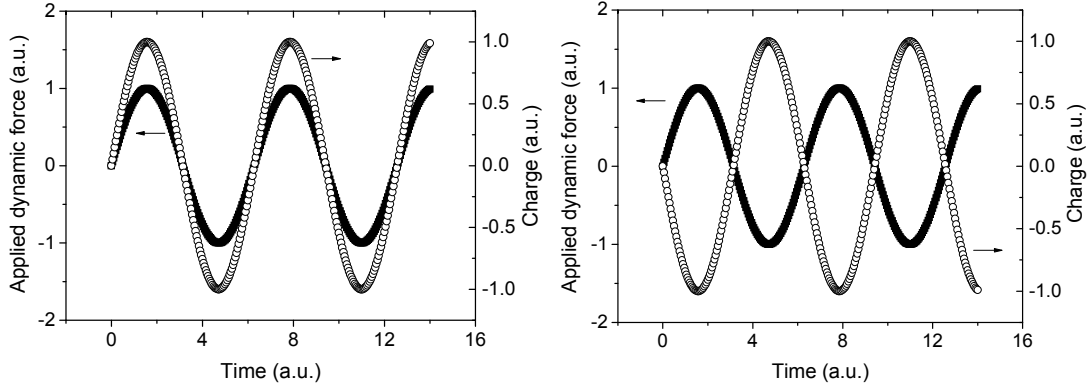


Figure 6.12: Signals of the applied dynamic force and the resulting charges, in the case of “in phase” (left) and “out of phase” (right), depending on the charge polarity facing the charge amplifier.

However, instead of using only the magnitude (peak-value) of the charge and force,  $d_{33}$  was achieved by averaging the slopes of the charge-force curve from the large amount of data gathered during a measurement period in order to decrease the error, i.e.

$$Q(t) = d_{33}(t)F(t), \quad (6.16)$$

and

$$d_{33} = \frac{\sum_{N, T_0} d_{33}(t)}{N}, \quad (6.17)$$

where  $N$  is the number of data-gathering cycles during a measurement period  $T_0$ . The error may come either from the “force part”, such as an non-perpendicular force to sensor or the friction of the ball bearing, or from the “charge part”, such as the contribution from space charges. In this work the dynamic measurements were always carried out at room temperature. A measurement was repeated 3 to 5 times on both sides of the sample in order to get the final average value for the piezoelectric  $d_{33}$  coefficients.

## 6.5 Dielectric-resonance spectroscopy (DRS)

The dynamic measurement, where the  $d_{33}$  coefficients are calculated by measuring generated charges and applied forces, is a simple method that derives from the direct piezoelectric effect. However, this standard electromechanical method relies on applying a mechanical stress to the sample which may cause irreversible or slowly reversible creep in samples with low elastic moduli [Taylor 2005]. In other words, samples with low elastic moduli may not recover their initial shape immediately after the release of force, or recover slowly. Therefore, dielectric-resonance spectroscopy as an electrical method, which depends on the reverse piezoelectric effect, was developed [Neuschwandtner 2000, Mellinger 2003]. The sample deforms if a voltage is applied, and it vibrates with a frequency if driven by an alternating voltage. If the frequency matches the sample’s natural mechanical oscillation frequency, a detectable resonance occurs. Dielectric-resonance spectra (DRS) have the advantage of yielding several important parameters in a single measurement compared to dynamic measurements. The theory of this technique is well

discussed in [\[Neugschwandtner 2000, Mellinger 2003\]](#).

Normally, upon application of an oscillating electric field  $E(t) = E_0 \exp^{i\omega t}$ , a piezoelectric sample exhibits length- (LE), width- (WE) and thickness-extension (TE) resonances at its eigenfrequencies, and the resonance of a thin piezoelectric film in the 33-direction is the TE resonance. With the applied voltage  $V$  and measured current  $I$ , the complex impedance  $Z$  or the complex admittance  $Y$  can be calculated from

$$\tilde{Z} = \frac{V}{\tilde{I}}, \quad (6.18)$$

and

$$\tilde{Y} = \frac{\tilde{I}}{V}. \quad (6.19)$$

In addition, the complex capacitance and admittance can be presented as

$$\tilde{Z}(\omega) = \frac{1}{i\omega\tilde{C}}, \quad (6.20)$$

and

$$\tilde{Y}(\omega) = i\omega\tilde{C}, \quad (6.21)$$

where  $\omega$  is the angular frequency. The complex capacitance is

$$\tilde{C} = \frac{1}{i\omega\tilde{Z}} = \frac{\tilde{Y}}{i\omega} = \frac{1}{i\omega\frac{V}{\tilde{I}}} = \frac{\tilde{I}}{i\omega V} = C' - iC'', \quad (6.22)$$

where  $C'$  and  $C''$  are the real and imaginary part of the complex capacitance, respectively. The complex capacitance of a thin planar film near the TE mode is given by [\[Ohigashi 1976, Neugschwandtner 2000, Mellinger 2003\]](#)

$$\tilde{C}_{TE}(\omega) = \frac{\varepsilon_0 \varepsilon_{33} A}{h} \frac{1}{1 - k_t^2 \frac{\tan(\omega/4f_{r,TE})}{\omega/4f_{r,TE}}} - iC_{loss}, \quad (6.23)$$

where the complex anti-resonance frequency  $f_{r,TE}$  and the complex electromechanical coupling factor  $k_t$  are expressed as

$$f_{r,TE} = \frac{1}{2h} \sqrt{\frac{c_{33}}{\rho}}, \quad (6.24)$$

for a free-standing sample,

$$f_{r,TE} = \frac{1}{4h} \sqrt{\frac{c_{33}}{\rho}}, \quad (6.25)$$

for a clamped (one side glued) sample, and

$$k_t = \frac{e_{33}}{\sqrt{\varepsilon_0 \varepsilon_{33} c_{33}}}, \quad (6.26)$$



respectively.  $\epsilon_{33}$  is the relative 33 component of the permittivity tensor of the material,  $A$  is the area of electrode on the sample,  $h$  and  $\rho$  are the thickness and the density of the sample,  $e_{33}$  is the piezoelectric stress coefficient, and  $c_{33}$  is the elastic modulus. In samples with small  $d_{31}$  and  $d_{32}$  coefficients, there is an approximation of  $e_{33}$ , which is

$$e_{33} \approx d_{33}c_{33}. \quad (6.27)$$

This approximation is reasonable for piezoelectric films because their piezoelectricity is strongly dominated by the longitudinal effect [Neugschwandtner 2001]. Therefore

$$k_t \approx d_{33} \sqrt{\frac{c_{33}}{\epsilon_0 \epsilon_{33}}}. \quad (6.28)$$

Via a least-squares fit, the quantities  $f_{r,TE}$ ,  $\epsilon_{33}$ ,  $k_t$ ,  $C_{\text{loss}}$ ,  $c_{33}$  and  $d_{33}$  can be determined with equations 6.24 to 6.28.

DRS were measured with a high-resolution dielectric analyzer (Novocontrol ALPHA) and a cryosystem (Novocontrol QUATRO) for temperature control. As shown in figure 6.13, the sample was mounted and contacted with two annular electrode plates at their edges so that it could vibrate freely with the applied sinusoidal voltage, with only minimal effects from the spring-loaded electrode contacts. In addition, the dielectric-resonance spectroscopy enables a measurement at different temperatures in the range from  $-160$  to  $350$  °C. Therefore spectra were also recorded at elevated temperatures to acquire the temperature dependent piezoelectric properties.

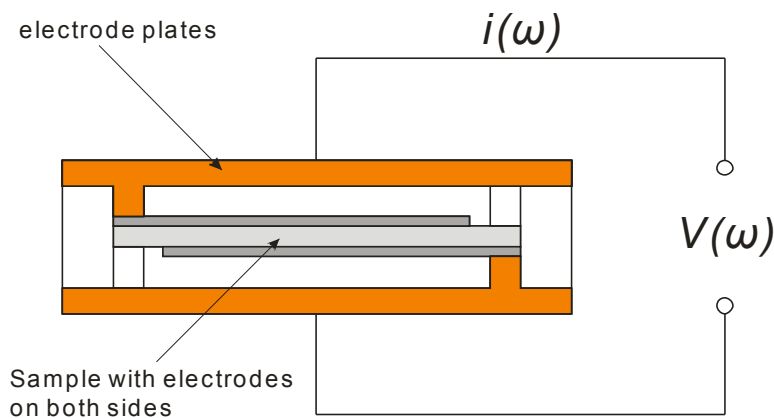


Figure 6.13: Experimental setup for the dielectric-resonance spectrum measurement.

## 6.6 Acoustic measurement

Acoustic measurement is also a mechanical method used to investigate the piezoelectric properties. There are two modes for the acoustic technique, one is the “loudspeaker mode”, where the reverse piezoelectric effect is used, and the other one is the “microphone mode”, where the direct piezoelectric effect is used. In the loudspeaker mode, a sample is investigated as an actuator, as depicted in figure 6.14: An alternating voltage is applied and sample vibrates at the same frequency as the voltage. Sound waves are generated and then recorded by an already calibrated standard microphone. By analyzing the sound signal, piezoelectric properties can be studied. In

the microphone mode, the sample is utilized as a sensor, as shown in figure 6.15: A sound signal is generated by a standard loudspeaker, and then recorded by the sample. As a result, an electric signal is produced. By analyzing the electric signal, the piezoelectric properties can be studied. Both for the loudspeaker and microphone mode, the generating voltage and the generating sound signal are applied with an increasing or decreasing frequency, so the frequency dependent piezoelectric properties can be investigated.

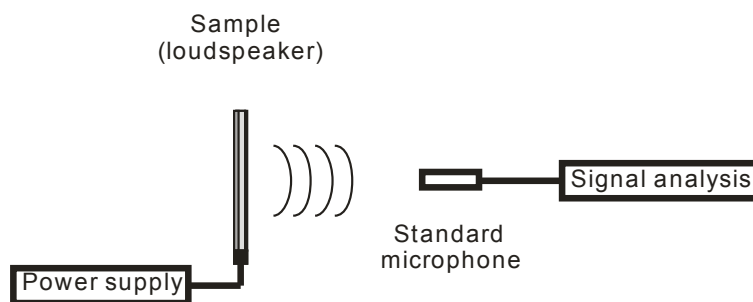


Figure 6.14: In a “loudspeaker mode”, sample is tested as a loudspeaker (actuator): Sound signal is generated by applying an alternating voltage, recorded by a standard microphone, and then analyzed by the program.

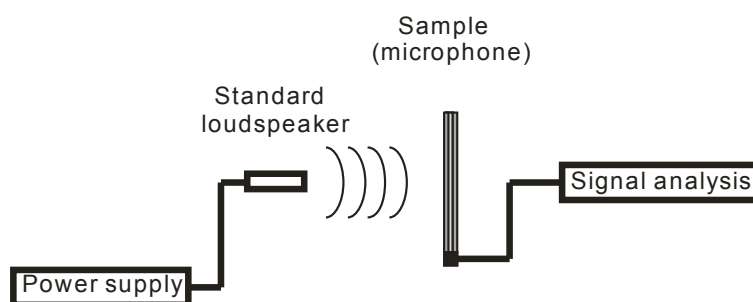


Figure 6.15: In a “microphone mode”, sample is tested as a microphone (sensor): Sound wave is generated by a standard loudspeaker, and recorded by the sample. An electric signal is therefore generated and then analyzed by the program.

Compared with the former two techniques, the acoustic measurement is especially suitable to investigate samples which are prepared with the aim of loudspeaker or microphone applications. Unlike the dynamic determination, there is no extra load (static force) on the sample, which is in many cases closer to the real applications. In an acoustic measurement, harmonics can be observed, the piezoelectric  $d_{33}$  coefficient can be deduced and its frequency response can be achieved.

In this work, limited by the present experimental techniques, only the loudspeaker mode was applied. Figure 6.16 illustrates the experimental setup for the loudspeaker mode measurement. A sample with electrodes on both sides was placed on a sample holder, with contact to the different poles of the power source, respectively. A computer controlled sinusoidal voltage was generated (Agilent 33220A 20MHz Function/Arbitrary Waveform Generator) and amplified (100 V~ Sinusgenerator self-made), and then applied to the sample. Simultaneously, the voltage signal was also monitored by the oscilloscope (Agilent MSO6104A Mixed Signal Oscilloscope). The sound waves generated by the sample were recorded by the microphone (Brüel&Kjær type4191),

amplified (Brüel&Kjær type2690 Conditioning Amplifier) and then transferred to the oscilloscope, where a fast Fourier transform (FFT) of the sound signal was applied. The sound signals recorded by the microphone were expressed as voltage, and after the amplification it was expressed in the logarithmic magnitude unit decibels.

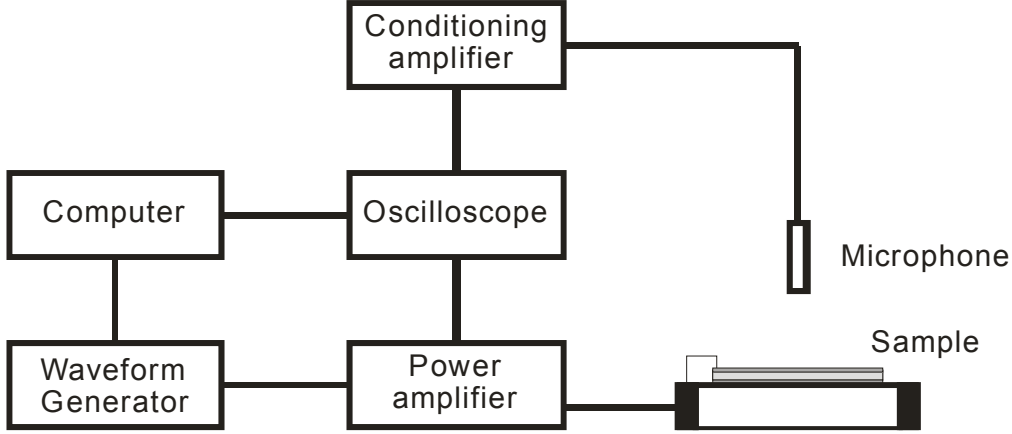


Figure 6.16: Illustration of the experimental setup for the acoustic measurement in loudspeaker mode.

According to the definition, there is a relation between the  $L_{dB}$  (unit: decibel) and the power

$$L_{dB} = 10 \log_{10} \left( \frac{P_1}{P_0} \right), \quad (6.29)$$

where  $P_1$  is the power at the detecting position, and  $P_0$  is the reference power, the equation above is called the 10-log-rule. In most applications power is proportional to the square of the amplitude, thus equation 6.29 can be expressed as

$$L_{dB} = 10 \log_{10} \left( \frac{P_1}{P_0} \right) = 10 \log_{10} \left( \frac{A_1^2}{A_0^2} \right) = 20 \log_{10} \left( \frac{A_1}{A_0} \right), \quad (6.30)$$

where  $A_1$  and  $A_0$  are the amplitude at the detecting position and the reference amplitude, respectively, and this equation is called the 20-log-rule.

In acoustics, sound pressure is the most used physical quantity to describe the sound wave. The measurement of sound pressure is technically easy, and several other parameters such as particle velocity can be determined from the sound pressure. Sound pressure is defined as the local pressure deviation from the ambient (average, or equilibrium) pressure caused by a sound wave. Sound pressure can be measured using a microphone in air and a hydrophone in water. In the acoustic measurement, the sound pressure recorded by a microphone is expressed by the voltage

$$L_{dB} = 20 \log_{10} \left( \frac{V_1}{V_0} \right). \quad (6.31)$$

By measuring of  $L_{dB}$  and knowing of the reference voltage  $V_0$ , the corresponding voltage at the detecting position  $V_1$  is

$$V_1 = V_0 \times 10^{\frac{L_{dB}}{20}}. \quad (6.32)$$

Similarly, the corresponding voltage due to the background can also be achieved through

$$V' = V_0 \times 10^{\frac{L'}{20}}, \quad (6.33)$$

where the background  $L'$  is measured in the absence of the sample. The corresponding effective sound pressure  $P_{eff}$  is calculated from the voltage and the amplification  $G$  (unit: V/Pa), which is given by

$$P_{eff} = \frac{V_1 - V'}{G}, \quad (6.34)$$

and the amplitude of the sound pressure is the effective value times the square root of two

$$P = P_{eff} \times \sqrt{2} = \frac{V_1 - V'}{G} \times \sqrt{2} = \frac{V_0 \times 10^{\frac{L_{dB}}{20}} - V_0 \times 10^{\frac{L'}{20}}}{G} \times \sqrt{2}. \quad (6.35)$$

The sound pressure can also be computed from the geometric parameters and sound frequency [Kressmann 2001], which is expressed as

$$P = \frac{1}{2r} \rho R^2 \omega^2 x, \quad (6.36)$$

where  $r$  is the perpendicular distance between sample and microphone on the main axis,  $\rho$  is the density of the medium,  $R$  is the radius of the sample (here the electrode radius),  $\omega$  is the angular frequency of the applied driving voltage, and  $x$  is the deflection amplitude of the surface. In addition, the perpendicular distance between sample and microphone should fulfill a “far-field” requirement [Möser 2005]

$$r \gg \frac{R^2}{\lambda} = \frac{R^2}{v/f} = \frac{R^2 f}{v}, \quad (6.37)$$

where  $\lambda$  and  $v$  are the wavelength and the velocity of the sound, respectively.  $f$  is the frequency of the sound, which is the same as that of the driving voltage.

Based on the layer-model of the ferroelectrets, the piezoelectric  $d_{33}$  coefficient can be calculated both for the sensor and the actuator mode [Kressmann 2001]

$$d_{33} = \frac{\varepsilon_{2r} \varepsilon_{1r} \sigma}{c_{33}} \frac{ss_1}{(\varepsilon_{2r} s_1 + \varepsilon_{1r} s_2)^2} = \frac{x}{U}, \quad (6.38)$$

where  $x$  is the deflection amplitude of the surface in equation 6.36 and  $U$  is the peak value of the driving voltage applied (the output of the power amplifier). By combination of the mechanical-acoustical conversion (equation 6.36) and the electro-mechanical conversion (equation 6.38), the electro-acoustical conversion can be deduced

$$d_{33} = \frac{x}{U} = \frac{2rP}{\rho R^2 \omega^2 U} = \frac{rP}{2\rho R^2 \pi^2 f^2 U}, \quad (6.39)$$

By combining equation 6.39 with equation 6.35,  $d_{33}$  can be calculated as

$$d_{33} = \frac{r}{2\rho R^2 \pi^2 f^2 U} \times \frac{V_0 \times 10^{\frac{L_{dB}}{20}} - V_0 \times 10^{\frac{L'}{20}}}{G} \times \sqrt{2}. \quad (6.40)$$

The reference voltage  $V_0$  is set as 1 V (the unit of  $L_{dB}$  is dBV by definition), so  $d_{33}$  is

$$d_{33} = \frac{r}{2\rho R^2 \pi^2 f^2 U} \times \frac{10^{\frac{L_{dB}}{20}} - 10^{\frac{L'}{20}}}{G} \times \sqrt{2}. \quad (6.41)$$

In the actual measurements of this work, a sinusoidal voltage with fixed amplitude  $U$  but increasing frequency  $f$  was applied. The fundamental and second harmonic sound pressures were recorded and analyzed,  $d_{33}$  coefficients at each frequency were calculated and therefore the frequency response could be discussed.

## 6.7 Fourier transform infrared (FTIR) spectroscopy

Fourier transform infrared (FTIR) spectroscopy is a technique which can be used to identify molecules by analysis of their constituent bonds. Each chemical bond in a molecule vibrates at a frequency which is characteristic of that bond. A group of atoms in a molecule (e.g.  $\text{CH}_2$ ) may have multiple modes of oscillation caused by the stretching and bending motions of the group as a whole. If an oscillation leads to a change in dipole moment in the molecule, then it will absorb a photon which has the same frequency. The vibration frequencies of most molecules correspond to the frequencies of infrared light. Typically, the technique is used to study organic compounds using light radiation from  $4000$  to  $400 \text{ cm}^{-1}$ , the mid-infrared and a spectrum of all the frequencies of absorption in a sample is recorded. This can be used to gain information about the sample composition in terms of the chemical groups present and also its purity (for example a wet sample will show a broad O-H absorption around  $3200 \text{ cm}^{-1}$ ). In this work, FTIR (Bruker, model Alpha-P) was used to verify the presence of the fillers added to the pure FEP films.

## 6.8 Differential scanning calorimetry (DSC)

Differential scanning calorimetry (DSC) is a thermo-analytical technique to determine phase transitions of polymers, such as the glass transition, Curie point, crystallization, and melting. In a DSC measurement, the sample and a reference, which has a well-defined heat capacity over the temperature range to be investigated, are both maintained at the same temperature during the whole scan. The heat capacity changes, when the sample undergoes a physical transformation during heating or cooling. Thus, in order to maintain both at the same temperature, more (or less) heat will be needed for the sample than for the reference. The heat difference between the sample and the reference required to increase the temperature is measured as a function of temperature. Crystalline polymers show crystallization and melting transitions, whereas amorphous polymers exhibit glass-transitions. Semi-crystalline polymers show all the transitions of both crystalline and amorphous polymers.

- Glass transition behavior (during heating)

The glass transition appears as a step in the baseline of the DSC curve. The temperature at the

midpoint of the heat capacity increment is considered as the glass-transition temperature ( $T_g$ ). The glass transition originates from the amorphous domains of the polymer and since only few polymers are 100% crystalline, the glass transition should be observed in most of the polymers. At the glass-transition temperature, a certain length of polymer chains has enough energy and becomes movable. Polymers are glassy and rigid below  $T_g$ , and soft and rubbery above  $T_g$ . The glass transition is a second-order transition, which involves a heat capacity change, but does not have a latent heat, i.e. no formal phase change takes place.

- Melting behavior (during heating)

With a further increase of temperature, the semicrystalline sample reaches the melting temperature of the crystallites ( $T_m$ ). At the melting interval, the molecules are mobile enough that the material becomes viscous and amorphous. The melting process results in an endothermic peak in the DSC curve. Melting is a first-order transition. The area under the heat-flow peak is a measure of the enthalpy of fusion

$$H_f = \frac{1}{mh} \int \Phi(T) dT, \quad (6.42)$$

where,  $m$  mass,  $h$  heating rate,  $\Phi$  heat flow. It can be used to calculate the degree of crystallinity  $c = H_f/H_{f,0}$ , where  $H_{f,0}$  is the enthalpy of fusion for the 100% crystalline polymer.

- Crystallization behavior (during cooling)

The transition from amorphous to crystalline solid is an exothermic process and appears as a peak in the DSC curve. The crystallization temperature ( $T_c$ ) is known as the point where the molecules may arrange themselves into a crystalline form, during the decrease of temperature. Crystallization is a first-order transition, which involves both a latent heat and a heat capacity change.

In this work, the thermal transition behaviors of non-voided polymers (FEP with or without fillers) were studied using power compensated DSC (Perkin Elmer Pyris Diamond DSC). DSC curves were measured during heating and subsequent cooling and the heating and cooling of the same sample was performed twice with a heating rate of 20 °C/min due to a possibility of a presence of water, solvent or strengths in the sample. Only the DSC curves of second heating were used.

## Chapter 7

# Polyethylene-naphthalate (PEN) foam ferroelectrets

### 7.1 Properties of PEN

Recently, ferroelectrets have been successfully developed from polyethylene-terephthalate (PET) films, and their properties demonstrate that PET ferroelectrets own several good characteristics for potential applications in electromechanical devices [Voronina 2008]. At the same time, new candidates for possible ferroelectret applications were still under investigation. Based on its chemical structure and properties, a thermoplastic polymer resin of the polyester family, polyethylene naphthalate (PEN), came into view. PEN is a kind of high-performance thermoplastic polyester, which was first produced in the middle of 20th century. It was introduced into the market by Teijin<sup>®</sup> as an extruded film in the early 1970s with “Q-polymer” as the trade name. The chemical structure of PEN is similar to that of PET, except the terephthalate structure is replaced by the double ring structure of naphthalene molecule, as shown in figure 7.1 (chemical structure of PET shown in figure 3.5).

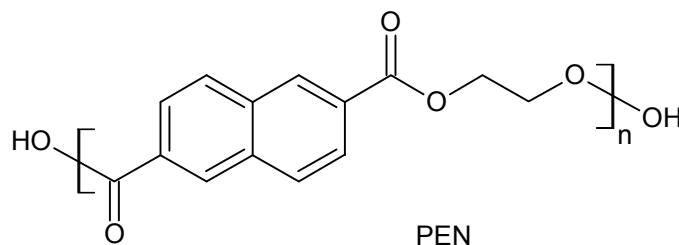


Figure 7.1: Chemical structures of polyethylene naphthalate (PEN).

As a kind of polyester, PEN contains an ester functional group, the carboxylic acid ester  $R^1-C(=O)-O-R^2$ , in the main chain, where  $R^1$  and  $R^2$  denote any alkyl ( $C_nH_{2n+1}$ ) and aryl (substituent derived from a double phenyl ring structure) groups. Due to the oxygen's high electronegativity compared to that of carbon, the electron density is shifted toward the oxygen atom. Consequently, the carbonyl group forms a dipole and PEN is a weakly-polar polymer. Due to the better structural stability at the molecular level, the double phenyl ring structure in the polyester chain improves PEN's performance compared to the polyester polymers based on the terephthalate structure. The thermal, mechanical, electrical, and barrier properties of PEN as well as its heat, chemical, hydrolytic, and radiation resistance are superior to those of PET. This means higher modulus, tenacity and resistance to stretching and shrinkage. PEN also has better resistance to thermal and chemical attack because of its more stable molecule structure. All these positive characteristics and properties make PEN an attractive candidate for new thermally stable ferroelectrets. In addition, the availability of homogeneous PEN films in large quantities as

industrial products opens an excellent opportunity to investigate this polymer in detail with relatively low cost.

	PEN	PET
Glass transition temperature ( $T_g$ , °C)	122	80
Melting point ( $T_m$ , °C)	269	258
Young's modulus (Mpa): (MD+TD)/2-50 $\mu\text{m}$ films	5200	3900
Thermal rating (°C): continuous operation according to UL746B	155	105
Thermal shrinkage (%): 30 min at 150 °C (balanced film)	0.6	1.3
Oligomer extraction ( $\text{mg}/\text{m}^2$ ): 1 hour in chloroform at 23 °C	0.8	20
Hydrolytic resistance (hr): time to retain 60% elongation at 130 °C in an autoclave	200	50
Resistance to radiation (MGy): dose to retain 50% elongation to x-rays in vacuum	100	2
Oxygen permeability ( $\text{cm}^3/[\text{m}^2 \times \text{day} \times \text{bar}]$ ): measured on 25 $\mu\text{m}$ films	20	56

Table 7.1: Some properties of PEN and PET [[www.dupontteijinfilms.com](http://www.dupontteijinfilms.com)].

The synthesis of PEN is analogous to that of PET. It can be synthesized by a direct esterification or a transesterification while the latter is more often used. The feedstock for the reactions is 2,6-Naphthalenedicarboxylic acid (2,6-NDA) and its dimethyl ester (2,6-NDC), as shown in figure 7.2.

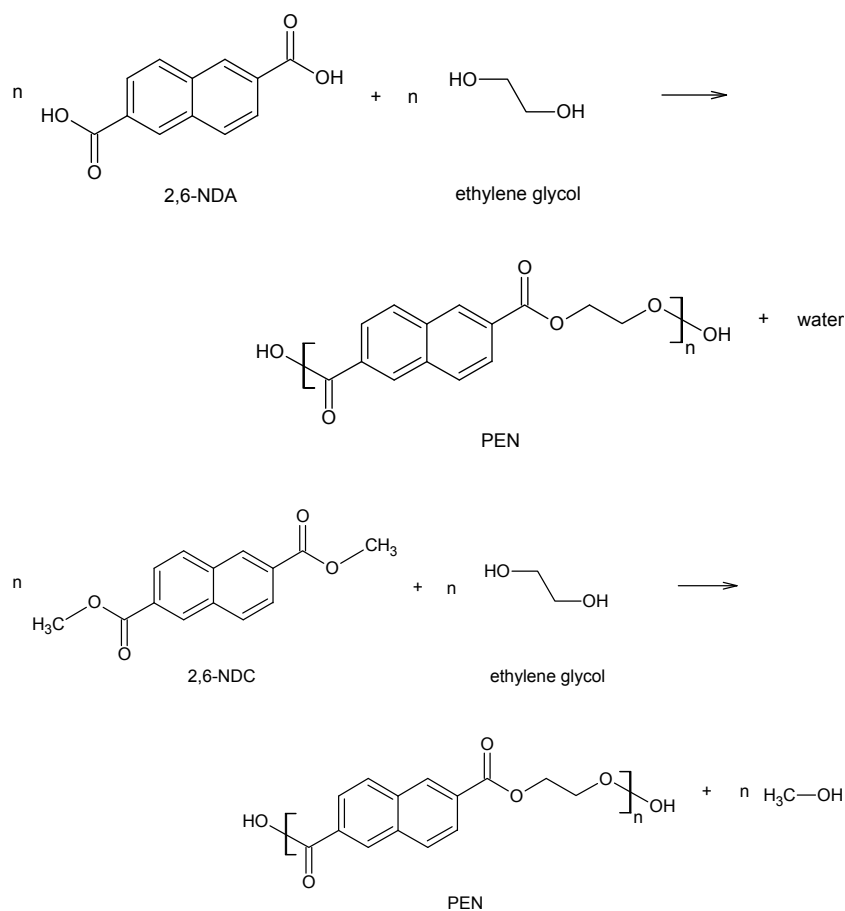


Figure 7.2: Synthesis of PEN by a direct esterification or a transesterification.



The starting material in this work is Teonex<sup>®</sup> Q51 PEN film (solid) produced by DuPont Teijin Films<sup>™</sup> with three thicknesses of 50, 100 and 188  $\mu\text{m}$ . The density is about  $1.45 \text{ g/cm}^3$ . All solid films are transparent and glazed. The flexibility and transparency decrease with the increase of thickness, and the 188  $\mu\text{m}$  thick films are quite stiff and opaque.

Good charge-storage ability is very critical for ferroelectrets with temporarily and thermally stable piezoelectricity. Figure 7.3 shows the surface potential decay for 50  $\mu\text{m}$  thick solid PEN films stored at room temperature for both positive and negative charges. Films were corona charged with different tip-to-plane voltages at room temperature, and a grid was used in the case that the control of the surface potential was needed. Films charged with a corona-tip voltage of  $\pm 15 \text{ kV}$  and a grid voltage of  $\pm 1 \text{ kV}$  show surface potentials of about  $\pm 1 \text{ kV}$ , which is the same as the grid voltage. Without grid, surface potentials are  $\pm 1.5$ ,  $\pm 3$ , and  $\pm 4 \text{ kV}$  when charged with a corona-tip of  $\pm 8$ ,  $\pm 12$ , and  $\pm 15 \text{ kV}$ , respectively. Relatively lower surface potentials are almost stable with time. However, if the initial surface potentials are higher than  $\pm 3 \text{ kV}$ , they decrease quickly within the first 10 hours after charging, and reach a stable value of about  $\pm 2.8 \text{ kV}$  after 7 days. The fast decay of the surface charges is due to the relatively higher internal electric field induced by the surface charges themselves.

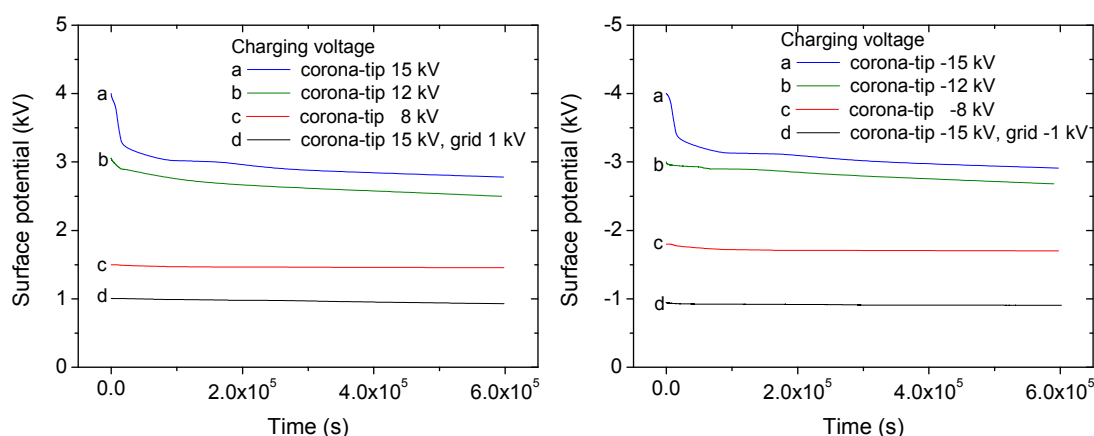


Figure 7.3: Temporal decay of the surface potential at room temperature for solid PEN films (50  $\mu\text{m}$  thick) positively (left) and negatively (right) charged. Films were corona charged at room temperature, with different corona tip-to-plane voltages as indicated.

Figure 7.4 shows the thermally stimulated decay of surface potential as a function of the temperature for both positive and negative charges. For PEN films, surface charges of both polarities show nearly the same thermal behavior. Films with thicknesses of 50, 100 and 188  $\mu\text{m}$  show similar thermal surface-charge stability (only the results for 50  $\mu\text{m}$  thick films are shown here). Significant decay of the surface potential starts at a temperature of  $120 \text{ }^\circ\text{C}$ , and almost all the surface charges are lost when the temperature is higher than  $160 \text{ }^\circ\text{C}$ .

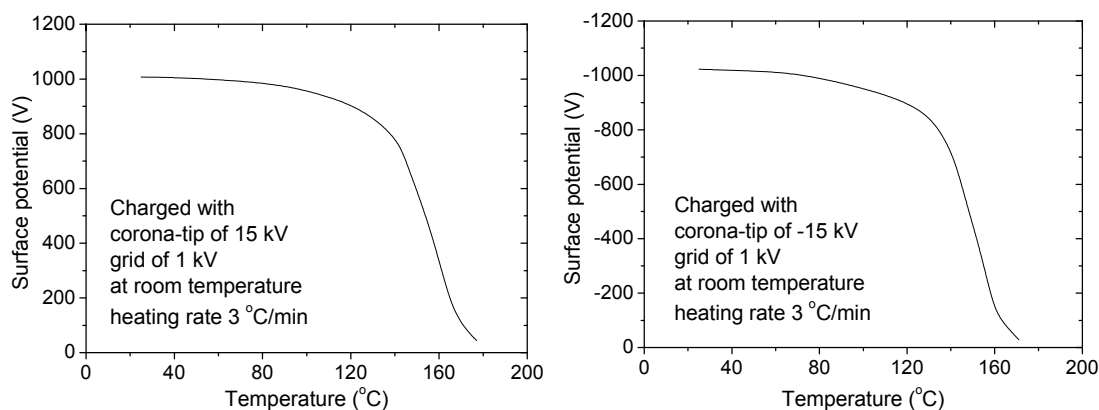


Figure 7.4: Thermally stimulated decay of surface potential for solid PEN films (50  $\mu\text{m}$  thick) positively and negatively charged. Films were charged with a corona tip-to-plane voltage of  $\pm 15$  kV and a grid voltage of  $\pm 1$  kV at room temperature. Heating rate is 3  $^{\circ}\text{C}/\text{min}$ .

## 7.2 Formation and optimization of PEN foam

### 7.2.1 Description of technique

As the chemical and mechanical properties of PEN are analogue to those of PET, the structure formation and optimization processes for cellular PET (section 4.2) were considered as the guideline for preparation of PEN. Therefore, a so-called “voiding + inflation + stretching” process was specifically developed under laboratory conditions. A high-pressure system (Sigmar Mothes Hochdrucktechnik, Germany), a heating system (Heating plate or oil bath, lab-built), and a stretching system (Karo IV, Brückner GmbH) were utilized. The several preparation steps, illustrated in figure 7.5, are discussed in the following.

(a) Film samples with a maximum size of  $9 \times 9$   $\text{cm}^2$  (limited by the dimensions of the high pressure chamber) cut from commercial PEN sheets were first placed into a high-pressure steel chamber, where the gas pressure could be adjusted up to 250 bars. Carbon dioxide ( $\text{CO}_2$ ) was used as the foaming agent. When samples were exposed to supercritical  $\text{CO}_2$  for a certain period of time, the polymer was saturated with the supercritical fluid. Immediately after reducing the high pressure, the samples were taken out of the chamber and underwent a heat treatment at a temperature above the material’s glass-transition temperature  $T_g$  (122  $^{\circ}\text{C}$ ) but below its melting temperature  $T_m$  (269  $^{\circ}\text{C}$ ), and the sudden volume increase of the supercritical fluid upon its phase change back to gas lead to the foaming of the film. In addition, the heat treatment stabilizes the structural change; otherwise the structure would return to its former form. Samples could be thermally treated between two pre-heated glass plates, or in an oil bath (Jojobe oil, organic). Treatment between glass plates was easier to operate, however, it may induce bubbles on the sample surfaces due to inhomogeneous heating. Homogeneous heating could be achieved in the oil bath, but samples might become crapy due to the disturbance from the movement of the oil.

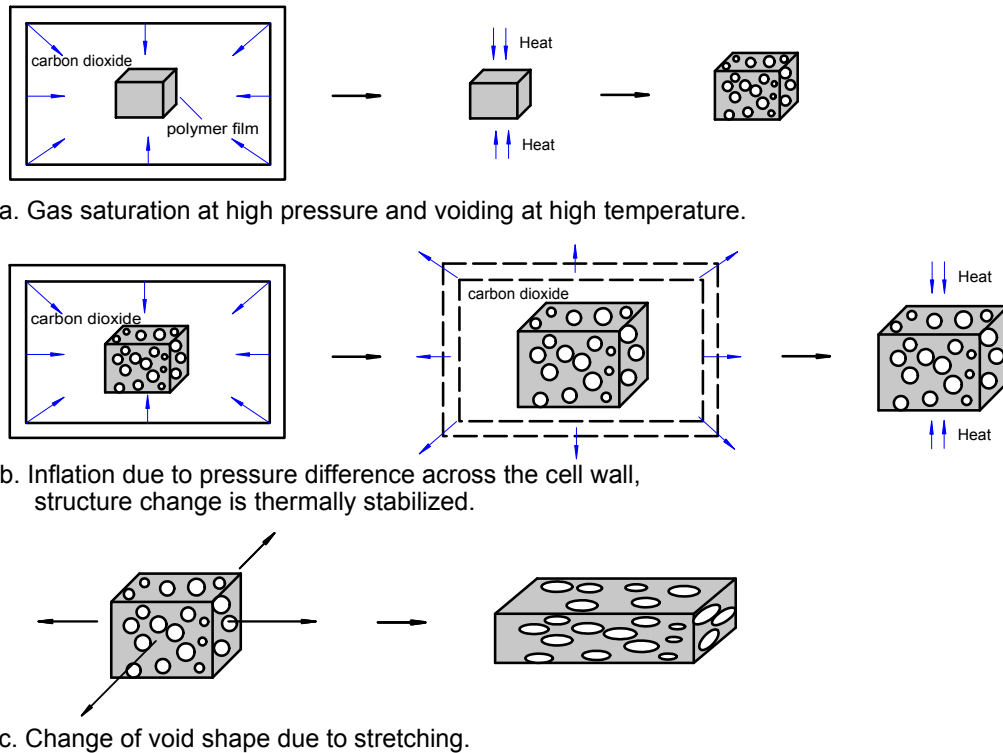


Figure 7.5: Illustration of the structure formation and optimization for PEN foams.

- (a) Solid film samples were saturated with supercritical CO<sub>2</sub>, and the voiding was achieved by a heat treatment (physical foaming).  
 (b) Voids were enlarged by controlled inflation (Gas-Diffusion Expansion, GDE) and the structure change was again stabilized by a heat treatment.  
 (c) The structure is further optimized by the biaxial stretching in order to lower the void height.

(b) After the saturation of supercritical CO<sub>2</sub> and voiding by heating, the solid films were primarily voided. However, most of the voids were still quite small, with dimensions of a few micrometers. A further inflation was applied in order to improve the geometry of the voids: The voided films were exposed to high-pressure CO<sub>2</sub> until the voids were full of the pressurized gas. When the ambient high pressure was suddenly reduced, the voids were inflated due to the large pressure differences across the cell walls. The change of the foam geometry was again stabilized by a heat treatment as described above. Although the operations of voiding and inflation are the same, the basic principle is different: Voiding is due to the phase change by heat treatment, and inflation is due to the pressure difference across the cell walls. During the inflation process, voiding could also take place. CO<sub>2</sub> ice was always observed around the sample after the release of high pressure. CO<sub>2</sub> underwent a phase transition from supercritical fluid to gas state by the release of high pressure, which absorbed heat. Thus the samples were cooled down to a temperature around or below the triple point of CO<sub>2</sub> (−56.4 °C).

(c) After the inflation, the voids were significantly enlarged, and most of them were spherical in shape. In order to achieve lens-shaped voids, a stretching was applied to decrease the void heights. Stretching was usually performed at a temperature around the polymer's  $T_g$ . Film samples could be stretched in machine direction (MD) and then in transverse direction (TD), so-called

uni-axial stretching, or stretched in MD and TD simultaneously, so-called biaxial stretching. In the biaxial stretching, the stretching forces were applied equally in both directions. Therefore the resulting cellular structure was more homogeneous and sample surfaces were smoother. The stretching ratio was usually controlled between  $1.2 \times 1.2$  and  $1.8 \times 1.8$  for the cellular film samples.

### 7.2.2 Investigation of foaming behavior

In order to find the optimized foaming conditions, several experimental parameters were varied, and the resulting foaming behaviors were investigated and compared. First, film samples were saturated with supercritical CO<sub>2</sub> at room temperature (RT), and at elevated temperatures of 50, 75 and 100 °C. The saturation pressure was kept at 150 bar for 150 min, and then the films were voided at 170 °C for 10 s. As illustrated in figure 7.6, the density of the voided films decreases only slightly with the increasing gas-saturation temperature, indicating that the influence of saturation temperature on sample density is not critical. Sample densities of about 0.6 g/cm<sup>3</sup> are achieved over a broad temperature range from RT to 100 °C. It is known that, due to Brownian motion the solubility of the gas in the polymer could decrease with increasing temperature. On one hand, the diffusion of CO<sub>2</sub> into the polymer is accelerated at higher temperatures, which shortens the saturation time, and at higher temperatures the polymer becomes softer, making it easier for gas saturation; On the other hand, the maximum amount of gas that can be saturated in the polymer is decreased at higher temperatures. As a result, elevated temperatures are not necessary to achieve samples with lower densities, and the gas saturation at room temperature was preferred in this work.

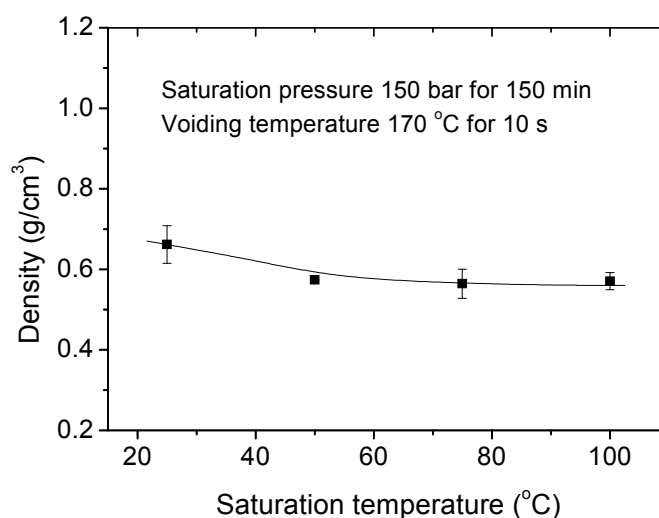


Figure 7.6: Dependence of the sample density on the saturation temperature. Samples were saturated at a pressure of 150 bar for 150 min, and voided at a temperature of 170 °C for 10 s. The line is to guide the eye.

The dependence of the sample density on the saturation time was also studied. Film samples were saturated with CO<sub>2</sub> for a period of time from 1 to 65 hours, and then voided under the same conditions. As shown in figure 7.7, when the saturation time is prolonged from 80 to 150 min, the sample density decreases from 1.3 to less than 0.8 g/cm<sup>3</sup>, which means that the gas diffusion is not

completed within a time period less than 150 min. The longer the sample is exposed to the supercritical CO<sub>2</sub>, the more CO<sub>2</sub> can diffuse into the polymer. If the saturation time is longer than 150 min, however, the sample density is not lowered further, which means the polymer is already saturated. Therefore, under the present condition a minimum saturation time of about 150 min is required.

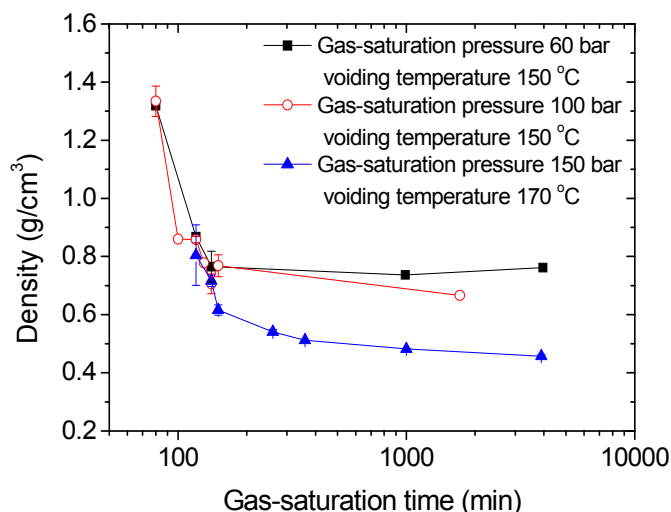


Figure 7.7: Dependence of the sample density on the gas-saturation time. A minimum period of about 150 min is required to achieve sufficient gas saturation.

The voiding temperature has significant influences on the sample density, as illustrated in figure 7.8. Samples saturated at pressures of 100, 150 and 200 bar were voided at different temperatures. Sample thicknesses were dramatically increased up to 300% of their initial values, and the lateral dimensions were slightly decreased by about 4%. As can be seen, sample densities decrease significantly from 0.9 to 0.6 g/cm<sup>3</sup> with the increased voiding temperatures from 140 to 180 °C. The voiding of the solid films is achieved by the sudden volume increase of the supercritical fluid upon its phase change back to gas state, and the higher the voiding temperature, the stronger is the voiding. It is found that the saturation pressure does not influence the sample density very much, since the samples saturated at 100, 150 and 200 bar show nearly the same density, if they are voided at the same temperature. This means a high pressure of 100 bar is sufficient to saturate supercritical CO<sub>2</sub> inside the PEN films under present conditions. It should be noted, however, a very strong voiding at very high temperatures is sometimes dangerous for the samples because it often induces bubbles on the sample surfaces.

In order to study the additional inflation behavior, film samples were first voided at the same condition and densities of about 0.65 g/cm<sup>3</sup> were achieved. Then the controlled inflation was applied in order to further enlarge the voids. To this end, the voided samples were exposed to pressurized CO<sub>2</sub> for 60 min, and then inflated by a fast release of the high pressure. Next, samples were thermally stabilized at different temperatures from 140 to 200 °C for 10 s. The sample density as a function of the stabilization temperature is illustrated in figure 7.9. The same as the voiding behavior, it is found that the higher the temperature, the lower are the densities. Different from the supercritical CO<sub>2</sub> saturation for voiding, where the resulting sample densities are

independent of the saturation pressures if the pressures are higher than 100 bar, however, in the controlled inflation process, lower densities are achieved if samples are exposed to higher pressures. The voiding is due to the sudden volume increase of the supercritical fluid upon its phase change back to gas. If the pressure is high enough the supercritical fluid is saturated in PEN, and no more CO<sub>2</sub> can be compressed into the polymer even if the pressure is further increased. Therefore the voiding is determined only by the voiding temperature. In contrast, the controlled inflation is due to the large pressure differences across the cell walls, and the higher the pressure, the larger is the pressure differences. Thus the inflation is controlled both by the high pressure and the stabilization temperature.

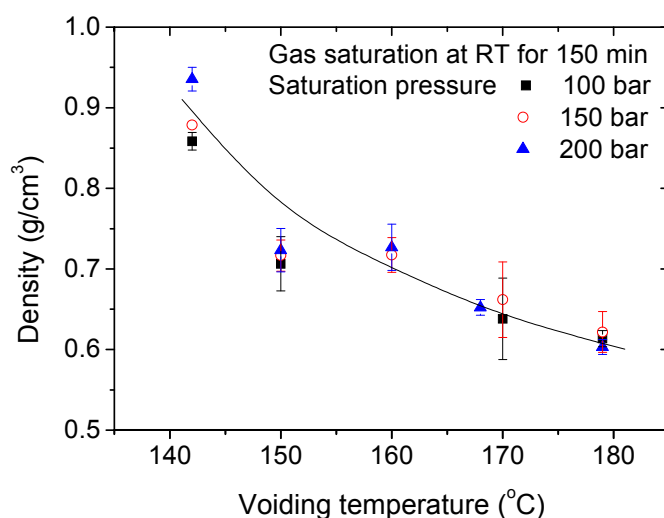


Figure 7.8: Sample density as a function of the voiding temperature. Samples were saturated with supercritical CO<sub>2</sub> at pressures of 100, 150, and 200 bar, at RT for 150 min, and then voided at different temperatures as indicated. The line is to guide the eye.

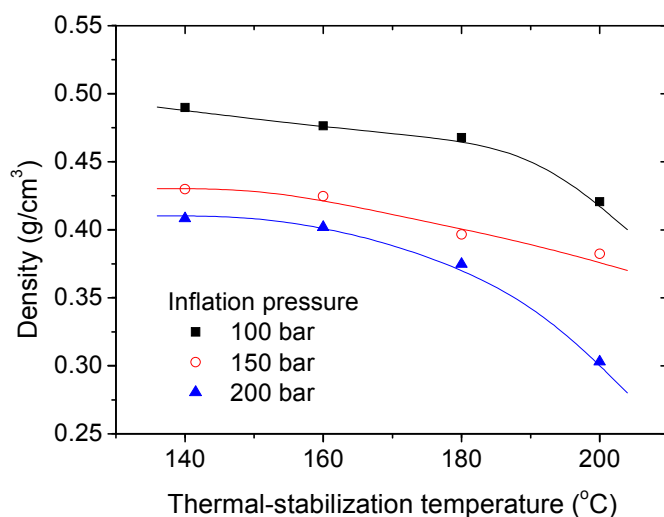


Figure 7.9: Sample density as a function of the thermal-stabilization temperature for the controlled inflation. Film samples were voided at the same condition, density of about 0.65 g/cm<sup>3</sup> was achieved. Then samples were exposed to CO<sub>2</sub> with different pressures for 60 min. After the release of high pressure, samples were thermally stabilized at different temperatures as indicated for 10 s. The lines are to guide the eye.

After the voiding and the controlled inflation, cellular voids were generated and significantly enlarged, but mostly with round shape. In order to lower the void heights and to achieve lens-like voids, a biaxial stretching was applied. Samples were stretched with stretching ratios between  $1.2 \times 1.2$  and  $2.0 \times 2.0$ . The resulting average sample densities after stretching are plotted in figure 7.10. A higher stretching ratio results in lower void heights, and therefore higher densities.

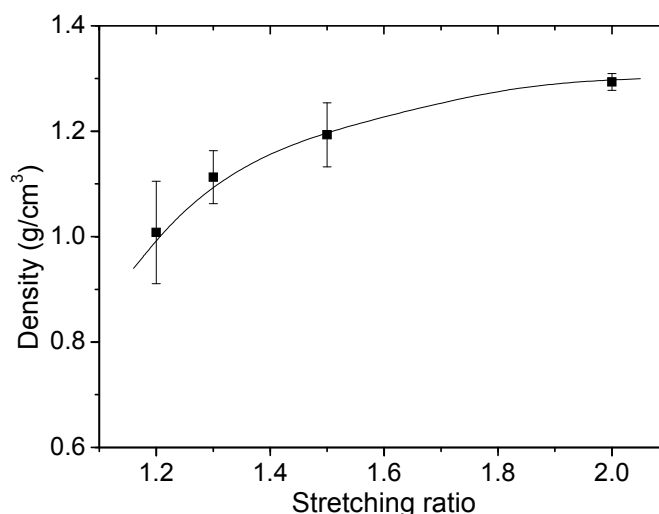


Figure 7.10: Sample density as a function of the biaxial-stretching ratio. The line is to guide the eye.

### 7.3 Investigation of cellular structure

Figure 7.11 shows the scanning electron microscopy (SEM) images for the cross section of two typical cellular PEN samples (initial solid film thickness 50 and 100  $\mu\text{m}$ , respectively), which demonstrates the successful formation of the lens-shaped voids inside the films by means of the “voiding + inflation + stretching” process. Voids are closed but inhomogeneous, with different sizes and large distributions. In addition, some parts of the films are still not foamed. The void shapes are detected and fitted with ellipses, as shown in figure 7.12. It should be noted that any cavity larger than a certain dimension is considered as a void, only a crack cannot be accepted as a void. The minor axes of the fitted ellipses are taken as the void heights and their distributions are calculated. As can be seen from figure 7.13, for these two samples, most voids have heights below 6 and 10  $\mu\text{m}$ , respectively, and the voids with relatively smaller heights ( $< 5 \mu\text{m}$ ) take the majority part. Taking into account the sample densities before and after the structure formation, the porosities of these two samples are calculated as 30.5% and 32.8%, respectively.

In a further experiment, a typical cellular sample metalized on both surfaces with aluminum electrodes (thickness 50 nm) was mounted in a sealed chamber in which the pressure could be adjusted between one millibar and a few bars. The sample capacitances were measured with a precision LCR meter (HP4284A). Firstly the chamber was pumped down until the pressure was as low as one millibar (100 Pa). As shown in figure 7.14, there is a sudden drop of the capacitance caused by the expansion of the sample, since the gas pressure of the vacuum environment is suddenly much lower than that inside the voids. However, there is no recovery of the capacitance

even after 5 h, which means that the gas inside the voids (CO<sub>2</sub>, the foaming agent) cannot penetrate through the void walls. Next, dry air at a pressure of 4 bar (400 kPa) was introduced into the chamber. A sudden capacitance increase is observed, as shown in figure 7.15, due to the compression of the sample by the ambient pressure. Even after 20 h, the capacitance has not decreased back to its initial value. Thus, there is not sufficient gas exchange between the voids and the ambient environment over the time scale of experiment and at the pressures in the range from a millibar to a few bars. The cellular voids are almost completely closed from the outer surroundings. To replace the CO<sub>2</sub> inside the voids by air is not possible at present experimental conditions, as a comparison, the gas-exchange of cellular PP films is quite easy under the same condition [Qiu 2008(1)]. This is due to the great structural stability at the molecular level of PEN, which makes it much more difficult for gases to penetrate into PEN than PP.

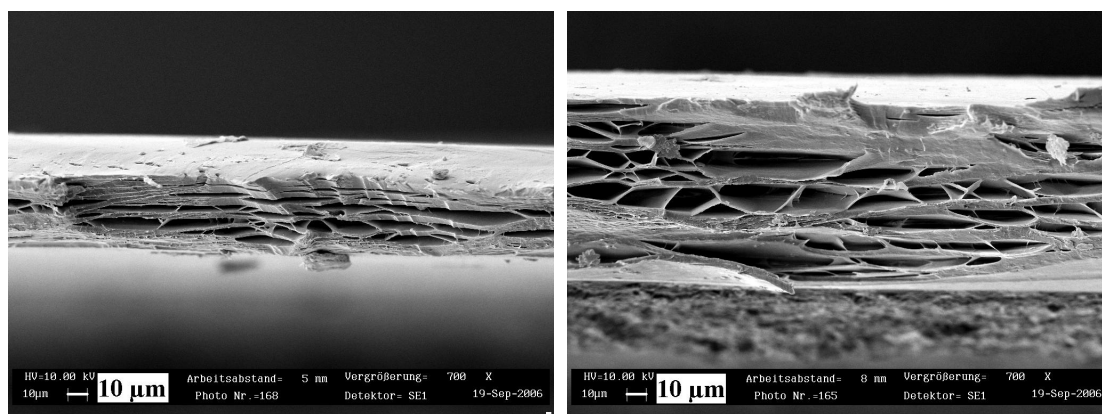


Figure 7.11: SEM images of the cellular samples with (Left) average thickness of 55.4 µm, density of 1.008 g/cm<sup>3</sup> (initial solid film thickness 50 µm, density 1.451 g/cm<sup>3</sup>), and (Right) average thickness of 97.9 µm, density of 0.985 g/cm<sup>3</sup> (initial solid film thickness 100 µm, density 1.465 g/cm<sup>3</sup>).

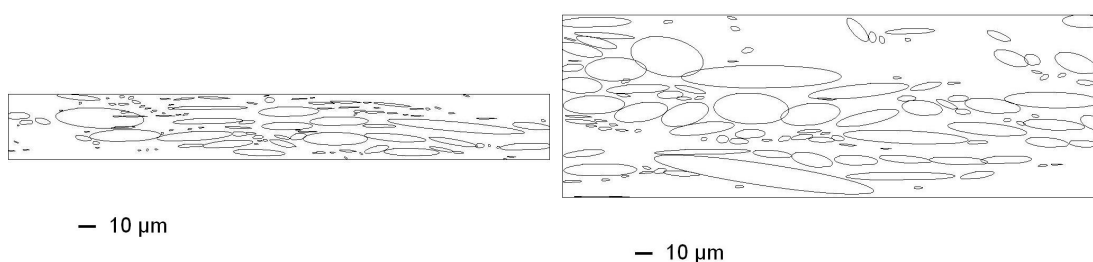


Figure 7.12: Fitting of the voids with ellipses, for the samples shown in figure 7.11.



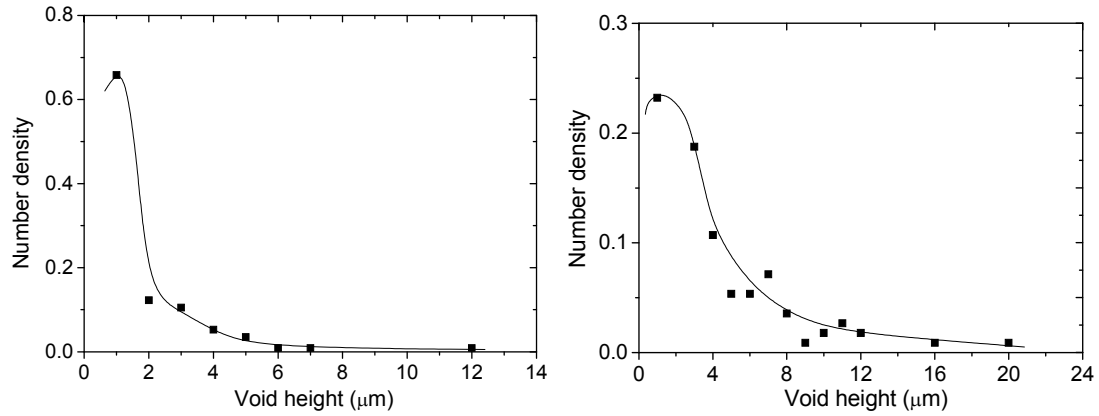


Figure 7.13: The calculated void-height-distribution. The maximum void height is 12  $\mu\text{m}$  but most voids have heights below 6  $\mu\text{m}$ , for the sample shown in figure 7.11 (left); and the maximum void height is 20  $\mu\text{m}$  but most voids have heights below 10  $\mu\text{m}$ , for the sample shown in figure 7.11 (right). The lines are to guide the eye.

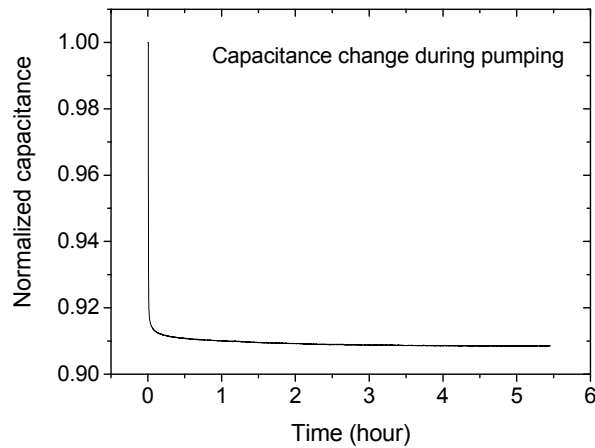


Figure 7.14: The normalized capacitance change of the cellular PEN film stored in a sealed chamber which was pumped until the internal pressure was as low as one millibar.

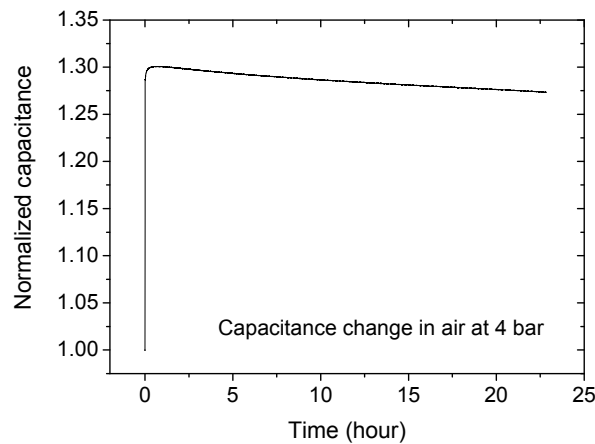


Figure 7.15: The normalized capacitance change of the cellular PEN film stored in a sealed chamber which was filled with air at 4 bar.

## 7.4 Investigation of electric charging behavior

Cellular films need to be electrically charged in order to show piezoelectric activities. Macroscopic dipoles are generated by the gas-breakdown inside the voids, which is triggered by the internal electric field. Both contact charging and corona charging can build an internal field across the voids. In contact charging, the internal field is induced by the voltage applied directly to the sample electrodes, and in corona charging, this field is induced by surface charges deposited on the sample surface. Therefore, in the case of corona charging, sufficient surface charges should be accumulated in order to induce an internal field larger than the breakdown threshold.

Figure 7.16 illustrates the resulting surface potential of a cellular PEN film as a function of the corona-tip voltage. With equation 5.4, 6.6, and 6.7, the corresponding average internal electric field in the voids can be calculated, as shown in the same figure. In order to avoid any gas destructive breakdown between the corona tip and the sample surface, the tip voltage of  $-50$  kV was applied in a  $\text{SF}_6$  atmosphere at a pressure of 3 bar. A tip voltage of  $-5$  kV is not high enough to generate a corona, therefore there is no measurable surface potential. With an increase of the tip voltage up to  $-50$  kV, there is a significant enhancement of the surface potential and hence the average internal electric field across void heights. A very high surface potential of  $-12$  kV or an internal field of  $395$  MV/m is achieved when the sample is charged with a corona tip of  $-50$  kV. According to Paschen's law, this internal field is quite sufficient to trigger gas-breakdown even in relatively smaller voids with heights of a few micrometers. In addition, it is found that the cellular PEN films with different thicknesses show approximately the same surface potential when charged with the same voltage. The average thicknesses for most cellular PEN samples prepared in this work are about  $52$ ,  $92$ , and  $100$   $\mu\text{m}$  from initial solid films with thicknesses of  $50$ ,  $100$  and  $188$   $\mu\text{m}$ , respectively. For relatively thicker samples, the calculated internal electric field is still as high as  $100$  MV/m, which is definitely sufficient to generate gas-breakdown in most of the voids.

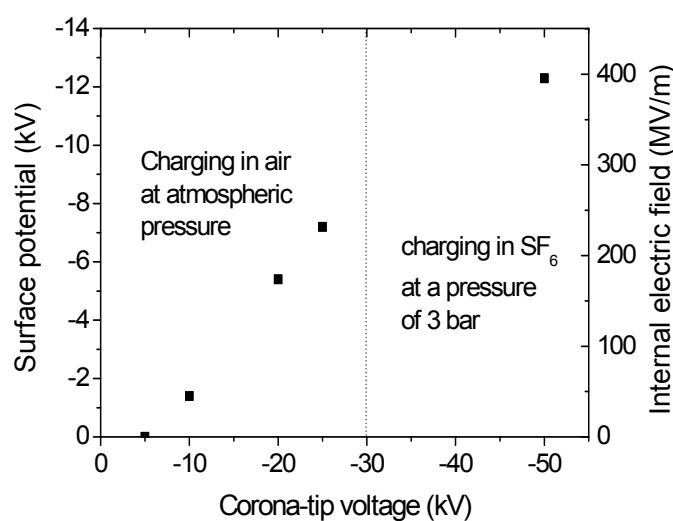


Figure 7.16: Surface potential and average internal electric field as a function of the corona-tip voltage for a cellular PEN film with a thickness of  $52$   $\mu\text{m}$ . The corona tip is  $3$  cm above the sample.

Figure 7.17 shows the decay of the surface potential as a function of time for a cellular sample stored at room temperature. The sample was corona charged with a corona-tip voltage of  $-25$  kV for 2 min at room temperature. The initial surface potential is about  $-7$  kV, but it decreases significantly to a very low value of about  $300$  V after 1 day. The decay of the surface potential does not indicate the loss of the internal charges, because the measured surface potential is contributed to by both the surface charges and the compensating charges. The surface charges only supply the internal electric field for gas-breakdown, and do not contribute to the piezoelectricity.

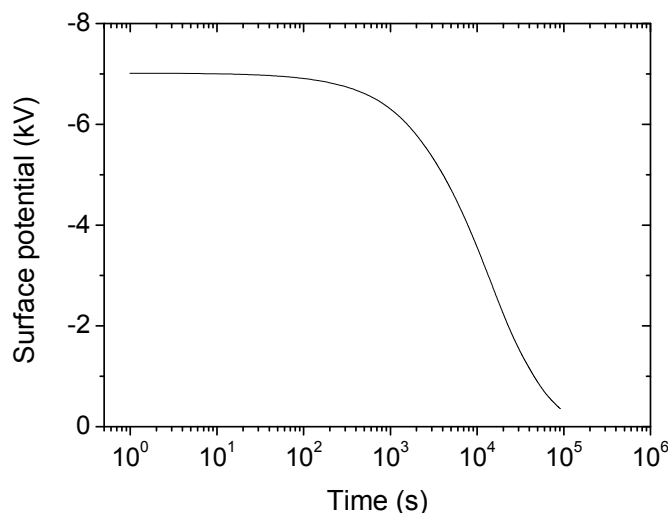


Figure 7.17: Decay of the surface potential as a function of time, for the cellular PEN film stored at room temperature. The sample was charged with corona tip-to-plane voltage of  $-25$  kV at room temperature.

Dielectric-barrier discharge (DBD) is always accompanied by light emissions, and therefore the internal gas-breakdown can also be studied by observing the emitted light during charging. Figure 7.18 shows the light emission for a cellular PEN sample (thickness  $129$   $\mu\text{m}$ , density  $1.31$   $\text{g}/\text{cm}^3$ ) under negative biased sinusoidal voltages with different peak-to-peak amplitudes of 4, 5, 6, 7, and 10 kV, at a frequency of 100 Hz. Light emission is observed whenever the absolute value of the voltage exceeds about 4 kV (average internal electric field in the voids is about  $70$   $\text{MV}/\text{m}$ ), which confirms the threshold behavior of the gas-breakdown. The higher the voltage, the stronger is the light emission, because barrier discharges are initiated in an increasing number of voids. The emission strongly decreases back to near-zero levels when the maximum voltage is reached. When the charging voltage decreases to values below 4 kV, the emission starts again. This emission is attributed to the back-discharges (inverse barrier discharges) which will destroy some of the previously deposited charges on the internal gas/polymer interfaces of the voids. The positive and negative charges deposited on the top and bottom surfaces induce an internal electric field opposite to the external field generated by the applied voltage. The internal field may over-compensate the external one if the applied voltage is reduced, and may thus trigger a back discharge [Kogelschatz 2001, Qiu 2007(1), Qiu 2007(2)]. Figure 7.19 shows the sample's color-coded photographic image of dielectric-barrier discharges taken by means of an EM-CCD camera. The voltage (peak-to-peak value) is  $-7$  kV, and the exposure time is 50 s. It can be clearly seen that the sample is not homogeneous all over. Only relatively large voids can be charged

effectively. Therefore, it can be concluded that larger voids contribute more substantially to the overall piezoelectricity, in spite of their relatively small numbers.

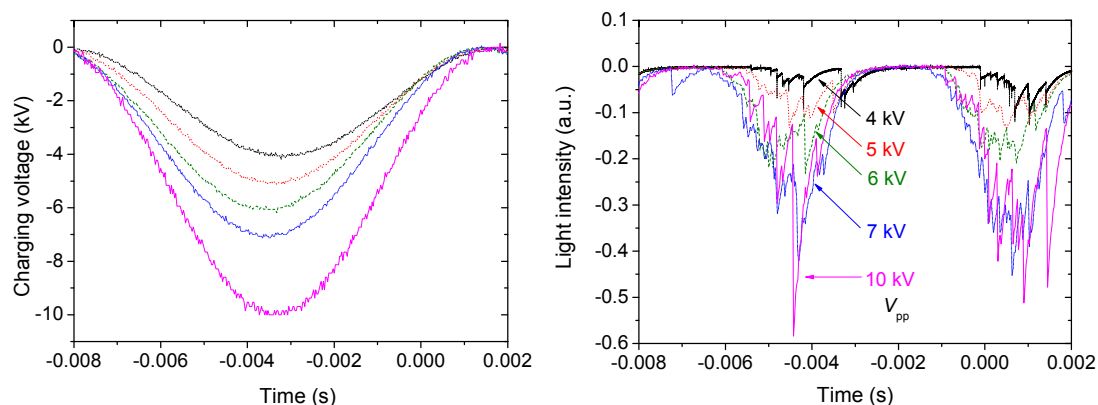


Figure 7.18: Charging voltages (left) and normalized light intensity (right) for the cellular PEN sample (thickness  $129 \mu\text{m}$ , density  $1.31 \text{ g/cm}^3$ ) under negatively biased sinusoidal voltages with a frequency of 100 Hz and peak-to-peak voltages as indicated.

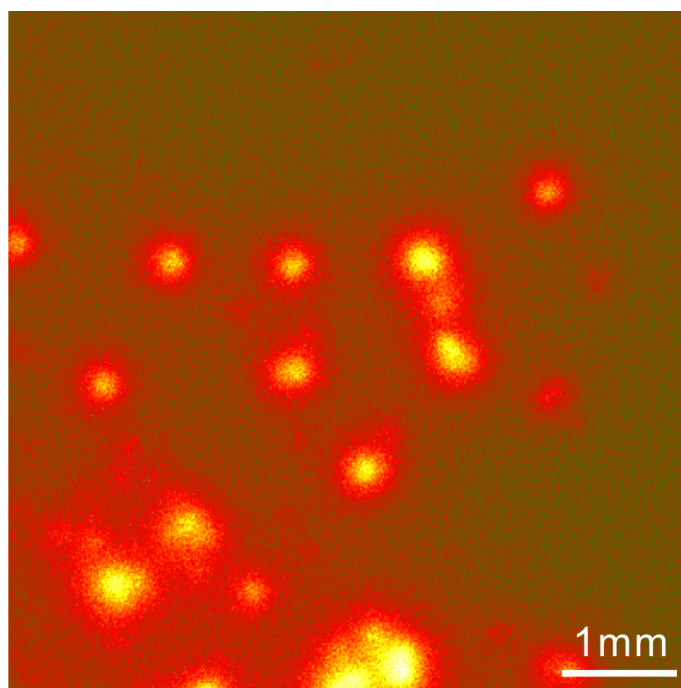


Figure 7.19: Color-coded EM-CCD image of a cellular PEN sample (thickness  $129 \mu\text{m}$ , density  $1.31 \text{ g/cm}^3$ ) under a negative sinusoidal voltage of  $-7 \text{ kV}$  (peak-to-peak value) at a frequency of 100 Hz. The CCD camera was internally triggered with an exposure time of 50 s.

The resulting piezoelectric  $d_{33}$  coefficients strongly depend on the charging voltage. As shown in equation 5.15, there is no  $d_{33}$  coefficient if the charging voltage is lower than the threshold; when the voltage is higher than the threshold,  $d_{33}$  increases linearly with the increase of voltage and reaches its maximum value when the voltage is twice the threshold. The threshold and saturation behaviors can be investigated by measuring the  $d_{33}$  coefficient as a function of the charging voltage, as shown in figure 7.20. Contact charging was applied on the sample for 30 s,

and the  $d_{33}$  coefficients were determined dynamically. As can be seen,  $d_{33}$  is very small when the charging voltage is lower than 4 kV. Above 4 kV (average internal electric field in the voids is about 62 MV/m),  $d_{33}$  increases significantly with the charging voltage, and reaches a saturation value of about 45 pC/N at approximately 8.5 kV. Therefore the threshold charging voltage and the saturation charging voltage are 4 and 8.5 kV for this sample, respectively. The experimental threshold voltage is slightly smaller than one half of the saturation voltage. This can be explained as, in the simplified model all voids are considered with homogeneous dimensions; however, there is a distribution of the void size, and the gas-breakdown may occur earlier in some relatively larger voids.

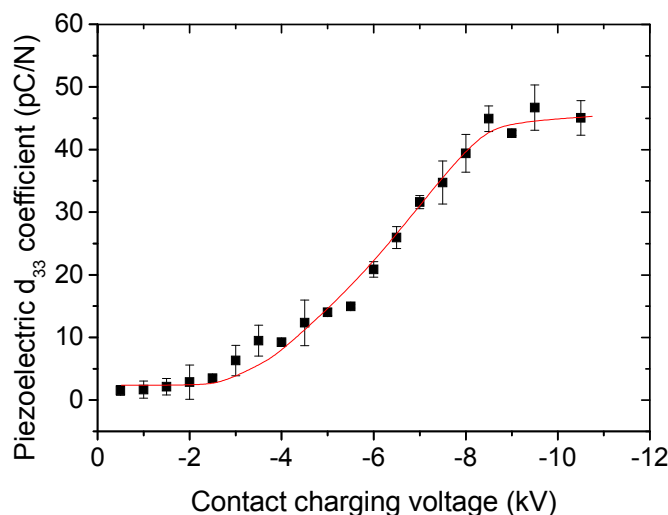


Figure 7.20: Piezoelectric  $d_{33}$  coefficient as a function of charging voltage applied between the sample electrodes (contact charging). Sample thickness and density are 130  $\mu\text{m}$  and 1.17  $\text{g}/\text{cm}^3$ , respectively.  $d_{33}$  coefficients were dynamically measured, with static force of 3 N and dynamic force of 1 N (peak-to-peak value) at 2 Hz. The line is to guide the eye.

## 7.5 Investigation of piezoelectric properties

### 7.5.1 Dynamic measurement

Dynamic measurement is the most used technique to determine piezoelectric  $d_{33}$  coefficient in the lab.  $d_{33}$  is determined directly by measuring the generated charges and the applied mechanic forces. Usually a static force (bias) is utilized to ensure good contact between sample and electrode, and a dynamic force at a certain frequency is utilized to generate charges.

As already mentioned, in the dynamical  $d_{33}$  determination, the applied static stress presses the cellular structure and therefore increases the elastic modulus, which results in decreased piezoelectricity. Figure 7.21 illustrates  $d_{33}$  as a function of the static force for a dynamic  $d_{33}$  determination. The sample shows a  $d_{33}$  of about 100 pC/N under a static stress of 10.5 kPa (static force of 1 N). Then the stress is gradually increased to 105 kPa (static force of 10 N) and decreased back to 10.5 kPa, with an interval of 10.5 kPa (1 N).  $d_{33}$  coefficients were dynamically

determined 2 min after each change of the stress. As can be seen, with increasing static stress,  $d_{33}$  decreases significantly to about 30 pC/N under a stress of 105 kPa, which is only one third of its initial value. The piezoelectricity depends on the elastic modulus, and samples with lower  $c_{33}$  show larger  $d_{33}$  coefficients. Therefore it is confirmed that the static pressure increases the elastic modulus of the sample. In the measurement, only the dynamic force is used to calculate  $d_{33}$ , and the static force is used to fix the sample on the sample holder. As a result, the cellular structure is compressed with the bias, with the increased elastic modulus and decreased  $d_{33}$ . When the stress is gradually reduced as indicated,  $d_{33}$  increases and the increase-curve can almost follow the decrease-curve, meaning that the interval of 2 min is enough for the PEN sample to revert back to its initial form. In the following dynamic measurements for  $d_{33}$ , a static force of 3 N is always used as a standard bias.

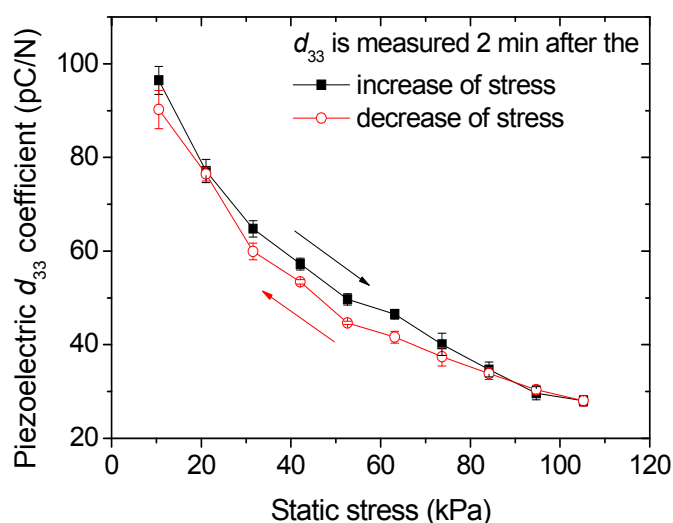


Figure 7.21: Piezoelectric  $d_{33}$  coefficient as a function of the static stress (static force, bias) in the dynamic  $d_{33}$  determination. A static force of 1 N corresponds to a pressure of 10.5 MPa. The force is applied perpendicularly onto the sample, and  $d_{33}$  are dynamically determined 2 min after the change of the stress.

Ferroelectrets are usually used as sensors to record mechanical signals with different frequencies; therefore the electromechanical property as a function of frequency, i.e. the frequency response, is one of the important parameters which determine the application range of the ferroelectrets. Here, a sample was loaded with a static force of 3 N and a dynamic force with a peak-to-peak value of 1 N with increasing frequency was applied, and the piezoelectric  $d_{33}$  coefficients were dynamically determined as a function of the frequency, as shown in figure 7.22. With the frequency increased from 2 to 100 Hz, the  $d_{33}$  coefficient decreases from 95 to 80 pC/N. If the frequency is further increased to 600 Hz,  $d_{33}$  increases up to 100 pC/N and then decreases to about 90 pC/N. Generally, in the frequency range from 2 to 600 Hz, the sample shows  $d_{33}$  between 80 and 100 pC/N, which indicates an acceptable frequency response. The deviation of  $d_{33}$  may be due to the frequency characteristic of the experimental equipment at the increased frequencies. In this work, a frequency of 2 Hz is always used for the dynamic force in the dynamic measurements.

The sustainability of the cellular structure with respect to the applied mechanical stress, i.e. the mechanical fatigue, is also important if the sample is supposed to be utilized for long-term

applications. In order to study this property, continuous dynamical  $d_{33}$  measurements (3 measurement-cycles/min) were performed, with a static force of 3 N, a dynamic force of 1 N (peak-to-peak value) at 2 Hz. Figure 7.23 shows the decay of the  $d_{33}$  with increasing measurement cycles for a sample with an initial  $d_{33}$  of about 120 pC/N. The sample still shows  $d_{33}$  of about 100 pC/N, which is around 80% of the initial value, after 1500 measurement cycles. Further measurements up to 2000 cycles do not decrease the  $d_{33}$  significantly. For polymer foam ferroelectrets, the piezoelectricity strongly depends on the mechanical properties of the cellular structure, e.g. the compressibility upon the application of mechanical stress and the reversibility upon the reduction of the stress. Polymer foams should be sustainable against the repeated external stress, can be compressed and can thereafter revert to their original forms. It is found that for the PEN foams, although the piezoelectricity decays with the increased measurement repeats, it finally becomes stable with an appreciable magnitude.

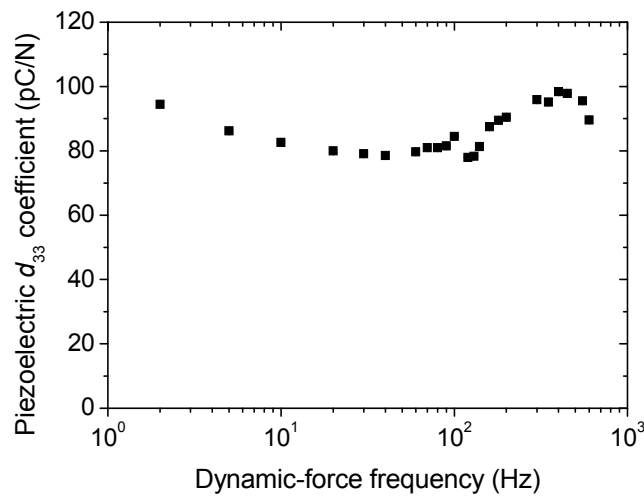


Figure 7.22: Piezoelectric  $d_{33}$  coefficient as a function of the dynamic-force frequency. The sample was loaded with a static force of 3 N and a dynamic force of 1 N (peak-to-peak) with an increasing frequency.

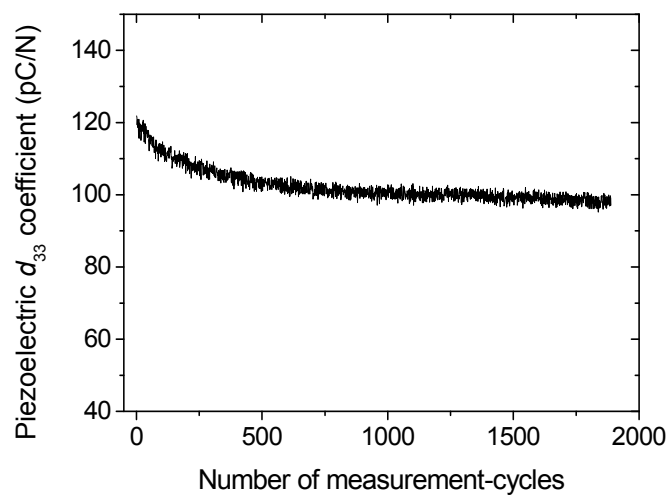


Figure 7.23: Mechanical fatigue for the PEN foams. Continuous dynamical  $d_{33}$  measurements with 3 measurement-cycles/min were carried out, at a static force of 3 N, and a dynamic force of 1 N (peak-to-peak value) at 2 Hz.

## 7.5.2 Dielectric-resonance spectroscopy (DRS)

Dielectric-resonance spectrum (DRS) is a resonance measurement based on the reverse piezoelectricity, by which several piezoelectric parameters can be measured by fitting of the resonance curves. Figure 7.24 shows the dielectric-resonance spectra for two typical samples with different piezoelectric activities. Normally, clear dielectric-resonance peaks in the TE (thickness extension) model can be observed only on the samples with relatively high piezoelectric  $d_{33}$  coefficients (usually  $> 20$  pC/N from the dynamical determination). This is because the height of the resonance profile for the samples with low  $d_{33}$  approaches the resolution limit of the dielectric spectrometer [Mellinger 2003]. As can be seen, at the anti-resonance frequency, there is a step for the real part of the capacitance  $C'$ , and a resonance loss peak for the imaginary part of the capacitance  $C''$ . Samples with relatively larger piezoelectric  $d_{33}$  coefficients usually show more pronounced resonance peaks. The resonance curves for  $C'$  are well fitted according to the TE model (equation 6.23), as shown in figure 7.25, and several parameters are acquired. For most PEN ferroelectrets prepared in this work, the anti-resonance frequencies are in the range from 0.2 to 0.8 MHz, the permittivity is around 2, and the electromechanical coupling factors are in the range from 0.016 to 0.069.

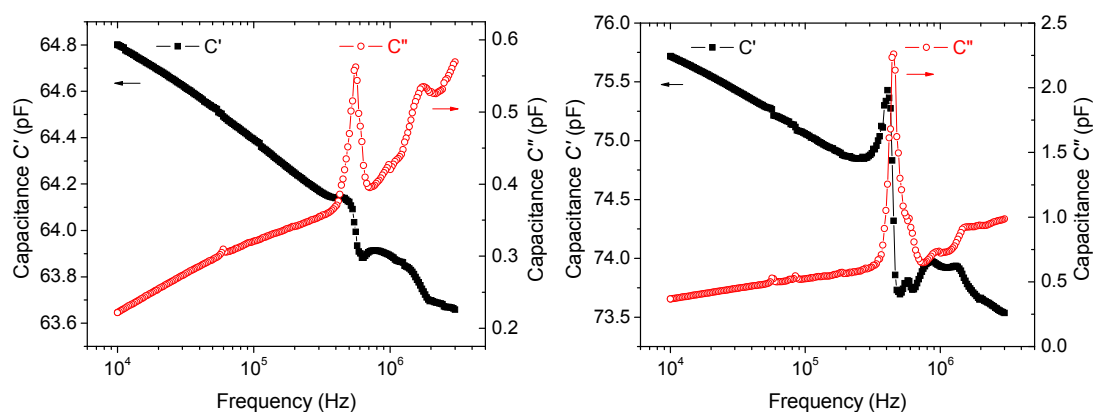


Figure 7.24: Typical dielectric-resonance spectra for the samples with piezoelectric  $d_{33}$  coefficients of 50 pC/N (left) and 203 pC/N (right), respectively.

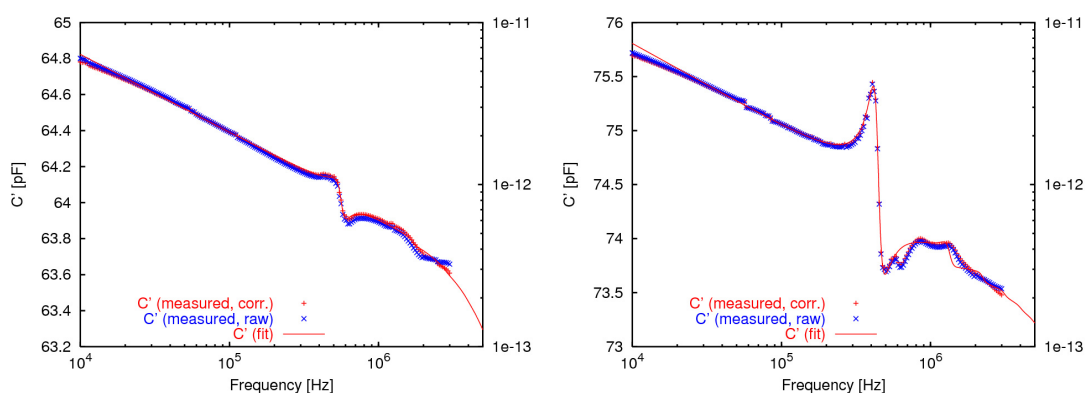


Figure 7.25: The fitting of the capacitance  $C'$  according to TE model, for the samples seen in figure 7.24.



Piezoelectric  $d_{33}$  coefficients up to 650 pC/N are calculated from the fitting of the dielectric-resonance spectra according to the TE mode. Generally,  $d_{33}$  coefficients from resonance measurements are in agreement with those from dynamic measurements. As illustrated in figure 7.26, each point represents one sample, with its resonance-determined  $d_{33}$  on the y-axis and the dynamically-determined  $d_{33}$  on the x-axis, respectively. The guiding line represents the ratio of 1:1 between the  $d_{33}$  acquired from the above two techniques. However, for a number of samples, their resonance-determined  $d_{33}$  are much larger than the dynamically-determined ones. This is because of the difference of the measurement conditions between these two techniques. For the dynamic determination, except for the dynamic force which is used to calculate  $d_{33}$ , the sample is loaded with a static force (bias) in order to be fixed on the sample holder. Consequently, the cellular structure is compressed with the bias, which increases the elastic modulus and therefore lowers the  $d_{33}$ . Especially for the samples with relatively lower elastic moduli and higher piezoelectric activities, the influence from the static force is highly enhanced. Contrarily, for the resonance determination, the sample is free-standing, and can vibrate freely without any extra load. Therefore the  $d_{33}$  from the resonance measurements are usually larger than those from the dynamic measurements. In addition, the precision of the dynamic determination depends on the proper application of both static and dynamic forces. If the forces are not applied exactly perpendicularly to the sample surface, errors for the final  $d_{33}$  coefficients are induced.

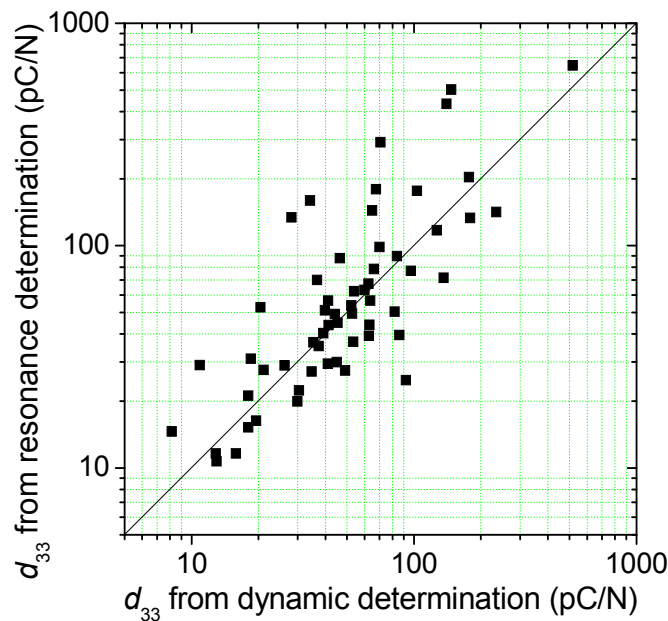


Figure 7.26: Each point represents one sample, with its  $d_{33}$  from resonance measurement on y-axis and dynamic measurement on x-axis, respectively. The guiding line represents the ratio of 1:1 between the  $d_{33}$  acquired from the above two techniques.

Piezoelectric  $d_{33}$  coefficients strongly depend on sample stiffness, and the decrease of the stiffness (elastic moduli) leads to the increase of  $d_{33}$ . Figure 7.27 shows the piezoelectric  $d_{33}$  coefficient as a function of the elastic modulus  $c_{33}$ . The  $c_{33}$  and  $d_{33}$  here are calculated from the dielectric-resonance spectra. Samples prepared in this work have a broad range of elastic moduli from approximately 1 to 12 MPa due to the large variation of foaming parameters. The overall

elastic modulus of the sample is combined from the modulus of the polymer matrix and the modulus of the gas inside the voids, since most of the voids are considered as closed (SEM images in figure 7.11). The elastic modulus of the gas inside the voids equals the gas pressure, which is approximately 0.1 MPa under normal conditions. As expected, it is found that relatively larger  $d_{33}$  are achieved on the samples with relatively lower  $c_{33}$ . This is because stiff samples are more difficult to deform by applied mechanical stress. Only properly foamed and optimized samples are relatively softer, with lower elastic modulus and higher piezoelectric coefficients. Most PEN samples prepared in this work are relatively stiffer than cellular PP films, for which a lower  $c_{33}$  of 0.6 MPa is reported [Wegener 2004(1)]. The errors for the  $d_{33}$  calculation are also shown, which depend on the fitted dielectric-resonance peaks. Several factors, even an imperfect placement of the sample in the sample holder, may cause deviations.

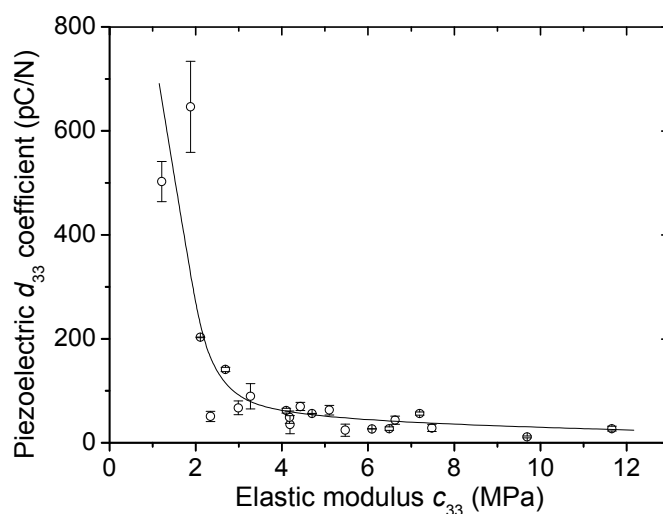


Figure 7.27: Piezoelectric  $d_{33}$  coefficient as a function of the elastic modulus  $c_{33}$ . The line is to guide the eye.

Figure 7.28 shows the dependence of the anti-resonance frequency on the elastic modulus  $c_{33}$  in a double-logarithmic scale. Lower resonance frequencies are obtained on samples with lower elastic moduli; in addition, the slope of the  $\ln(f_{\text{res}}) \sim \ln(c_{33})$  curve is 0.497, which is in good agreement with the theoretical slope of 0.5 as shown in equation 6.24. Figure 7.29 shows the electromechanical coupling factor  $k_{33}$  as a function of the elastic modulus  $c_{33}$ . Lowering elastic modulus by adjusting the sample structure leads to an increase of the electromechanical coupling factor, which is in agreement with equation 6.26. The coupling factors for most of the present PEN ferroelectrets prepared in this work are quite limited. Although  $k_{33}$  as high as 0.2 is achieved, however, most of them are less than 0.05. During the structure optimization, the controlled inflation enlarges the void height, and hence increases the elastic modulus and the sample thickness, but decreases the sample density; the additional biaxial stretching lowers the void height, and thus decreases the elastic modulus and the sample thickness, but increases the sample density. Therefore by adjusting the foaming and the structure optimization parameters several piezoelectric properties can be varied.

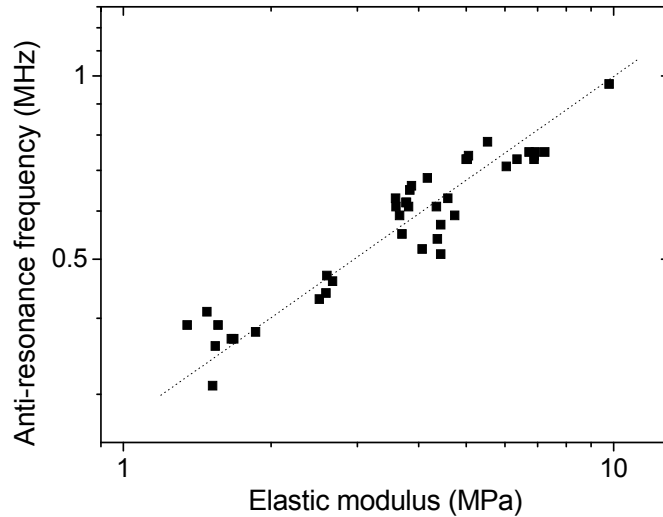


Figure 7.28: Anti-resonance frequency as a function of the elastic modulus  $c_{33}$ . The line is to guide the eye.

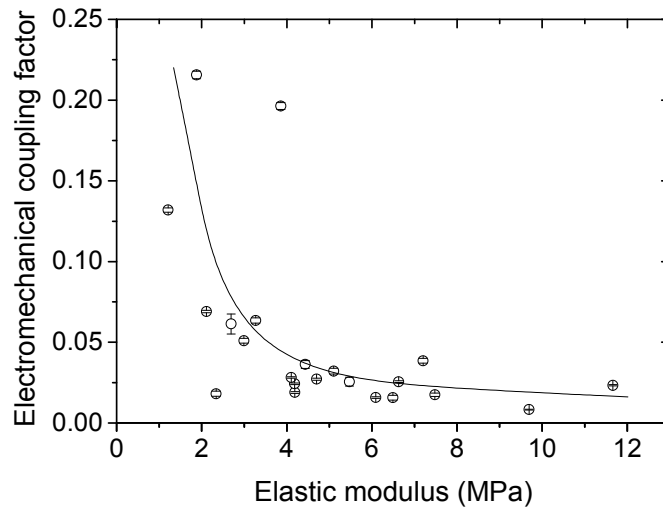


Figure 7.29: Electromechanical coupling factor  $k_{33}$  as a function of the elastic modulus  $c_{33}$ . The line is to guide the eye.

Dielectric-resonance spectra were also measured at different temperatures where the capacitances were recorded as a function of both frequency and temperature. The spectra shown in figure 7.30 were measured in a temperature range from  $-10$  to  $130$  °C, at frequencies from  $0.01$  to  $3$  MHz (only the range from  $0.3$  to  $1$  MHz is shown). The data were acquired as a function of the frequency under nearly isothermal conditions ( $\Delta T_{\max} = 0.43$  °C) at  $10$  °C intervals. As can be seen, the loss peak gradually decreases with increasing temperature especially in the high-temperature region, due to the thermally stimulated loss of the piezoelectricity.

Several temperature dependent electromechanical parameters can be measured from the frequency-temperature map for the dielectric resonance. Figure 7.31 shows the temperature dependent elastic modulus  $c_{33}$ , which decreases with increasing temperature above  $40$  °C. As figure 7.32 shows, the piezoelectric  $d_{33}$  coefficient first increases with increasing temperature in the range from  $40$  to  $60$  °C, due to a decreasing  $c_{33}$  and a nearly constant  $k_{33}$ . The piezoelectricity

is strongly dependent on the elastic modulus, which in turn depends on the morphology of the material: Higher piezoelectric activities are found on samples with lower elastic moduli. When samples are heated further,  $d_{33}$  decreases and reaches approximately 55% of its initial value at 110 °C due to the thermally stimulated loss of internal charges. Although the sample is still piezoelectric at even higher temperatures, there is no resonance peak detectable due to the decreased piezoelectricity and the height of the resonance profile for the samples with low  $d_{33}$  approaches the resolution limit of the dielectric spectrometer.

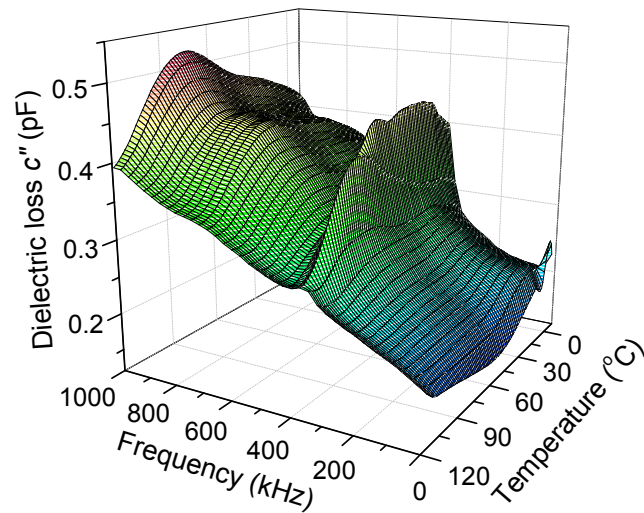


Figure 7.30: Frequency-temperature map of the dielectric loss (imaginary part of the capacitance  $C''$ ) for a cellular PEN sample with a thickness of 47  $\mu\text{m}$  and a density of 0.99  $\text{g}/\text{cm}^3$ .

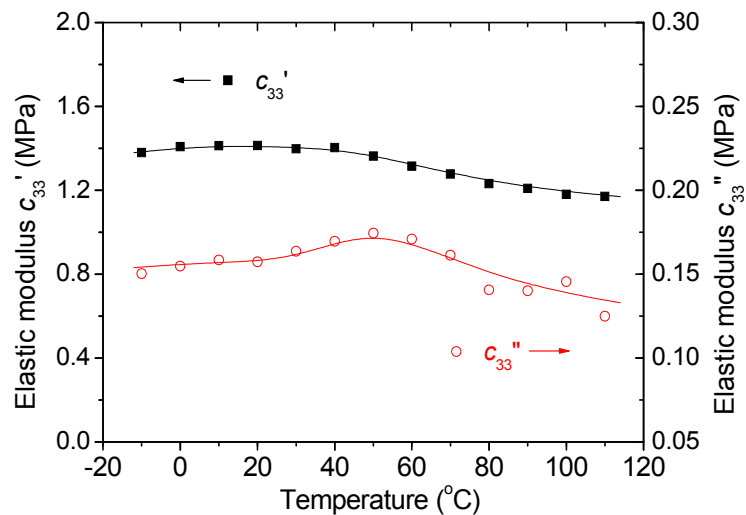


Figure 7.31: The real and imaginary part of the elastic modulus as a function of temperature, achieved from the fitting of the dielectric-resonance spectra recorded at different temperatures. The lines are to guide the eye.

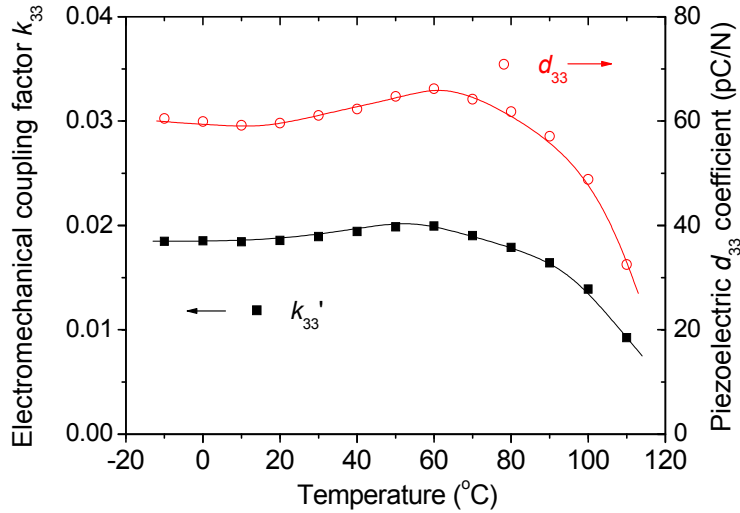


Figure 7.32: Temperature dependent electromechanical coupling factor  $k_{33}$  and the piezoelectric  $d_{33}$  coefficient, achieved from the fitting of the dielectric-resonance spectra recorded at different temperatures. The lines are to guide the eye.

### 7.5.3 Acoustic measurement

Due to the limit of the equipment, the dynamic  $d_{33}$  determination cannot be applied at the frequencies higher than 600 Hz. In addition, loudspeakers and microphones are the usual applications for ferroelectrets, where appreciate acoustic characteristics are required. Therefore acoustic measurements were performed for the present PEN ferroelectrets. In this work only the “loudspeaker mode” (section 6.6) was utilized, where the samples were tested as actuators to generate sound waves driven by an AC voltage. By recording the sound signal with a calibrated standard microphone, the sound pressure and therefore the corresponding  $d_{33}$  coefficients as a function of the frequency were calculated. Samples were investigated in the frequency range from 20 Hz to 25 kHz (the hearing range of human ears is 20 Hz to 20 kHz). Recording distances, i.e. the distance between the microphone and the sample, were varied as 1, 3, 15, and 30 cm. Figure 7.33 and 7.34 show the fundamental and the second harmonic sound pressure as a function of the frequency for different recording distances. The third and the higher harmonic signals cannot be detected under present experimental conditions. In addition, at frequencies lower than 100 Hz, no reasonable sound pressures can be calculated. Reasonable fundamental sound pressures are obtained for the frequencies of 300 Hz, 400 Hz, 1 kHz, and 1.5 kHz, for the recording distances of 1 cm, 3 cm, 15 cm, and 30 cm, respectively. When the microphone is placed far from the sample, the influence of noise is highly enhanced. Therefore the curves for short recording distances are much smoother than those for long recording distances. With increased frequencies from  $10^2$  to  $10^4$  Hz, the corresponding sound pressure increases over a few magnitudes from  $10^{-5}$  to  $10^{-1}$  Pa.

Theoretical computation shows that the sound pressure is in direct proportion to the second order of the frequency (equation 6.35). Therefore, in the logarithmic scale there is a linear relation between the sound pressure and the frequency

$$\log P \sim 2 \log f, \quad (7.1)$$

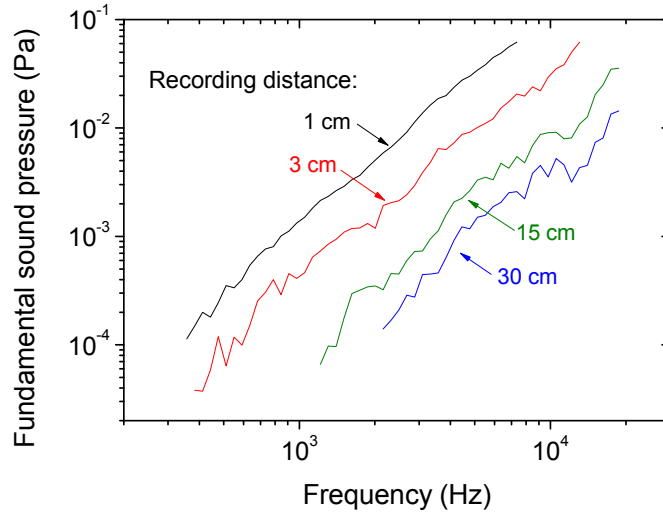


Figure 7.33: Fundamental sound pressure as a function of frequency for different recording distances (the distance between the microphone and the sample) as indicated.

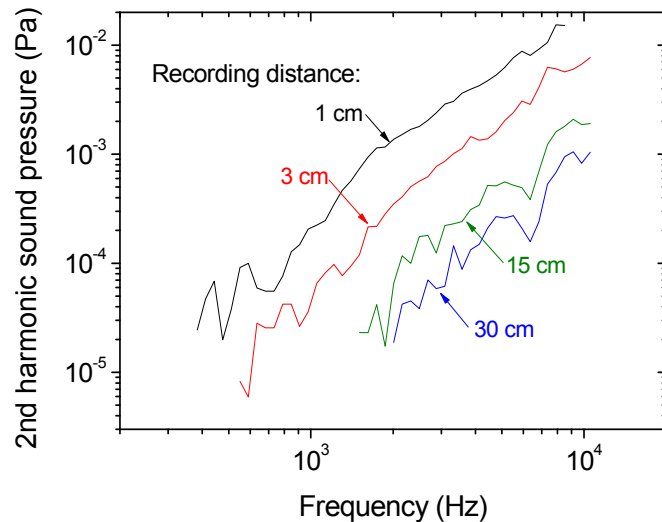


Figure 7.34: The second harmonic sound pressure as a function of frequency for different recording distances (the distance between the microphone and the sample) as indicated.

with a slope of 2. It means that only in the frequency range where the above relation is satisfied is the acquired data reliable, as shown in table 7.2. For the very short recording distance of 1 cm, the lower frequency limit is as low as 350 Hz, but the upper limit is only 7.5 kHz. When the recording distance is increased to 3 cm, sound pressures can be measured up to 13 kHz. For relatively longer recording distances of 15 and 30 cm, the lower limits are 1.2 and 1.5 kHz, respectively, due to the enhanced disturbance by low frequency noise. However, the long recording distances enable reasonable measurements up to 25 kHz. As already mentioned, the recording distance (distance between the microphone and the sample) should satisfy the relation as represented in equation 6.37. Taking into account that the radius of the sample electrode is 8 mm, the velocity of the sound wave is 340 m/s, at a frequency of 1 and 10 kHz, the recording distance should be much larger than 0.19 and 1.9 mm, respectively. Therefore, at relatively higher frequencies, a short

recording distance of 1 cm cannot be applied for a reasonable measurement. A longer recording distance should be used, despite the increased influence from noise.

Recording distance	Trustable frequency range
1 cm	350 Hz – 8 kHz
3 cm	400 Hz – 13 kHz
15 cm	1.2 kHz – 20 kHz
30 cm	1.5 kHz – 20 kHz

Table 7.2: Reliable frequency range for fundamental sound pressure at different recording distances under the present experimental conditions.

The piezoelectric  $d_{33}$  coefficients are calculated and plotted as a function of frequency in figure 7.35. Taking into account that a short recording distance with low noise is limited at relatively higher frequencies, and a long recording distance can be applied for higher frequencies but with increased noise, the final  $d_{33}$  coefficients are calculated from the combination of the sound pressure data acquired at different recording distances, as indicated, 1 cm for the frequencies from 500 Hz to 7.5 kHz, and 15 cm for those from 7.5 kHz to 20 kHz. In the broad frequency range from 500 Hz to 20 kHz, the sample shows stable  $d_{33}$  coefficients between 80 and 100 pC/N, indicating an appreciable frequency response. The relatively large fluctuation of  $d_{33}$  is due to the noise from the experimental surroundings. In addition, the  $d_{33}$  from the acoustic measurements are in good agreement with those achieved from the dynamic measurement and the dielectric-resonance spectra, which are 75 and 82 pC/N, respectively, for the same sample shown in figure 7.35.

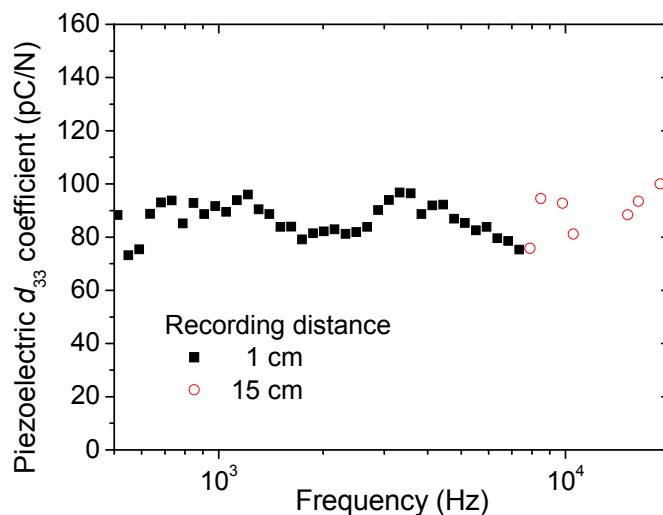


Figure 7.35: Piezoelectric  $d_{33}$  coefficient as a function of frequency. Taking into account the frequency limit for the recording distance and the surrounding noises,  $d_{33}$  coefficients are calculated from the sound pressure data acquired at different recording distances of 1 cm and 15 cm.

### 7.5.4 Density dependent piezoelectricity

Figure 7.36 illustrates the piezoelectric  $d_{33}$  coefficient as a function of the sample density. Samples were charged with a corona tip under different conditions: (a) in air at atmospheric pressure with a corona-tip voltage of  $-21$  kV and (b) in sulfur hexafluoride ( $\text{SF}_6$ ) at a pressure of 3 bar with a corona-tip voltage of  $-50$  kV. Piezoelectric  $d_{33}$  coefficients were dynamically determined and plotted as a function of the sample density as shown. It is found that samples charged at higher voltage show much enhanced piezoelectricity. In addition, samples with densities of about  $1.1 \text{ g/cm}^3$  show the largest  $d_{33}$  coefficients, and samples with higher or lower densities show smaller  $d_{33}$  (initial density for solid PEN films is about  $1.45 \text{ g/cm}^3$ ). The piezoelectricity strongly depends on the morphology of the cellular structure, i.e. the shape of the voids. Lens-shaped voids have relatively lower elastic modulus and therefore enhanced piezoelectricity. High density samples with small voids are stiff and show only low piezoelectric activity. Low density samples have more spherical voids, which also results in large stiffness and small  $d_{33}$ .

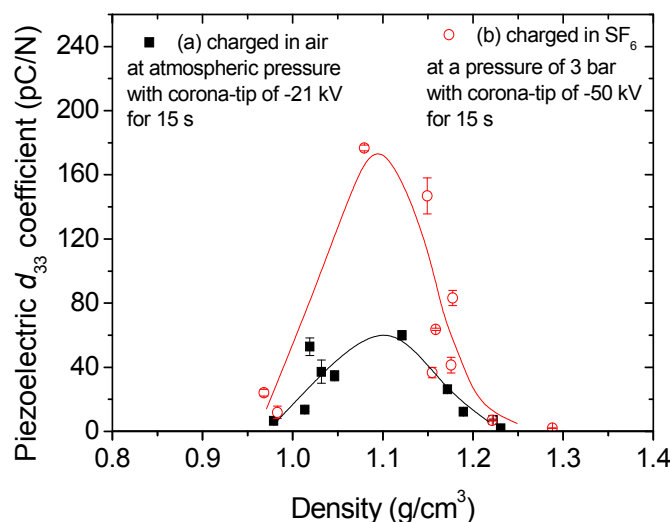


Figure 7.36 Piezoelectric  $d_{33}$  coefficient as a function of the sample density. Samples were charged under different conditions as indicated and  $d_{33}$  coefficients were dynamically determined. Initial density for solid PEN films is about  $1.45 \text{ g/cm}^3$ . The lines are to guide the eye.

### 7.5.5 Temporal stability of piezoelectricity

Figure 7.37 shows the short-term temporal decay of the piezoelectric  $d_{33}$  coefficient at room temperature.  $d_{33}$  coefficients were dynamically determined and the sample showed an initial  $d_{33}$  of  $105 \text{ pC/N}$ . Due to the inhomogeneity of the cellular structure, the measurements at different positions may vary. Therefore the sample was fixed on the sample holder during the whole measurement time scale of about 20 hours, and all the data were acquired at exactly the same position on the sample. Figure 7.38 shows the long-term temporal decay of piezoelectric  $d_{33}$  coefficient at room temperature for the same sample. The decay of  $d_{33}$  becomes slow with time, and about 80% of the initial value is retained after 45 days. The scattering in the  $d_{33}$ -curve can be attributed to the change of the measurement position, since the sample was removed from the



sample holder after each measurement. Consequently the measurements were not taken at exactly the same position. In addition, as the experimental period was extended to more than one month, the experimental conditions, including temperature and humidity were not well controlled and were varying over time.

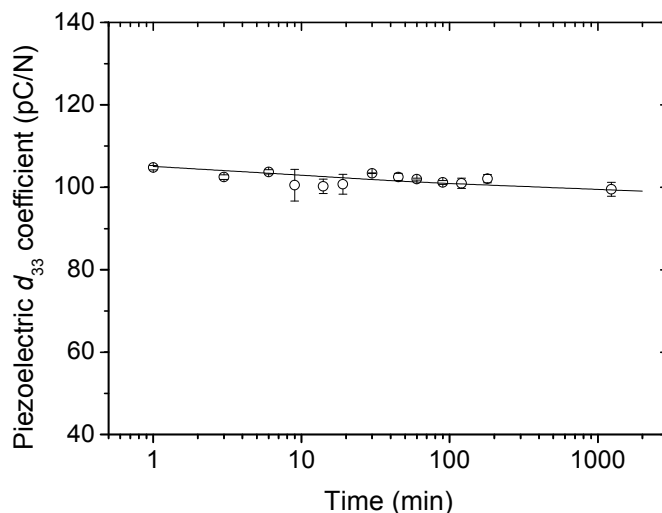


Figure 7.37: The short-term temporal decay of piezoelectric  $d_{33}$  coefficient at room temperature. The sample was fixed on the sample holder during the whole measurement time scale, so each measurement was at exactly the same position on the sample. The line is to guide the eye.

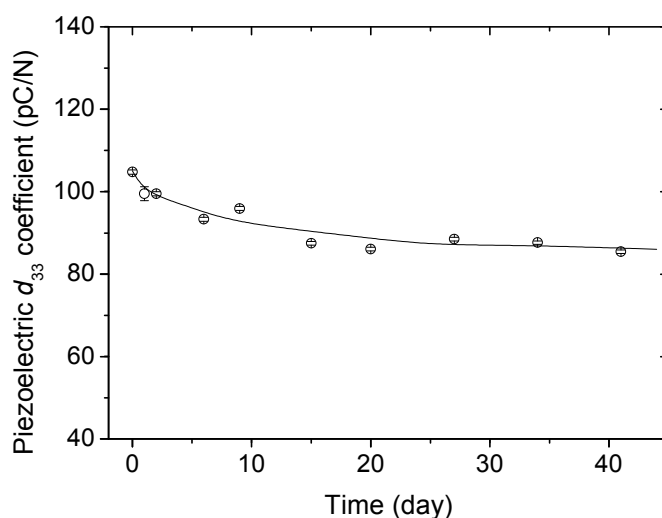


Figure 7.38: The long-term temporal decay of piezoelectric  $d_{33}$  coefficient at room temperature. The line is to guide the eye.

### 7.5.6 Thermal stability of piezoelectricity and its improvement

One of the most critical characteristics which determine the application area for ferroelectrets is the thermal stability and the preparation of new ferroelectrets with enhanced working temperatures is one of the main aims of this work. Therefore the thermal stability for PEN ferroelectrets and its improvement are investigated in detail in the following. Figure 7.39 shows

the short-term thermal stability of the piezoelectric  $d_{33}$  coefficient. Samples with an initial  $d_{33}$  of 60 pC/N were thermally treated in an oven with an air flow at pre-determined temperatures for 1 hour. Then  $d_{33}$  coefficients were dynamically determined outside the oven after the samples had cooled down to room temperature. As can be seen, there is only a slight decay of  $d_{33}$  when treated at 60 and 80 °C. However, with further increase of the temperature to 100 and 120 °C,  $d_{33}$  decreases significantly to about 70% and 40% of its initial value, respectively. The piezoelectricity depends both on the dipoles formed by the internal charges, and on the cellular structure. In ferroelectrets, charges are stored in the traps of the material. At higher temperatures, charges earn more thermal energy which enables them to de-trap, and the higher the temperature, the more charges can de-trap. Thus the piezoelectricity decreases with the increase of temperature. In addition, the glass transition temperature ( $T_g$ ) of PEN is about 122 °C, and if the sample is treated at temperatures higher than its  $T_g$ , the molecular chains can move more freely and hence the cellular structure is destroyed. The sample is not piezoelectric active anymore when it is treated at 140 °C. A very low value of about 5 pC/N (9%) at 140 °C is not very reliable because the sample is noticeably deformed due to the thermal treatment and therefore the sample is considered as non-piezoelectric.

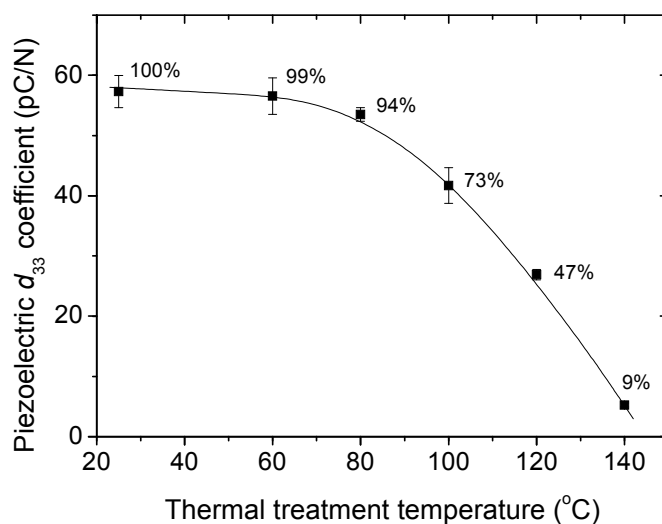


Figure 7.39: Short-term thermal stability: thermally stimulated decay of piezoelectric  $d_{33}$  coefficient at different temperatures. The sample was treated at each temperature for 1 h.  $d_{33}$  coefficients were dynamically determined after the sample was cooled down to room temperature. The line is to guide the eye.

Next, samples were thermally treated at fixed temperatures for periods of up to 120 hours, and  $d_{33}$  coefficients were dynamically determined at selected time points after the sample had cooled down to room temperature. Figure 7.40 illustrates the long-term thermal stability of  $d_{33}$  at temperatures of 60 and 100 °C, respectively. Samples were prepared and charged under the same conditions as detailed above and showed an initial  $d_{33}$  of about 60 pC/N. As can be seen, the fast decay of  $d_{33}$  takes place in the first one or two days, and then the decay becomes slower afterwards. Samples still retain about 80% and 40% of their initial  $d_{33}$  after 5 days of treatment at 60 and 100 °C, respectively. The short- and long-term thermal treatments indicate that the present PEN ferroelectrets can work at surrounding temperatures as high as 100 °C. Compared with that of cellular PP, the thermal stability of cellular PEN ferroelectrets is obviously superior.

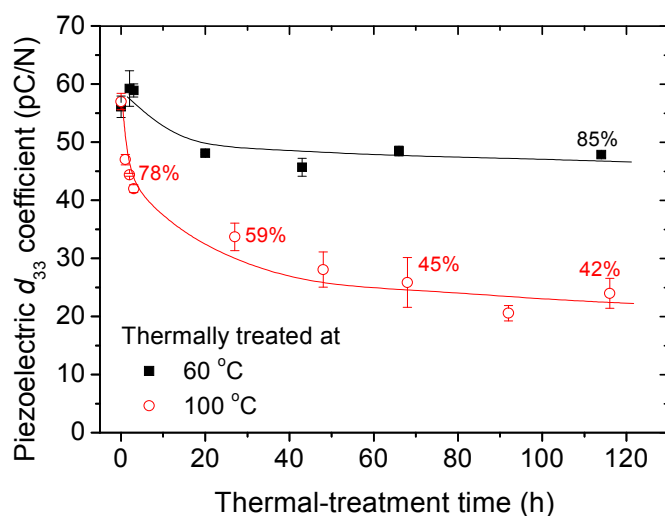


Figure 7.40: Long-term thermal stability: thermally stimulated decay of piezoelectric  $d_{33}$  coefficient with the treatment time.  $d_{33}$  coefficients were dynamically determined after the sample was cooled down to room temperature. The lines are to guide the eye.

Although PEN ferroelectrets show appreciable thermal stability up to 80 – 100 °C, they can still not be employed when higher temperatures are encountered. It is known that processing at elevated temperatures, such as controlled aging or annealing after charging, charging at elevated temperatures, and quenching or pre-aging before charging, has a significant influence on the charge stability of polymer electrets. Figure 7.41 illustrates the dependence of the remaining  $d_{33}$  on the thermal treatment temperatures for pre-annealed samples. For comparison, the decay of  $d_{33}$  for a non-annealed sample is also shown. All samples were charged at room temperature and showed an initial  $d_{33}$  of about 50 pC/N. The annealing was carried out for 1 hour in an oven at pre-determined temperatures. After annealing at 100 and 120 °C, the remaining piezoelectric  $d_{33}$  coefficients were around 30 and 25 pC/N, respectively. In the next step, all samples were thermally treated for 1 h at the temperatures as indicated. As can be seen, the  $d_{33}$  of two types of annealed samples are nearly constant for the treatment temperature up to the respective annealing temperatures of 100 and 120 °C.  $d_{33}$  are found to decrease only when the treatment temperature is higher than the respective annealing temperatures. However,  $d_{33}$  of the non-annealed sample decays already during a thermal treatment at 80 °C. All samples are deformed and non-piezoelectric at temperatures above 120 °C. The decay of  $d_{33}$  is caused by the thermally stimulated discharge processes. When the sample is annealed at an elevated temperature, charges that are trapped in relatively shallow traps are thermally de-trapped, leading to a higher portion of charges in deep traps compared to those in shallow traps. As a result, the thermal stability of the remaining charges and hence also of  $d_{33}$  is improved, as shown in figure 7.42. It should, however, be noted that the annealing process itself reduces the initial piezoelectricity of PEN ferroelectrets, and there is no improvement of stability in the temperature range above the annealing temperature.

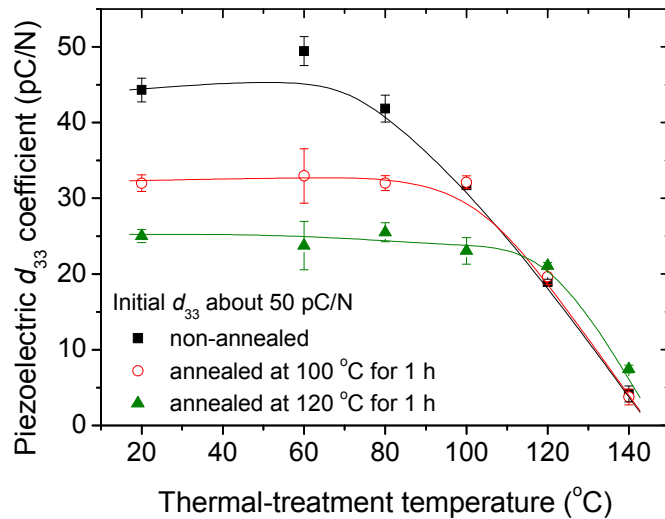


Figure 7.41: Piezoelectric coefficient  $d_{33}$  of non-annealed and pre-annealed PEN ferroelectrets as a function of the thermal-treatment temperature. The lines are to guide the eye.

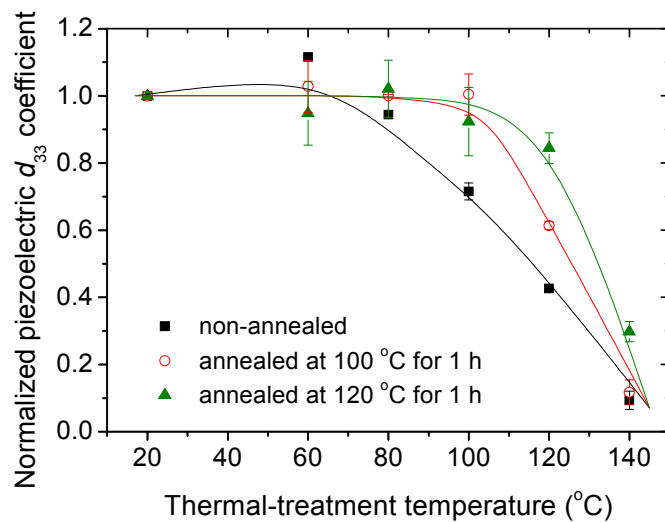


Figure 7.42 Normalized piezoelectric coefficient  $d_{33}$  of non-annealed and pre-annealed PEN ferroelectrets as a function of the thermal-treatment temperature. The lines are to guide the eye.

Another possibility for enhancing the thermal stability of  $d_{33}$  is charging the samples at elevated temperatures. To this end, a corona voltage was applied while the sample was heated on a heating plate. The selected charging temperature was maintained for 5 min. The charging voltage was only switched off when the sample had already cooled down to room temperature. Different charging temperatures up to 200 °C were selected. Dynamical  $d_{33}$  determination shows that the samples charged at room temperature, 100, and 120 °C show considerable  $d_{33}$  of a few dozen pC/N. However, samples charged at 150 and 200 °C exhibit  $d_{33}$  of only around 10 pC/N. The glass-transition temperature  $T_g$  of PEN is about 122 °C, and charging temperatures higher than  $T_g$  lead to visible deformation of the samples. The electromechanical properties of ferroelectrets strongly depend on the cellular structure, so samples charged at temperatures higher than  $T_g$  show only low  $d_{33}$ . In the next step, all samples were thermally treated for 1 h at the temperatures as

indicated, and  $d_{33}$  coefficients were dynamically determined after the samples were cooled down to room temperature. Figure 7.43 shows the temperature dependent  $d_{33}$  for the samples charged at different temperatures. There is almost no decay of  $d_{33}$  at 60 °C, but at and above 80 °C,  $d_{33}$  of the sample charged at room temperature decreases significantly. Samples charged at elevated temperatures show better thermal stability than those charged at RT. The higher the charging temperature, the better is the thermal stability, as shown in figure 7.44. For the sample charged at 100 °C, significant decay of  $d_{33}$  starts at 110 °C. The sample charged at 120 °C can retain its  $d_{33}$  up to 120 °C.

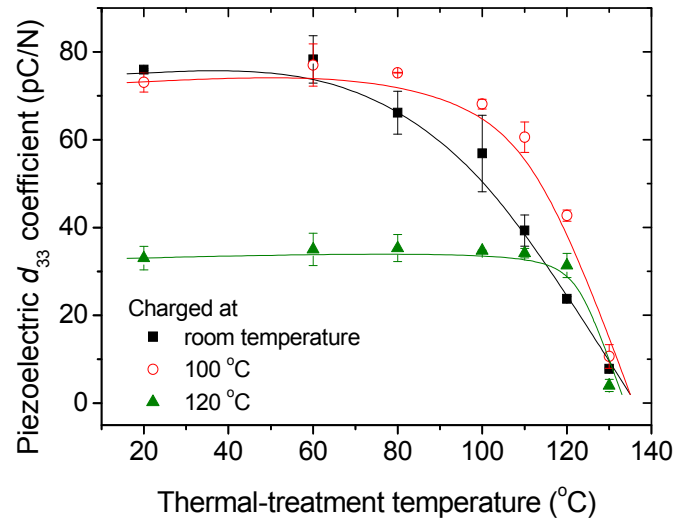


Figure 7.43: Piezoelectric  $d_{33}$  coefficient as a function of the thermal-treatment temperature for samples charged at different temperatures as indicated.  $d_{33}$  coefficients were dynamically determined. The lines are to guide the eye.

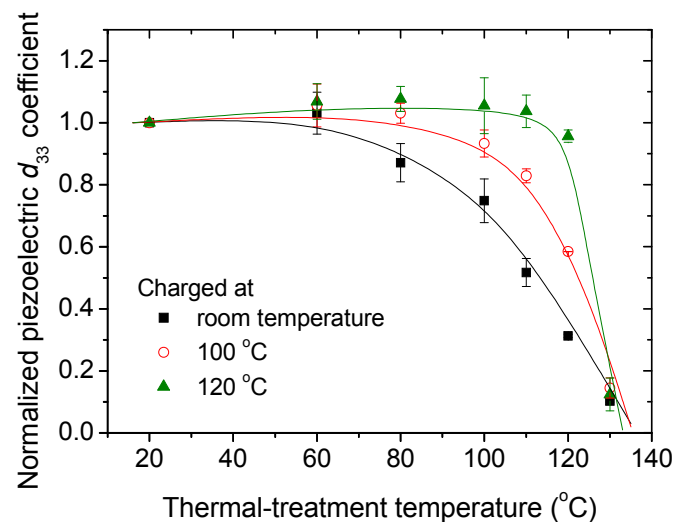


Figure 7.44 Normalized  $d_{33}$  as a function of the thermal-treatment temperature for samples charged at different temperatures as indicated.  $d_{33}$  coefficients were dynamically determined. The lines are to guide the eye.

Dielectric-resonance spectra were also measured to investigate the thermal stability. Different from the dynamic measurement, where  $d_{33}$  coefficients are determined at room temperature after the thermal treatment, in the resonance measurement,  $d_{33}$  are calculated from the spectra which are recorded at each treatment temperature. In other words, the resonance measurement delivers the synchronous  $d_{33}$  during the thermal treatment. Figure 7.45 shows the frequency-temperature maps of the dielectric loss for samples charged at room temperature and at 120 °C. The sample charged at room temperature shows relatively larger dielectric-loss peaks, indicating stronger piezoelectricity. However, the peaks start to decrease when the temperature is above 80 °C, and disappear gradually with the increasing temperature. Although the sample charged at 120 °C shows relatively smaller resonance peak, it is still piezoelectric until 120 °C. Figure 7.46 and 7.47 show the corresponding thermal stability of  $d_{33}$  which is calculated from the resonance curves. The sample charged at room temperature shows relatively larger  $d_{33}$  but worse thermal stability, where significant decay of  $d_{33}$  is observed when the surrounding temperature is higher than 80 °C. The sample charged at 120 °C shows relatively smaller  $d_{33}$ , but with much enhanced thermal stability up to 110 °C.

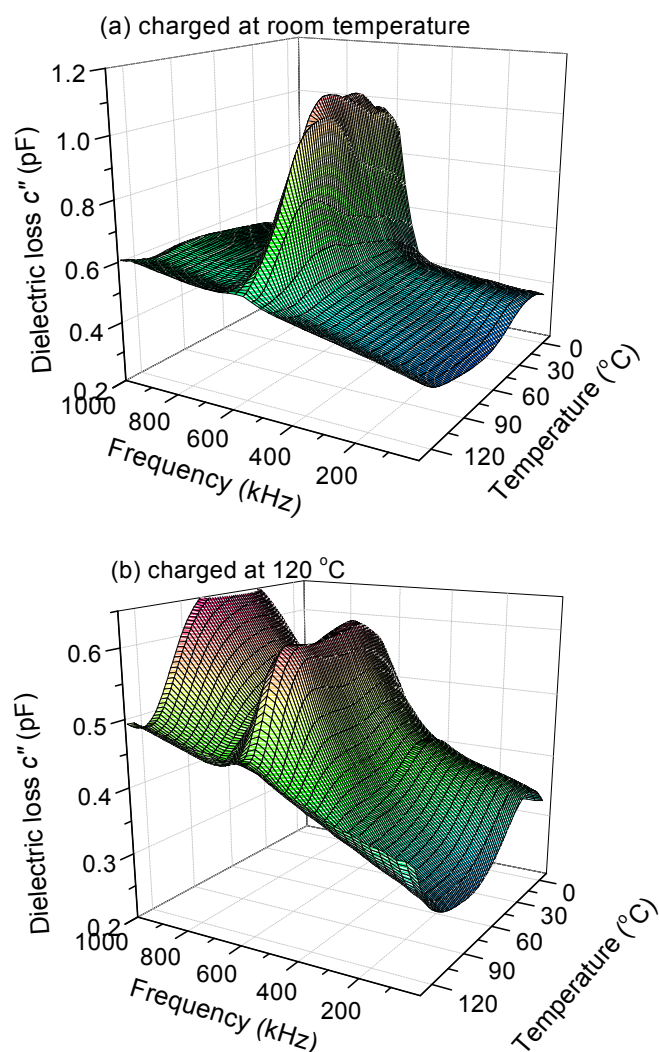


Figure 7.45: Frequency-temperature maps of the dielectric loss for the sample charged at (a) room temperature and (b) 120 °C.

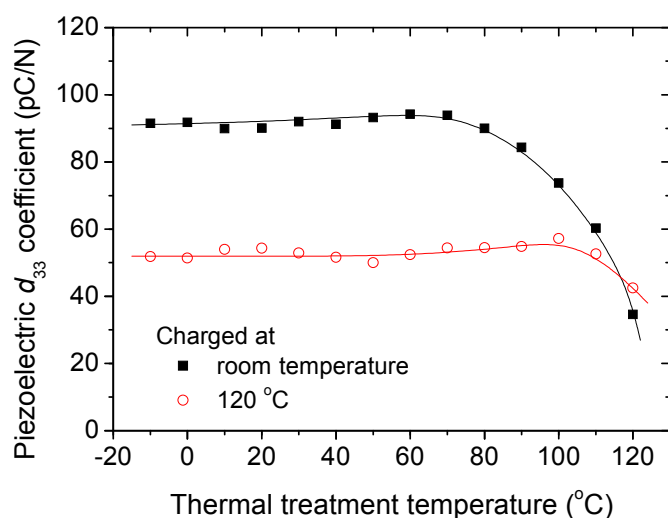


Figure 7.46: Thermal stability of the piezoelectric  $d_{33}$  coefficient calculated from the dielectric-resonance spectra, for samples charged at room temperature and at 120 °C. The lines are to guide the eye.

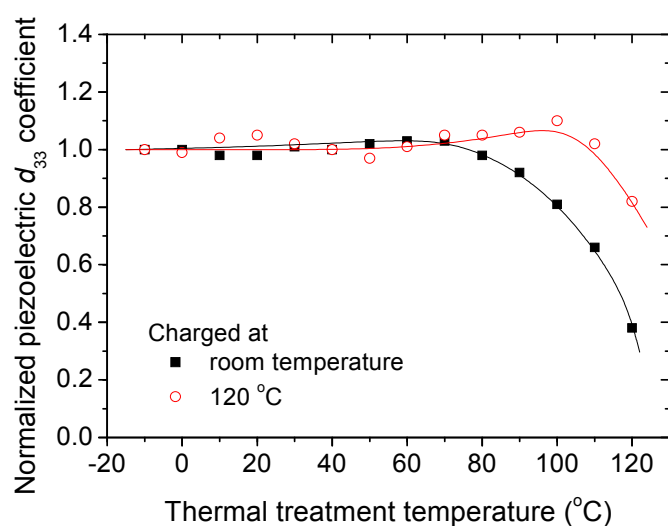


Figure 7.47 Normalized thermal stability of  $d_{33}$  calculated from the dielectric-resonance spectra, for samples charged at room temperature and at 120 °C. The lines are to guide the eye.

It is found that, the working temperature for PEN ferroelectrets charged at room temperature is as high as 80 – 100 °C, which is much higher than that of PP ferroelectrets. The enhancement of the thermal stability broadens the application range of the ferroelectrets. With proper thermal treatments such as annealing after charging or charging at elevated temperatures, the thermal stability of piezoelectricity can be significantly enhanced. The highest working temperature for PEN ferroelectrets is increased up to 120 °C by charging the sample at 120 °C. The further enhancement of the working temperature is limited by the glass transition temperature of PEN which is 122 °C. However, the thermal treatments themselves lower the initial piezoelectricity. Therefore, for any special application, a proper charging temperature should be considered. For example, if good stability is preferred, then charging at elevated temperatures can be applied, and if a strong piezoelectricity is preferred, then charging can be carried out at room temperature. For

the PEN ferroelectrets prepared in this work, a charging temperature of about 100 °C is optimal because it enhances the thermal stability but does not lower the piezoelectricity very much.



## Chapter 8

# Fluorinated ethylene-propylene (FEP) foam ferroelectrets

### 8.1 Properties of FEP

Fluorinated ethylene-propylene (FEP) is a copolymer of tetrafluoroethylene (TFE) and hexafluoropropylene (HFP). The molecular structure of FEP is asymmetrical, compared to the symmetrical chain structure of polytetrafluoroethylene (PTFE). The PTFE chain adopts a twisting helix that comprises 13  $-\text{CF}_2-$  groups every  $180^\circ$  turn such that every main chain bond is rotated  $20^\circ$  from the next [Hougham 1999]. The structure of FEP resembles that of PTFE, except that a perfluoromethyl side group  $-\text{CF}_3$  (carbon-fluorine) replaces a fluorine atom on each repeat unit, as shown in figure 8.1. FEP was invented by DuPont<sup>®</sup> and is sold under the brand name of Teflon<sup>®</sup>-FEP. Similar product is available from Daikin<sup>®</sup> with the brand name of Neoflon<sup>®</sup>-FEP, and also from some other companies.

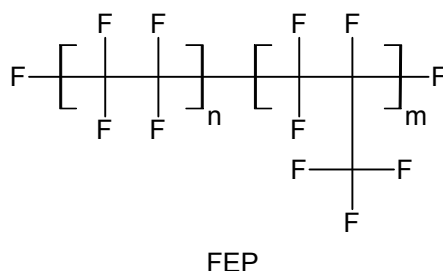


Figure 8.1: Chemical structure of fluorinated ethylene-propylene (FEP).

FEP can be described as a fluoropolymer resin with most of the excellent physical, chemical and electrical properties of PTFE [Scheirs 1997]. PTFE is known to exhibit the highest thermal stability because of its regular  $-\text{CF}_2-$  crystalline structure due to the mutual repulsion of the adjacent fluorine atoms. The extremely high molecular weight of PTFE results in a melt viscosity about a million times higher than that of the most other polymers. Theoretically PTFE melts at  $327^\circ\text{C}$ , but its melt viscosity is virtually infinite. Due to its very high melt viscosity, PTFE cannot be melt-processed but can only be shaped by powder sintering methods. The upper working temperature of PTFE is in the range from  $180$  to  $260^\circ\text{C}$ . However, cellular PTFE films have a fibrillar structure that makes them unsuitable for ferroelectrets. The presence of the bulky  $-\text{CF}_3$  side group in FEP tends to distort the highly crystalline structure of the main chain and results in a higher amorphous fraction.  $-\text{CF}_3$  groups may be regarded as defects, which are incorporated into the crystallites and thereby lead to a decrease of the melting point. Therefore, FEP is a thermoplastic which is melt-processible using conventional injection molding and screw extrusion techniques. FEP shares PTFE's useful properties of low friction and non-reactivity, but are more

easily formable. FEP is softer than PTFE and melts at 260 °C; it is highly transparent and resistant to sunlight. FEP has very high impact strength, excellent high frequency electrical properties, and good weathering resistance. FEP is widely applied as wire insulation due to its distinguishing features, e.g. high extrusion speed, high thermal stability, high continuous use temperatures, superior electrical properties, high flame retardance and very low smoke emission. FEP also exhibits other properties which make it appropriate for some special applications, such as chemical resistance, etc [[www.dyneon.com](http://www.dyneon.com)].

	FEP	PTFE
Density (kg/m <sup>3</sup> )	2150	2200
Elastic modulus (MPa)	480	500
Tensile strength (MPa)	23	23
Elongation at break	325%	250%
Melting point (°C)	260	327
Maximum operating temperature (°C)	204	260
Dielectric constant at 1 MHz	2.1	2.1

Table 8.1: Some properties of FEP and PTFE.

FEP can be synthesized by an addition polymerization of tetrafluoroethylene (TFE) and hexafluoropropylene (HFP). End products of FEP are known for their excellent chemical resistance, superior electrical properties and high service temperatures of up to 200 °C. In addition, FEP provides outstanding low temperature toughness and unique flame resistance. Typical applications of FEP include valve and pump linings, pipe liners, release applications or similar uses where resistance to chemicals at elevated temperatures or serviceability at extremely low temperatures is desired. In addition, FEP can also be used as coatings, protective linings, chemical apparatus, wire coverings, glazing films for solar panels.

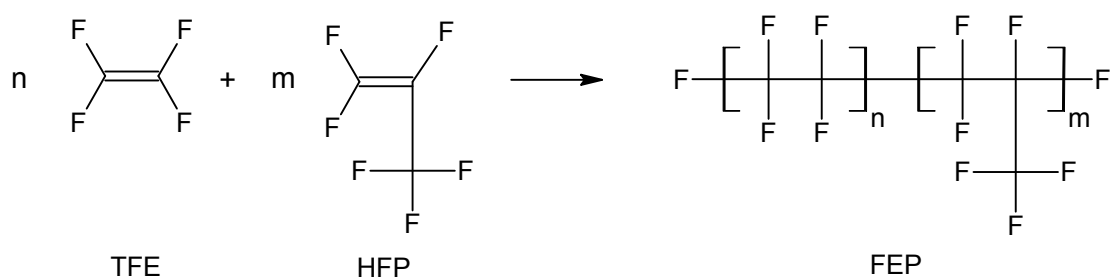


Figure 8.2: Synthesis of FEP by an addition polymerization of tetrafluoroethylene (TFE) and hexafluoropropylene (HFP).

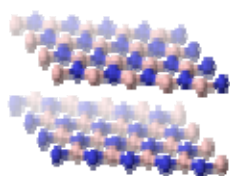
## 8.2 Investigation of solid FEP film

### 8.2.1 Preparation

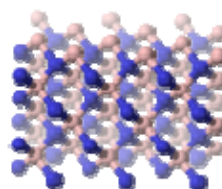
Commercially available powders with various molar masses, provided by Dyneon<sup>®</sup>, Daikin<sup>®</sup> and DuPont<sup>®</sup>, were used to prepare solid (non-voided) FEP films (The sample preparation was done by the project partner at the Institute of Polymer Material, University of Erlangen-Nürnberg, Germany). Compared to other polymers, the processing of fluoropolymers is more complex not only due to the higher manufacturing temperatures, but also to the tendency of fully fluorinated thermoplastic melts to release small amounts of hydrofluoric acid during processing. Therefore, the apparatus for FEP extrusion has to be equipped with special corrosion-resistant components. Finally, solid FEP films were produced by compression moulding in an evacuated hot press.

In this work, four types of solid FEP films have been investigated: Dyneon<sup>®</sup>-, Daikin<sup>®</sup>-, and DuPont<sup>®</sup>-FEP, prepared and supplied by the project partner as mentioned above, and Goodfellow<sup>®</sup>-FEP, supplied by the company Goodfellow. All FEP films are transparent, with varying thicknesses as listed in table 8.2. In addition, the Dyneon<sup>®</sup>-FEP films are divided into three groups: Dyneon<sup>®</sup>-FEP 6303, 6307 and 6322. The last two numbers of the sample description give the Melt Flow Index (MFI) of the material: how much polymer melt flows through a die in a defined time under a defined load. It expresses the viscosity of the material, meaning that a low number corresponds to a high viscous material. The different viscosities result from different molar masses of the polymer: higher viscosity material has higher molar mass. Therefore the type 6303 has the highest molar mass and the type 6322 has the lowest one.

As well as the pure films, the Dyneon<sup>®</sup>-FEP films with fillers have also been supplied as listed in table 8.2. Boron nitride (BN) was added as filler at two weight concentrations wt-0.5% and wt-4%. Boron nitride exists in various polymorphic forms, one of which is analogous to graphite and the other one analogous to diamond, as shown in figure 8.3. Boron nitride has several excellent thermal and electrical properties such as high thermal conductivity, high electrical resistance, low dielectric constant and high dielectric breakdown strength, which enable it to be used as electrical insulators and so on. The transparency of the as-prepared solid FEP films with fillers depends on the filler-concentration, films with wt-0.5% BN are semitransparent and films with wt-4% BN are white in color.



Hexagonal boron nitride (h-BN)



Cubic boron nitride (c-BN)

Figure 8.3: The hexagonal structure of boron nitride (h-BN), which is similar to graphite, and the cubic structure of boron nitride (c-BN), which is similar to diamond.

Film type	Thickness	Average density
	$\mu\text{m}$	$\text{g/cm}^3$
Daikin	140 – 210	1.979
DuPont	135 – 200	2.097
Goodfellow	100 – 105	2.124
Dyneon 6303	195 – 240	2.142
Dyneon 6303+wt-0.5%BN	115 – 160	2.098
Dyneon 6303+wt-4%BN	110 – 155	2.037
Dyneon 6307	150 – 220	2.081
Dyneon 6307+wt-0.5%BN	120 – 135	2.08
Dyneon 6307+wt-4%BN	130 – 170	2.074
Dyneon 6322	140 – 160	2.125
Dyneon 6322+wt-0.5%BN	115 – 125	2.098
Dyneon 6322+wt-4%BN	85 – 125	2.065

Table 8.2: Thicknesses for different types of solid FEP films.

Figure 8.4 shows the Fourier transform infrared (FTIR) spectra for the pure Dyneon<sup>®</sup>-films and Dyneon<sup>®</sup>-films with boron nitride fillers of different weight concentrations, respectively. The wave-number range from 600 to 1700  $\text{cm}^{-1}$  is enlarged in figure 8.5. Compared with the pure films, extra peaks at around 800 and 1400  $\text{cm}^{-1}$  are observed for the films with BN fillers, which are due to the stretching vibration of B–N molecules [Phani 1994]. The higher the filler concentration, the larger are the peaks. The investigations by differential scanning calorimetry (DSC) indicate that the films with boron nitride fillers show relatively higher melting temperatures and melting heat. Films with filler concentration of wt-4% show a melting temperature of about 4  $^{\circ}\text{C}$  higher than the pure films.

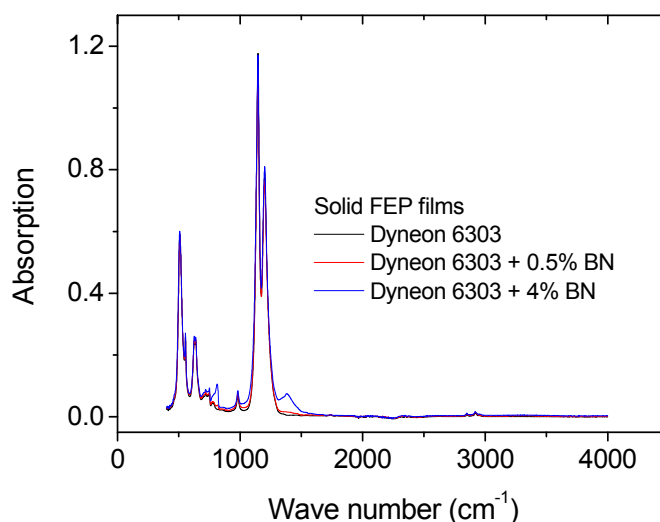


Figure 8.4: FTIR absorption spectra for the pure Dyneon<sup>®</sup>-FEP films and Dyneon<sup>®</sup>-FEP films with boron nitride fillers with weight concentrations of wt-0.5% and wt-4%, respectively.

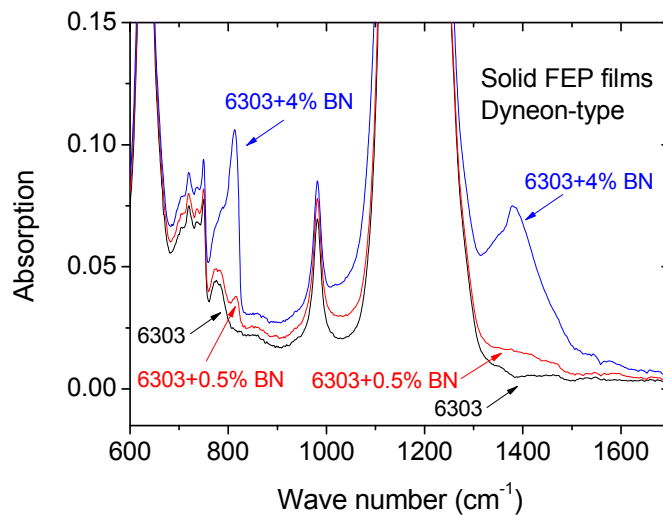


Figure 8.5: The enlargement of the wave-number range from 600 to 1700  $\text{cm}^{-1}$  for the spectra shown in the last figure.

### 8.2.2 Charge stability

Several researchers [Gerhard-Multhaupt 1999(2)] have investigated the charging and charge retention behavior of fluoropolymers of the Teflon<sup>TM</sup> family, in particular on FEP, in view of their relevance for electret applications. Teflon<sup>TM</sup>-FEP films corona-charged at room temperature usually exhibit only a surface charge layer. Uniform charge spreading throughout the bulk was found in the FEP charged at elevated temperatures [Gerhard-Multhaupt 1992, Künstler 1998]. The negative bulk charge was caused by the drift of shallow-trapped holes to a near-surface charge layer and such uniform bulk charge could only be obtained on negatively charged FEP. Charge stability in FEP is of great interest and is the subject of many investigations. The thermal stability of the positive charges by charging at room temperature is not as good as that of the negative charges, and the enhancement of the thermal positive-charge stability in Teflon<sup>TM</sup>-FEP was demonstrated using corona charging through a controlling grid at elevated temperatures [Seggern 1984]. It is reported that in FEP, electrons and holes in the traps are de-trapped (correlated with molecular motion) at temperatures of about 80, 150, and in the range from 200 to 270 °C [Stark 1994]. By thermal aging at elevated temperatures, the charges in shallow traps can be mostly de-trapped, resulting in a highly increased portion of the charges in deep traps. Therefore the remaining charges can be stable up to higher temperatures. Teflon<sup>TM</sup>-FEP is widely used in electret microphones in view of its ability of storing negative charges for a long time [Gerhard-Multhaupt 1999(2)].

Here, the thermal charge stabilities for different types of solid FEP films, including films with and without fillers, are compared. To this end, the thermally stimulated decay of surface potential as a function of temperature was investigated. Film samples were evaporated with aluminum electrode (thickness 50 nm) on one side. A tip-to-plane corona voltage of  $\pm 15$  kV and a controlling grid voltage of  $\pm 1$  kV were applied to the non-metalized surface of the sample for 1 min at room temperature, while the metalized surface was grounded. Next, samples were heated from room

temperature to 250 °C with a heating rate of 3 °C/min. The surface potentials were recorded in situ.

Figure 8.6 shows the decay of the surface potential as a function of temperature for different film types as indicated. It is found that the solid FEP films from different companies show varied thermal charge stabilities. For negative charges, there is almost no decay of the surface potential for all samples until 150 °C; however, when the temperature is further increased, significant decay is observed. For positive charges, the decay starts at relatively lower temperatures. Generally speaking, the DuPont®-FEP shows the best thermal charge stability for both positive and negative charges. Except for the Dyneon®-FEP, the thermal stability of negative charges is better than that of positive charges. In addition, there is normally an increase of surface potential (about 5%) for most of the samples at the temperature range between 70 and 120 °C. This is probably because samples are deformed by the heat treatment and are closer to the probe device.

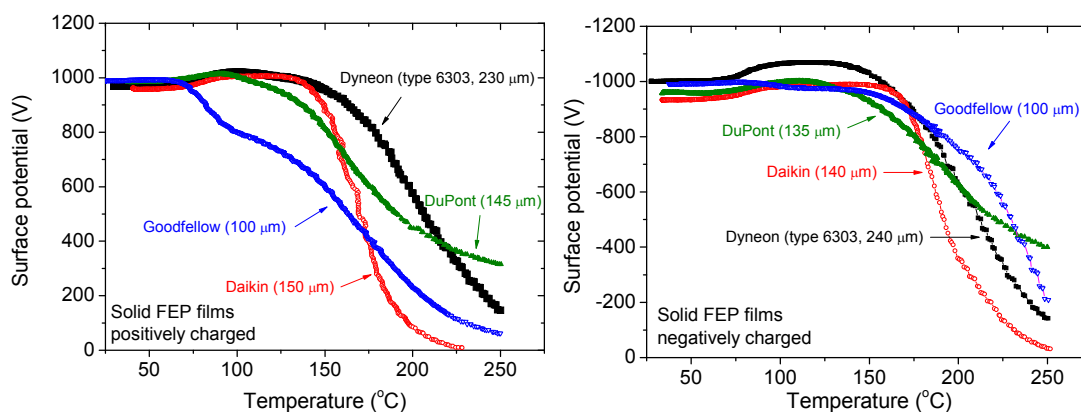


Figure 8.6: Thermally stimulated decay of surface potential for different solid film types. Charging condition: tip-to-plane corona voltage  $\pm 15$  kV, grid voltage  $\pm 1$  kV, for 1 min at room temperature. Heating rate is 3 °C/min.

Figure 8.7 shows the decay of the surface potential as a function of temperature for solid Dyneon®-FEP films with different Melt Flow Indexes (MFI). It is found that, for both positive and negative charges, films with lower MFI (high viscosity, high molar mass) show better thermal charge stability than those with higher MFI. In addition, the difference of the thermal stability between positive and negative charges is not very critical.

The thermal charge stability is strongly influenced by the fillers of boron nitride. As shown in figure 8.8, 8.9, and 8.10, both for positive and negative charges, Dyneon®-FEP films with fillers show better stability than the pure films, especially when the temperature is higher than 150 °C. It is found that the higher the filler concentration, the better is the charge stability. However, the enhancement of the stability is not very dramatic when the filler concentration is increased from wt-0.5% to wt-4%, compared to the enhancement when wt-0.5% fillers are added to the pure films. In addition, for the films with fillers, the dependence of the charge stability on the MFI (viscosity, molar mass) is not very critical. All the Dyneon®-FEP 6303, -6307 and -6322 films with the same filler concentration show similar charge stability. It can be concluded that the thermal charge

stability is dramatically improved by adding fillers due to the excellent electrical resistance of boron nitride.

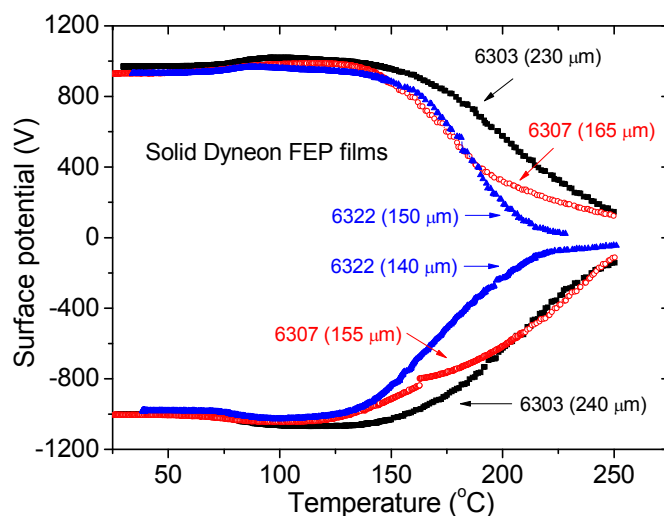


Figure 8.7: Thermally stimulated decay of the surface potential for solid Dyneon<sup>®</sup>-6303, -6307, and -6322 FEP films. Charging condition: tip-to-plane corona voltage  $\pm 15$  kV, grid voltage  $\pm 1$  kV, for 1 min at room temperature. Heating rate is 3 °C/min.

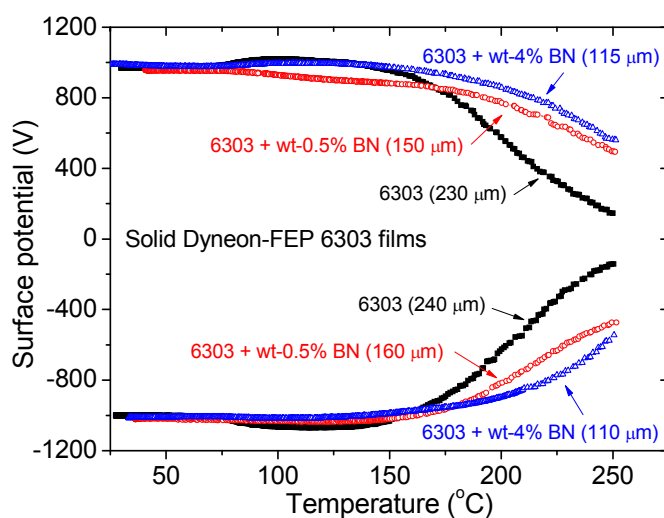


Figure 8.8: Thermally stimulated decay of the surface potential for solid Dyneon<sup>®</sup>-FEP 6303 films without and with boron nitride fillers of different weight concentrations (wt- %) as indicated. Charging condition: tip-to-plane corona voltage  $\pm 15$  kV, grid voltage  $\pm 1$  kV, for 1 min at room temperature. Heating rate is 3 °C/min.

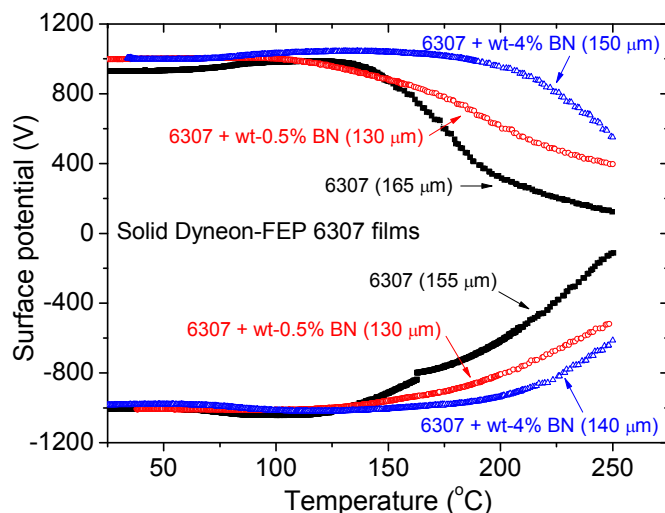


Figure 8.9: Thermally stimulated decay of the surface potential for solid Dyneon<sup>®</sup>-FEP 6307 films without and with boron nitride fillers of different weight concentrations (wt- %) as indicated. Charging condition: tip-to-plane corona voltage  $\pm 15$  kV, grid voltage  $\pm 1$  kV, for 1 min at room temperature. Heating rate is  $3$   $^{\circ}\text{C}/\text{min}$ .

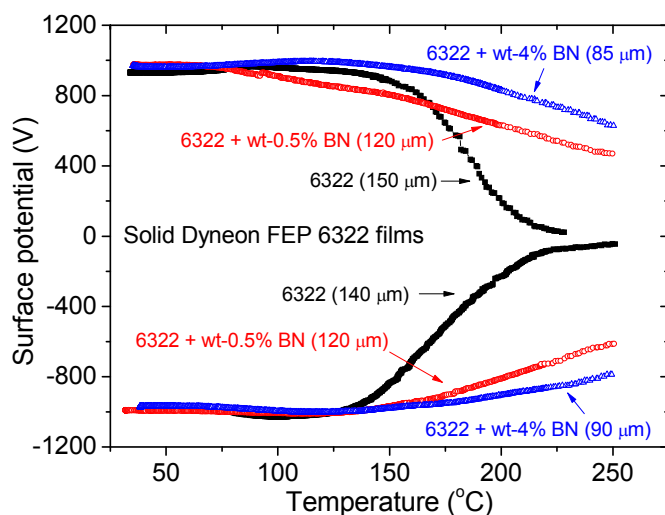


Figure 8.10: Thermally stimulated decay of the surface potential for solid Dyneon<sup>®</sup>-FEP 6322 films without and with boron nitride fillers of different weight concentrations (wt- %) as indicated. Charging condition: tip-to-plane corona voltage  $\pm 15$  kV, grid voltage  $\pm 1$  kV, for 1 min at room temperature. Heating rate is  $3$   $^{\circ}\text{C}/\text{min}$ .

## 8.3 Preparation and investigation of FEP foam

### 8.3.1 Description of technique

The foaming of FEP is much more difficult compared with that of other polymers such as PP, PET, and PEN, because much higher processing temperatures are needed due to the special properties of FEP. The two-step process consisting of supercritical- $\text{CO}_2$  saturation and



high-temperature voiding for preparation of PET and PEN foams could not be applied on FEP, due to a very fast diffusion of the dissolved CO<sub>2</sub> out of the film before the voiding step. The resulting low porosity of the films made the FEP foams unsuitable for ferroelectrets. Therefore, this process was altered to a one-step process, performing the pressure release after the supercritical-CO<sub>2</sub> saturation and the high-temperature voiding at the same time inside an autoclave. The autoclave together with the FEP samples was heated up to the final foaming temperature. CO<sub>2</sub> was fed into the heated cylinder at the selected pressure. After the saturation, the pressure was subsequently released in a very short time. At the temperature higher than the melting point of FEP, the polymer is soft enough to be foamed by the fast volume expansion due to the phase change of the supercritical CO<sub>2</sub> to gas. Finally FEP foams were prepared from the solid FEP films with an initial thickness of 100 μm, by means of CO<sub>2</sub> saturation at a pressure of 300 bar and voiding at a temperature of about 235 °C. In addition, the voided foams were subsequently biaxially stretched at 120 °C with stretching ratios between 1.3 × 1.3 and 1.8 × 1.8 in order to lower the void heights (The sample preparation was done by the project partner at the Institute of Polymer Material, University of Erlangen-Nürnberg, Germany). The cellular samples have thicknesses in the range between 100 and 150 μm, and densities in the range between 0.9 and 1.3 g/cm<sup>3</sup>. For some samples, further inflated by the supercritical CO<sub>2</sub> at a pressure of 150 bar at room temperature was tried and then they were thermally treated at 120 or 235 °C. The inflated samples have thicknesses in the range between 150 and 200 μm and densities in the range between 0.9 and 1.5 g/cm<sup>3</sup>. Unfortunately, the additional inflation did not decrease the sample density because samples shrank when heated, resulting in smaller sample areas despite the increased sample thicknesses. Therefore the inflation did not improve the cellular structures, but only changed them back to their previous form.

### 8.3.2 Investigation of cellular structure

Figure 8.11 (left) shows a scanning electron microscopy (SEM) image of the cross section of a cellular FEP sample (Dyneon<sup>®</sup>-6303, stretching ratio 1.7 × 1.7). It is found that the foaming is inhomogeneous, with voids of different dimensions and a large distribution. In addition, some parts of the film are still not sufficiently foamed. The voids are fitted with ellipses as shown in figure 8.11 (right), where a cavity larger than a set dimension is considered as a void and only a crack is not accepted as a void. The minor axes of the fitted ellipses are considered as the void heights and their distribution is consequently calculated. As can be seen in figure 8.12, most of the voids have heights below 12 μm. The voids with relatively small heights are the majority of the voids. The porosity is calculated taking into account the density before and after foaming, which is 50.7%.

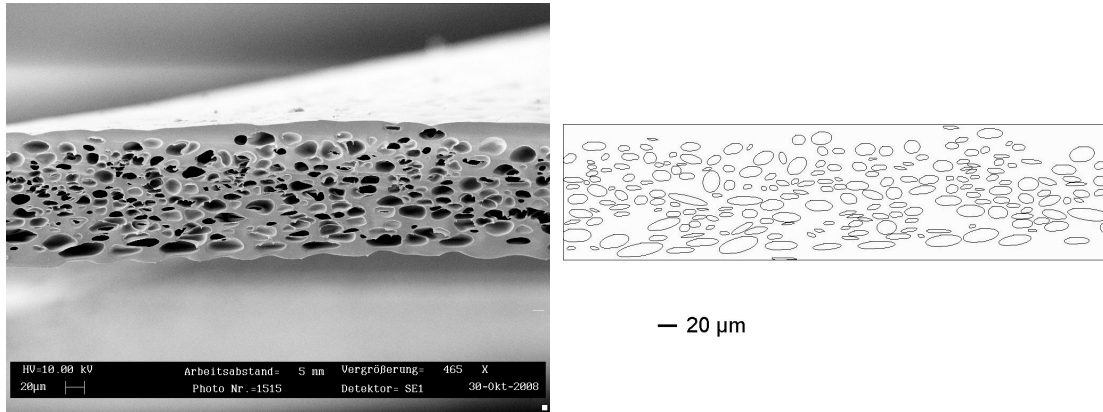


Figure 8.11 Left: SEM image of a cellular FEP sample (Dyneon<sup>®</sup>-6303, stretching ratio  $1.7 \times 1.7$ ) with average thickness of 140 µm and density of 1.056 g/cm<sup>3</sup> (initial density of 2.142 g/cm<sup>3</sup>). Right: Fitting of the voids with ellipses.

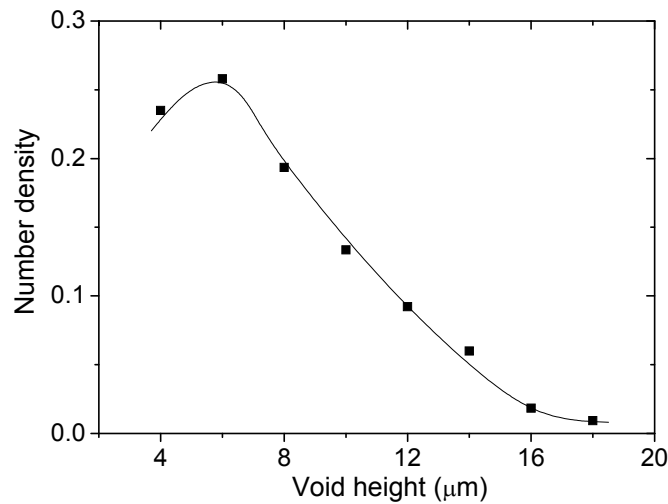


Figure 8.12: The calculated void-height-distribution. The maximum void height is 18 µm but most voids have heights below 12 µm. The line is to guide the eye.

The elastic moduli of the as-received FEP foams were determined dynamically (The measurements were done by the project partner at the Soft Matter Physics Division, Institute of Experimental Physics, Johannes Kepler University Linz, Austria.). Figure 8.13 illustrates the elastic modulus  $c_{33}$  as a function of the applied static stress. It is found that the sample stiffness increases dramatically from less than 5 MPa to 40 MPa, when the static stress is increased to 60 kPa. If the stress is further increased to more than 120 kPa,  $c_{33}$  becomes about 43 MPa.

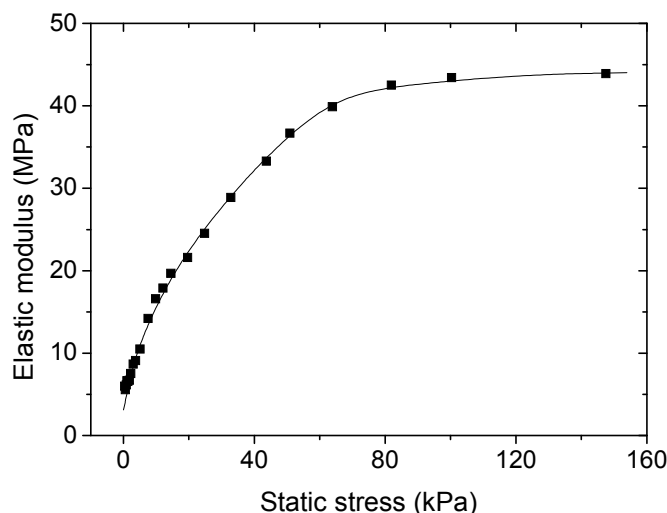


Figure 8.13: Elastic modulus  $c_{33}$  as a function of the applied static stress. The line is to guide the eye.

### 8.3.3 Investigation of electric charging behavior

The gas-breakdown inside the voids is triggered by the internal electric field. Both contact charging and corona charging can generate an internal field across the voids. For contact charging, the internal field is induced directly by the applied charging voltage and for corona charging the field is induced by the charges deposited on the sample surface. Corona charging was first applied to FEP foams. Figure 8.14 illustrates the surface potential achievable on cellular Dyneon<sup>®</sup>-FEP films with and without boron nitride fillers at different corona tip-to-plane voltages. The charging up to  $-25$  kV was carried out in air at atmospheric pressure. In order to avoid any destructive gas-breakdown between the corona tip and the sample surface, a voltage of  $-50$  kV was applied in an atmosphere of sulfur hexafluoride ( $\text{SF}_6$ ) at 3 bar. Low tip-to-plane voltage of  $-5$  kV cannot generate a corona therefore a zero surface potential is measured. With increasing corona voltage, surface potential is enhanced gradually but slowly. After charging with  $-50$  kV corona, surface potentials of  $-3.7$  and  $-2.6$  kV are achieved for the pure Dyneon<sup>®</sup>-FEP 6303 and 6322 films, respectively. For those films with boron nitride fillers, surface potential is detectable only when the tip voltage reaches  $-15$  kV. Relatively higher surface potentials of around  $-4$  to  $-4.5$  kV are achieved with a voltage tip of  $-50$  kV for the Dyneon<sup>®</sup>-FEP 6303 and 6322 films with wt-0.5% BN fillers, respectively. It is found that the surface potentials achievable on the present Dyneon<sup>®</sup>-FEP films are much lower than those achieved on PEN samples, for which the surface potential up to  $-12$  kV can be measured when charged with a corona tip of  $-50$  kV.

Taking into account the sample densities and thicknesses, the corresponding average internal electric fields in the voids are calculated with equations 5.4, 6.6, and 6.7, as shown in figure 8.15. When charged in air (corona-tip voltage lower than  $-25$  kV), electric field higher than  $-20$  MV/m cannot be achieved, which is quite insufficient to generate gas-breakdown in most of the voids. However, even at a very high corona-tip voltage of  $-50$  kV, the internal field is still relatively low. The highest average internal electric field is achieved on Dyneon<sup>®</sup>-FEP 6303 films with wt-0.5% BN fillers, which is around 44 MV/m, and for the pure Dyneon<sup>®</sup>-FEP 6303 films the maximum field is 34 MV/m. Due to the large sample thicknesses, the maximum internal fields are even

lower, 26 MV/m and 16 MV/m for Dyneon<sup>®</sup>-FEP 6322 films with wt-0.5% BN fillers and without fillers, respectively. Compared with the pure films, higher internal electric fields can be achieved on the films with fillers, indicating that boron nitride enhances the electric properties of the cellular FEP films. However, the internal electric fields are still not high enough to generate sufficient gas-breakdown. As a comparison, a very high surface potential of  $-12$  kV and an average internal field of 395 MV/m are achieved on a PEN foam when charged with corona-tip voltage of  $-50$  kV. Therefore, the corona charging under present experimental conditions cannot fulfill an effective charging for the present cellular FEP films. Contact charging is subsequently tried, as discussed later.

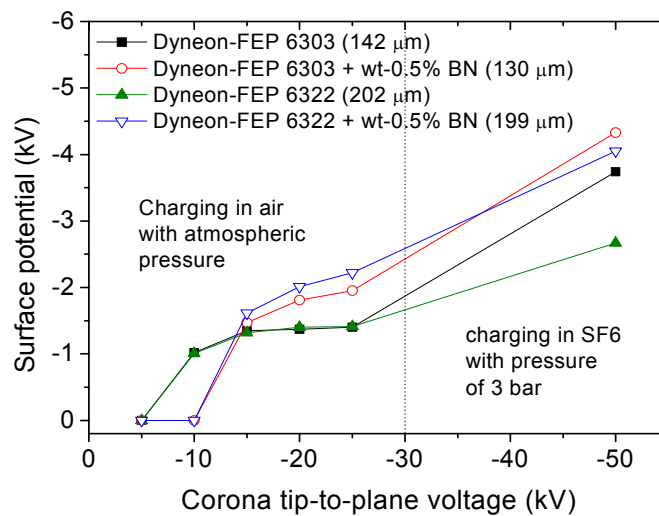


Figure 8.14: Surface potential achievable as a function of the corona tip-to-plane voltage, for foam samples of Dyneon<sup>®</sup>-FEP 6303, Dyneon<sup>®</sup>-FEP 6303 with wt-0.5% BN, Dyneon<sup>®</sup>-FEP 6322, and Dyneon<sup>®</sup>-FEP 6322 with wt-0.5% BN, respectively.

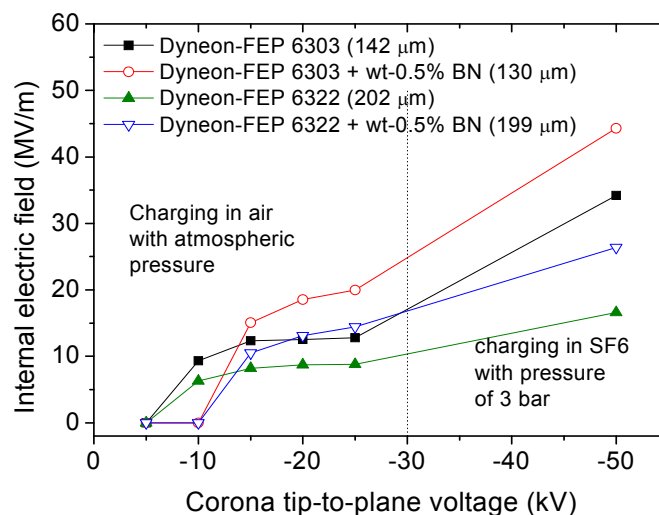


Figure 8.15: Average internal electric field in the voids, for the samples shown in figure 8.14.

Figure 8.16 shows the thermally stimulated decay of the surface potential as a function of temperature, for the cellular Dyneon<sup>®</sup>-FEP 6303 and 6322 films with and without boron nitride fillers. In analogue to the solid films, the cellular films with fillers also show better surface charge stabilities than the pure cellular films, in the temperature range between 200 and 250 °C. Figure 8.17 shows the decay of the surface potential as a function of time at room temperature, for the cellular Dyneon<sup>®</sup>-FEP 6303 and 6322 films with and without boron nitride fillers. The initial surface potentials are the maximum values achievable when charged with a corona-tip voltage of -50 kV. Surface potentials decrease very fast to a low level smaller than 2 kV in a few hours, and thereafter become stable.

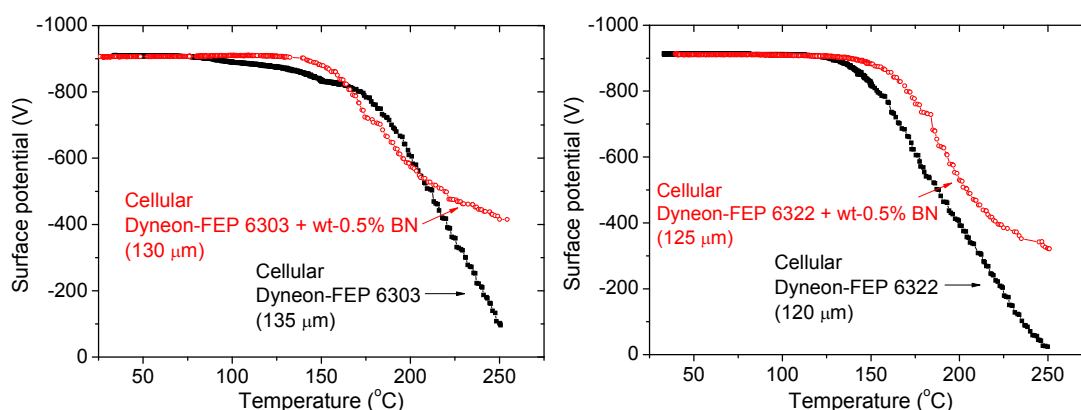


Figure 8.16: Thermally stimulated decay of the surface potential for cellular Dyneon<sup>®</sup>-FEP films. Charging condition: tip-to-plane corona voltage of -15 kV, controlling grid voltage of -1 kV, for 1 min at room temperature. Heating rate is 3 °C/min.

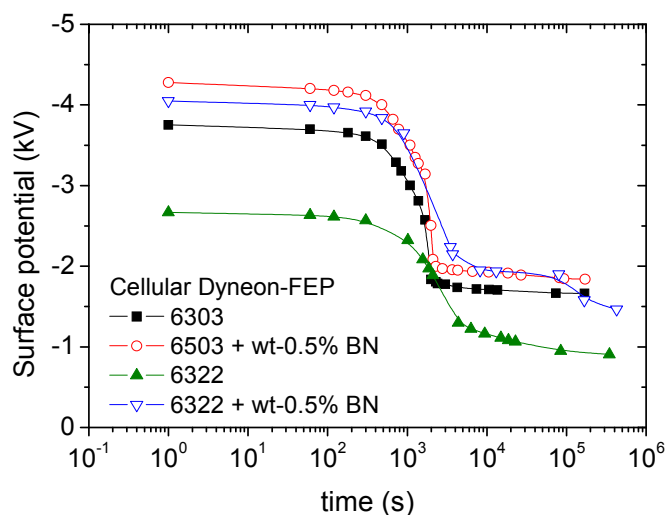


Figure 8.17: Decay of the surface potential with time at room temperature. Samples were charged with corona tip-to-plane voltage of -50 kV.

As discussed above, only a low internal electric field could be achieved even at a very high corona-tip voltage of -50 kV, indicating that corona charging is not successful at generating gas-breakdown in the cellular voids. Consequently, contact charging was tried to charge the

samples. However, for most of the present samples, breakdown of the polymer always occurs at a voltage lower than 3 kV, both for positive and negative charging. Figure 8.18 shows the breakdown measurement for a cellular Dyneon<sup>®</sup>-FEP 6303 film with a thickness of 146  $\mu\text{m}$ . A contact voltage was applied between the sample electrodes, with an increasing rate of 100 V/s. The corresponding current was recorded simultaneously. For this sample, with increasing voltage, the current is still limited at a very low level with a magnitude of  $10^{-7}$  A. However, when the voltage is increased to 2880 V a sudden increase of the current up to  $10^{-4}$  A is observed and the breakdown of the FEP bulk takes place, which destroys the sample and makes a hole across the sample thickness. Both for Dyneon<sup>®</sup>-FEP 6303 and 6322 films with and without boron nitride fillers, the breakdown experiments show similar behaviors. Table 8.3 shows the corresponding electric field in the polymer bulk layer (breakdown strength) and in the voids when the breakdown of polymer bulk occurs for Dyneon<sup>®</sup>-FEP 6303 and 6322 films with and without BN fillers, respectively. It is found that the breakdown strength of the polymer bulk is quite low for these FEP foams, although it is slightly increased by the fillers due to the high breakdown strength of boron nitride.

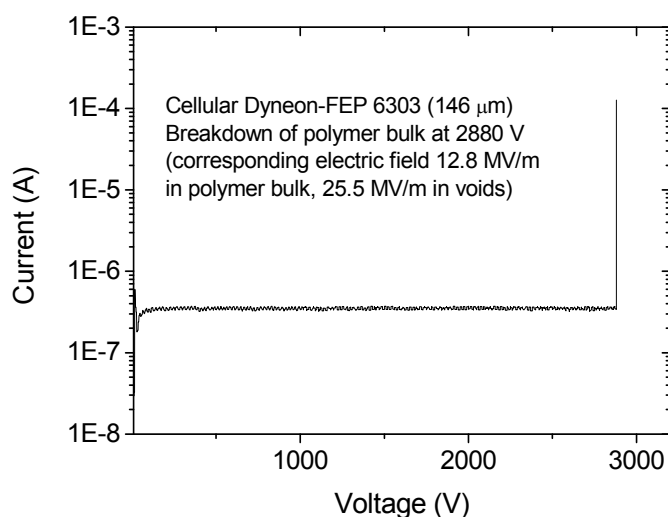


Figure 8.18: Breakdown experiment for a cellular Dyneon<sup>®</sup>-FEP 6303 sample with a thickness of 146  $\mu\text{m}$  and a density of  $0.975 \text{ g/cm}^3$ . An increasing contact voltage was applied between the sample electrodes, and the current was recorded. Voltage increase rate: 100 V/s.

Sample	Breakdown strength of polymer bulk	Corresponding electric field in the voids
	MV/m	MV/m
Dyneon <sup>®</sup> -FEP 6303	~12.8	~25.5
Dyneon <sup>®</sup> -FEP 6303 with wt-0.5% BN	~13.6	~27.1
Dyneon <sup>®</sup> -FEP 6322	~8	~16
Dyneon <sup>®</sup> -FEP 6322 with wt-0.5% BN	~9.3	~18.7

Table 8.3: When the breakdown of polymer bulk occurs, the electric field in the polymer layer (breakdown strength of polymer) and the corresponding electric field in the voids, for different types of FEP foams as indicated.

In the contact charging, the maximum internal electric field for gas-breakdown across the void heights is limited by the breakdown of the polymer bulk, and this field is even smaller than the one achieved during corona charging. With electrodes on the surfaces, even a very small defect of the material at any position below the electrode area could induce the breakdown of the polymer bulk. In contrast to the corona charging, where the sample surface is non-conductive, charging can still occur even if there is a hole across the sample thickness. Generally speaking, corona charging is safer for the sample than contact charging. Due to the very early breakdown of the polymer bulk at relatively low voltages, high internal electric fields in the voids cannot be generated and therefore a sufficient gas-breakdown cannot be triggered. This was also confirmed by the fact that no obvious light emission could be observed during charging. A possible explanation for the unsuccessful charging is that during the foaming, some chemical and electric properties of the FEP might be changed, which decreases the breakdown strength.

## 8.4 Investigation of piezoelectric properties

Piezoelectric  $d_{33}$  coefficients were dynamically determined, with a static force of 3 N, a dynamic force of 1 N (peak-to-peak) at a frequency of 2 Hz. Only some of the samples show measurable  $d_{33}$  coefficients. Among these samples, half of them show very low  $d_{33}$  less than 5 pC/N, while the rest mostly show  $d_{33}$  in the range between 5 and 25 pC/N, and the highest  $d_{33}$  is about 40 pC/N, as the number density of each  $d_{33}$  range shown in Figure 8.19. Although some samples with very rough surfaces, for example with bubbles, also show relatively high signals up to a few dozen pC/N, these cannot be considered as the piezoelectricity since they are not from the piezoelectricity. Samples with signals less than 1 pC/N are also neglected, because these minor values are beyond the precision range of the experimental equipment.

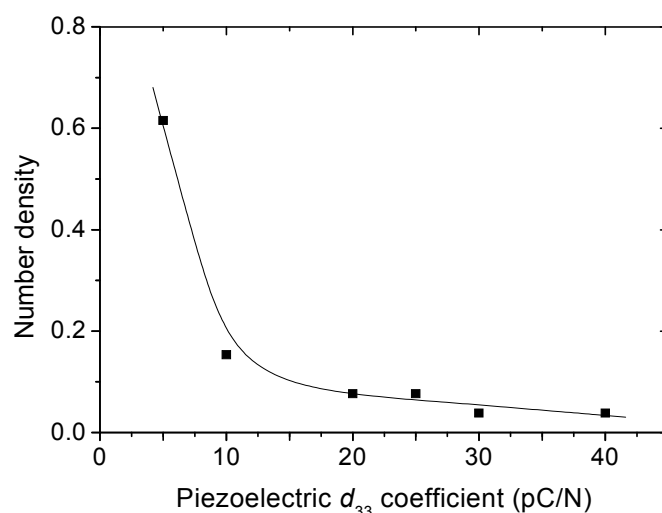


Figure 8.19: Number density for each  $d_{33}$  range. Piezoelectric  $d_{33}$  coefficients were dynamically measured, with a static force of 3 N and a dynamic force of 1 N (peak-to-peak) at a frequency of 2 Hz. The line is to guide the eye.

All the present samples show a broad density range from 0.8 to 1.8 g/cm<sup>3</sup>, and the majority has a density of around 1.2 g/cm<sup>3</sup>. Unlike PP and PEN ferroelectrets for which there is a “reverse-U” relation between  $d_{33}$  and sample density, no obvious dependence of piezoelectricity on the sample density is found for FEP foams. Dielectric-resonance spectra cannot be achieved because no reasonable resonance curve exists due to the low piezoelectricity. The reason for the present FEP ferroelectrets with quite limited piezoelectricity may be the insufficient charging. As discussed, the internal electric field in the voids by corona charging is limited to values lower than 44 MV/m, and for the contact charging, the possible maximum field is as low as 25 MV/m due to the easy breakdown of the polymer bulk. According to Paschen’s law, an electric field of 44 MV/m can only trigger internal gas-breakdown in the voids with heights larger than 8  $\mu\text{m}$ . However, the investigation of the cellular structure shows that these relatively large voids are only a small portion of all the voids. In order to trigger gas-breakdown in relatively smaller voids, a higher internal electric field is needed, which is, however, not possible for the present FEP foams both by corona and contact charging.

Figure 8.20 shows the mechanical fatigue test, where a non-stop dynamical  $d_{33}$  measurement (3 measurement-cycles/minute, static force 3 N, dynamic force 1 N (peak-to-peak) at 2 Hz) was applied on a FEP foam with initial  $d_{33}$  of about 27 pC/N. After about 2000 measurement cycles, the sample still shows  $d_{33}$  of about 20 pC/N, which is around 75% of its initial value. Further measurements up to 5000 cycles do not lower the  $d_{33}$  significantly. This result indicates that the cellular structures of the present FEP foams are appreciable for the potential ferroelectret applications.

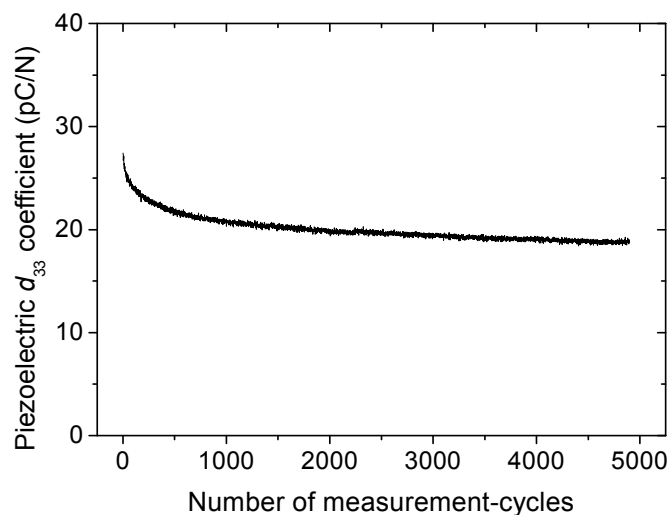


Figure 8.20: Mechanical fatigue for a FEP ferroelectret. A non-stop dynamical  $d_{33}$  measurement (3 measurement-cycles/minute, static force 3 N, dynamic force 1 N (peak-to-peak) at 2 Hz) was applied.

In the dynamic  $d_{33}$  measurements, a static stress (static force, bias) is applied in order to fix the sample onto the sample holder, and as already found for most polymer foam ferroelectrets, the  $d_{33}$  is strongly influenced by this extra stress. As illustrated in figure 8.21, a cellular FEP shows a  $d_{33}$  coefficient of about 47 pC/N under a static stress of 21 kPa (static force of 2 N) by a dynamic determination. The stress was gradually changed with an interval of 10.5 kPa (static force of 1 N),



and  $d_{33}$  was measured 2 min after the change of stress, in order to obtain complete structure deformation due to the stress. With the increase of the stress to 105 kPa (static force of 10 N),  $d_{33}$  decreases first dramatically and then slowly to about 10 pC/N, which is 21% of its initial value under a stress of 21 kPa. Next, the stress is decreased with the same interval. As can be seen, however,  $d_{33}$  cannot follow their initial values, especially when the stress is lower than 63 kPa, meaning that the cellular structure cannot recover its initial form within 2 min. Thus, the waiting time is extended to 10 min and  $d_{33}$  is again measured. As indicated in the figure, the structure recovery is much better in this case. For ferroelectrets, piezoelectricity strongly depends on sample's stiffness. Large  $d_{33}$  coefficients are achieved on samples with smaller elastic moduli. This result is in good agreement with the elastic modulus measurement as shown in figure 8.13 which shows that sample stiffness is dramatically increased with the increase of applied stress.

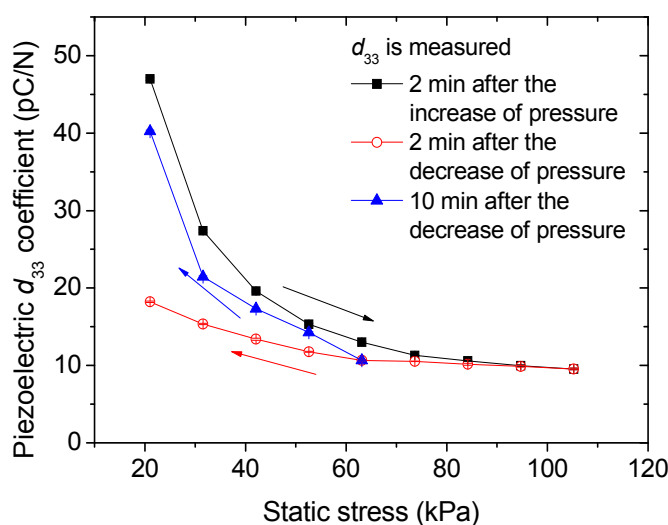


Figure 8.21: Piezoelectric  $d_{33}$  coefficient as a function of the applied static stress (static force, bias). A static force of 1 N corresponds to a stress of 10.5 kPa.  $d_{33}$  coefficients were dynamically determined 2 min or 10 min after the change of the stress, as indicated.

The frequency response of the present FEP ferroelectrets to a mechanical signal was also investigated. The sample was held with a fixed static force of 3 N and a dynamic force with a fixed peak-to-peak value of 1 N but varying frequency. Piezoelectric  $d_{33}$  coefficients were dynamically determined and plotted as a function of frequency, as illustrated in figure 8.22. The sample shows a quite stable  $d_{33}$  of about 28 pC/N in the frequency range from 2 to 100 Hz. In the range from 100 to 600 Hz, however, there is a fluctuation of  $d_{33}$  between 29 and 33 pC/N. The relatively large fluctuation is partly due to the frequency characterization of the equipment. Generally speaking, in the frequency range between 2 and 600 Hz, the same sample shows piezoelectric  $d_{33}$  coefficient between 28 and 33 pC/N, which is appreciable for frequency-independent applications.

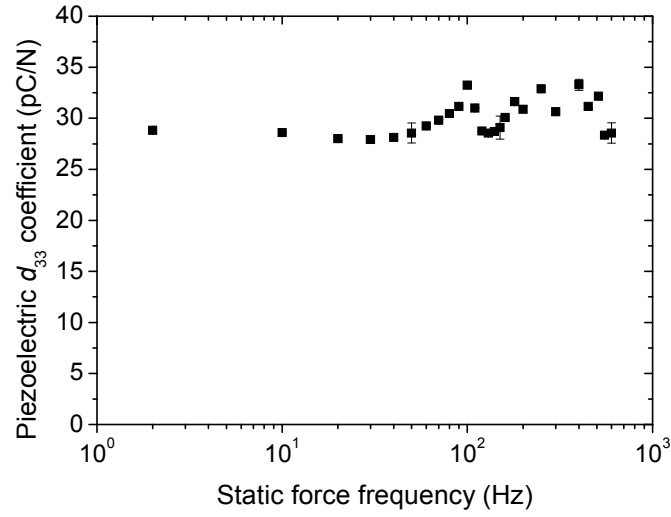


Figure 8.22: Piezoelectric  $d_{33}$  coefficient as a function of the dynamic force frequency. In the dynamic measurement, the sample was applied with a static force of 3 N and a dynamic force with peak-to-peak value of 1 N but varied frequencies.

## Chapter 9

# Fluorinated ethylene-propylene (FEP) layer ferroelectrets

Polymer foam ferroelectrets are very attractive for sensors and actuators with specific and sometimes unusual property combinations [Bauer 2004]. In comparison to ferroelectrics based on polar polymers such as  $\beta$ -phase polyvinylidene fluoride ( $\beta$ -PVDF) and some of its copolymers with trifluoroethylene (P(VDF-TrFE)), polymer foam ferroelectrets from non-polar polymers show a number of advantages including enhanced piezoelectric activity and higher working temperatures. During the last two decades, polymer foams from polypropylene (PP), polyethylene terephthalate (PET), and cyclo-olefin copolymers (COC) have been investigated in view of their potential piezoelectric applications [Lekkala 1999, Sessler 1999(3), Saarimäki 2006, Wirges 2007, Voronina 2008]. There are, however, still some shortcomings that limit the usefulness of the present polymer foam ferroelectrets. For example, PP ferroelectrets may exhibit  $d_{33}$  coefficients of 600 pC/N and more, but their operating temperature cannot be much higher than 60 °C. PET ferroelectrets show slightly better  $d_{33}$  thermal stability up to 80 °C, with  $d_{33}$  less than 200 pC/N [Lekkala 1999, Sessler 1999(3), Wirges 2007, Voronina 2008]. An enhanced thermal stability of COC ferroelectrets up to 110 °C has been reported, but at the price of smaller  $d_{33}$  value of about 15 pC/N [Saarimäki 2006, Voronina 2008]. In addition, the properties of the polymer foam ferroelectrets strongly depend on the cellular morphology, i.e. on the size and the distribution of the voids. However, for most of the present polymer foams, their cellular voids always have a rather wide and not well-controlled size and shape distribution so that only some of the voids are optimal for charging and for transducer operation. On the other hand, controlled preparation of an optimized cellular structure is still technically a challenge. To overcome these two main disadvantages (insufficient thermal stability and the difficulty to achieve ideal cellular structure), several alternative approaches have been proposed. Polymer systems with relatively large thermoformed voids between fluoropolymer-electret films [Altafim 2003, Altafim 2006], or with laser-perforated holes in the central layer of a three-layer fluoropolymer sandwich [Basso 2007], have been suggested and demonstrated. However, they are difficult to charge optimally and do not lend themselves easily to large-scale production with good reproducibility. More recently, a concept of new template-based fluorinated ethylene-propylene (FEP) ferroelectrets with tubular channels has also been presented, which can serve as a material platform for several types of piezoelectric or even multifunctional ferroelectrets films [Altafim 2009]. A structure with well-defined uniform tubular channels is formed by means of a lamination process. Due to the excellent thermal charge stability of FEP, a maximum operating temperature up to 130 °C can be achieved on the samples which are properly charged at 140 °C. On the other hand, however, the lamination is carried out at an elevated temperature of approximately 300 °C, which increases the operation complexity and the fabrication cost during the sample preparation.

Here, a new versatile technique for preparation of new polymer layer ferroelectrets, which is with low cost and easy to handle, is proposed. The as-prepared ferroelectrets have well-designed uniform structure, and illustrate appreciable piezoelectric properties.

## 9.1 Preparation of FEP layer system

Fluorinated ethylene-propylene (FEP) was chosen to prepare samples due to its chemical, mechanical, and electric properties, especially the excellent charge-storage abilities. The properties of FEP have been introduced in section 8.1. The starting material was the commercially available solid DuPont Teflon<sup>®</sup> FEP films of 50  $\mu\text{m}$  thickness. The films are transparent, soft, and glazed, with average density of 2.09  $\text{g}/\text{cm}^3$ . Samples were prepared by means of a “laser-cutting + high-field charging + laser-bonding” procedure, as described by the following.

(1) An FEP mesh was prepared by laser cutting (VersaLaser, F. Huhn & Sohn GmbH). It contained a regular pattern of square holes ( $3 \times 3 \text{ mm}^2$ ) separated by 1 mm wide FEP stripes. Two uniform FEP films were cut from the sample sheet and metalized with 50 nm thick aluminum electrode on their respective outer surfaces. The overall area of both the mesh and films was  $29 \times 29 \text{ mm}^2$ , with  $6 \times 6$  holes, as shown in figure 9.1 (Left).

(2) The mesh was sandwiched between the two uniform films. In order to charge the sample, a DC voltage was applied directly onto the electrodes, as depicted in figure 9.1 (Right). As long as the internal electric field in the voids was higher than the threshold, a gas-breakdown occurs (Paschen’s law). Positive and negative charges were deposited on the upper and lower surfaces of the uniform FEP films, forming macroscopic dipoles. Alternatively, the uniform films could be charged by means of a tip-to-plane corona with opposite polarities before sandwiching. Then the charged surfaces were placed face to face, and the mesh was sandwiched between them, as shown in figure 9.2. It should be noted that, when the charged surfaces were moved more and more close to each other, a back-discharge may occur if the charge induced electric field was larger than the breakdown threshold. Therefore part of the formerly deposited charges would be destroyed. The corona charging can be applied on large scale in a short time, which is suitable for industrial fabrications.

(3) After charging, the three layers were locally bonded, as illustrated in figure 9.3. A laser beam (VersaLaser, F. Huhn & Sohn GmbH) with a diameter of 0.1 mm was applied at selected points on the stripes of the mesh, with a separation of 2 mm. The laser beam melted the FEP locally within a very short time. When the laser moved away, the molten polymer material in adjacent layers solidified together, so that the mesh and the films were fused. In addition, as an option for actual fabrication, the drilling holes can be filled with non-conductive glue by means of injection, in order to further fix the bonding.

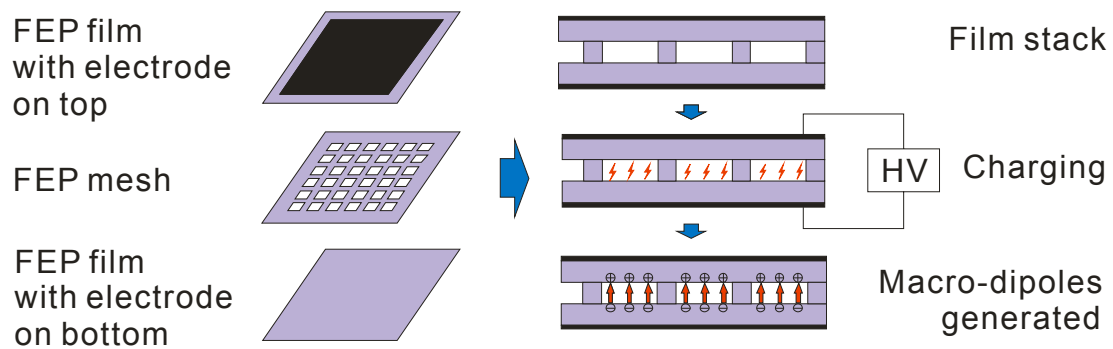


Figure 9.1 Left: Structure description of a sandwich ferroelectret. A layer of FEP mesh was sandwiched between two layers of solid FEP film. The FEP mesh was prepared by laser-cutting. Right: Electric charging of the sandwich. High field voltage was applied directly between the electrodes, and gas-breakdown occurs inside the voids. The deposited charges form macro dipoles across the voids.

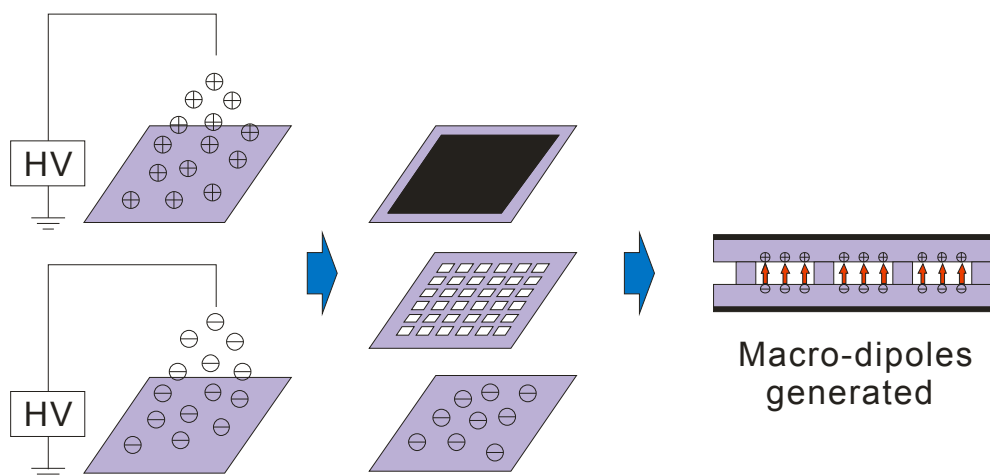


Figure 9.2: An alternative approach for charging. Two uniform films were corona charged with opposite polarities, and then the mesh was sandwiched between these two films. The charged sides were placed face to face, forming macro dipoles.

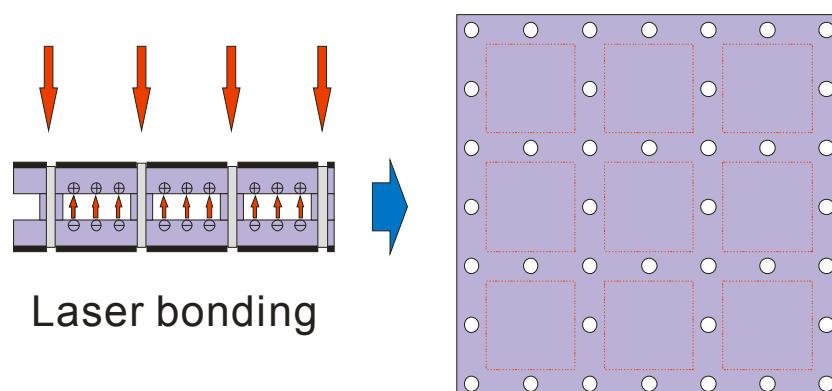


Figure 9.3: After sandwiching and charging (or charging and sandwiching), the film stack was combined locally by means of laser-bonding.

This “laser-cutting + high-field charging + laser-bonding” process is versatile, since there is no limit with respect to the sample size and shape. The preparation process can be finished in a very short period, and the technique can be applied on large scale for industrial fabrication. Unlike the foaming of the polymer foams such as cellular PP and PEN, the structure preparation is not related to the polymer itself. Polymer films are used as the charge holder, and any polymer that has good charge-storage ability can be candidate for this sandwich. All the voids have the same size as designed, and there is no void distribution like polymer foams prepared by foaming, i.e. the cellular structure in this sandwich is uniform and homogeneous. The transverse dimension of the voids is determined by the dimension of the mesh holes, and the void height is determined by the thickness of the mesh layer, both of which can be adjusted easily with respect to actual requirements. It should be noted that if the contact charging is utilized, the charging process should be performed before the laser bonding, because the holes across the whole sample after the laser bonding may cause short-circuit when a contact voltage is applied.

The working principle of the polymer sandwich is mostly the same as that of the polymer foams, where the piezoelectricity derives from the change of dipole moment due to the applied mechanical stress. For polymer foams, the change of dipole moment is achieved by the compression of the whole anisotropic cellular structure; for the sandwich, however, the change of dipole moment comes from the bending of the solid films. As illustrated in figure 9.4, after sample preparation, macroscopic dipoles are generated across the void heights, and the compensating charges are formed on the electrodes. If a mechanical stress is applied, the solid films bend and decrease the dipole moment. Consequently, the amount of the compensating charge is decreased and therefore a current flow is generated. Contrarily, if a voltage is applied onto the electrodes, films will deform due to the reverse-piezoelectricity. Driven by an alternating voltage, vibration of the films occurs.

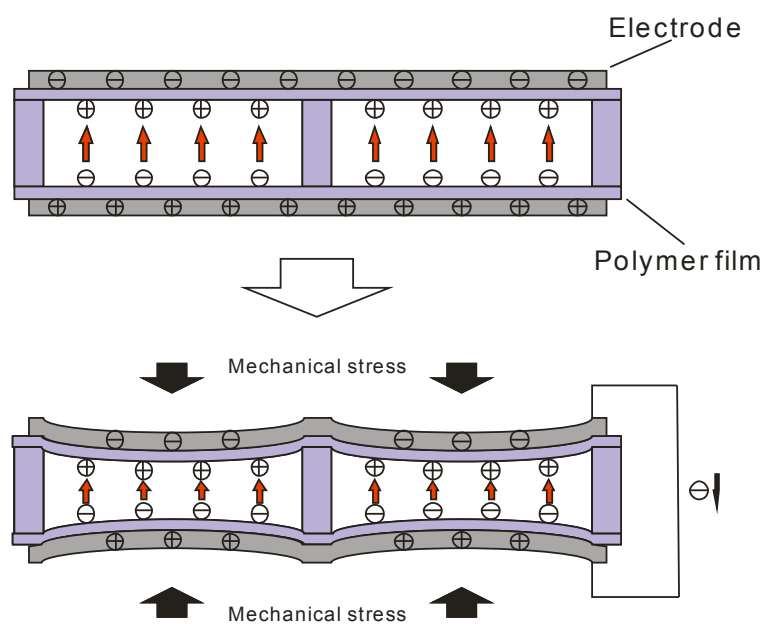


Figure 9.4: After proper preparation arrangements of bonding and charging, macroscopic dipoles are formed and compensating charges are generated. Mechanical stress bends the films and thus decreases the dipole moment. Therefore the amount of the compensating charge is decreased and a current flow is generated.

## 9.2 Investigation of cellular structure

The sandwich structure was observed by means of an optic microscope. Figure 9.5 shows the image of the cross section covering one mesh unit, from a welding point, over a complete void, to the neighboring point. It can be clearly seen that two parallel uniform solid films are separated by a homogenous air gap. However, the average thickness of the air gap is about  $70\ \mu\text{m}$ , which is larger than the designed value of  $50\ \mu\text{m}$ . The reason for this deviation can be seen in figure 9.6, that the imperfect welding leads to some additional separation between the outer films and the grid. The molten and thereafter solidified polymers may occupy these additional spaces, resulting in increased air-gap thicknesses. In addition, the laser beam was not applied exactly on the middle of the stripe of grid. The average diameter of the welding hole is about  $200\ \mu\text{m}$ , which is much larger than the diameter of the laser beams of  $100\ \mu\text{m}$ , because the polymer not only at, but also around the welding points, was melted by the high temperature of the laser beam.

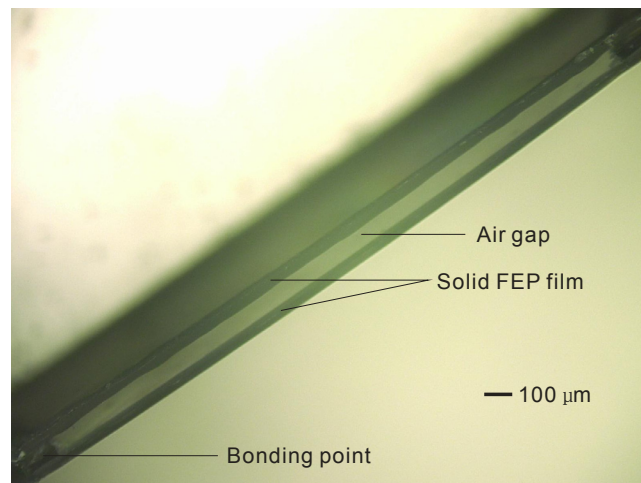


Figure 9.5: The optical-microscopy image illustrates the cross section of the FEP-sandwich covering one mesh unit.

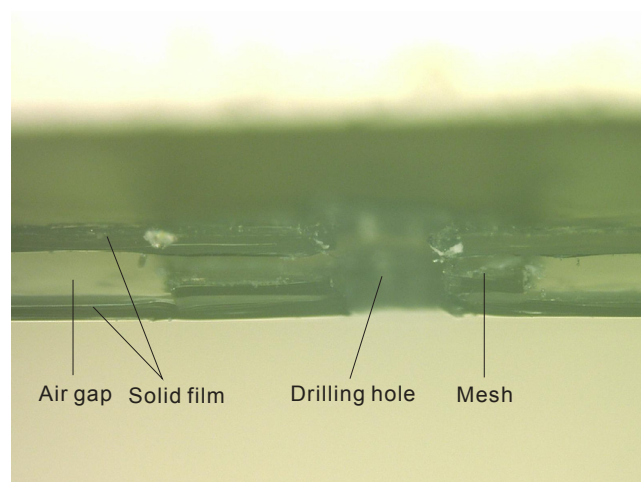


Figure 9.6: Image of a welding point. Imperfect welding led to some additional separation between the outer films and the grid.

According to the cross-section image, a modified model for the structure is illustrated in figure 9.7. Here the two uniform solid films are considered exactly parallel to each other and the air gap is exactly homogenous. The actual air gap is 70  $\mu\text{m}$  in thickness from the cross section image, taking into account that the thickness of the mesh  $d$  is 50  $\mu\text{m}$ , thus the additional air gap  $X$  is 20  $\mu\text{m}$  in total. It is assumed that the upper and lower additional air gaps both are  $X/2 = 10 \mu\text{m}$ . Thus in the void area, there are air gap of  $d + X = 70 \mu\text{m}$  and FEP of  $2d = 100 \mu\text{m}$ ; in the mesh stripe area, there are air gap of  $X = 20 \mu\text{m}$ , and FEP of  $3d = 150 \mu\text{m}$ . The total sample area is  $29 \times 29 \text{ mm}^2$ . The dielectric permittivity of FEP is approximatively 2.

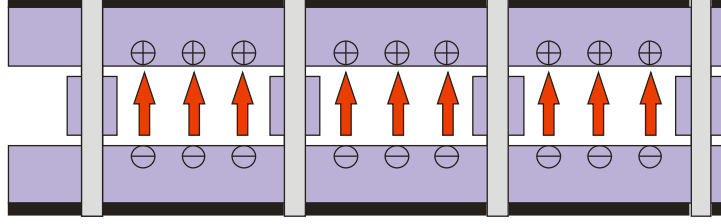


Figure 9.7: A modified model according to the image of cross section. Imperfect welding led to some additional separation between the outer films and the grid.

The capacitance of the FEP-air-FEP area (void area)  $C_1$  is

$$C_1 = \varepsilon_0 \frac{A_1}{d + X + \frac{2d}{\varepsilon_r}} = \varepsilon_0 \varepsilon_r \frac{A_1}{\varepsilon_r \times d + \varepsilon_r \times X + 2d}. \quad (9.1)$$

The capacitance of the FEP-air-FEP-air-FEP area (mesh stripe area)  $C_2$  is

$$C_2 = \varepsilon_0 \frac{A_2}{X + \frac{3d}{\varepsilon_r}} = \varepsilon_0 \varepsilon_r \frac{A_{total} - A_1 - A_{LaserHole}}{\varepsilon_r \times X + 3d}. \quad (9.2)$$

Therefore the total capacitance of a sample is

$$C_{total} = C_1 + C_2 = \varepsilon_0 \varepsilon_r \frac{A_1}{\varepsilon_r \times d + \varepsilon_r \times X + 2d} + \varepsilon_0 \varepsilon_r \frac{A_{total} - A_1 - A_{LaserHole}}{\varepsilon_r \times X + 3d} \approx 72 \times 10^{-12} (F). \quad (9.3)$$

## 9.3 Investigation of piezoelectric properties

### 9.3.1 Limitation of dynamic measurement

The dynamic determination of  $d_{33}$  which is mostly used for polymer foams cannot be applied directly to the sandwich systems. For polymer foams, the whole cellular structure can be compressed; however, for the sandwich, only the films in the void area can be bended, and in principle the stripe area cannot be compressed. If the cross section of the top-electrode is larger



than the area of a void, the most applied force is operated onto the stripes, but not to bend the films. In the present experimental setup for dynamic  $d_{33}$  determination, the diameter of the top-electrode is 11 mm, which is much larger than the dimension of the void (3 mm  $\times$  3 mm), thus this top-electrode cannot properly transfer force to the films. One possible approach is to use a smaller top-electrode, with a cross section smaller than the dimension of the voids. Another possibility is to use air or liquid to transfer static and dynamic pressure to the sample. However, both approaches are not possible due to the technical limit. Alternatively, the resonance measurement (dielectric-resonance spectroscopy) and the acoustic measurement in “loudspeaker mode”, which are based on the reverse piezoelectricity, are suitable for the sandwich structure. In addition, the acoustic measurement in “microphone mode” can also be used, because the mechanical stress is applied by sound wave and the limit with respect to this special structure is avoided.

### 9.3.2 Dielectric-resonance spectroscopy (DRS)

Figure 9.8 shows the dielectric-resonance spectrum for a typical sample. A clear dielectric-resonance peak is observed at the anti-resonance frequency  $f_{res}$  of about 30.9 kHz, demonstrating the piezoelectricity of the FEP-sandwich. The sample shows a capacitance of about 72.2 pF (the real part  $C'$  on the left y-axis), which is in agreement with the approximated value of about 72 pF from the calculation (equation 9.3). If apply the experimental capacitance of 72.2 pF back to equation 9.3, the actual average air-gap thickness of about 68  $\mu\text{m}$  can be calculated. The resonance curve of  $C'$  is well fitted according to the TE (thickness extension) model, as the fit-line (real line in the figure) indicates. Fitting of the dielectric-resonance curves shows an elastic modulus of about 0.30 MPa, an average dielectric permittivity of about 1.49, an electromechanical coupling factor of about 0.054 (error 0.9%), and an piezoelectric  $d_{33}$  coefficient of about 350 pC/N.

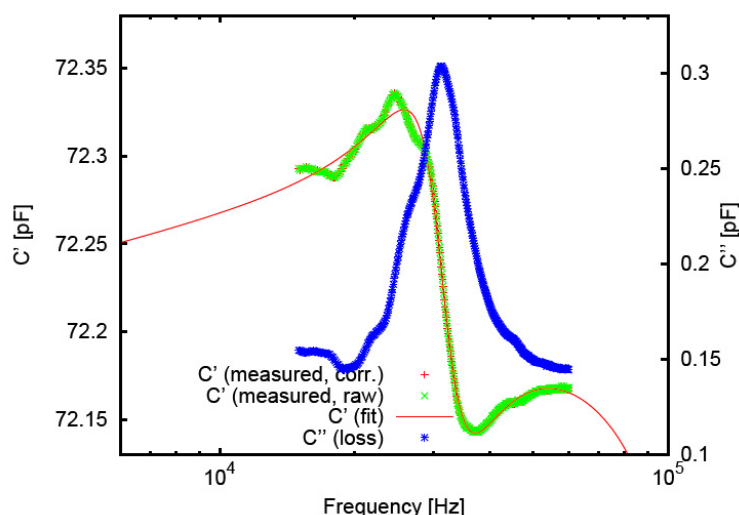


Figure 9.8: Dielectric-resonance spectrum (DRS) for a typical sample with the real part of capacitance  $C'$  (a sudden jump at  $f_{res}$ ) and the imaginary part  $C''$  (a loss peak at  $f_{res}$ ). The real line is the fitting of the measured dotted lines.

The angular anti-resonance frequency  $\omega_{res}$  ( $= 2\pi f_{res}$ ) agrees with the model calculations [Basso \*], in which the  $\omega_{res}$  value of each cell, composed of two membranes and an air gap, is given by

$$\omega_{res} = \sqrt{\omega_1^2 + \gamma_d \frac{\kappa_{pneum}}{d_0}}. \quad (9.4)$$

Here,  $\omega_1$  is the angular resonance frequency of a square membrane in fundamental mode, calculated with the finite-element method. The additional term  $\gamma_d \kappa_{pneum}/d_0$  takes into account the elasticity of the air in the gap (that may be considered as an additional “spring”, characterized by  $\kappa_{pneum}$ ) and depends on the real air-gap thickness  $d_0$ , and on the thermodynamic factor  $\gamma_d$  (between 1 for a perfectly isothermal situation and 1.4 for a perfectly adiabatic one) since there is some heat exchange between the gas and the polymer walls. Figure 9.9 indicates how  $\omega_{res}$  depends on  $d_0$  and on the limiting values of  $\gamma_d$ . Theoretically the possible values of  $\omega_{res}$  should be in the area between the two limiting lines. The point shows the experimental value with the angular resonance frequency of 194 krad/s ( $2\pi \times 30.9$ ) and the air-gap thickness of 68  $\mu\text{m}$ , indicating that in this system, the vibration of the films is very close to an adiabatic process.

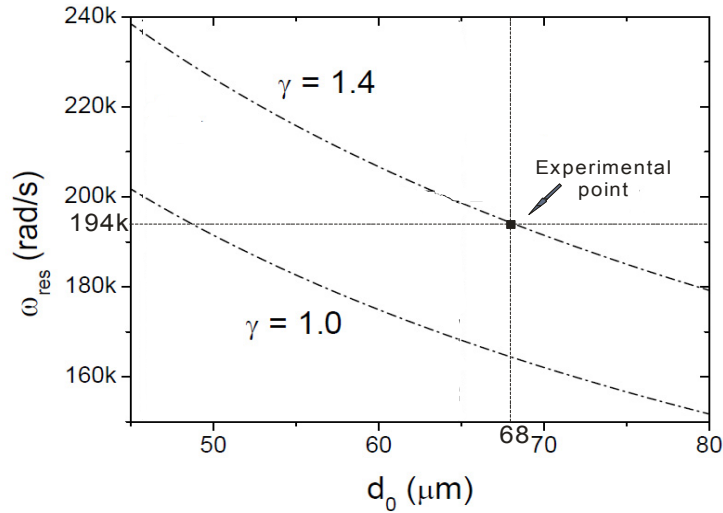


Figure 9.9: Resonance frequency as a function of the air gap thickness  $d_0$  and the thermodynamic factor  $\gamma$  according to equation 9.4. The horizontal and the vertical line indicate the measured value of  $\omega_{res}$  and  $d_0$ , respectively.

### 9.3.3 Acoustic measurement

In the acoustic measurements, samples were investigated in the “loudspeaker mode” in the frequency range from 20 Hz to 25 kHz, which is almost the hearing range of human ears (20 Hz to 20 kHz). Recording distances (the distance between the standard microphone and the sample) were varied as 1, 3, 15, and 30 cm. Only the fundamental and the second harmonic sound signals could be recorded, the third and the higher harmonic signals could not be detected under present experimental conditions.

Figure 9.10 and 9.11 show the fundamental and the second harmonic sound pressure as a function of frequency at each recording distance for a typical sample. No reasonable sound pressure can be achieved at low frequencies from a few dozen to a few hundred Hz. As discussed (section 7.5.3), a short recording distance is limited at relatively higher frequencies although the noise is small, and a longer recording distance can be applied at relatively higher frequencies, but with more noise. The applicable frequency range for each recording-distance is listed in Table 7.2.

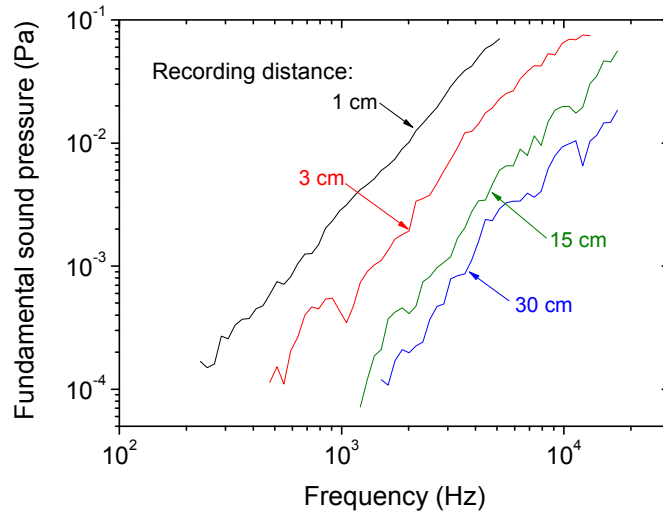


Figure 9.10: Fundamental sound pressure as a function of frequency for different recording distances (the distance between the microphone and the sample) as indicated.

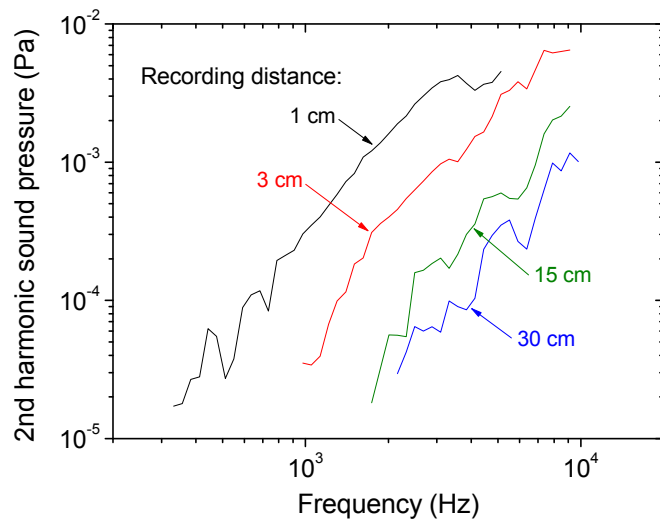


Figure 9.11: The second harmonic sound pressure as a function of frequency for different recording distances (the distance between the microphone and the sample) as indicated.

The piezoelectric  $d_{33}$  coefficients are calculated and plotted as a function of frequency, as illustrated in figure 9.12. The final  $d_{33}$  coefficients are calculated from the combination of the experimental data measured at different recording distances of 1 and 15 cm, taking into account the applicable frequency for different recording distances, and as well the influence from the surrounding noises, as indicated, 1 cm for the frequencies from 300 Hz to 5.5 kHz, and 15 cm for

the frequencies from 5.5 kHz to 20 kHz. In the broad frequency range from 300 Hz to 20 kHz, the sample shows stable  $d_{33}$  coefficients of around 300 pC/N, indicating a constant frequency response. The relatively large fluctuation of  $d_{33}$  may come from the noise of the surroundings. This result is also in agreement with the calculation from the dielectric resonance spectrum which shows around 280 pC/N for the same sample shown in figure 9.12.

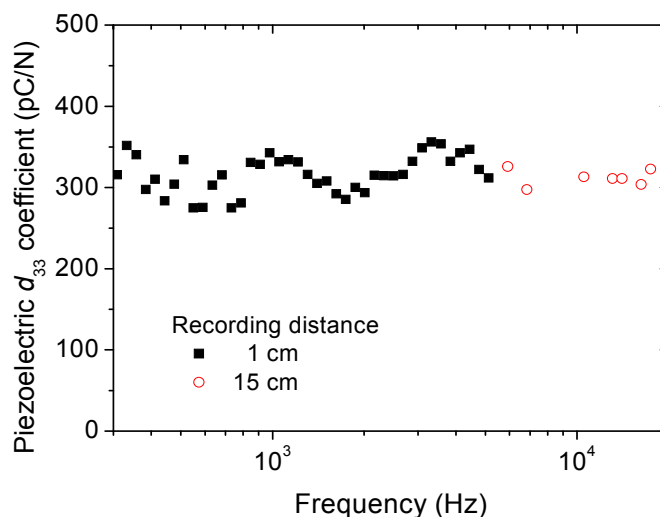


Figure 9.12: Piezoelectric  $d_{33}$  coefficient as a function of frequency. Taking into account the frequency limit for the recording distance and the surrounding noise,  $d_{33}$  coefficients are calculated from the data acquired at different recording distances of 1 cm and 15 cm.

### 9.3.4 Thermal stability of piezoelectricity and its improvement

Dielectric-resonance spectra at elevated temperatures enable the possibility to investigate samples' thermal behavior including the thermal stability of piezoelectricity. Samples were charged at room temperature (RT) and at selected temperatures of 110 and 140 °C, respectively. When charging was performed at elevated temperatures, the voltage was still kept after charging, until samples had cooled down to RT. Dielectric-resonance spectra were measured in the temperature range from 20 to 150 °C, and at the frequencies from 1 kHz to 1 MHz (only the range from 1 to 100 kHz is shown in the spectra). The data were acquired as a function of the frequency under nearly isothermal conditions ( $\Delta T_{\text{max}} = 0.43$  °C) at 10 °C intervals. Figure 9.13 (a), (b), and (c) show the dielectric-loss spectra (imaginary capacitance  $C''$ ) for the samples charged at different temperatures as indicated, respectively.

Resonance peaks are observed at the frequencies of about 30.9, 49.0, and 52.5 kHz for the sample charged at RT, 110 °C, and 140 °C, respectively, when measured at RT. Samples charged at elevated temperatures show higher anti-resonance frequencies than the one charged at RT. During the high-temperature charging, FEP films underwent a thermal annealing process and thereafter films were cooled down to RT again. Therefore, films shrank, and became stiffer than before. As a result, resonance frequencies are increased due to the increased film stiffness by thermal treatment.

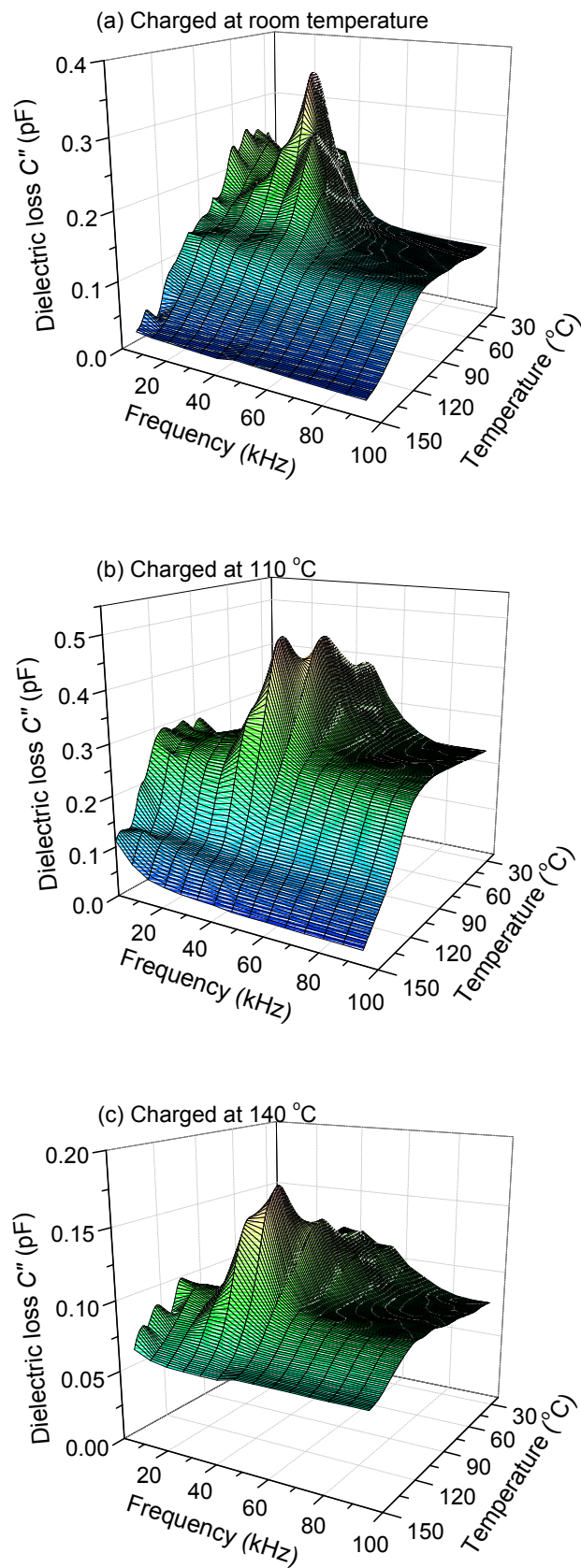


Figure 9.13: Dielectric-loss spectra (imaginary capacitance  $C''$ ) for the sample charged at (a) room temperature, (b) 110 °C, and (c) 140 °C.

With the increase of temperature, the dielectric-loss peaks decrease due to the gradual loss of piezoelectricity (figure 9.13). At the same time, several parameters change as well. Figure 9.14 shows the anti-resonance frequency as a function of the temperature. Here, the anti-resonance frequencies are directly read from the dielectric-loss peaks of the spectra at each temperature. For the sample charged at RT, its anti-resonance frequency increases with the increasing temperature. Because this sample has not undergone any prior thermal annealing, films shrink due to the heat treatment. On the other hand, however, films are fixed at the bonding point. Therefore, they are more and more tautened, which increases the elastic modulus and the resonance frequency. The enhancement of the anti-resonance frequency stops at the temperature of 80 °C, which is approximately the glass-transition temperature ( $T_g$ ) of FEP. Films become soft, especially at temperatures higher than their  $T_g$ , which lowers the elastic modulus. These two opposite effects (tauten and soften) compensate each other, so the elastic modulus and therefore the anti-resonance frequency do not increase. The RT-charged sample does not show any detectable dielectric resonance when treated at temperatures higher than 100 °C. For the samples charged at elevated temperatures, however, their anti-resonance frequencies always decrease with the increasing temperature, especially when the temperature is above 80 °C ( $T_g$  of FEP). Since these samples have been annealed during charging, there is no more shrinkage due to this second thermal treatment. Films become softer, especially when the temperature is above  $T_g$ . Due to the decreased elastic modulus, the anti-resonance frequency is decreased. Figure 9.15 shows the calculated elastic modulus as a function of the temperature. For the sample charged at RT, its modulus increases from about 0.3 MPa and then keeps at around 0.7 MPa; for the samples charged at elevated temperatures, their moduli are always decreasing from the initial value of about 0.8 MPa.

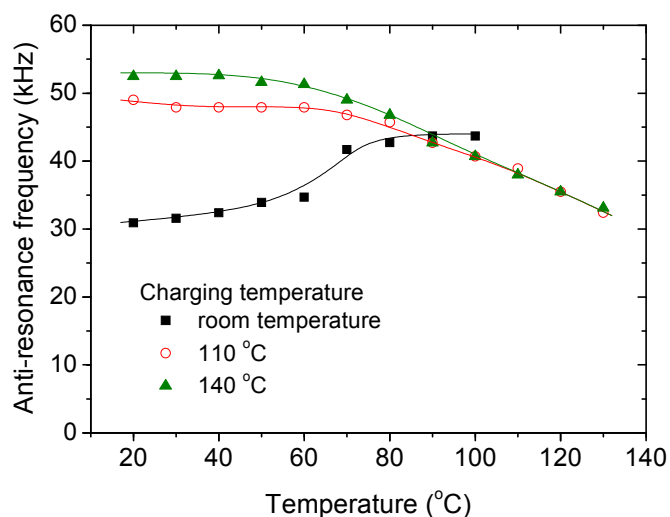


Figure 9.14: Anti-resonance frequency as a function of the temperature for the samples charged at different temperatures as indicated. The lines are to guide the eye.

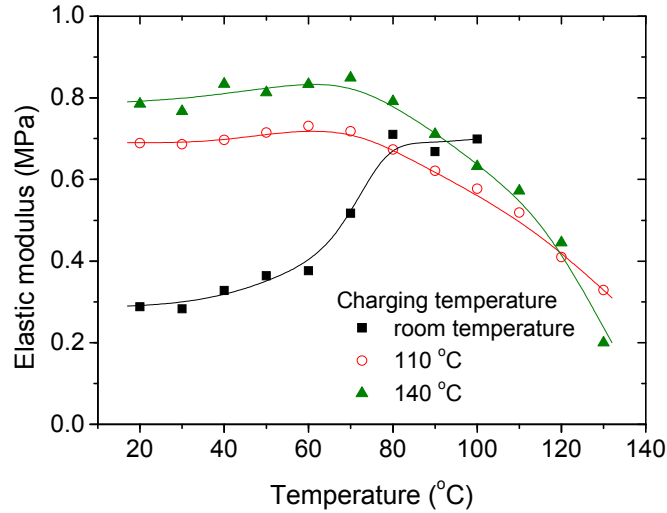


Figure 9.15: Elastic modulus as a function of the temperature for the samples charged at different temperatures as indicated. The lines are to guide the eye.

Figure 9.16 shows the electromechanical coupling factor  $k_{33}$  as a function of the temperature. For the present sandwich samples, their coupling factors are limited less than 0.06, which is almost in the same range as that of PEN foam ferroelectrets, but much smaller than that of  $\beta$ -PVDF which is about 0.5.

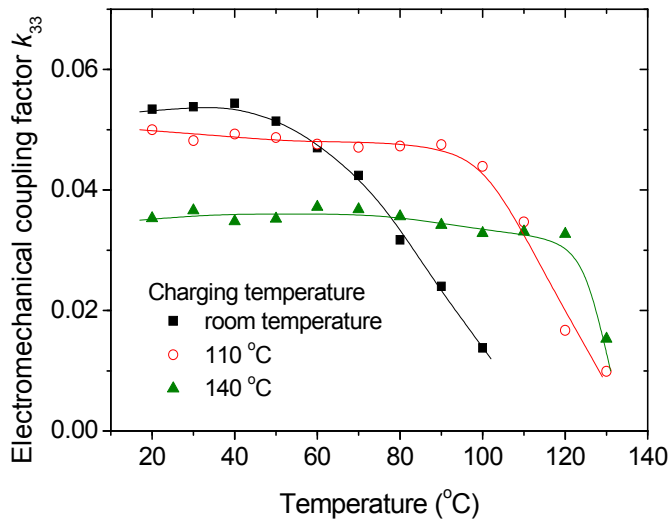


Figure 9.16: Electromechanical coupling factor  $k_{33}$  as a function of the temperature for the samples charged at different temperatures as indicated. The lines are to guide the eye.

Figure 9.17 and 9.18 depict the thermal stability of piezoelectric  $d_{33}$  coefficient, the absolute and the normalized one, respectively. Samples exhibit  $d_{33}$  as high as 350 pC/N when charged at RT, but only 250 and 160 pC/N when charged at 110 and 140 °C, respectively. For the RT-charged sample, there is a significant and continuous decay of  $d_{33}$ , and its piezoelectric activity is almost lost when temperature is above 100 °C, since there is no more resonance peak detectable (Figure 9.13 (a)). The overall piezoelectric thermal stability depends on the stability of

both positive and negative charges. It is, however, known that positive charges are not very stable on RT-charged FEP electrets compared with negative charges [Gerhard-Mulhaupt 1999(1)].

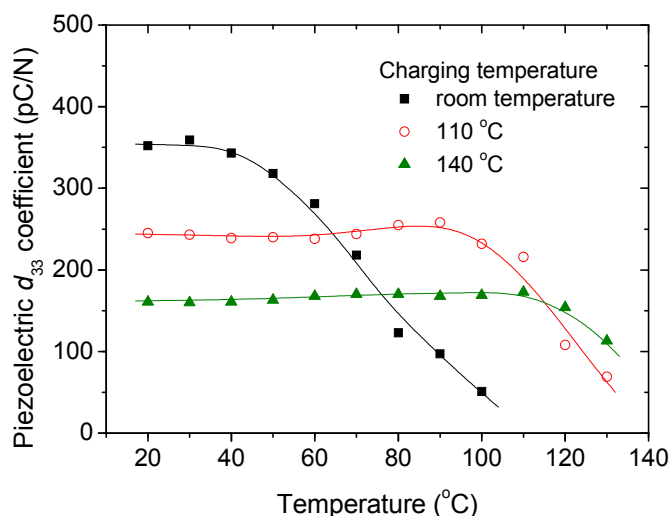


Figure 9.17: Piezoelectric  $d_{33}$  coefficient as a function of the temperature for the samples charged at different temperatures as indicated. The lines are to guide the eye.

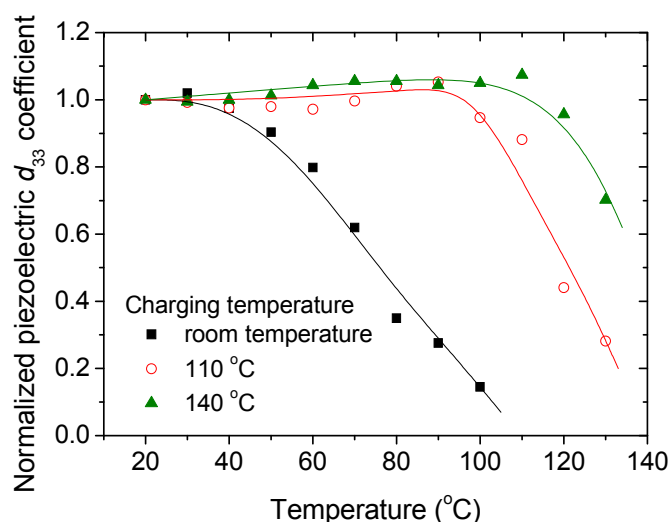


Figure 9.18: Normalized  $d_{33}$  as a function of the temperature for the samples charged at different temperatures as indicated. The lines are to guide the eye.

One possible way to improve the thermal charge stability is charging at elevated temperatures [Perlman 1974, Turnhout 1975, Seggern 1984, Xia 1991]. It is also found that samples charged at elevated temperatures show much better thermal stability than those charged at RT. The higher the charging temperature, the better is the stability. For the sample charged at 110 °C, there is no decay of  $d_{33}$  until 100 °C, and 85% of initial  $d_{33}$  is still retained at 110 °C. If it is treated at 120 °C or higher, there is a significant loss of piezoelectricity. For the sample charged at 140 °C, however, there is nearly no loss of piezoelectricity at least up to 110 °C, only a slight decay of  $d_{33}$  at 120 °C, while more than 70% of initial  $d_{33}$  is still retained at 130 °C. Although samples are still piezoelectric at even higher temperatures, no obvious resonance curve can be observed, because



the height of the resonance profile of the samples with low  $d_{33}$  approach the resolution limit of the dielectric spectrometer [Mellinger 2003]. It should be noted, that charging at elevated temperature itself lowers the initial piezoelectricity. Therefore, for a special application, a proper charging temperature should be considered taking into account both the stability and the magnitude.

In the sandwich structure, the polymer films are used as the charge holder, and thus any polymer that has good charge-storage ability can be candidate for this sandwich ferroelectrets. The thermal stability of piezoelectricity is determined by two aspects: the stability of the cellular structure, and the stability of the dipoles, i.e. the charges. For the structure, lots of polymer films can be applied at the temperatures even higher than 200 °C, which is much above the working temperatures for sensors and actuators. Therefore, the most critical point is the thermal stability of the charges. For polymer foams, the charge-storage mechanism is quite complicated, because after a series of preparation arrangements, the electrical and thermal properties of the polymer may be changed largely. However, in the case of the sandwich, where the charges are stored on the surfaces of the solid films, the charge-storage mechanism is much simpler. The dipole stability can be determined directly by the surface charge stability on the solid films. Different charging conditions and charging methods can be applied in order to improve the thermal charge stability on the solid polymer films.

## 9.4 Extension of structure

Due to its versatility, there is no limit with respect to the structure size and shape; therefore the sandwich structure can be extended into various forms according to actual requirements. Instead of square mesh, strip-shaped mesh can also be applied, as shown in figure 9.19, cuboid air-gaps are sandwiched between the solid films. Here, only two sides of a void are fixed, so the vibration behaviors will be different from the samples with square mesh, where four sides of a void are fixed. Figure 9.20 illustrates another structure arrangement for a five-layer system, where crossbedded meshes are sandwiched between three layers of solid film. It can also be considered as the combination of two three-layer sandwiches shown in figure 9.1. In this system, because the mesh-stripe in one layer is facing the mesh-hole in the other layer, the stress applied to the mesh-stripe can be transferred to the corresponding voids. Consequently, the dynamic technique for piezoelectricity determination, which is limited on the three-layer sandwiches as discussed in section 9.3.1, can be applied here. This crossbedded arrangement overcomes the shortcoming that in the three-layer sandwiches the external force can not bend the films if the force cross section is larger than the dimension of the voids, and therefore broaden the application range of the layer-system. However, there is a special requirement for the bonding that the drilling hole should not be punched throughout the whole sample, as shown in the figure, in order not to destroy the cellular voids. Therefore a laser-bonding with highly controlled penetration depth is required. Alternatively, other possible bonding approaches based on thermal or chemical techniques can be applied.

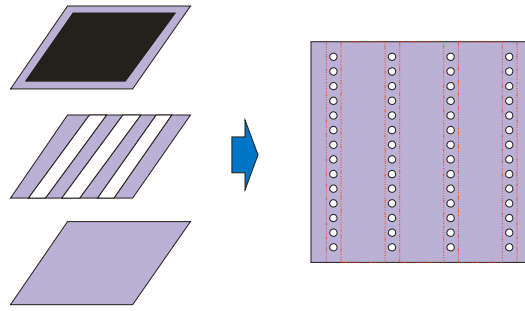


Figure 9.19: Structure extension: sandwich with strip-shaped mesh.

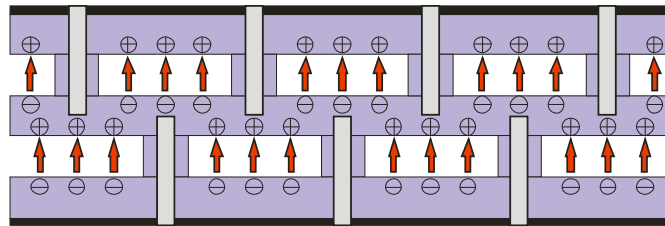


Figure 9.20: Structure extension: five-layer system with crossbedded meshes.

# Chapter 10

## Conclusion and outlook

### 10.1 Conclusion

In this work, novel polymer ferroelectrets have been developed from polyethylene naphthalate (PEN) and fluorinated ethylene-propylene (FEP). Two types of the cellular structure were prepared: foam system with microscopic voids and layer system (sandwich) with macroscopic voids. The structure formation processes, the electrical charging procedures, and the resulting piezoelectric properties were investigated by means of several techniques and discussed in detail.

Recently, polyethylene-terephthalate (PET) foams were developed for ferroelectret applications which show appreciable piezoelectric properties such as enhanced working temperatures. Both PEN and PET belong to the family of polyester, but the thermal, mechanical, electrical, and barrier properties of PEN are superior to those of PET, which make PEN an attractive candidate for new thermally stable ferroelectrets. In this work, PEN foams were successfully developed from commercial solid films (initial density of  $1.45 \text{ g/cm}^3$ ) by means of a procedure consisting of “voiding + inflation + stretching”. Due to its good solubility in several polymers, supercritical carbon dioxide ( $\text{CO}_2$ ) was chosen as the foaming agent. Solid PEN films can be sufficiently saturated by supercritical  $\text{CO}_2$  at room temperature (RT) for a few hours at pressures of 100 – 200 bar. The voiding temperatures should be higher than the glass-transition temperature ( $T_g$ ) of PEN ( $122 \text{ }^\circ\text{C}$ ), and a high temperature results in a stronger voiding and therefore lowers the sample density. Samples voided at  $180 \text{ }^\circ\text{C}$  show densities as low as  $0.6 \text{ g/cm}^3$ . A controlled inflation was performed in order to enlarge the void dimension. Cellular voids were filled with pressurized  $\text{CO}_2$  and were expanded by the fast reduction of the surrounding high pressure, where the change of structure was thereafter stabilized by a thermal treatment. An additional biaxial stretching with ratios of 1.2 – 2.0 was also performed in order to decrease the elastic modulus of the sample. The scanning electron microscopy (SEM) images demonstrate the successful development of the PEN foams. Samples show porosities of 30% – 40% and most voids have void heights below  $12 \text{ }\mu\text{m}$ . Samples could be properly charged by corona charging or by contact charging. The samples charged with corona-tip voltage of 25 kV in air at atmospheric pressure show surface potential up to 7 kV and average internal electric field in the voids as high as 250 MV/m, and those charged with 50 kV in  $\text{SF}_6$  at 3 bar show much higher surface potential up to 12 kV and internal field as high as 400 MV/m. According to Paschen breakdown, the internal field in the voids is high enough to generate sufficient gas-breakdown, which was also demonstrated by observing the light emission during charging. If the charging voltage is higher than the threshold, piezoelectric  $d_{33}$  coefficient increases with the voltage until a saturation value. Clear dielectric-resonance spectra demonstrate the piezoelectricity of the PEN foams. Samples prepared in this work show elastic moduli of 1 – 12 MPa, anti-resonance frequencies of

0.2 – 0.8 MHz, permittivities of about 2, and electromechanical coupling factors of 0.016 – 0.069. The samples with low elastic moduli show larger  $d_{33}$  and exhibit  $d_{33}$  up to a few hundred pC/N when properly foamed and charged. In a short-term thermal treatment of one hour, the samples charged at RT retain the same  $d_{33}$  up to 80 °C, and more than 70% of their initial  $d_{33}$  up to 100 °C. In long term treatment, 40% of the initial  $d_{33}$  is still retained after 5 days at 100 °C. PEN foams show superior thermal stability than PP and PET foams, for which the working temperatures are limited below 60 and 80 °C, respectively. Controlled annealing at elevated temperatures after charging can improve the thermal stability up to the respective annealing temperatures; however, the annealing process itself reduces the initial  $d_{33}$ . Electric charging at elevated temperatures is also possible to improve the thermal stability. It is found that samples charged at elevated temperatures show much better thermal stability than those charged at RT. In the short-term thermal treatment of 1 hour, samples almost retain their initial  $d_{33}$  up to the respective charging temperature. However, a too high temperature may deform the cellular structure and therefore lower the initial  $d_{33}$ . Generally speaking, charging temperatures of 100 – 110 °C are preferred, where samples can exhibit both appreciable piezoelectricity and thermal stability. Limited by the  $T_g$  of PEN (122 °C), samples cannot be properly utilized at the temperatures higher than this temperature. The mechanical fatigue tests (non-stop dynamical  $d_{33}$  measurements) show that samples still exhibit 80% of the initial  $d_{33}$  after 1500 measurement cycles. Further measurements up to 2000 cycles do not decrease the  $d_{33}$  significantly. PEN foams are sensitive to the applied stress, and  $d_{33}$  decreases significantly with increasing external stress due to the increased elastic modulus. The dynamic measurements and the acoustic measurements show that the samples exhibit appreciable frequency response in the frequency range from 2 Hz to 20 kHz.  $d_{33}$  measured and calculated from the dynamic determination, the dielectric-resonance spectra, and the acoustic measurement are highly in agreement with each other, which verifies the reliability of different measurement techniques.

Fluorinated ethylene-propylene (FEP) is a fluoropolymer resin with most of the excellent physical, chemical and electrical properties. In addition, it is a thermoplastic which is melt-processible using conventional injection molding and screw extrusion techniques. The charge-storage abilities for different solid FEP films from Dyneon<sup>®</sup>, Daikin<sup>®</sup>, DuPont<sup>®</sup>, and Goodfellow<sup>®</sup> have been compared by investigating the thermally stimulated decay of surface potential. It is found that the Dyneon<sup>®</sup>- and DuPont<sup>®</sup>-FEP show relatively better thermal charge stabilities. For Dyneon<sup>®</sup>-FEP, the high molar mass films show high viscosity and better thermal charge stabilities. Except for the pure FEP, the films with boron nitride (BN) fillers were also studied. FEP films with BN fillers show better thermal charge stability than the pure films and a higher filler concentration results in a better charge stability. A one-step process was operated to void FEP films. After the supercritical-CO<sub>2</sub> saturation at 300 bar, the high pressure was fast reduced and at the same time, the high-temperature voiding was performed at 235 °C. A biaxial stretching with ratio of 1.3 – 1.8 was thereafter performed in order to lower the void heights (The sample preparation was done by the project partner at the Institute of Polymer Material, University of Erlangen-Nürnberg, Germany). Structure investigations by means of SEM show that the present FEP foams have porosities of about 50% and most void heights are below 12 μm. Samples' elastic moduli depend strongly on the applied stress, which increase dramatically from 5 to 45 MPa with the stress increased to 150 kPa. However, the charging of the present samples was not so

successful. For the samples charged with corona tip-voltage up to 50 kV, the surface potential and the corresponding average internal electric field in the voids are limited below 4.5 kV and 45 MV/m, respectively, which is not high enough to generate sufficient gas-breakdown inside the voids. For contact charging, the breakdown of the polymer bulk shows that the FEP has very low breakdown strength below 12.8 MV/m, where the internal field in the voids is limited lower than 25.5 MV/m, indicating that no sufficient internal gas-breakdown can be triggered. As a result, only parts of the samples show reasonable  $d_{33}$ , where half of them show very low  $d_{33}$  less than 5 pC/N, the most rest show  $d_{33}$  of 5 – 25 pC/N, and the highest  $d_{33}$  is about 40 pC/N. In the mechanical fatigue test, sample still exhibits  $d_{33}$  of about 75% of its initial value after about 2000 measurement-cycles, and further measurements up to 5000 cycles do not lower the  $d_{33}$  significantly, meaning that the present cellular structures of FEP foams is appreciable for potential ferroelectret applications. As expected, piezoelectricity decreases significantly with increasing stress due to the largely increased elastic modulus. The dynamic measurements also show that in the frequency range from 2 to 600 Hz,  $d_{33}$  coefficients are stable.

Although polymer-foam ferroelectrets are very attractive, however, some shortcomings, such as the relatively low working temperatures, still limit their applications. More important, the piezoelectric properties of the polymer foams strongly depend on the cellular morphology, i.e. on the size and the distribution of the voids. On the other hand, the controlled preparation of an optimized cellular structure is still technically a challenge. Consequently, new ferroelectrets based on layer systems (sandwich) have been prepared from solid FEP films due to the excellent charge-storage abilities of FEP. An FEP mesh containing regular grid of holes prepared by means of laser cutting was sandwiched between two solid FEP films. Samples were charged in contact and thereafter locally fused by means of laser bonding. With this easy-handling and versatile preparation technique, well-designed macroscopic cellular structure with uniform voids is formed, and there is no limit with respect to sample size and shape. Dielectric-resonance spectra demonstrate the piezoelectricity of the FEP sandwiches. Samples show elastic moduli of about 0.3 MPa, anti-resonance frequencies of about 30 kHz, permittivities of about 1.5, electromechanical coupling factors of about 0.05, and appreciable piezoelectric  $d_{33}$  coefficient as high as 350 pC/N. For the samples charged at RT, their elastic moduli increase with the increasing treatment temperature until the  $T_g$  of FEP (about 80 °C) due to the shrinkage and the resulting tautness of the films. However, the RT-charged samples do not show appreciable thermal stability because the positive charges are not so stable when thermally treated. Samples charged at elevated temperatures show relatively larger initial elastic moduli up to 0.8 MPa due to the thermal annealing during the charging, and become softer when heated again. It is found that the samples charged at elevated temperatures show much improved thermal stabilities than those charged at RT, and they can mostly be utilized up to the respective charging temperatures. Although high charging temperatures lower the initial  $d_{33}$ , the samples charged at 140 °C still exhibit appreciable  $d_{33}$  as high as 160 pC/N. In the short-term thermal treatment of 1 hour, samples charged at 140 °C retain the same  $d_{33}$  at least to 120 °C, and 70% of the initial  $d_{33}$  up to 130 °C. The acoustic measurements show that in the frequency range from 200 Hz to 20 kHz, the FEP sandwiches exhibit stable  $d_{33}$  coefficients, indicating a appreciable frequency response in this range.

	PEN foam	FEP foam	FEP sandwich
Preparation	voiding + inflation + stretching	voiding + stretching	sandwiching + laser bonding
Structure	lens-shaped voids, with size and shape distributions, porosity about 30%	lens-shaped voids, with size and shape distributions, porosity about 50%	well-designed, uniform voids
Anti-resonance frequency	0.2 – 0.8 MHz	----- -----	30 kHz
Elastic modulus	1 – 12 MPa (Dielectric-resonance spectra)	5 – 40 MPa (dynamic measurement)	0.3 MPa (Dielectric-resonance spectra)
Electromechanical coupling factors	0.016 – 0.069	----- -----	0.05
Piezoelectric $d_{33}$ coefficient	up to 500 pC/N	up to 40 pC/N	350 pC/N
Working temperature	80 – 100 °C for the samples charged at room temperature, up to 120 °C for the samples charged at suitable elevated temperatures (at the price of lower $d_{33}$ of a few dozen pC/N).	----- ----- ----- ----- ----- ----- -----	about 60 °C for the samples charged at room temperature, up to 130 °C for the samples charged at suitable elevated temperatures (at the price of lower $d_{33}$ below 200 pC/N).
Frequency response	stable $d_{33}$ at 2 Hz – 20 kHz (dynamic measurement and acoustic measurement)	stable $d_{33}$ at 2 Hz – 600 Hz (dynamic measurement)	stable $d_{33}$ at 200 Hz – 20 kHz (dynamic measurement and acoustic measurement)

Table 10.1: Summary of the properties for the PEN-foam, FEP-foam, and FEP-sandwich ferroelectrets.

## 10.2 Outlook

Further research is needed in order to improve and optimize the structure preparation process for polymer foams. Under present experimental conditions, the porosity is limited below 40% for PEN foams, and the foaming of the polymer bulk is inhomogeneous. Different experimental parameters can be varied to achieve the optimized cellular structure. A new foaming system can be designed, with built-in high-pressure saturation and high-temperature voiding equipments. With the standard foaming technique, the reproducibility can be highly improved and therefore makes it possible for industrial production on large scale.

The reason for the unappreciable electric charging in the present FEP foams should be investigated. The electric properties for the as-prepared FEP foams are not suitable for effective charging: breakdown of the FEP bulk occurs at relatively low electric field by contact charging, and only low surface potential can be achieved by corona charging. The properties of the FEP may be changed during the foaming process. Some possible improvement, or other foaming techniques, should be proposed.

More heterogeneous polymer-layer systems with prominent macroscopic cellular structures can be suggested. Due to the easy-control of the structure, ferroelectrets with uniform properties can be produced. Usually, the preparation of the macroscopic structure is more easy-handling with lower cost than that of the microscopic structure.

Some proper treatments, such as plasma- or chemical-treatment, are possible to enhance the charge-storage ability both for polymer foams and for polymer layers. The replacement of the gas inside the voids of polymer foams may increase the charging efficiency and therefore enhance the piezoelectric properties. Except for the corona and contact charging, several other charging techniques, e.g. electron beams, can be applied on the polymer layers in order to deposit more stable charges.

The piezoelectric properties under different conditions, such as in humid air, in water and under irradiation, can also be investigated to find the most possible application areas for the ferroelectrets.





# References

## A

[Altafim 2003] R. A. C. Altafim, C. Dias, L. G. Neto, H. C. Basso, C. Murakami, P. R. Veronese, and E. F. Rodrigues, "Piezoelectricity of multi-layers space-charge electrets from Teflon FEP film with homogeneous voids distributed on its surface", Annual Report, Conference on Electrical Insulation and Dielectric Phenomena, 19-22 October 2003, Albuquerque, NM, USA (IEEE Service Center, Piscataway, NJ, USA 2003), pp. 225-228.

[Altafim 2006] R. A. C. Altafim, H. C. Basso, R. A. P. Altafim, L. Lima, C. V. de Aquino, L. G. Neto, and R. Gerhard-Multhaupt, "Piezoelectrets from thermo-formed bubble structures of fluoropolymer-electret films", IEEE Trans. Dielect. Electr. Insul., vol. 13 (5), pp. 979-985, 2006.

[Altafim 2009] R. A. P. Altafim, X. Qiu, W. Wirges, R. Gerhard, R. A. C. Altafim, H. C. Basso, W. Jenninger, and J. Wagner, "Template-based fluoroethylenepropylene piezoelectrets with tubular channels for transducer applications", J. Appl. Phys., vol. 106 (1), no. 014106, 2009.

[Anderson 2002] R. A. Anderson, R. R. Lagasse, E. M. Russick, and J. L. Schroeder, "Effects of void size and gas content on electrical breakdown in lightweight, mechanically compliant, void-filled dielectrics", J. Appl. Phys., vol. 91 (5), pp. 3205-3212, 2002.

[Arora 1999] K. A. Arora, A. J. Lesser, and T. J. McCarthy, "Synthesis, characterization, and expansion of Poly(tetrafluoroethylene-co-hexafluoropropylene)/Polystyrene blends processed in supercritical carbon dioxide", Macromol., vol. 32 (8), pp. 2562-2568, 1999.

## B

[Backman 1990] J. Backman. "Audio applications of electrothermomechanical film (ETMF)", J. Aud. Eng. Soc., vol. 38 (5), pp. 364-371, 1990.

[Basso 2007] H. C. Basso, R. A. P. Altafim, R. A. C. Altafim, A. Mellinger, P. Fang, W. Wirges, and R. Gerhard, "Three-layer ferroelectrets from perforated Teflon<sup>®</sup>-PTFE 1ms fused between two homogeneous Teflon<sup>®</sup>-FEP 1ms", Annual Report, Conference on Electrical Insulation and Dielectric Phenomena, 14-17 October 2007, Vancouver, Canada (IEEE Service Center, Piscataway, NJ, USA 2007), pp. 453-456.

[Basso \*] unpublished.

[Bauer 2004] S. Bauer, R. Gerhard-Multhaupt, and G. M. Sessler, "Ferroelectrets: soft electroactive foams for transducers", Physics Today, vol. 57 (2), pp. 37-43, 2004.

[Bauer 2006] S. Bauer, “Piezo-, pyro- and ferroelectrets: soft transducer materials for electromechanical energy conversion”, IEEE Trans. Dielect. Electr. Insul., vol. 13 (5), pp. 953-962, 2006.

[Bazelyan 1998] E. M. Bazelyan and Y. P. Raizer, *Spark discharge*, CRC Press, Boca Raton, FL, 1998, p. 32.

[Behrendt 2006] N. Behrendt, G. Greiner, F. Fisher, T. Frese, V. Altstädt, H. -W. Schmidt, R. Giesa, J. Hillenbrand, and G. M. Sessler, “Morphology and electret behaviour of microcellular high glass temperature films”, Appl. Phys. A: Mater. Sci. Process., vol. 85 (1), pp. 87-93, 2006.

[Blinov 2000] L. M. Blinov, V. M. Fridkin, S. P. Palto, A. V. Bune, P. A. Dowben, and S. Ducharme, “Two-dimensional ferroelectrics”, Physics Uspekhi, vol. 43 (3), pp. 243-257, 2000.

## C

[Cooper 2003] A. I. Cooper, “Porous materials and supercritical fluids”, Adv. Mater., vol. 15 (13), pp. 1049-1059, 2003.

## D

[Dansachmüller 2005] M. Dansachmüller, R. Schwödiauer, S. Bauer-Gogonea, S. Bauer, M. Paajanen, and J. Raukola, “Elastic and electromechanical properties of polypropylene foam ferroelectrets”, Appl. Phys. Lett., vol. 86 (3), no. 031910, 2005.

## E

[Eliasson 1987] B. Eliasson, M. Hirth, and U. Kogelschatz, “Ozone synthesis from oxygen in dielectric barrier discharges”, J. Phys. D: Appl. Phys., vol. 20 (11), pp. 1421-1437, 1987.

## G

[Gerhard-Multhaupt 1992] R. Gerhard-Multhaupt, G. Eberle, Z. Xia, G. Yang, and W. Eisenmenger, “Electric-field profiles in corona- or electron-beam-charged and thermally treated Teflon PTFE, FEP, and PFA films”, Annual Report, Conference on Electrical Insulation and Dielectric Phenomena, 18-21 October 1992, Victoria, Canada (IEEE Service Center, Piscataway, NJ, USA 1992), pp. 61-66.

[Gerhard-Multhaupt 1999(1)] R. Gerhard-Multhaupt (Ed.), *Electrets*, 3<sup>rd</sup> Edition, vol. 2, Laplacian Press, Morgan Hill, California, USA, 1999, ch. 9-10.

[Gerhard-Multhaupt 1999(2)] R. Gerhard-Multhaupt (Ed.), *Electrets*, 3<sup>rd</sup> Edition, vol. 2, Laplacian Press, Morgan Hill, California, USA, 1999, ch. 9, pp. 12-15, ch. 10, pp. 49-52.

[Gerhard-Multhaupt 2002] R. Gerhard-Multhaupt, “Less can be more: Holes in polymers lead to a new paradigm of piezoelectric materials for electret transducers”, *IEEE Trans. Dielect. Electr. Insul.*, vol. 9 (5), pp. 850-859, 2002.

[Giacometti 1999] J. A. Giacometti, S. Fedosov, and M. M. Costa, “Corona charging of polymers: Recent advances on constant current charging”, *Braz. J. Phys.*, vol. 29, no. 2, pp. 269-279, 1999.

[Gibson 1997] L. J. Gibson and M. F. Ashby, *Cellular solids: structure and properties*, 2<sup>nd</sup> Edition, Cambridge University Press, Cambridge, UK, 1997, ch. 5-6.

[Gonzalo 2005] J. A. Gonzalo and Basilio Jimenez (Ed.), *Ferroelectricity: The Fundamentals Collection*, WILEY-VCH Verlag GmbH & Co. KGaA, Weinheim, 2005, ch. Foreword.

[Graz 2006] I. Graz, M. Kaltenbrunner, C. Keplinger, R. Schwödiauer, S. Bauer, S. P. Lacour, and S. Wagner, “Flexible ferroelectret field-effect transistor for large-area sensor skins and microphones”, *Appl. Phys. Lett.*, vol. 89 (7), no. 073501, 2006.

[Guarrotxena 2000] N. Guarrotxena, H. Millán, G. M. Sessler, and G. Hess, “Charge decay properties of poly(propylene) samples (PP) with various stereochemical compositions”, *Macromol. Rapid Commun.*, vol. 21 (10), pp. 691-696, 2000.

## H

[Hämäläinen 1996] M. K. Hämäläinen, J. K. Parvianen, and T. Jaaskelainen, “A novel micromovement actuator manufactured using plastic electromechanical film”, *Rev. Sci. Instrum.*, vol. 67 (4), pp. 1598-1601, 1996.

[Hillenbrand 2000] J. Hillenbrand and G. M. Sessler, “Piezoelectricity in cellular electret films”, *IEEE Trans. Dielect. Electr. Insul.*, vol. 7 (4), pp. 537-542, 2000.

[Hillenbrand 2004] J. Hillenbrand and G. M. Sessler, “High-sensitivity piezoelectric microphones based on stacked cellular polymer films”, *J. Acoust. Soc. Am.*, vol. 116 (6), pp. 3267-3270, 2004.

[Hillenbrand 2005] J. Hillenbrand, G. M. Sessler, and X. Zhang, “Verification of a model for the piezoelectric  $d_{33}$  coefficient of cellular electret films”, *J. Appl. Phys.*, vol. 98 (6), no. 064105, 2005.

[Hougham 1999] G. Hougham, P. E. Cassidy, K. Johns, and T. Davidson (Ed.), *Fluoropolymers 2. Properties*, Kluwer Academic/Plenum Publishers, New York, USA, 1999.

[Hu 2006] Z. Hu and H. von Seggern, “Breakdown-induced polarization buildup in porous fluoropolymer sandwiches: a thermally stable piezoelectret”, *J. Appl. Phys.*, vol. 99 (2), no. 024102, 2006.

## I

[IEEE Micro Electro Mechanical Systems Workshop 1991] IEEE Micro Electro Mechanical Systems Workshop, January-February 1991, Nara, Japan, p. 118.

## J

[Jacobs 2004] M. A. Jacobs, “Measurement and modeling of thermodynamic properties for the processing of polymers in supercritical fluids”, Dissertation, Technische Universiteit Eindhoven, 2004.

[Japon 2000] S. Japon, Y. Leterrier, and J. -A. E. Manson, “Recycling of Poly(ethylene Terephthalate) into closed-cell foams”, *Polym. Eng. Sci.*, vol. 40 (8), pp. 1942-1952, 2000.

## K

[Kawai 1969] H. Kawai, “Piezoelectricity of poly(vinylidene fluoride)”, *Japan J. Appl. Phys.*, vol. 8 (7), pp. 975-976, 1969.

[Kogelschatz 1990] U. Kogelschatz, “Silent discharges for the generation of ultraviolet and vacuum ultraviolet excimer radiation”, *Pure Appl. Chem.*, vol. 62 (9), pp. 1667-1674, 1990.

[Kogelschatz 2001] U. Kogelschatz and J. Salge, “Fundamental aspects and applications”, *Low Temperature Plasma Physics*, edited by R. Hippler, S. Pfau, M. Schmidt, and K. H. Schoenback, Wiley VCH, New York, USA, 2001, ch. 13, pp. 331-357.

[Kogelschatz 2003] U. Kogelschatz, “Dielectric-barrier discharges: Their history, discharge physics, and industrial applications”, *Plasma Chem. Plasma Process.*, vol. 23 (1), pp. 1-46, 2003, and references therein.

[Krause 2001] B. Krause, G. Koops, N. F. A. van der Vegt, M. Wessling, M. Wübbenhorst, and J. van Turnhout, “Novel thin film polymer foaming technique for low and ultra low-k dielectrics”, *Proceedings, 7<sup>th</sup> International Conference on Solid Dielectrics, 25-29 Jun 2001, Eindhoven, Netherlands (IEEE Service Center, Piscataway, NJ, USA 2001)*, pp. 187-190.

[Kressmann 2001] R. Kressmann, “New piezoelectric polymer for air-borne and water-borne sound transducers”, *J. Acoust. Soc. Am.*, vol. 109 (4), pp. 1412-1416, 2001.

[Künstler 1998] W. Künstler and R. Gerhard-Multhaupt, “Charge profiles in corona- or electrodecharged fluoropolymers”, Annual Report, Conference on Electrical Insulation and Dielectric Phenomena, 25-28 October 1998, Atlanta, Georgia, USA (IEEE Service Center, Piscataway, NJ, USA 1998), pp. 613–616.

## L

[Lekkala 1996] J. Lekkala, R. Poramo, K. Nyholm, and T. Kaikkonen, “EMF force sensor - a flexible electret film for physiological applications”, *Med. Biol. Eng. Comput.*, vol. 34, pp. 67-68, 1996.

[Lekkala 1999] J. Lekkala and M. Paajanen, “EMFi - New electret material for sensors and actuators”, Proceedings, 10<sup>th</sup> International Symposium on Electrets, 22-24 September 1999, Delphi, Greece (IEEE Service Center, Piscataway, NJ, USA 1999), pp. 743-746.

[Liang 2000] M. -T. Liang and C. -M. Wang, “Production of engineering plastics foams by supercritical CO<sub>2</sub>”, *Ind. Eng. Chem. Res.*, vol. 39 (12), pp. 4622-4626, 2000.

[Lindner 2002] M. Lindner, S. Bauer-Gogonea, S. Bauer, M. Paajanen, and J. Rankola, “Dielectric barrier microdischarges: Mechanism for the charging of cellular piezoelectric polymers”, *J. Appl. Phys.*, vol. 91 (8), pp. 5283-5287, 2002.

## M

[Mellinger 2003] A. Mellinger, “Dielectric resonance spectroscopy: a versatile tool in the quest for better piezoelectric polymers”, *IEEE Trans. Dielectr. Electr. Insul.*, vol. 10 (5), pp. 842-861, 2003.

[Mellinger 2006] A. Mellinger, M. Wegener, W. Wirges, R. R. Mallepally, and R. Gerhard-Multhaupt, “Thermal and temporal stability of ferroelectret films made from cellular polypropylene/air composites”, *Ferroelectrics*, vol. 331, pp. 189-199, 2006.

[Möser 2005] M. Möser, *Technische Akustik*, 6<sup>th</sup> Edition, Springer, 2005.

## N

[Neugeschwandtner 2000] G. S. Neugeschwandtner, R. Schwödauer, M. Vieytes, S. Bauer-Gogonea, S. Bauer, J. Hillenbrand, R. Kressmann, G. M. Sessler, M. Paajanen, and J. Lekkala, “Large and broadband piezoelectricity in smart polymer-foam space-charge electrets”, *Appl. Phys. Lett.*, vol. 77 (23), pp. 3827-3829, 2000.

[Neugeschwandtner 2001] G. S. Neugeschwandtner, R. Schwödauer, S. Bauer-Gogonea, S. Bauer, M. Paajanen, and J. Lekkala, “Piezo- and pyroelectricity of a polymer-foam space-charge electret”, *J. Appl. Phys.*, vol. 89 (8), pp. 4503-4511, 2001.

## O

[Ohigashi 1976] H. Ohigashi, “Electromechanical properties of polarized polyvinylidene fluoride films as studied by piezoelectric resonance method”, *J. Appl. Phys.*, vol. 47 (3), pp. 949-955, 1976.

[Oversluizen 2000] G. Oversluizen, M. Klein, S. de Zwart, S. van Heusden, and T. Dekker, “Discharge efficiency in plasma displays”, *Appl. Phys. Lett.*, vol. 77 (7), pp. 948-950, 2000.

## P

[Paajanen 1999] M. Paajanen, H. Välimäki, and J. Lekkala, “Modelling the sensor and actuator operations of the ElectroMechanical Film EMFi”, *Proceedings, 10<sup>th</sup> International Symposium on Electrets, 22-24 September 1999, Delphi, Greece (IEEE Service Center, Piscataway, NJ, USA 1999)*, pp. 735-738.

[Paajanen 2000(1)] M. Paajanen, H. Välimäki, and J. Lekkala, “Modelling the electromechanical film (EMFi)”, *J. Electrostat.*, vol. 48 (3-4), pp. 193-204, 2000.

[Paajanen 2000(2)] M. Paajanen, J. Lekkala, and K. Kirjavainen, “Electromechanical film (EMFi) - a new multipurpose electret material”, *Sens. Actu. A: Phys.*, vol. 84 (1-2), pp. 95-102, 2000.

[Paajanen 2001(1)] M. Paajanen, “The cellular polypropylene electret material - Electromechanical properties”, *Dissertation, VTT Publications 436, Technical Research Center of Finland, Tampere University of Technology, 2001.*

[Paajanen 2001(2)] M. Paajanen, J. Lekkala, and H. Välimäki, “Electromechanical modeling and properties of the electret film EMFi”, *IEEE Trans. Dielect. Electr. Insul.*, vol. 8 (4), pp. 629-636, 2001.

[Paajanen 2001(3)] M. Paajanen, M. Wegener, and R. Gerhard-Multhaupt, “Understanding the role of the gas in the voids during corona charging of cellular electret films - a way to enhance their piezoelectricity”, *J. Phys. D: Appl. Phys.*, vol. 34 (16), pp. 2482-2488, 2001.

[Paajanen 2002] M. Paajanen, H. Minkkinen, and J. Raukola, “Gas diffusion expansion - increased thickness and enhanced electromechanical response of cellular polymer electret films”, Proceedings, 11<sup>th</sup> International Symposium on Electrets, 1-3 October 2002, Melbourne, Australia (IEEE Service Center, Piscataway, NJ, USA 2002), pp. 191-194.

[Perlman 1974] M. M. Perlman and S. Unger, “Electron-bombardment of electret foils”, Appl. Phys. Lett., vol. 24 (12), pp. 579-580, 1974.

[Phani 1994] A. R. Phani, “Thin films of boron nitride grown by CVD”, Bull. Mater. Sci., vol. 17 (3), pp. 219-224, 1994.

## Q

[Qiu 2007(1)] X. Qiu, A. Mellinger, M. Wegener, W. Wirges, and R. Gerhard, “Barrier discharges in cellular polypropylene ferroelectrets: How do they influence the electromechanical properties”, J. Appl. Phys., vol. 101 (10), no. 104112, 2007.

[Qiu 2007(2)] X. Qiu, A. Mellinger, W. Wirges, and R. Gerhard, “Spectroscopic study of dielectric barrier discharges in cellular polypropylene ferroelectrets”, Appl. Phys. Lett., vol. 91, no. 132905, 2007.

[Qiu 2008(1)] X. Qiu, A. Mellinger, and R. Gerhard, “Influence of gas pressure in the voids during charging on the piezoelectricity of ferroelectrets”, Appl. Phys. Lett., vol. 92 (5), no. 052901, 2008.

[Qiu 2008(2)] X. Qiu and R. Gerhard, “Effective polarization fatigue from repeated dielectric barrier discharges in cellular polypropylene ferroelectrets”, Appl. Phys. Lett., vol. 93 (15), no. 152902, 2008.

## R

[Räisänen 1995] L. Räisänen, K. Kirjavainen, K. Korhonen, and J. Sarlin, “Electromechanical film - a new promising material”, High Technology Finland, pp. 164-165, 1995.

[Rasband 1996] W. S. Rasband, ImageJ, U.S. National Institutes of Health, Bethesda, Maryland, USA, 1996.

[Raukola 1998] J. Raukola, “A new technology to manufacture polypropylene foam sheet and biaxially oriented foam films”, Dissertation, VTT Publications 361, Technical Research Center of Finland, Tampere University of Technology, 1998.

[Raukola 2002] J. Raukola, N. Kuusinen, and M. Paajanen, “Cellular electrets - from polymer granules to electromechanically active films”, Proceedings, 11<sup>th</sup> International Symposium on Electrets, 1-3 October 2002, Melbourne, Australia (IEEE Service Center, Piscataway, NJ, USA 2002), pp. 195-198.

## S

[Saarimäki 2006] E. Saarimäki, M. Paajanen, A. -M. Savijarvi, H. Minkkinen, M. Wegener, O. Voronina, R. Schulze, W. Wirges, and R. Gerhard-Multhaupt, “Novel heat durable electromechanical film: processing for electromechanical and electret applications”, IEEE Trans. Dielect. Electr. Insul., vol. 13 (5), pp. 963-972, 2006.

[Sankaran 2001] R. M. Sankaran and K. P. Giapis, “Maskless etching of silicon using patterned microdischarges”, Appl. Phys. Lett., vol. 79 (5), pp. 593-595, 2001.

[Santos 2001] A. O. dos Santos, W. H. Yaegashi, R. Marcon, B. B. Li, R. V. Gelamo, L. P. Cardoso, J. M. Sasaki, M. A. R. Miranda, and F. E. A. Mello, “Rochelle salt piezoelectric coefficients obtained by x-ray multiple diffraction”, J. Phys.: Condens. Matter, vol. 13 (46), pp. 10497-10505, 2001.

[Savolainen 1989] A. Savolainen and K. Kirjavainen, “Electromechanical film. Part I. Design and characteristics”, J. Macromol. Sci., Part A: Pure Appl. Chem., vol. A26, pp. 583-591, 1989.

[Scheirs 1997] J. Scheirs (Ed.), *Modern Fluoropolymers: High performance polymers for diverse applications*, John Wiley & Sons Ltd, Chichester, UK, 1997.

[Seggern 1984] H. von Seggern and J. E. West, “Stabilization of positive charge in fluorinated ethylene propylene copolymer”, J. Appl. Phys., vol. 55 (7), pp. 2754-2757, 1984.

[Sessler 1981] G. M. Sessler, “Piezoelectricity in polyvinylidene fluoride”, J. Acou. Soci. Am., vol. 70 (6), pp. 1596-1608, 1981.

[Sessler 1998(1)] G. M. Sessler (Ed.), *Electrets*, 3<sup>rd</sup> Edition, vol. 1, Laplacian Press, Morgan Hill, California, 1998, ch. 2, pp. 54-57, 60-66.

[Sessler 1998(2)] G. M. Sessler (Ed.), *Electrets*, 3<sup>rd</sup> Edition, vol. 1, Laplacian Press, Morgan Hill, California, 1998, ch. 7, p. 347.

[Sessler 1998(3)] G. M. Sessler (Ed.), *Electrets*, 3<sup>rd</sup> Edition, vol. 1, Laplacian Press, Morgan Hill, California, 1998, ch. 2, pp. 30-32.

[Sessler 1999(1)] G. M. Sessler and J. Hillenbrand, “Electromechanical response of cellular electret films”, Appl. Phys. Lett., vol. 75 (21), pp. 3405-3407, 1999.



[Sessler 1999(2)] G. M. Sessler and J. Hillenbrand, “Electromechanical response equations of cellular electret films”, Proceedings, 10<sup>th</sup> International Symposium on Electrets, 22-24 September 1999, Delphi, Greece (IEEE Service Center, Piscataway, NJ, USA 1999), pp. 261-264.

[Sessler 1999(3)] G. M. Sessler and J. Hillenbrand, “Electromechanical response of cellular electret films”, Appl. Phys. Lett., vol. 75 (21), pp. 3405-3407, 1999.

[Stark 1994] W. Stark and R. Danz, “Charge stability of Teflon-FEP electrets charged at melting temperatures”, Proceedings, 8<sup>th</sup> International Symposium on Electrets, 7-9 September 1994, Paris, France (IEEE Service Center, Piscataway, NJ, USA 1994), pp. 83-88.

## T

[Taylor 2005] D. M. Taylor and O. Fernández, “Thermal instability of electromechanical films of cellular polypropylene”, IEEE Trans. Dielect. Electr. Insul., vol. 12 (4), pp. 768-778, 2005.

[Tuncer 2005(1)] E. Tuncer, M. Wegener, and R. Gerhard-Multhaupt, “Modeling electro-mechanical properties of layered electrets: application of the finite-element method”, J. Electrostat., vol. 63 (1), pp. 21-35, 2005.

[Tuncer 2005(2)] E. Tuncer, “Numerical calculations of effective elastic properties of two cellular structures”, J. Phys. D: Appl. Phys., vol. 38 (3), pp. 497-503, 2005.

[Turnhout 1975] J. van Turnhout, *Thermally Stimulated Discharge of Polymer Electrets*, Elsevier, Amsterdam, 1975.

## V

[Voronina 2008] O. Voronina, “Structure-property relations in polymer ferroelectrets”, Dissertation, University of Potsdam, 2008.

## W

[Wang 1988] T. T. Wang, J. M. Herbert, and A. M. Glass, *The Applications of Ferroelectric Polymers*, Chapman & Hall, New York, USA, 1998, ch. Introduction.

[Wegener 2002] M. Wegener, M. Paajanen, W. Wirges, and R. Gerhard-Multhaupt, “Corona-induced partial discharges, internal charge separation and electromechanical transducer properties in cellular polymer films”, Proceedings, 11<sup>th</sup> International Symposium on Electrets, 1-3 October 2002, Melbourne, Australia (IEEE Service Center, Piscataway, New Jersey, USA 2002), pp. 54-57.

[Wegener 2004(1)] M. Wegener, S. Bergweiler, W. Wirges, A. Pucher, and R. Gerhard-Multhaupt, “Voided space-charge electrets - piezoelectric transducer materials for electroacoustic applications”, J. Audio Engin. Soc., Convention Paper 6149 (Audio Engineering Society, New York, USA 2004), pp. 1-8.

[Wegener 2004(2)] M. Wegener, W. Wirges, J. Fohlmeister, B. Tiersch, and R. Gerhard-Multhaupt, “Two-step inflation of cellular polypropylene films: void-thickness increase and enhanced electromechanical properties”, J. Phys. D: Appl. Phys., vol. 37 (4), pp. 623-627, 2004.

[Wegener 2004(3)] M. Wegener, W. Wirges, R. Gerhard-Multhaupt, M. Dansachmüller, R. Schwödiauer, S. Bauer-Gogonea, S. Bauer, M. Paajanen, H. Minkkinen, and J. Raukola, “Controlled inflation of voids in cellular polymer ferroelectrets: optimizing electromechanical transducer properties”, Appl. Phys. Lett., vol. 84 (3), pp. 392-394, 2004.

[Wegener 2005(1)] M. Wegener and S. Bauer, “Microstorms in cellular polymers: a route to soft piezoelectric transducer materials with engineered macroscopic dipoles”, ChemPhysChem, vol. 6, pp. 1014-1025, 2005.

[Wegener 2005(2)] M. Wegener, S. Bergweiler, W. Wirges, A. Pucher, E. Tuncer, and R. Gerhard-Multhaupt, “Piezoelectric two-layer stacks of cellular polypropylene ferroelectrets: transducer response at audio and ultrasound frequencies”, IEEE Trans. Ultras. Ferroelectr. Freq. Contr., vol. 52, pp. 1601-1607, 2005.

[Wegener 2005(3)] M. Wegener, W. Wirges, and R. Gerhard-Multhaupt, “Piezoelectric polyethylene terephthalate (PETP) foams - Specifically designed and prepared ferroelectret films ”, Adv. Engi. Mat., vol. 7 (12), pp. 1128-1131, 2005.

[Wegener 2005(4)] M. Wegener, W. Wirges, J. P. Dietrich, and R. Gerhard-Multhaupt, “Polyethylene terephthalate (PETP) foams as ferroelectrets”, Proceedings, 12<sup>th</sup> International Symposium on Electrets, 11-14 September 2005, Salvador, Bahia, Brazil (IEEE Service Center, Piscataway, New Jersey, USA 2005), pp. 28-30.

[Wegener 2005(5)] M. Wegener, M. Paajanen, O. Voronina, R. Schulze, W. Wirges, and R. Gerhard-Multhaupt, “Voided cyclo-olefin polymer films: ferroelectrets with high thermal stability”, Proceedings, 12<sup>th</sup> International Symposium on Electrets, 11-14 September 2005, Salvador, Bahia, Brazil (IEEE Service Center, Piscataway, New Jersey, USA 2005), pp. 47-50.

[Wilson 2007] S. A. Wilson, R. P. J. Jourdian, Q. Zhang, R. A. Dorey, C. R. Bowen, M. Willander, Q. U. Wahab, M. A. H. Safaa, O. Nur, E. Quandt, C. Johansson, E. Pagounis, M. Kohl, J. Matovic, B. Samel, W. van der Wijngaart, E. W. H. Jager, D. Carlsson, Z. Djinovic, M. Wegener, C. Moldovan, R. Iosub, E. Abad, M. Wendlandt, C. Rusu, and K. Persson, “New materials for micro-scale sensors and actuators: an engineering review”, Mater. Sci. Eng. R, vol. 56, pp. 1-129, in particular pp. 78-83 by M. Wegener, 2007.

[Wirges 2007] W. Wirges, M. Wegener, O. Voronina, L. Zirkel, and R. Gerhard-Multhaupt, “Optimized preparation of elastically soft, highly piezoelectric, cellular ferroelectrets from nonvoided Poly(ethyleneterephthalate) films”, *Adv. Funct. Mater.*, vol. 17 (2), pp. 324-329, 2007.

[[www.dupontteijinfilms.com](http://www.dupontteijinfilms.com)] Dupont® company

[[www.dyneon.com](http://www.dyneon.com)] Dyneon® company

[[www.emfit.com](http://www.emfit.com)] Emfit® company

[[www.screentec.com](http://www.screentec.com)] Screentec® company

## X

[Xia 1991] Z. Xia, H. Ding, G. Yang, T. Lu, and X. Sun, “Constant-current corona charging of Teflon PFA”, *IEEE Trans. Electr. Insul.*, vol. 26 (1), pp. 35-41, 1991.

[Xu 1998] X. P. Xu and M. J. Kushner, “Multiple microdischarge dynamics in dielectric barrier discharges”, *J. Appl. Phys.*, vol. 84 (8), pp. 4153-4160, 1998.

## Y

[Yang 1993] G. M. Yang, “Thermally stimulated discharge of electron-beam- and corona-charged polypropylene films”, *J. Phys. D: Appl. Phys.*, vol. 26, pp. 690-693, 1993.

## Z

[Zhang 2004] X. Zhang, J. Hillenbrand, and G. M. Sessler, “Improvement of piezoelectric activity of cellular polymers using a double-expansion process”, *J. Phys. D: Appl. Phys.*, vol. 37, pp. 2146-2150, 2004.

[Zhang 2006(1)] X. Zhang, J. Hillenbrand, and G. M. Sessler, “Thermally stable fluorocarbon ferroelectrets with high piezoelectric coefficient”, *Appl. Phys. A: Mater. Sci. Process.*, vol. 84 (1-2), pp. 139-142, 2006.

[Zhang 2006(2)] P. Zhang, Z. Xia, X. Qiu, F. Wang, and X. Wu, “Influence of charging parameters on piezoelectricity for cellular PP film electrets”, *Chin. Phys. Soc.*, vol. 55 (2), pp. 904-909, 2006.

[Zhukov 2007] S. Zhukov, and H. von Seggern, “Breakdown-induced light emission and poling dynamics of porous fluoropolymers”, *J. Appl. Phys.*, vol. 101 (8), no. 084106, 2007.

[Zirke] 2009] L. Zirke, M. Jakob, and H. Münstedt, "Foaming of thin films of a fluorinated ethylene propylene copolymer using supercritical carbon dioxide", J. Supercrit. Fluid., vol. 49 (1), pp. 103-110, 2009.

# Contributions

Parts of this work have been published in the following journals and presented at the listed conferences as oral presentation or poster.

## Publications

“FEP-sandwich piezoelectrets: a new production process and its piezoelectric properties”

Peng Fang, Feipeng Wang, Werner Wirges, Heitor Cury Basso, and Reimund Gerhard  
accepted for publication in Appl. Phys. A, 2010, online publication: 31.08.2010.

“Polyethylene-naphthalate (PEN) ferroelectrets: Cellular structure, piezoelectricity and thermal stability”

Peng Fang, Xunlin Qiu, Werner Wirges, Larissa Zirkel, and Reimund Gerhard  
IEEE Trans. Dielectr. Electr. Insul., vol. 17 (4), pp. 1079-1087, 2010.

“Charging conditions for cellular-polymer ferroelectrets with enhanced thermal stability”

Peng Fang, Werner Wirges, Larissa Zirkel, and Reimund Gerhard  
Proceedings, 13<sup>th</sup> International Symposium on Electrets, 15-17 September 2008, Tokyo, Japan (IEEE Service Center, Piscataway, NJ, USA 2008), p. 104.

“Cellular polyethylene-naphthalate films for ferroelectret applications: foaming, inflation and stretching, assessment of electromechanically relevant structural features”

Peng Fang, Werner Wirges, Michael Wegener, Larissa Zirkel, and Reimund Gerhard  
e-polymers, no. 043, 2008.

“Three-layer ferroelectrets from perforated Teflon<sup>®</sup>-PTFE films fused between two homogeneous Teflon<sup>®</sup>-FEP films”

Heitor Cury Basso, Ruy Alberto Pisani Altafim, Ruy Alberto Correa Altafim, Axel Mellinger, Peng Fang, Werner Wirges, and Reimund Gerhard  
Annual Report, Conference on Electrical Insulation and Dielectric Phenomena, 14-17 October 2007, Vancouver, Canada (IEEE Service Center, Piscataway, NJ, USA 2007), pp. 453-456.

“Cellular polyethylene-naphthalate ferroelectrets: Foaming in supercritical carbon dioxide, structural and electrical preparation, and resulting piezoelectricity”

Peng Fang, Michael Wegener, Werner Wirges, Larissa Zirkel, and Reimund Gerhard  
Appl. Phys. Lett., vol. 90 (19), no. 192908, 2007.

## Presentation at conferences

“FEP-sandwich piezoelectrets: a simple arrangement and the resulting piezoelectric activity”

Peng Fang, Feipeng Wang, Werner Wirges, Heitor Cury Basso, and Reimund Gerhard

Oral presentation, Spring Meeting of the Deutsche Physikalische Gesellschaft, 21-26 March 2010, Regensburg, Germany.

“Preparation of cellular polyethylene-naphthalate piezo- and ferroelectrets: Foaming in supercritical carbon dioxide plus structural improvement through inflation and stretching”

Peng Fang, Werner Wirges, Michael Wegener, Larissa Zirkel, and Reimund Gerhard

Poster, Polydays 2008, 01-02 October 2008, Berlin, Germany.

“Charging conditions for cellular-polymer ferroelectrets with enhanced thermal stability”

Peng Fang, Werner Wirges, Larissa Zirkel, and Reimund Gerhard

Poster, 13<sup>th</sup> International Symposium on Electrets, 15-17 September 2008, Tokyo, Japan.

“Cellular polyethylene-naphthalate piezo- and ferroelectrets: Foaming in supercritical carbon dioxide, structure improvement through inflation and stretching”

Peng Fang, Michael Wegener, Werner Wirges, Larissa Zirkel, and Reimund Gerhard

Poster, Spring Meeting of the Deutsche Physikalische Gesellschaft, 25-29 February 2008, Berlin, Germany.

# Curriculum Vitae

## Personal data

Family name: **Fang**  
Given name: **Peng**  
Gender: Male  
Date of birth: 31.01.1982  
Place of birth: Hunan  
Nationality: China

## Education

- 12.2006-10.2010: Applied Condensed-Matter Physics, Institute of Physics and Astronomy,  
Faculty of Science, University of Potsdam, Germany  
PhD study  
Thesis title: Preparation and Investigation of Polymer-Foam Films and Polymer-Layer  
Systems for Ferroelectrets  
Supervisor: Prof. Dr. Reimund Gerhard
- 10.2004-10.2006: Polymer Science Program,  
Free University of Berlin, Humboldt University of Berlin,  
Technical University of Berlin, and University of Potsdam, Germany  
Degree: Master of Science in Polymer Science  
Thesis title: Preparation and investigation of Polyethylene-naphthalate (PEN)  
ferroelectrets  
Supervisor: Prof. Dr. Reimund Gerhard
- 09.2000-07.2004: Department of Modern Physics, School of Physics,  
University of Science and Technology of China, Hefei, China  
Degree: Bachelor of Science in Applied Physics  
Thesis title: Atmospheric-pressure plasma enhanced chemical vapour deposition  
(PECVD) of SiO<sub>x</sub> films  
Supervisor: Prof. Dr. Rujuan Zhan